Application of deep learning to turbulent combustion modeling of real jet fuel for the numerical prediction of particulate emissions

Andréa Seltz

Normandie Université

THÈSE

Pour obtenir le diplôme de doctorat

Spécialité Energétique

Préparée à l'INSA de Rouen Normandie

APPLICATION OF DEEP LEARNING TO TURBULENT COMBUSTION MODELING OF REAL JET FUEL FOR THE NUMERICAL PREDICTION OF PARTICULATE EMISSIONS

présentée et soutenue par

ANDRÉA SELTZ

Thèse soutenue publiquement le 30 Septembre 2020 devant le jury composé de		
O. GICQUEL	Professeur à l'école CentraleSupélec, EM2C - CNRS	Rapporteur
O. COLIN	Ingénieur de Recherche, CNRS, IFPEN	Rapporteur
F. GRISCH	Professeur à l'INSA de Rouen, CORIA	Examinateur
A. CAYRE	Expert combustion, Safran Aircraft Engines	Examinateur
L. VERVISCH	Professeur à l'INSA de Rouen, CORIA - CNRS	Directeur de thèse
P. DOMINGO	Directrice de recherche CNRS, CORIA - CNRS	Co-directrice de thèse

Thèse dirigée par Luc VERVISCH et Pascale DOMINGO, laboratoire CORIA (UMR 6614 CNRS)

INSA INSTITUT NATIONAL DES SCIENCES APPLIQUÉES ROUEN NORMANDIE

ED PSIME

CORIA UMR 6614

Abstract

With the climate change emergency, pollutant and fuel consumption reductions are now a priority for aircraft industries. In combustion chambers, the chemistry and soot modeling are critical to correctly quantify engines soot particles and greenhouse gases emissions. This thesis aimed at improving aircraft numerical pollutant tools, in terms of computational cost and prediction level, for engines high fidelity simulations. It was achieved by enhancing chemistry reduction tools, allowing to predict CO emissions of an aircraft engines at affordable cost for the industry. Next, a novel closure model for unresolved terms in the LES filtered transport equations is developed, based on neural networks (NN), to propose a better flame modeling. Then, an original soot model for engine high fidelity simulations is presented, also based on NN. This new model is applied to a one-dimensional premixed sooted flame, and finally to an industrial combustion chamber LES with measured soot comparison.

Remerciements

Je tiens à remercier en premier lieu l'ensemble des membres du jury pour l'intérêt montré à ce travail de thèse, ainsi que pour leur présence à ma soutenance malgré la situation anxiogène d'une seconde vague de COVID-19 en France.

Je remercie également mes deux directeurs de thèse qui m'ont guidées, soutenue et fait confiance durant ces trois années et demi de thèse.

Merci aux doctorants du clan SiTCom-B & co, pour leur accueil, leur amitié et la bonne ambiance du bureau. Merci aux petits nouveaux d'avoir perpétué cette ambiance.

Merci à toi Nico sans qui je n'aurai même pas même pas eu connaissance du CORIA et de cette thèse.

Merci également au clan YALES2, les permanents d'abord pour leur encadrement et leur amitié, sans qui cette thèse n'aurai pas pu aller aussi loin, puis aux doctorants, anciens et nouveaux, pour leur soutien et leur amitié.

Je remercie également ma famille de Paris de s'être déplacée pour ma soutenance et pour avoir organisé les réjouissances de la journée.

Un grand merci à mon propriétaire qui m'a soutenu sans faille ces trois dernières années.

Merci également à papi qui m'a inspirée et guidée toutes ces années à Paris vers cette thèse.

À mon père.

Science sans conscience n'est que ruine de l'âme.
François Rabelais (1494-1553)

Contents

Nomenclature

Abbreviations

Symbol	Description
ACARE	Advisory Council for Aeronautics Research in Europe
AFOLU	Agriculture, Forestry and Other Land Use
AI	Artificial Intelligence
CAEP	Committee on Aviation environmental Protection
CORSIA	ICAO's Carbon Offsetting and Reduction Scheme for International Aviation
CFD	Computational Fluid Dynamics
CFL	Courant Friedrichs Lewy
CPU	Central Processing Unit
DNS	Direct Numerical Simulation
DRG	Directed Relation Graph
DRGEP	DRG with Error Propagation
FGM	Flamelet Generated Manifold
GFIR	gradient-free regime identification
GHG	GreenHouse Gas
ICAO	International Civil Aviation Organisation
IPCC	Intergovernmental Panel on Climate Change
INSA	National Institute of Applied Sciences
LEMCOTEC	Low EMissions COre-Engine TEChnologies
LES	Large-Eddy Simulation
LTO	Landing Take-Off
MERMOSE	Mesure et étude de la réactivité des émissions de moteurs aéronautiques
ONERA	Office National d'Études et de Recherches Aérospatiales
ORCh	Optimised and Reduced Chemistry
ORCHydS	Optimised and Reduced Chemistry with Hybrid Soot description
PAH	Polycyclic Aromatic Hydrocarbon
PDF	Probability Density Function

PPS	Pegasor particle sensor
RQL	Rich-Quench-Lean
SKA	Square Kilometre Array
SMPS	Scanning Mobility Particle Sizer
SDSS	Sloan Digital Sky Survey
TFLES	Thickened Flame for Large-Eddy Simulation
VLT	Very Large Telescope
WHO	World Health Organisation
YALES2	LES solver developed at CORIA

Roman letters

Symbol	**Description**	**Unit**
$\mathcal{A}_j$	Pre-exponential factor of reaction j	Variable
c	Normalised progress variable	$-$
C_k	Consumption rate of species k	kg.m^{-3}.s^{-1}
C_p	Mixture mass heat capacity at constant pressure	J.kg^{-1}.K^{-1}
$C_{p,k}$	Specific heat capacity of species k at constant pressure	J.kg^{-1}.K^{-1}
C_p^m	Mixture molar heat capacity at constant pressure	J.mol^{-1}.K^{-1}
$C_{p,k}^m$	Molar heat capacity of species k at constant pressure	J.mol^{-1}.K^{-1}
C_S	Smagorinski model constant	$-$
C_W	Wale model constant	$-$
d_j	Droplet diameter for inlet j	m
D_k^H	Hirschfelder and Curtiss diffusion coefficient of species k	m^2.s^{-1}
D_{kj}	Binary diffusion coefficient of species j into species k	m^2.s^{-1}
d_p	Diameter of particle p	m
D_{th}	Thermal diffusivity coefficient	m^2.s^{-1}
E_j	Activation energy of reaction j	J.mol^{-1}
$\mathcal{E}$	Efficiency factor	$-$
$\mathcal{F}$	Thickening factor	$-$
F	Troe or Lindemann fall-off correction term	$-$
F_{ext}	External force	$-$
F_i	Component i of the force applied onto the Lagrangian particle	$-$
f	Fitness function for genetic algorithm	$-$
f_1	Fitness function for gradient-based optimisation	$-$
$\mathcal{G}$	Convolution kernel of the filter	$-$

H	Mixture mass enthalpy	J.kg^{-1}
H_k	Mass enthalpy of species k	J.kg^{-1}
H^m	Mixture molar enthalpy	J.mol^{-1}
H_k^m	Molar enthalpy of species k	J.mol^{-1}
HRR	Heat Release Rate	J.s^{-1}
h_s	Mass sensible enthalpy	J.kg^{-1}
$h_{s,k}$	Mass sensible enthalpy of species k	J.kg^{-1}
$\mathcal{I}_k$	Error assuming k in QSS	–
K_j	Arrhenius term of reaction j	Variable
K_0	Low pressure limit Arrhenius term of reaction j	Variable
K_∞	High pressure limit Arrhenius term of reaction j	Variable
$K_{\text{eq},j}$	Equilibrium constant of reaction j	–
K_{fj}	Forward Arrhenius term of reaction j	Variable
K_{rj}	Reverse Arrhenius term of reaction j	Variable
k_t	Turbulent kinetic energy	m^2.s^{-2}
L_e	Energetic length	m
L_v	Latent heat of evaporation	J.kg^{-1}
l_k	Kolmogorov length	m
l_t	Integral length	m
L	Characteristic size of the flow	m
$\mathcal{M}_k$	Molecular formula of species k	–
m_p	Mass of particle p	kg
n	Normal to the flame front	–
N_{bits}	Number of chromosome binary digits	–
N_p	Number of stochastic particles	–
N_r	Number of reactions	–
N_{sp}	Number of species	–
P°	Reference pressure	Pa
P	Pressure	Pa
P_k	Production rate of species k	kg.m^{-3}.s^{-1}
P_r	Fall-off pressure correction term	mol.m^{-3}
$\dot{Q}$	External heat sources	W.m^{-3}
$\dot{Q}_m$	Total mass flow rate	kg.s^{-1}
$\dot{q}_m$	Elementary mass flow rate	kg.s^{-1}
$\dot{q}_{m_G}$	Gaseous elementary mass flow rate	kg.s^{-1}
$\dot{q}_{m_L}$	Liquid elementary mass flow rate	kg.s^{-1}

$\dot{Q}_{fj}$	Forward rate of reaction j	mol.m^{-3}.s^{-1}
$\dot{Q}_i$	Heat flux	W.m^{-2}
$\dot{Q}_j$	Rate of reaction j	mol.m^{-3}.s^{-1}
$\dot{Q}_{rj}$	Reverse rate of reaction j	mol.m^{-3}.s^{-1}
$\mathcal{R}$	Ideal gas constant	J.mol^{-1}.K^{-1}
$r_{\text{A-B}}$	DRG interaction of species 'B' to produce/consume species 'A'	$-$
$r^{\star}_{\text{A-B}}$	DRGEP interaction of species 'B' to produce/consume 'A'	$-$
s	Stoichiometric ratio	$-$
S	Mixture mass entropy	J.kg^{-1}.K^{-1}
$\mathbf{S}$	Strain tensor	s^{-1}
$\mathcal{S}$	Flame sensor	$-$
S_{ij}	Strain tensor component	s^{-1}
S_k	Mass entropy of species k	J.kg^{-1}.K^{-1}
S^m	Mixture molar entropy	J.mol^{-1}.K^{-1}
S^m_k	Molar entropy of species k	J.mol^{-1}.K^{-1}
S^0_L	Laminar flame speed	m.s^{-1}
T	Temperature	K
T_{eq}	Equilibrium temperature	K
T_0	Fresh gases temperature	K
T°	Reference temperature	K
T^{∞}	Temperature in the ambient atmosphere surrounding a particle	K
$\mathcal{T}_l$	Threshold for lumping	$-$
$\mathcal{T}_{QSS}$	Threshold for the QSS analysis	$-$
$\mathcal{T}_r$	Threshold for the DRGEP reaction analysis	$-$
$\mathcal{T}_s$	Threshold for the DRGEP species analysis	$-$
t	Time	s
$\mathbf{u}$	Velocity vector	m.s^{-1}
u_i	Component i of the velocity vector	m.s^{-1}
$V_{c,i}$	Correction velocity of species k in direction i	m.s^{-1}
$V_{k,i}$	Diffusion velocity of species k in direction i	m.s^{-1}
W	Mean molecular weight	kg.mol^{-1}
W_k	Species k molecular weight	kg.mol^{-1}
$\mathbf{x}$	Vector of position	m
x_i	Component i of the position vector	m
X_k	Species k mole fraction	$-$
$[X_k]$	Species k concentration	mol.m^{-3}

Y_k	Mass fraction of species k	–
$Y_{k,\infty}$	Mass fraction of species k in the ambient atmosphere of a particle	–
$Y_{F,0}$	Fuel mass fraction in fresh gases	–
$Y_{O,0}$	Oxidiser mass fraction in fresh gases	–
$Y_{F,eq}$	Fuel mass fraction at equilibrium	–
Z	Mixture fraction	–

Greek letters

Symbol	Description	Unit
β_j	Temperature exponent for reaction j	–
β_k	Third body coefficient of species k	–
δ_{ij}	Kronecker symbol	–
δ_L	Laminar flame thickness	m
δ_L^{th}	Thermal thickness	m
Δ	Mesh size	m
$\Delta h_{f,k}^{\circ,m}$	Molar standard enthalpy of species k at reference conditions	J.mol^{-1}
ΔG_j°	Gibbs free energy change per mole of reaction j	J.mol^{-1}
ϵ	Viscous dissipation of the turbulent kinetic energy	m^2.s^{-3}
θ_k	Thermal diffusion coefficient of species k	m^2.s^{-1}.K^{-1}
θ	Source term for the Lagrangian phase	Variable
λ_{th}	Mixture thermal conductivity	W.m^{-1}.K^{-1}
μ	Dynamic viscosity coefficient	kg.m^{-1}.s^{-1}
ν	Kinematic viscosity coefficient	m^2.s^{-1}
ν_{kj}	$\nu_{kj}^{''} - \nu_{kj}^{'}$	–
$\nu_{kj}^{'}$	Species k stoichiometric coefficient in the reactants of reaction j	–
$\nu_{kj}^{''}$	Species k stoichiometric coefficient in the products of reaction j	–
ρ	Density	kg.m^{-3}
ρ_0	Fresh gases density	kg.m^{-3}
ρ_k	Partial density of species k	kg.m^{-3}
ρ_p	Density of particle p	kg.m^{-3}
τ	Characteristic time	s
τ_{ij}	Viscous tensor	kg.m^{-1}.s^{-2}
χ_j	Thermal diffusion ratio of species j	K^{-1}
χ_q	Quenching dissipation rate	s^{-1}
$\dot{\omega}_k$	Mass reaction rate of species k	kg.m^{-3}.s^{-1}

$\dot{\omega}_T$	Combustion heat release	J.m^{-3}.s^{-1}

Mathematical operators

Symbol	Description
$< \phi >$	Statistical averaging
$\overline{\phi}$	Spatial filtering
$\widehat{\phi}$	Fourier transform
$\widetilde{\phi}$	Favre averaging
$\phi^{'}$	Deviation from the mean: $\phi^{'} = \phi - < \phi >$
$\phi^{''}$	Fluctuations: $\phi^{''} = \phi - \overline{\phi}$

Non dimensional numbers

Symbol	Description
B_M	Mass Spalding number
B_T	Thermal Spalding number
Da	Damköhler number
Ka	Karlovitz number
Le_k	Lewis number associated to species k
Nu	Nusselt number
Pr	Prandtl number
Re	Reynolds number
Sc	Schmidt number
Sh	Sherwood number

Principal chemical species

Symbol	Description
CH	Methylidyne
CH_2	Methylene
CH_3	Methyl radical
CH_4	Methane
CH_2O	Formaldehyde
CH_3O	Methoxy radical
C_2H_2	Acetylene

C_2H_3	Vinyl radical
C_2H_4	Ethylene
C_2H_5	Ethyl radical
C_2H_6	Ethane
CO	Carbon monoxide
CO_2	Carbon dioxide
H	Hydrogen atom
H_2	Dihydrogen
H_2O	Water
HCO	Formyl radical
HO_2	Hydroperoxyl radical
H_2O_2	Hydrogen peroxide
O	Oxygen atom
OH	Hydroxyl radical
N_2	Nitrogen
NO	Nitric oxide
N_2O	Nitrous oxide
NO_2	Nitrogen dioxide

Chapter 1

Introduction

Contents

1.1 Context

We are living in a troubled yet passioning time. The development of humanity in term of knowledge, technical skills, economy, has led on one hand to deeply negative consequences on biosphere, pollution that are now endangering human species among several others.

On the other hand, along with the progress of research, our comprehension of the world around us, from the proof of existence of Higgs boson in 2012 [1] to the first detection of gravitational waves on 14 September 2015 [2], has never been so advanced.

In consequence, humanity has to face more and more complex and critical problems, with more and more performant tools and knowledge.

1.1.1 Machine learning algorithms : A powerful tool for modern problems

With the rapid increase of computational resources and data storage capabilities in recent years, the powerful tools that are developed based on artificial intelligence have now a tremendous impact in our society.

It is in the early 1950s that several scientists like Alan Turing asks the question "*can machines think ?*" [3]. In other words, can computers replace human decision or analysis ? But it is only in the late 80s that machine learning appeared, introducing new types of algorithms. Machine learning algorithms can learn from many examples to make predictions. Several models can be trained by machine learning, to cite only a few, regression analysis to which an example is given Fig. 1.1, decision trees or even artificial neural networks, described more deeply in chapter 3.

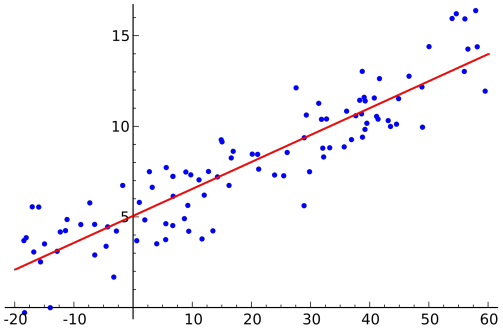

Figure 1.1: Illustration of a linear regression on a dataset.

There are also different learning paradigms for the training of these models, the main ones being:

- Supervised learning, the model is given the inputs X associated with their desired outputs Y, also called labels. Is is like finding the probability density p(Y|X), finding Y knowing X.
- Unsupervised learning, where no labels are given, only datas, so the algorithm can find all kind of unknown patterns in data. In other terms it is like finding something to say on the probability density p(X).
- Reinforcement learning, where datas are given with a certain goal or rule such as driving a vehicle. Models are given feedbacks of predictions and will try to learn by themself to complete the given rules.

Over the years, these algorithms illustrated themselves, by defeating the world chess champion Gary Kasparov in 1996 with the supercomputer IBM's Deep Blue, and more recently by beating Go champion Lee Seedol in March 2016, with the computer program AlphaGo, based on supervised learning.

In order to understand how those algorithms can perform better than humans, we can first consider in chess that given enough computing power, every move can be considered including the ones allowing to win the party, without talking about training. For the Go game, this technique is not possible because despite its simple rules, Go has, compared to chess, both a larger board with more scope and many more alternatives to consider per move.

AlphaGo, developed by Google, learned to play with 160 000 cases with 30 Millions moves played only by the best Go players.

More interestingly, AlphaZero was then developed in 2017 [4] and learned Go and chess with reinforcement learning: It was given only the rules, and self-played millions of time without any human example. AlphaZero then played against AlphaGo 100 times and won every time, showing the force of reinforcement learning against supervised one. It was also showed that AlphaZero developed strategies different from human ones, which is interesting as we can say that this algorithm is creative and have the capacity to solve problem with strategies never thought before.

Today, machine learning models and their ability to treat large amount of data are already employed for many applications, such as economics, financial market analysis, speech recognition, medical diagnosis, agriculture, insurance among many others.

Also, machine learning algorithms are keys for unsolvable problems, one may cite the treatment of datas send by telescopes. The current generation of telescopes like the VLT or the SDSS are already recording several gigaoctets of data per night, and the future generation of telescopes, among those the 200 South Africa paraboly of the SKA observatory, will be recording several teraoctets of data per second, starting in 2022 [5]. Those extremely high quantities of data raise issues on the storage capacity, suggesting algorithm treatments to eliminate unwanted noised data, and on the other hand the treatment and classification of celestial objects. Historically, humans have classified manually the space picture, one may cite the Map of the Sky project, vast project to catalogue and map the positions of millions of stars as faint as 11th or 12th magnitude, initiated in 1887 by Amédée Mouchez, director of the Paris Observatory, and abandoned in 1970, which employed several “human computers" to classify the photographic plates and calculate the stars position. More recently, in 2007, because of the data deluge from telescopes, several projects appeared, Stardust@home from NASA, or even Galaxy Zoo from the Oxford University, asking the internet community to assist the morphological classification of galaxies. These solutions which allow today to gain years of data processing won't maybe enough for the next deluge.

Nevertheless, these methods also bring ethical questions and drawbacks. We already know the capacity of the digital conglomerates (Alphabet, Apple, Facebook, Amazon and Microsoft) to collect behavioural data on individuals for profit purpose. Machine learning algorithms are, since early 2000s with Google patented methods called “AdSense", used to extract, analyse and predict web people behaviours for targeted advertising purposes. The new quote in the economic field could be “Data is the new oil" [6] . Indeed, just taking the example of Facebook in 2018, 98.5 % of its 55 billions revenues comes from target advertising, according to their annual report [7]. For Google, target advertising generated 85 % of their 136 billions 2018 revenues [8].

Moreover, machine learning prediction capacity associated to big data analyses leads to ethically questionable researches. One may cite the capacity to link criminality to physiology thanks to machine learning [9], or even to predict a person's health and sexuality based on its face [10].

1.1.2 Pollutants

Let's talk about one of the critical issues that endangers our species: pollutants. What is it ? Where does it come from ? Why is it problematic and how ?

The most common definition retained for pollutants is their negative impact, chemical or physical, on ecosystem and organisms. Pollution is mainly, directly or not, generated by human activities, and is classified into three categories.

- Light pollutants, not substances but energy introduced in the environment through artificial lights that now completely modify the landscape, see image 1.2. Synonym of security and progress, their negative impact became more and more present. First on biodiversity, nocturnal species are disturbed in their reproduction, their migration, leading to their diminution. Light-sensitive species are now endangered and more deeply the whole food chain is modified [11]. Light pollutants also impact human organism. With a day-night circle modified, it causes change of metabolism, growth and mood disorder [12].

- Background pollutants, that react with the environment and have limited impacts if they don't

Figure 1.2: Nocturnal sky with and without light pollution. These photos were taken in Goodwood, Ontario, a small town about 45 minutes northeast of Toronto during (left) and the night after the region wide 14 August 2003 blackout (right). The lights inside the house in the blackout picture were created by candles and flashlights. [11]

overpass the environment's absorptive capacity. Fund pollutants can be easily converted and are not harmful in small quantities. Let's take the example of the Greenhouse gases (GHG), in which carbon dioxide CO_2 is the major element. They have several sources of anthropogenic emission, see figure 1.3, and can be absorbed by plants and oceans, but as the emission / absorption ratio increases since the Industrial Revolution, see 1.4, the GHG atmospheric concentration is becoming critical, leading to successive irreversible disasters too numerous to be all cited. The major ones are:

  - Sea and atmospheric temperature increase,
  - Snow and glacier decrease,
  - Sea level increase,
  - Extreme natural disaster frequencies increase (tornado, tsunami, drought, floods),
  - Biodiversity disappearance,
  - Forest fires more abundant,
  - Reduced soil fertility and drinkable water ... etc, see the 5th IPCC report [13].

- Stock polluants, characterised by their low degradation. The environnement have difficulties to absorb them so they accumulate over time and continue to impact negatively their surrounding long after they are emitted. For example, non-biodegradable plastics with a life time between one hundred and one thousand years, have a long term effect on ocean biodiversity, also persistent organic pollutants (POPs) resulting from pesticides and industrial chemicals, impacting human health and environnement, with the capacity to travel far from the initial emission location and also the capacity to be stocked in living tissues (bioaccumulation) [14], or polycyclic aromatic hydrocarbons (PAHs), leading to particulates and soots described in the next section.

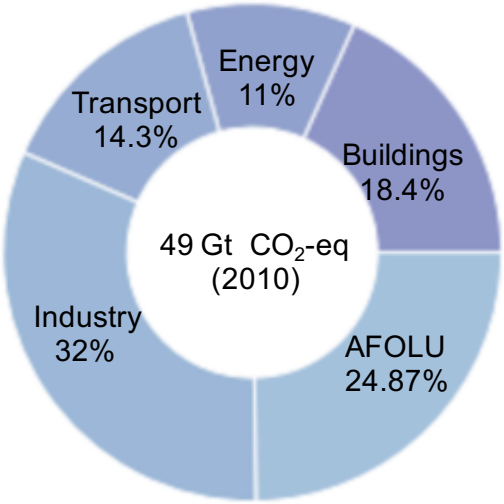

Figure 1.3: Total (direct and indirect) anthropogenic greenhouse gas (GHG) emissions (gigatonne of CO2- equivalent per year) from economic sectors in 2010 [13]. Emissions are converted into CO2-equivalents based on 100-year Global Warming Potential (GWP100), taken from the IPCC Second Assessment Report (SAR).

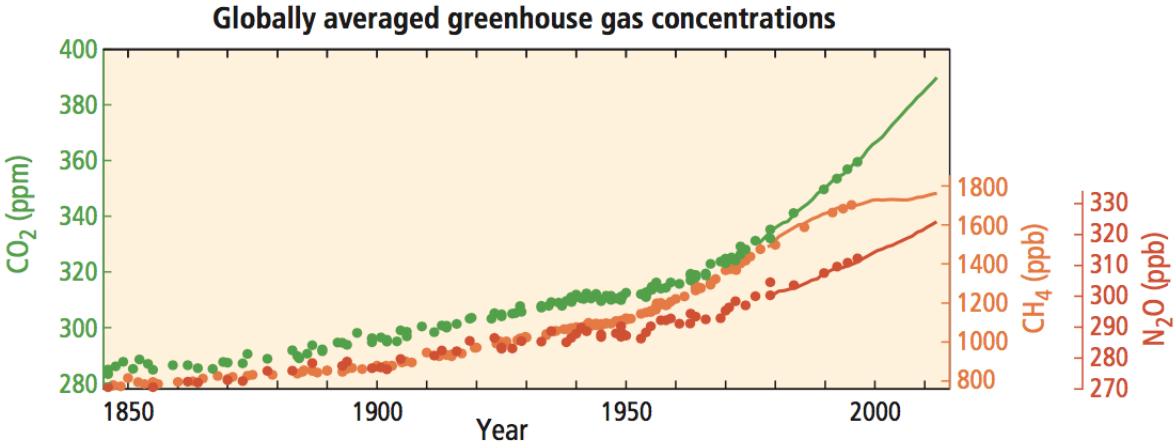

Figure 1.4: Atmospheric concentrations of the greenhouse gases carbon dioxide (CO2, green), methane (CH4, orange) and nitrous oxide (N2O, red) determined from ice core data (dots) and from direct atmospheric measurements (lines) [13].

1.1.3 Soot

Soot, that provides the orange/red light of a flame 1.5, is essentially composed of carbon and has many properties, wanted and unwanted.

There are several paths for soot production. It is a natural component of interstellar dust, that is studied in order to understand many phenomenon like the mass loss on star's evolution and fate [15], or in the star's formation process in nebulae like the one in Fig. 1.6, essentially composed of interstellar dust [16].

On earth, soot production is caused by humans through several activities, see figure 1.7, like mining

Figure 1.5: Radiative soot properties wanted for candle lightening.

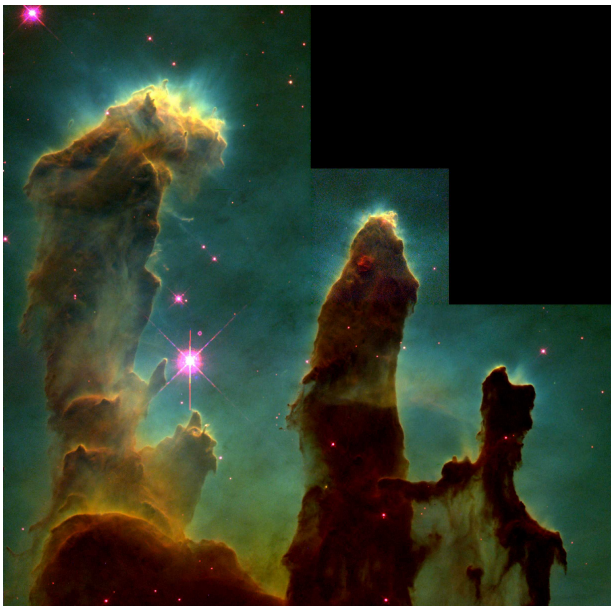

Figure 1.6: The Pillars of Creation in the Eagle Nebula, taken on 04/02/95 by the Hubble telescope, NASA, Jeff Hester and Paul Scowen, Arizona university.

industries, domestic heating, fire, and also car, maritime and aircraft transports. Fig. 1.8 shows the main atmospheric soot concentration over the planet. The values are still debated, nevertheless the tendencies clearly show that the main concentrations are located in Southeast Asia where the strong growth of energy demand has caused increase of soot production by domestic solid combustion and Chinese coal mine development. The strong particulates concentrations in Africa also show coal combustion dependencies. Another important cause of soot production is the biomass burning in South America and central Africa. More generally, in industrialised countries (Europe, United States), the soot emissions are principally linked with densely populated areas [17].

Soot applications are numerous. They are part of rubber and newsprint fabrication, but are mostly used with their radiative properties for lighting and in industrial burners and furnaces.

Soot has nevertheless mostly negative impacts, their radiative effect largely contribute to fire propagation, and their transport and incrustation are known to accelerate climate change through several mechanisms. Their direct effect are linked to radiation forcing, the difference between energy emission and received energy in a climate system in Watt by unit area. In the case of climate change, this parameter gives the ability of a factor to disturb the energy equilibrium of the earth. In other words it is the

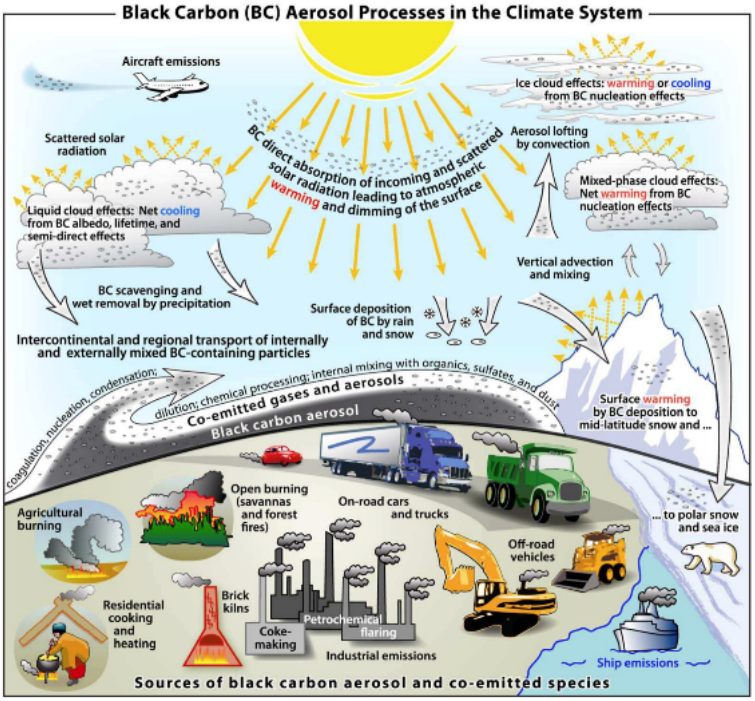

Figure 1.7: Main soot emission source and climatic consequences, [17].

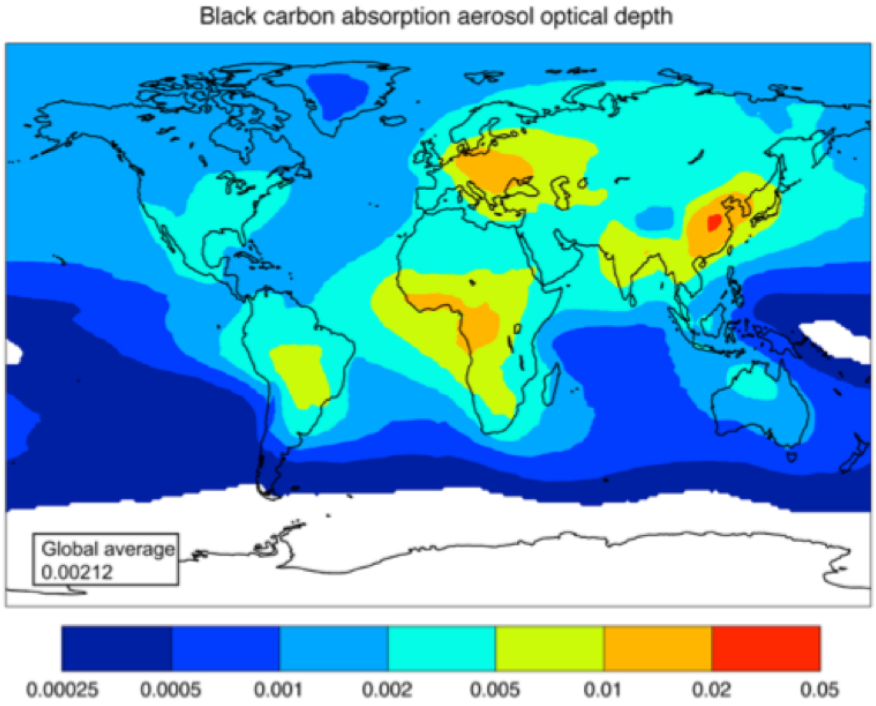

Figure 1.8: Global atmospheric soot concentration distribution model, AeroCom red [18]

equilibrium between entering solar radiation and leaving infrared radiation from the atmosphere [13].

Atmospheric soot has a unique impact on the total radiation forcing. Reports from the IPCC [13] reveal cooling effect due to negative soot radiation forcing, see Fig 1.9. This effect is partially compensated

by solar radiative absorption by soot, creating a warming.

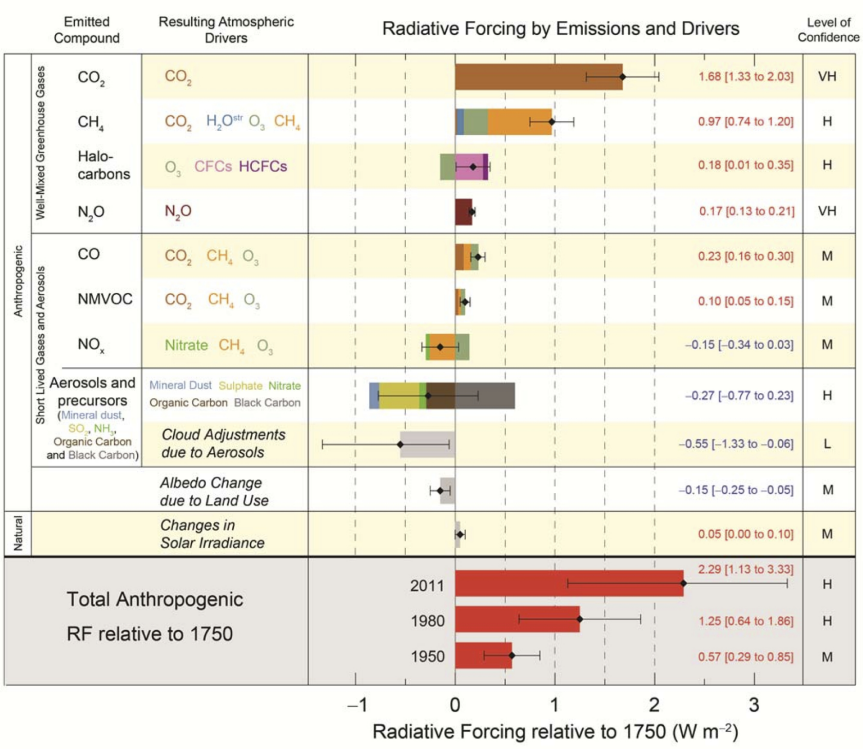

Figure 1.9: radiation forcing of the main climate factors, IPCC AR5 [13].

As for indirect impacts, soot is linked to the cloud lifetime, but this effect is hardly quantifiable. Moreover, another widely studied effect is their incrustation on glaciers, diminishing the albedo of the glaciers and accelerating their melting [17]. The difficulty of quantifying such effects stay the main uncertainties in the modelling of global radiative forcing.

One may also note the inconvenient of soot incrustation on historical landmarks, threatening their conservation, see Fig 1.10.

Figure 1.10: Soot incrustation on glaciers and landmarks.

Another negative effect is on human health. The small size of soot particles allows them to penetrate

deeply in the respiratory system and then in all the organs through the bloodstream. Studies are also on going about the soot penetration through skin. The result is 19 000 deaths per year in Europe because of fines particles, that mostly trigger or aggravate cardiovascular diseases. According to WHO [19] the World Health Organization, 3 million people die each year around the world because of soot, witch cause important expenses in the health field.

At last, soot is unwanted in many industries as they are evidence of incomplete combustion, thus of efficiency loss.

All these issues have led to a progressive inclusion of soot in anti-pollution norms. For example, the European norms euro 5b and euro 6b impose the soot particle counting for diesel engines since 2011 and for gasoline engines since 2014.

1.1.4 Aeronautical field

In the aeronautical field, pollutants like GHGs are mainly caused by aircraft engines, and more specifically inside the combustion chamber. The use of carbon-based fuels, see chapter 5, in the combustion chamber produces unwanted combustion products like soot but also nocive gaseous species like NOx, CO and CO2.

In 2010, aircraft traffic was responsible of 1.49 % of the total anthropogenic GHG emissions, see 1.11. It may seems quite small compared to the part that car take (72.6% of the total transport sector and 10.16 % of the total GHG emissions) or even the livestock farming responsible for 14.5 % of the total emissions [20].

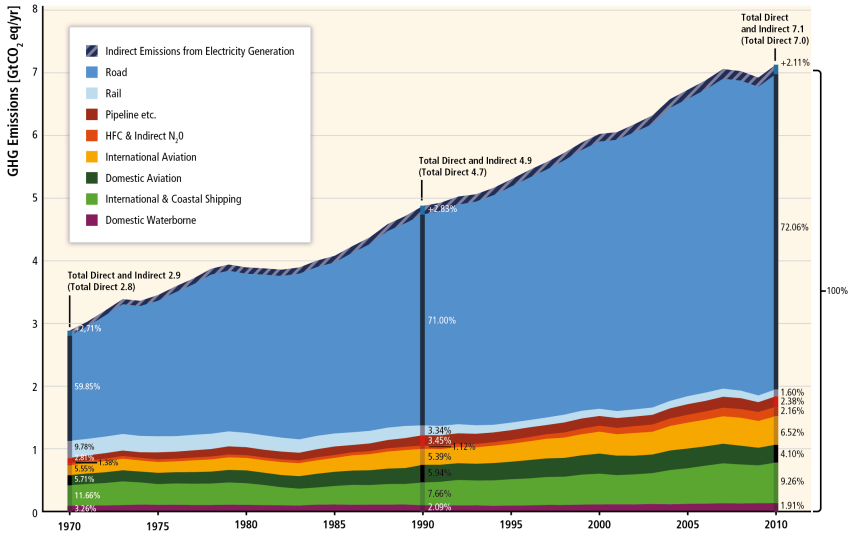

Figure 1.11: Total (direct and indirect) anthropogenic greenhouse gas (GHG) emissions (gigatonne of CO2- equivalent per year) from the transport sector [13]

But if we look closer to the traffic demand and forecast, see figure 1.12, it has proven to double every 15 years. Despite the current crisis, companies such as Airbus forecast a constant growth in the near future due to emerging countries, middle class and low cost companies development. ICAO standard values for emission limits are imposed for aero-jet certification and projects like CAEP and ACARE are targeting pollutant reduction and fuel consumption reduction over the next decades. Moreover, with the official launch of the CORSIA project on 22 June 2020, ICAO stands by its pollution reduction program even in such challenging time for the aeronautical field.

Concerning soots, a new norm has been discussed for engines certification on February 2016 during the 10th ICAO meeting, and was agreed by the ICAO's environment committee in February 2019.

Manufacturers have to develop experimental and numerical tools to face these challenges. These developments have already led to significant combustion chamber improvement, see the fuel burn reduction since the 60s on Fig. 1.13, even if they don't compensate the energy demand growth.

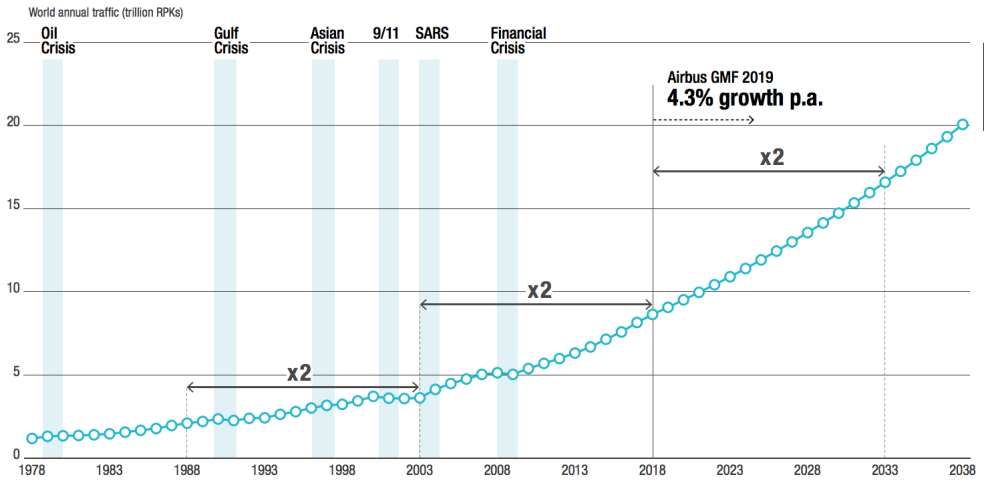

Figure 1.12: World annual traffic in term of RPK (revenue passengers kilometers) [21]

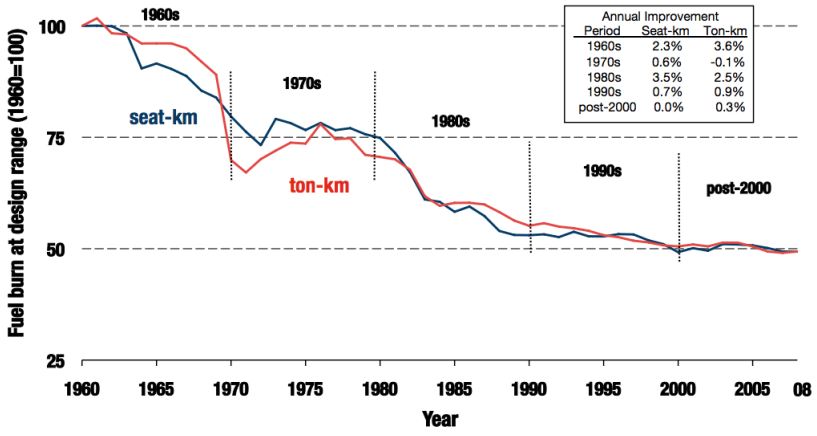

Figure 1.13: Average fuel burn for new aircraft [22]

1.2 Thesis objectives

1.2.1 CFD tools

Computational Fluid Dynamics (CFD) is a part of fluid mechanics that uses numerical methods to solve fluid flow problems. It is an essential tool for a large variety of field such as air and naval transportation, energy generation, chemical processing, medical research, meteorology and astrophysics. Thanks to the constant increase of computational ressources, numerical solving of the equations allows for accessing

any physical quantity at every point of the discretised calculation domain for more and more complex problems. CFD tools in the manufacture industries are part of development process, in complement of test campaigns, as they shorten the number of necessary physical experiments, thus the design cost and time of the whole chain process, and give access to physical quantities unreachable otherwise.

This is the case for the study and the design of combustion systems, as experiments are difficult and expensive to operate essentially because of the temperature and pressure levels achieved. The operation of a burner is piloted by a complex multi-physics that couple fluid mechanics to chemistry under a variety of different time-scales. Depending on the application, the problem may be complicated by introducing liquid atomisation, evaporation, radiation effects, heat transfer through the combustor walls. The majority of these phenomena are already difficult to quantify when seen separately. Capturing a detailed interaction of these physical effects within a real geometry is a true challenge than can be solved only with simulation. In that context, most of the industries relying on combustion share the interest of being able to perform reactive flow simulations at reasonable costs.

1.2.2 The role of chemistry

In combustion chambers, fuel combustion leads to complex chemical processes including heat release and change of mixture composition, from reactants to burnt gases products including pollutants. The accurate modelling of these processes is then primordial for achieving reliable simulations including pollutant prediction. Chemists work on the elaboration of detailed kinetic mechanisms, with the numerous chemical species and reactions appearing in the combustion process. These detailed mechanisms allow for obtaining accurate predictions of complex combustion phenomena and are generally valid under a large range of operating conditions in term of pressure, temperature, equivalent ratio found in industrial combustion chambers. However, when it comes to the implementation of these mechanisms in high fidelity CFD simulation of industrial burners, two issues arise, as detailed below.

First, an additional transport equation is needed for every species in the detailed mechanism.

Secondly, an important number of species implies a large variety of different chemical time-scales. In order to capture the tiniest ones, the whole flow domain needs to be discretised with smaller mesh sizes. As a result, actual available computational ressources are not enough for industrial 3D simulations of real combustion systems with detailed chemistry, this approach can be only used for studying simplified reactive flow problems.

Several solutions have been proposed to overcome this limitation in industry. One typical approach relies on a simplified description of the chemical system with a limited number of species and reactions. This is the approach the present thesis is focused on, with the improvement of an automated tool for detailed mechanisms reduction and optimisation. The obtained mechanism needs to be as reliable as the detailed one for important species, and at reasonable cost for its introduction into 3D simulations.

1.2.3 Soot modelling in industry

Soot formation modelling is a difficult and challenging task. The involved processes differ from those entering in the formation of gaseous chemical species, because they include longer characteristic times and heterogeneous phase reactions. The need for predictive models in various conditions of combustion, at different levels of pressure and using different fuels has driven the work on soot modelling in the last decades [23]. Although some sooting phenomena are still not explained, numerous models with different levels of complexity have been elaborated. The research field is still on-going, but when it comes to meet

the industrial simulation constraints, limited options are available today. This thesis focus on developing an accurate soot model for industrial aircraft engine simulations at reasonable costs. In order to do so, machine learning algorithms are introduced, to propose an innovative alternative to implement detailed soot models in high fidelity simulations.

1.2.4 Manuscript content

Chapter 2: Equations and models for reacting turbulent and two-phase flows
The manuscript first introduces the equations of aerothermochemistry used to model reactive turbulent flows. The methods employed for the calculation of the species thermodynamic, of the associated chemical equilibrium and of the source terms are highlighted. The combustion regimes are then presented with their specific characteristics. The chapter ends with a presentation of the interaction between turbulence, combustion and evaporating liquid droplets. The CFD solvers used in this thesis are presented.

Chapter 3: Turbulent combustion models in LES formalism : The potential of neural networks
Chapter 3 first presents a review on turbulent combustion models for Large Eddy simulations. Then, machine learning algorithms are presented. A unified modelling framework for all unresolved terms in the filtered progress variable transport equation in large-eddy simulations of turbulent premixed flames is proposed, using convolutional neural networks. A direct numerical simulation database of a turbulent premixed jet flame is used in order to train convolutional neural networks to predict both the filtered progress variable source term and the unresolved scalar transport terms. A single variable readily available from the large-eddy simulation is required in order to calculate all inputs to networks, namely the Favre-filtered progress variable $\tilde{c}$.

Chapter 4: Chemical schemes reduction for industrial applications
In chapter 4, a review on chemical scheme reduction methodologies is shown. The automatic Optimised and Reduced Chemistry code ORCh is then presented along with its embedded reduction stochastic configuration, and improvements for ORCh reduction capacity is provided. These improvements are then validated on an industrial air-kerosene 3D Lemcotec simulation.

Chapter 5: Review on soot and fuel model issues
Chapter 5 provides a review on jet fuel models, how they are different from real fuel, how they are used in industrial simulations and what are their impacts on chemistry and soot prediction. Also, a review of soot characterisation and evolution is made, and few models are presented.

Chapter 6: Soot prediction in a real combustion chamber
This last chapter presents a new strategy using neural networks in order to offer an alternative way to obtain accurate soot evolution predictions for industrial 3D simulation at limited costs. This strategy is first tested on a 1D premixed flame, secondly on a 0D representative stochastic configuration of an industrial chamber operating point.

Chapter 7: Conclusion
The final chapter resumes the general conclusions on this thesis and the perspective to this work.

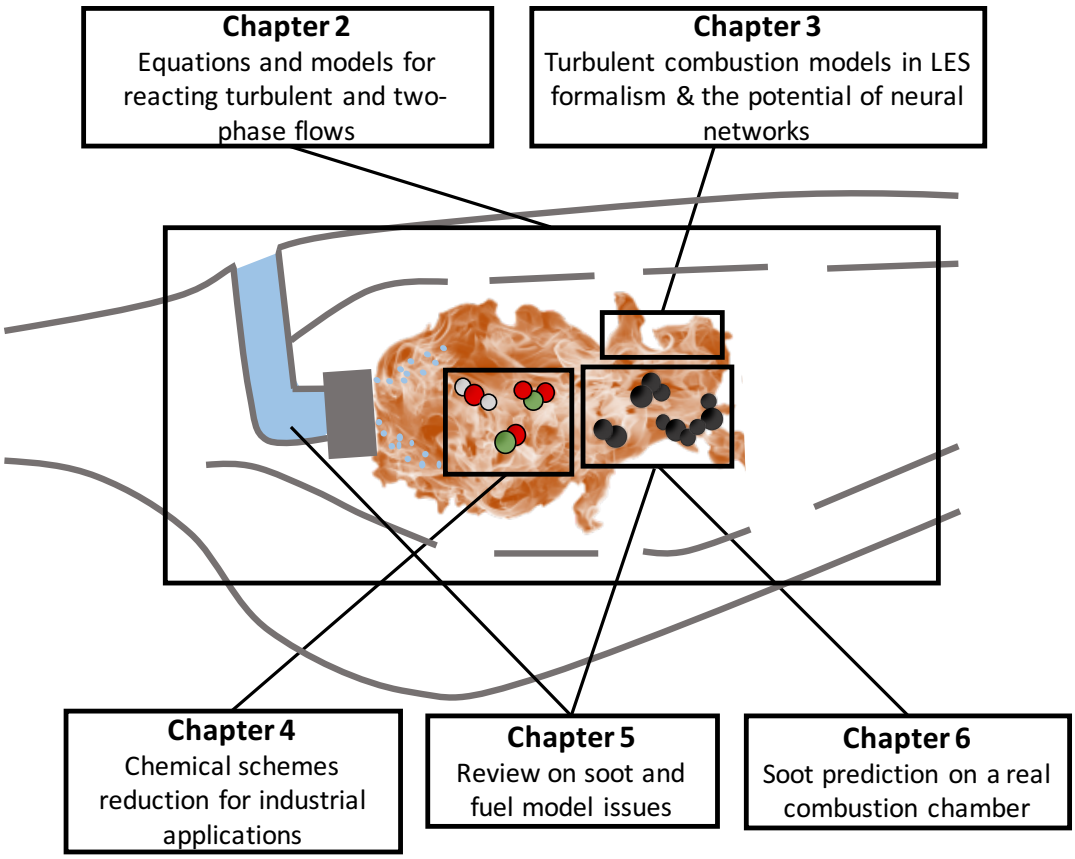

Figure 1.14: Manuscript content

1.3 Publications

1.3.1 Peer-reviewed international journals

- A. Seltz, P. Domingo, L. Vervisch, Z. Nikolaou, *Direct mapping from LES resolved scales to filtered-flame generated manifolds using convolutional neural networks*, Combustion and Flame 210, pp.71-82 (2019).

- A. Seltz, L. Vervisch, P. Domingo, *Solving the population balance equation for non-inertial particles dynamics using PDF and machine learning: Application to a sooting flame*, Phys. Fluids, submitted.

1.3.2 International conferences

- A. Seltz, P. Domingo, L. Vervisch, *Machine learning for turbulent combustion modeling in high-fidelity LES*, in 1^{st} HiFiLeD Symposium, Bruxelles, Belgium, 2018.

- A. Seltz, P. Domingo, L. Vervisch, *Machine learning for sub-grid scale turbulent combustion modeling*, in 9^{th} ECM, Lisbonne, Portugal, 2019.

- A. Seltz, P. Domingo, L. Vervisch, *Large-eddy simulation of premixed turbulent combustion using a convolutional neural network*, in SIAM Int. Conf. on Numerical Combustion, Aix-la-Chapelle,

Germany,2019.

- A. Seltz, P. Domingo, L. Vervisch, *Machine learning for sub-grid scale turbulent combustion modeling*, in 15^{th} US National Congress on Computational Mechanics, Austin, United States, 2019.

- A. Seltz, A. Bouaniche, P. Domingo, L. Vervisch, *A digital-twin population balance equation for solving soot PSD*, ETMM13, May 12-14 2021.

- A. Seltz, P. Domingo, L. Vervisch, *Solving the population balance equation for non-inertial particles dynamics using PDF and machine learning: Application to a sooting flame*, ICFD2020, oct 28-30, Sendai, Japan.

Chapter 2

Equations and models for reacting turbulent and two-phase flows

Contents

2.1 Balance equations for reactive turbulent flows

2.1.1 Mixture properties

The subsequent composition and thermodynamical properties will be used to describe the mixture. They will serve for the definition of the aerothermochemical conservation equations.

2.1.1.1 Mixture composition

The mixture composition that is considered is assumed to rely on N_{sp} chemical species referenced by letter k. The mixture density is estimated from the sum of the partial density ρ_k of each chemical species,

$$\rho = \sum_{k=1}^{N_{sp}} \rho_k \, . \tag{2.1}$$

The species k mass fraction Y_k is defined by the species individual density to the mixture density ratio,

$$Y_k = \frac{\rho_k}{\rho} \, . \tag{2.2}$$

The definitions of equations 2.1 and 2.2 ensure that species mass fractions are bounded between zero and unity and that the sum of the N_{sp} mass fractions equals unity:

$$\sum_{k=1}^{N_{sp}} Y_k = 1 \, . \tag{2.3}$$

W is defined as the mean molecular weight of the mixture that is considered. It is computed from each species molecular weight W_k and from their mass fractions through the relation:

$$\frac{1}{W} = \sum_{k=1}^{N_{sp}} \frac{Y_k}{W_k} \, . \tag{2.4}$$

The molar fraction X_k of species k is then deducted from relation 2.5:

$$X_k = \frac{W}{W_k} Y_k \, , \tag{2.5}$$

and its concentration (number of moles per unit volume), from relation 2.6:

$$[X_k] = \frac{\rho_k}{W_k} \, . \tag{2.6}$$

2.1.1.2 Thermodynamic of the mixture

The molar heat capacity at constant pressure $C^m_{p,k}(T, P^\circ)$ of the species k is computed at standard pressure $P^\circ = 1$ atm according to the temperature T using the so-called NASA polynomials (relation 2.7) which have been designed in the early seventies to fit with experimental measurements:

$$\frac{C^m_{p,k}(T, P^\circ)}{\mathcal{R}} = a_{1,k} + a_{2,k}T + a_{3,k}T^2 + a_{4,k}T^3 + a_{5,k}T^4 \, , \tag{2.7}$$

where $\mathcal{R} = 8.314$ J.mol^{-1}.K^{-1} is the ideal gas constant.

Molar enthalpy and entropy of species k are expressed as a function of the heat capacity at constant pressure through the relations:

$$H_k^m(T,P^\circ) = \int_{\theta=T^\circ}^{T} C_{p,k}^m(\theta,P^\circ)d\theta + \Delta h_{f,k}^{\circ,m} \,, \tag{2.8}$$

$$S_k^m(T,P^\circ) = \int_{\theta=T^\circ}^{T} \frac{C_{p,k}^m(\theta,P^\circ)}{\theta}d\theta \,, \tag{2.9}$$

in which $\Delta h_{f,k}^{\circ,m}$ refers to the molar standard enthalpy of formation of species k at reference pressure P° and reference temperature T°. The standard temperature is commonly set to the atmospheric conditions (T° = 298.15 K) at which experiments are easier to perform. The NASA polynomials approximation is extended to the enthalpy and entropy properties through the relations,

$$\frac{H_k^m(T,P^\circ)}{\mathcal{R}T} = a_{1,k} + a_{2,k}T + a_{3,k}T^2 + a_{4,k}T^3 + a_{5,k}T^4 + \frac{a_{6,k}}{T} \,, \tag{2.10}$$

$$\frac{S_k^m(T,P^\circ)}{\mathcal{R}} = a_{1,k}\log(T) + a_{2,k}T + \frac{a_{3,k}}{2}T^2 + \frac{a_{4,k}}{3}T^3 + \frac{a_{5,k}}{4}T^4 + a_{7,k} \,. \tag{2.11}$$

Note that the coefficient $a_{6,k} = \Delta h_{f,k}^{\circ,m}/\mathcal{R}$, which gives the relation $H_k^m(T^\circ,P^\circ) = \Delta h_{f,k}^{\circ,m}$ when species k is at standard pressure and temperature. For each chemical species, there is two sets of polynomials corresponding to low temperatures commonly ranging from 300 K to 1000 K and high temperatures which corresponds to variations between 1000 K and 5000 K.

The following mixture laws are used to find the molar thermodynamic properties of the mixture from species individual properties.

$$C_p^m(T,P^\circ) = \sum_{k=1}^{N_{\text{sp}}} X_k C_{p,k}^m(T,P^\circ) \,, \tag{2.12}$$

$$H^m(T,P^\circ) = \sum_{k=1}^{N_{\text{sp}}} X_k H_k^m(T,P^\circ) \,, \tag{2.13}$$

$$S^m(T,P^\circ) = \sum_{k=1}^{N_{\text{sp}}} X_k \left(S_k^m(T,P^\circ) - \mathcal{R}\log\left(\frac{P}{P^\circ}\right) - \mathcal{R}\log\left(X_k\right)\right) \,. \tag{2.14}$$

Finally the mixture heat capacity at constant pressure expressed per unity of mass C_p, the mixture mass specific enthalpy H and mass specific entropy S are given by:

$$C_p = \frac{C_p^m}{W} \,, \tag{2.15}$$

$$H = \frac{H^m}{W} \,, \tag{2.16}$$

$$S = \frac{S^m}{W} \,. \tag{2.17}$$

2.1.1.3 Equation of state

The ideal gas law is an hypothesis that is frequently used in combustion and that relies on the assumptions that the molecules (1) behave as rigid spheres that are (2) homogeneously distributed on the macroscopic scale, that are (3) sufficiently separated from each other leading to negligible intermolecular forces and

that these molecules are submitted to (4) perfectly elastic collisions. Following this hypothesis, the following equation of state will be used all along this thesis:

$$P = \rho \frac{\mathcal{R}}{W} T = \rho \left(\sum_{k=1}^{N_{\text{sp}}} \frac{Y_k}{W_k} \right) \mathcal{R} T \,, \tag{2.18}$$

where ρ stands for the mixture density, W is the mixture mean molecular weight and $\mathcal{R} = 8.314$ J.mol^{-1}.K^{-1} is the ideal gas constant.

2.1.2 Conservation equations

Combustion takes place under the coupling effects of transport by velocity and diffusion, chemical kinetic and thermodynamic. First, the equations describing aerothermochemistry are given along with the associated thermodynamic and equilibrium principles. The derivation of the conservation equations is reported in [24, 25]. The balanced equations express mass, momentum and energy conservations.

2.1.2.1 Mass conservation

The continuity equation that describes mass conservation reads:

$$\frac{\partial \rho}{\partial t} + \frac{\partial \rho u_i}{\partial x_i} = 0 \,. \tag{2.19}$$

with u_i, the velocity projected on the i^{th} axis.

2.1.2.2 Momentum conservation

The equation of momentum expressed neglecting the volume force that acts on the fluid reads:

$$\frac{\partial \rho u_j}{\partial t} + \frac{\partial \rho u_i u_j}{\partial x_i} = -\frac{\partial P}{\partial x_j} + \frac{\partial \tau_{ij}}{\partial x_i} \,, \tag{2.20}$$

where τ_{ij} refers to the viscous tensor and is defined for Newtonian fluids by:

$$\tau_{ij} = -\frac{2}{3} \mu \frac{\partial u_k}{\partial x_k} \delta_{ij} + \mu \left(\frac{\partial u_i}{\partial x_j} + \frac{\partial u_j}{\partial x_i} \right) \,, \tag{2.21}$$

in which μ describes the mixture dynamic viscosity and δ_{ij} is the Kronecker symbol.

2.1.2.3 Species conservation

Mass conservation applied to the conservation of the N_{sp} chemical species is written:

$$\frac{\partial \rho Y_k}{\partial t} + \frac{\partial}{\partial x_i} \left(\rho \left(u_i + V_{k,i} \right) Y_k \right) = \dot{\omega}_k \,, \tag{2.22}$$

where $\dot{\omega}_k$ is the species k chemical source term which must verify the relation:

$$\sum_{k=1}^{N_{\text{sp}}} \dot{\omega}_k = 0 \,. \tag{2.23}$$

$V_{k,i}$ represents the diffusion velocity of species k in the direction i. The V_k diffusion velocities are obtained by solving the $\mathrm{N_{sp}}$ linear system :

$$\sum_{j=1}^{N_{\mathrm{sp}}} \frac{X_k X_j}{D_{kj}}(V_j - V_k) = \nabla X_k + (X_k - Y_k)\frac{\nabla P}{P} + \frac{\rho}{P}\sum_{j=1}^{N_{\mathrm{sp}}} Y_k Y_j (F_{ext,j} - F_{ext,k}) + \sum_{j=1}^{N_{\mathrm{sp}}} \frac{X_k X_j}{\rho D_{kj}}\left(\frac{D_{th,k}}{Y_k} - \frac{D_{th,j}}{Y_j}\right)\frac{\nabla T}{T}$$

The last term is neglected since the Soret effect (the diffusion of mass due to temperature gradients) is not accounted for.

The high cost associated to the resolution of this system often leads to the use of a "mixture averaged" simplified estimation proposed by Hirschfelder and Curtiss [26]:

$$D_k^H = \frac{1 - Y_k}{\sum_{j \neq k} X_j / D_{kj}} \tag{2.24}$$

Using this approximation, the diffusion velocity $V_{k,i}$ reads:

$$V_{k,i} = -\frac{D_k^H}{X_k}\frac{\partial X_k}{\partial x_i} + V_{c,i}\ . \tag{2.25}$$

$V_{c,i}$ is a correction velocity introduced to ensure mass conservation.

$$V_{c,i} = \sum_{k=1}^{N_{\mathrm{sp}}} D_k^H \frac{W_k}{W}\frac{\partial X_k}{\partial x_i}\ . \tag{2.26}$$

2.1.2.4 Energy conservation

The conservation equation for the energy is written in terms of sensible enthalpy. The sensible enthalpy is expressed through the relation:

$$h_s(T) = \int_{\theta=T^\circ}^{T} C_p(\theta) d\theta\ , \tag{2.27}$$

and the corresponding conservation equation reads:

$$\frac{\partial \rho h_s}{\partial t} + \frac{\partial}{\partial x_i}(\rho u_i h_s) = \frac{DP}{Dt} + \frac{\partial \mathcal{Q}_i}{\partial x_i} + \tau_{ij}\frac{\partial u_i}{\partial x_j} + \dot{\mathcal{Q}} + \dot{\omega}_T\ . \tag{2.28}$$

The term $\mathcal{Q}_i$ represents the heat flux:

$$\mathcal{Q}_i = \lambda_{th}\frac{\partial T}{\partial x_i} - \sum_{k=1}^{N_{\mathrm{sp}}} \rho h_{s,k} Y_k V_{k,i}\ , \tag{2.29}$$

where λ_{th} refers to the thermal conductivity of the mixture. The term $\dot{Q}$ represents the external heat sources (for instance, coming from a spark or from radiative fluxes) and $\dot{\omega}_T$ is the chemical heat source term written:

$$\dot{\omega}_T = -\sum_{k=1}^{N_{\mathrm{sp}}} \Delta h_{f,k}^0 \dot{\omega}_k \tag{2.30}$$

where $\Delta h^0_{f,k}$ is the formation enthalpy of species k. The operator $D\cdot/Dt$ is called the material derivative which corresponds to $D\cdot/Dt = \partial\cdot/\partial t + u_i\partial\cdot/\partial x_i$

Several approximations are set. The studied cases do not account for external heat sources, hence the source term $\dot{Q}$ is neglected. The viscous forces term $\tau_{ij}\frac{\partial u_i}{\partial x_j}$ is not taken into account since it varies like the square of the Mach number and only low Mach number flows are considered in this work. Finally, without accounting for the Soret and Dufour effects, the initial formulation of the energy equation is simplified to:

$$\frac{\partial \rho h_s}{\partial t} + \frac{\partial}{\partial x_i}\left(\rho u_i h_s\right) = \frac{DP}{Dt} + \frac{\partial}{\partial x_i}\left(\lambda_{th}\frac{\partial T}{\partial x_i}\right) - \frac{\partial}{\partial x_i}\left(\rho\sum_{k=1}^{N_{sp}} h_{s,k}Y_k V_{k,i}\right) + \dot{\omega}_T\ . \tag{2.31}$$

2.2 Introduction to chemical kinetics

In reactive flows, the species source terms $\dot{\omega}_k$ that appear in equation 2.22 and the sensible enthalpy source term $\dot{\omega}_T$ of equation 2.30 are modelled from chemistry. Although in a global manner, the combustion of any hydrocarbon may be cast in the form of equation 2.32, in reality hundreds of species are involved interacting together over thousands of different reactions.

$$\mathrm{C}_n\mathrm{H}_m + \left(n + \frac{m}{4}\right)\mathrm{O}_2 \rightarrow n\mathrm{CO}_2 + \frac{m}{2}\mathrm{H}_2\mathrm{O} \tag{2.32}$$

Some of these chemical reactions occur in both direct and reverse directions. From a macroscopic point of view, a system appears to be at equilibrium when the concentrations of the species are stable. However, on a microscopic level, both forward and backward reactions occur but at equal rates. The balance between the direct and reverse rates is described using an equilibrium constant computed from thermodynamic considerations.

Detailed mechanisms describing these chemical paths are found in the literature and are reliable today for the simulation of a large range of operating conditions (pressure, temperature, equivalence ratio). Unfortunately, these mechanisms cannot be directly used to compute for 3D turbulent combustion essentially because of the amount of chemical species, i.e. the amount of transport equations, involved and because of the very small time and space resolutions necessary to capture the intermediate species that are present within these mechanisms (typically a few μm and μs). Several alternatives to lower the costs associated to the computation of such chemical schemes are found in the literature including the chemistry reduction and tabulation methodologies. The two approaches are briefly introduced below. The reduction approach will be discussed in detail over the chapter 4 since it is the retained approach in this manuscript. First, the overall equations that govern chemical kinetics are given.

2.2.1 Species source terms

A chemical mechanism is made up of N_{sp} chemical species combined over N_{r} reversible reactions. The j^{th} reaction is associated to ν'_{kj} and ν''_{kj} which are respectively the reactants and products stoichiometric coefficients associated to the chemical species k with molecular formula $\mathcal{M}_k$.

$$\sum_{k=1}^{N_{\mathrm{sp}}}\nu'_{kj}\mathcal{M}_k \rightleftharpoons \sum_{k=1}^{N_{\mathrm{sp}}}\nu''_{kj}\mathcal{M}_k,\ \text{with } j = 1, N_{\mathrm{r}}\ . \tag{2.33}$$

The rate associated to a given reaction j quantifies the mass variation of the chemical species involved within this reaction per unit of time:

$$\dot{Q}_j = \frac{\dot{\omega}_{kj}}{W_k \nu_{kj}} \, , \tag{2.34}$$

where $\nu_{kj} = \nu''_{kj} - \nu'_{kj}$. Species variation rates over every j^{th} reaction are deduced from relation 2.34, and the total reaction rate of species k corresponds to the sum of the $\dot{\omega}_{kj}$ over the N_r reactions of the mechanism:

$$\dot{\omega}_k = \sum_{j=1}^{N_\mathrm{r}} \dot{\omega}_{kj} = W_k \sum_{j=1}^{N_\mathrm{r}} \nu_{kj} \dot{Q}_j \, . \tag{2.35}$$

Summing the $\dot{\omega}_k$ source terms over the N_sp chemical species of the mechanism returns a null value, thus ensuring mass conservation.

2.2.2 Reaction rates

The reaction rate $\dot{Q}_j$ of every reaction is computed from both direct and reverse rates.

$$\dot{Q}_j = \dot{Q}_{fj} - \dot{Q}_{rj} \tag{2.36}$$

The forward rate of the j^{th} reaction is modeled through the use of a relation that correlates the concentration of the reactants to a chemical constant K_{fj}. Same applies to the backward rate using this time, the products concentrations and K_{rj}, the reverse chemical constant of reaction j:

$$\dot{Q}_{fj} = K_{fj} \prod_{k=1}^{N_\mathrm{sp}} [X_k]^{\nu'_{kj}}, \quad \dot{Q}_{rj} = K_{rj} \prod_{k=1}^{N_\mathrm{sp}} [X_k]^{\nu''_{kj}} \, , \tag{2.37}$$

where $[X_k] = \rho Y_k / W_k$ refers to the molar concentration of species k.

2.2.2.1 Arrhenius law

The determination of the rate constant of a reaction has driven many experimental studies which have led to the description of empirical laws based on a temperature dependency. Conventionally, a modified Arrhenius form is used in combustion:

$$K_{fj} = \mathcal{A}_j T^{\beta_j} \exp\left(-\frac{E_j}{\mathcal{R}T}\right) \tag{2.38}$$

where the rate of the reaction K_{fj} is computed from the absolute temperature T of the mixture related to an activation energy E_j expressed in J.mol^{-1}, an exponent β_j used to properly address the range of temperatures found in combustion, a pre-exponential collision frequency factor $\mathcal{A}_j$ and $\mathcal{R}$, the ideal gas constant. The importance of the activation energy term E_j is illustrated on figure 2.1. To dissociate the initial reactants into intermediate and radical species a sufficient amount of energy must be provided to the system. The dissociated species then recombine into more stable products while delivering energy through the form of heat. The process is called combustion, because in all cases, the amont of energy necessary to ensure the dissociation of the molecules is lower than the energy released by the recombination step.

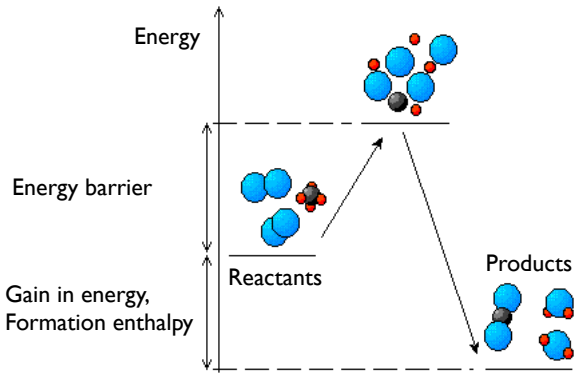

Figure 2.1: Activation energy diagram E_j

2.2.2.2 Reverse reaction rate constant and equilibrium

The backward rate is balanced with the forward one defining an equilibrium constant. Equilibrium is achieved when the forward rate $\dot{Q}_{fj}$ equals the backward rate $\dot{Q}_{rj}$, hence when:

$$K_{fj} \prod_{k=1}^{N_{\text{sp}}} [X_k]^{\nu'_{kj}} = K_{rj} \prod_{k=1}^{N_{\text{sp}}} [X_k]^{\nu''_{kj}} \tag{2.39}$$

The equilibrium constant is defined as the ratio of the reactants concentrations by the products concentrations at equilibrium:

$$K_{eq,j} = \prod_{k=1}^{N_{\text{sp}}} [X_k]^{\nu_{kj}} = \frac{K_{fj}}{K_{rj}} \tag{2.40}$$

The reverse reaction rate constant is deduced from $K_{rj} = K_{fj}/K_{eq,j}$ after computing the equilibrium constant that is deduced from the thermodynamic properties of the species involved within reaction j. These thermodynamic properties are given from the computation of the Gibbs free energy.

2.2.2.3 Gibbs free energy

The estimation of the chemical equilibrium of a reaction necessitates the definition of the standard Gibbs free energy change. This reference state is used to describe the chemical potential of species and enables to quantify the difference in potential that exists between the reactants and the products of a given reaction. This is expressed, for the j^{th} reaction, through:

$$\Delta G_j^\circ = -\mathcal{R}T \ln K_{p,j} \ , \tag{2.41}$$

where index $^\circ$ refers to all the products and reactants in their standard state and $K_{p,j}$ is the equilibrium constant of reaction j expressed from the partial pressure of the species involved within reaction j. Note that the more negative is ΔG_j°, the larger is the equilibrium constant of reaction j and the more spontaneous is the reaction. In addition, if the Gibbs free energy of the reactants of j is similar to the one of its products, the reaction has no tendency to proceed ($\Delta G_j^\circ = 0$). The equilibrium constant in pressure relates to the one in concentration terms $K_{eq,j}$ by:

$$K_{p,j} = K_{eq,j} \left(\frac{\mathcal{R}T}{P^\circ} \right)^{\sum_{k=1}^{N_{\text{sp}}} \nu_{kj}} \tag{2.42}$$

with P°, the reference pressure. Combining this relation with equation 2.41 allows to get an expression of the equilibrium constant in terms of concentrations $K_{eq,j}$ as a function of the standard Gibbs free energy variation across the j^{th} reaction, here expressed in terms of entropy and enthalpy change, respectively noted ΔS_j° and ΔH_j°.

$$K_{eq,j} = \exp\left(\frac{\Delta S_j^\circ}{\mathcal{R}} - \frac{\Delta H_j^\circ}{\mathcal{R}T}\right)\left(\frac{P^\circ}{\mathcal{R}T}\right)^{\sum_{k=1}^{N_{\text{sp}}}\nu_{kj}} \tag{2.43}$$

In practice, the entropy and enthalpy change necessary to calculate the equilibrium constants are computed from the NASA relations introduced in 2.10 and 2.11.

2.2.2.4 Reactions orders

Rate equations are mathematical expressions that describe the relationship between the rate of a chemical reaction and the concentration of its reactants. The exponents in a rate equation describe the effects of the reactant concentrations on the reaction rate and define the reaction order.

The unit for the chemical rate constant and the unit for the pre-exponential factor $\mathcal{A}_j$ varies with the order of the reaction. The $\mathcal{A}_j$ in a reaction of 1^{st} order is expressed in $\text{s}^{-1}.\text{K}^{-\beta_j}$, of 2^{nd} order in $\text{m}^3.\text{mol}^{-1}.\text{s}^{-1}.\text{K}^{-\beta_j}$ and the pre-exponential factor have the unit $\text{m}^6.\text{mol}^{-2}.\text{s}^{-1}.\text{K}^{-\beta_j}$ for 3^{rd} order reactions .

2.2.2.5 Third-body reactions

Three-body reactions involve two species 'A' and 'B' as reactants and a third body 'M'. They yield as products, the species 'AB' and the unchanged catalyst species 'M' which is used to stabilise the excited product 'AB*' through the release of heat. On the contrary, in the reverse direction, heat provides the energy necessary to break the link between 'A' and 'B'. Although three-body reactions are described by only one Arrhenius equation, the chemical process undergoes the 3 steps detailed within table 2.1. The third body 'M' can be any inert molecule. The notation usually is $\text{A} + \text{B} + \text{M} \rightleftharpoons \text{AB} + \text{M}$. The

Forward direction	Backward direction
$\text{A} + \text{B} \rightarrow \text{AB}^*$	$\text{M} + \text{heat} \rightarrow \text{M}^*$
$\text{AB}^* + \text{M} \rightarrow \text{AB} + \text{M}^*$	$\text{AB} + \text{M}^* \rightarrow \text{AB}^* + \text{M}$
$\text{M}^* \rightarrow \text{M} + \text{heat}$	$\text{AB}^* \rightarrow \text{A} + \text{B}$

Table 2.1: Forward and backward decomposition of a three-body reaction.

concentration of the third body can be defined from either a single species or from a combination of species. In the first case, the notation usually takes the form $\text{A}+\text{B}+\text{N}_2 \rightleftharpoons \text{AB}+\text{N}_2$ (here with the azote species). In the second case, each of the species is seen as a more or less effective collisional partner. Third body efficiencies β_k are thus defined and the calculation of the concentration $[X_\text{M}]$ is done on the basis of equation 2.44. Species which are associated to a high efficiency are given a value above 1.0; on the contrary a value below 1.0 is defined for the species which are not effective collisional partners. A default efficiency of 1.0 is declared for all the other species.

$$[X_\text{M}] = \sum_{k=1}^{N_{\text{sp}}} \beta_k [X_k] \tag{2.44}$$

2.2.2.6 Fall-off correction

Under specific conditions, some reaction rate expressions are dependent on pressure and temperature. This is especially true for the rate associated to unimolecular/recombination fall-off reactions which increases with pressure. As an example, let us consider the unimolecular/recombination reaction that describes the methyl recombination (table 2.2). If the chemical process takes place at either a low or high-

High pressure limit	$CH_3 + CH_3 \rightleftharpoons C_2H_6$
Low pressure limit	$CH_3 + CH_3 + M \rightleftharpoons C_2H_6 + M$

Table 2.2: Low and high-pressure reactions for methyl recombination

pressure limit, typical Arrhenius laws are applicable to the reactions described in table 2.2. However, if the pressure is in between, an accurate description of the phenomenon requires a more complicated rate expression. In such a case, the reaction is said to be in the “fall-off" region. Common practice is

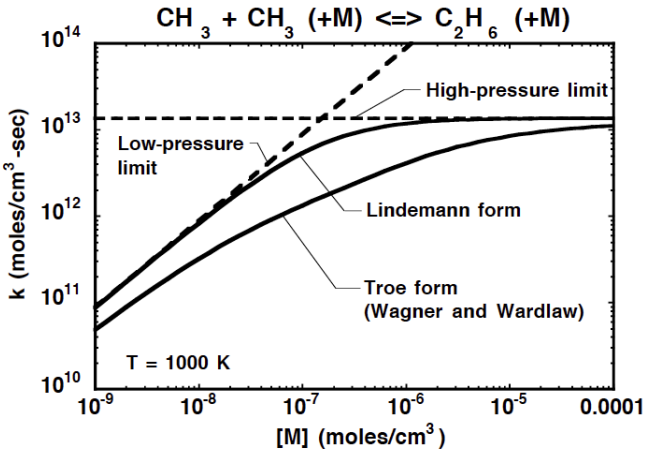

Figure 2.2: Lindemann form and Troe form applied to the methyl recombination [27]

to write the overall reaction as $CH_3 + CH_3\ (+M) \rightleftharpoons C_2H_6\ (+M)$. Several formulas (derived from the Lindemann description [28]) are available to smoothly relate the limiting low and high-pressure rate expressions. With the Lindemann approach, Arrhenius parameters need to be given for both the low pressure limit K_0 and the high pressure limit K_∞.

$$K_0 = \mathcal{A}_0 T^{\beta_0} \exp\left(-\frac{E_0}{\mathcal{R}T}\right) \tag{2.45}$$

$$K_\infty = \mathcal{A}_\infty T^{\beta_\infty} \exp\left(-\frac{E_\infty}{\mathcal{R}T}\right) \tag{2.46}$$

The expression taken at any pressure is based on a combination of both K_0 and K_∞ (see equation 2.47). The term P_r is here equivalent to a pressure and $[M]$ represents the concentration of the mixture, possibly estimated from third-body efficiencies.

$$K = K_\infty \left(\frac{P_r}{1+P_r}\right) F \tag{2.47}$$

$$P_r = \frac{K_0[\mathrm{M}]}{K_\infty} \tag{2.48}$$

The expression for the F coefficient is equal to unity with the Lindemann description. Other descriptions of F such as the Troe form have been proposed:

$$log(F) = \left[1 + \left(\frac{\log(P_r) + c}{n - d(\log(P_r) + c)}\right)^2\right]^{-1} \log(F_{cent}) \tag{2.49}$$

where the coefficients c, n and d are estimated through:

$$\begin{aligned} c &= -0.4 - 0.67\log(F_{cent}) \\ n &= 0.75 - 1.27\log(F_{cent}) \\ d &= 0.14 \end{aligned} \tag{2.50}$$

and F_{cent} through the equation 2.51 where the parameters α, T^*, T^{**}, T^{***} have to be specified as inputs (T^{**} is not always used).

$$F_{cent} = (1-\alpha)\exp\left(\frac{-T}{T^{***}}\right) + \alpha\exp\left(\frac{-T}{T^*}\right) + \exp\left(\frac{-T^{**}}{T}\right) \tag{2.51}$$

2.2.3 Reducing the costs for solving chemistry

As introduced earlier, the detailed combustion mechanisms available in the literature require the use of a high resolution both in time and space. Typically, the size of the cells found within the flame thickness, at atmospheric pressure, should be of the order of ten micrometers to properly solve for the intermediate and radical species. Moreover the time steps necessary to capture the entire chemistry of the flame are always smaller than the time steps used to solve for turbulence by several orders of magnitude. The actual computer resources are not sufficient enough to support the expensive and long simulations resulting from these tiny time and space resolutions. As a result, the use of detailed chemistry is limited to a very small number of academic studies and as of today such large mechanisms are seldom employed in industry. Accordingly, most of the reactive computations are today performed from either a tabulation or from a reduction of the chemistry. The two approaches are briefly discussed here.

2.2.3.1 Chemistry reduction

The reduction of chemistry consists in lowering the complexity of the combustion mechanism by removing chemical species and reactions without significantly modifying the results for the conditions under study. A large amount of methodologies have been developed for the derivation of reduced mechanisms. A brief review of some of these techniques employed in the present thesis is proposed in Chapter 4.

2.2.3.2 Chemistry tabulation

Another largely employed methodology for the reduction of the costs associated to chemistry consists in storing the chemical responses obtained from canonical 1D flame simulations into a library relying on a reduced number of parameters. The mixture composition, temperature and species source terms are thus obtained from this library also called a lookup chemical table. The sub-space coordinates (table input parameters) are either expressed from one thermochemical variable or from the linear combination of independent variables.

Maas and Pope [29] observed that there exist a composition sub-space called manifold in which the evolution of the reactive system converges towards a group of similar trajectories. This set is called *Intrinsic Low Dimensional Manifold* (ILDM) or variety attractor. Knowing the trajectory for the attractor enables the reconstruction of the evolution of the entire system. The validity range of the attractor is directly related to the number of dimensions of the composition sub-space.

Two main models have been constructed from the ILDM methodology and from the flamelet (discussed in section 2.3.1) hypothesis namely the FPI (*Flamelet Prolongation of ILDM*) model developed by Gicquel [30] and the FGM model (*Flamelet Generated Manifold*) of Van Oijen [31]. These models rely on the assumption that there is an analogue response between the local flame front and the tabulated laminar canonical flamelet. The laminar flame responses are computed for given conditions and projected in the reduced space: tabulated as a function of a few parameters.

2.3 Combustion regimes

Two canonical combustion regimes exist. A premixed configuration is characterised by a perfect mixing of the fuel and of the oxidiser before combustion while a diffusion regime is achieved when combustion occurs at the interface between the fuel injection and the oxidiser injection.

Premixed flames are interesting in the sense that they provide high burning efficiency because the mixing between the fuel and the oxidiser is done prior to the combustion. The temperature of the burnt gases is also easily monitored through the equivalence ratio of the mixture. This exhaust temperature is a key parameter for a number of industrial applications and also controls the pollutants formation. Unfortunately because of the premixing, these flames are difficult to design and finally, the reaction may accidentally be initiated which poses real safety problems.

On the other hand, diffusion flames are much easier to design and also much safer to operate. Indeed, because no premixing is present, the flame cannot propagate in the fuel stream since the oxidiser is missing and vice versa. Notwithstanding these facts, non-premixed flames have drawbacks because the mixing governed by molecular diffusion is less efficient and because the maximum temperature is difficult to control.

Most industrial applications cannot be simply described by these two ideal cases. Real systems lie in a regime that is neither strictly premixed nor non-premixed flames and that shares characteristics with both of them. This last regime is referred as partially-premixed combustion. The three regimes are introduced and illustrated in this section.

2.3.1 Canonical problem: The perfectly premixed flame

2.3.1.1 Premixed flame structure

The unstretched premixed flame is the most common canonical model employed to describe combustion processes at constant pressure. Premixed combustion is characterised by a fresh mixture of reactants separated from the burned gases by a flame front that freely propagates in the direction of the fresh gases at a velocity S_L^0, as illustrated on figure 2.3. The structure of a premixed flame is characterised by three regions:

- A **preheat zone**, where fresh reactants are heated by the thermal diffusion fluxes,

- A **reactive layer** defined by a reaction thickness in which the fuel is first decomposed in series of intermediate fuels which in turn are decomposed to form radical species as for instance H, O and OH,
- A **post-flame region** where the intermediates are combined together to form major combustion products such as CO_2 and H_2O.

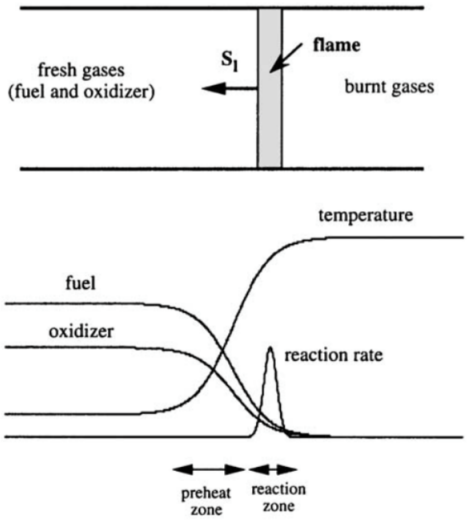

Figure 2.3: Structure of a laminar premixed flame [32].

2.3.1.2 Simplified equations for freely propagating 1D flames

The conservation equations introduced within section 2.1.2 are further simplified in the context of 1D premixed flames propagating in the x direction (at constante pressure). For a steady flame in the reference frame of the flame, mass is conserved at each point so that:

$$\frac{\partial \rho u}{\partial x} = 0 \longrightarrow \rho u = \rho_0 S_L^0 \,, \tag{2.52}$$

where ρ_0 is the fresh gases density and S_L^0 is the laminar flame speed defined in section 2.3.1.4. Thanks to the relation 2.52, the momentum equation is no more necessary. Regarding the species conservation, the steady evolution of the chemical species along the x axis is simplified to the relation:

$$\frac{\partial}{\partial x}(\rho(u + V_k)Y_k) = \dot{\omega}_k \,, \tag{2.53}$$

and finally, in this context, the enthalpy conservation reads:

$$\frac{\partial}{\partial x}\left(\rho u h_s\right) = \frac{\partial}{\partial x}\left(\lambda_{th}\frac{\partial T}{\partial x}\right) - \frac{\partial}{\partial x}\left(\rho \sum_{k=1}^{N_{\text{sp}}} h_{s,k} Y_k V_k\right) + \dot{\omega}_T \,. \tag{2.54}$$

2.3.1.3 Controlling variables

The chemical process taking place within the reactive front of a premixed flame may be described using a progress variable c which is normalised in order to be equal to 0 in the fresh gases and 1 in the burned

gases region. On the basis of the temperature variation across the flame, this progress variable reads:

$$c = \frac{T - T_0}{T_{eq} - T_0} \,. \tag{2.55}$$

with T_{eq} the equilibrium temperature. Under the hypothesis of unity Schmidt and Lewis numbers, it is also commonly expressed from Y_c which is estimated from a linear combination of the combustion products:

$$c = \frac{Y_c - Y_{c,0}}{Y_{c,eq} - Y_{c,0}} \,. \tag{2.56}$$

Typically $Y_c = Y_{\mathrm{CO}} + Y_{\mathrm{CO_2}} + Y_{\mathrm{H_2O}}$, $Y_{c,eq}$ being Y_c at equilibrium. This definition is valid for the great majority of premixed combustion problems, however it does not apply well for some specific cases including the capture of the $\mathrm{NO_x}$ levels. The progress variable c is particularly suitable for the analysis of the flame structure, to estimate the location of the reactive layer and to define the normal to the flame front through the relation:

$$n = \frac{-\nabla c}{|\nabla c|} \,. \tag{2.57}$$

For a premixed flame, the perfect mixing of the fuel and oxidiser is characterised by an equivalence ratio which is computed from relation:

$$\phi = s \frac{Y_{F,0}}{Y_{O,0}} \,, \tag{2.58}$$

where $Y_{F,0}$ and $Y_{O,0}$ respectively represent the fuel and oxidiser mass fractions in the fresh gases. The term s is the stoichiometric ratio defined by relation 2.59.

$$s = \frac{\nu_O W_O}{\nu_F W_F} \,, \tag{2.59}$$

where W_F and W_O are the fuel and oxidiser molecular weights. The terms ν_F and ν_O respectively stand for the fuel and oxidiser stoichiometric coefficients within the global reaction:

$$\nu_F F + \nu_O O \rightarrow \nu_P P \,, \tag{2.60}$$

with F, O and P the species formula of the fuel, oxidiser and the product of the global reaction. The equivalence ratio equals unity for a stoichiometric mixture. The mixture is said to be “lean" when the fuel mass fraction in the fresh gases $Y_{F,0}$ is lower than in stoichiometric conditions *i.e.* when the equivalence ratio is lower than 1. On the other hand it is called “rich" for higher fuel mass fractions in the fresh gases *i.e.* for ϕ greater than 1.

2.3.1.4 Flame speed, flame thickness

Multiple definitions of the flame speed are commonly employed whether the combustion is analysed in an absolute reference frame (absolute speed), relatively to the local flow velocity (displacement speed) or considering the speed at which the the fuel reacts (consumption speed). The so-called **laminar flame speed** is the only one studied in this thesis. It corresponds to the speed at which the fuel is consumed. It is computed from the integral of the burning rate across the flame brush:

$$S_L^0 = -\frac{1}{\rho_0 (Y_{F,0} - Y_{F,\infty})} \int_{-\infty}^{+\infty} \dot{\omega}_F dx \,, \tag{2.61}$$

where x corresponds to the direction of the flame domain, and ρ_0, $Y_{F,0}$ are respectively the density and the fuel mass fraction in the fresh gases and where $Y_{F,\infty}$ is the fuel mass fraction in the burned gases.

The laminar flame is also described through its thickness which varies according to the composition of the burning mixture (fuel and oxidiser type, equivalence ratio), the initial temperature and pressure. Several definitions exist including the thermal thickness δ_L^{th}, the diffusive thickness δ_L^d, the blint thickness δ_L^b and the reaction zone thickness δ_L^r. The **thermal thickness** [33] is computed from the temperature gradient:

$$\delta_L^{th} = \frac{T_{eq} - T_0}{\left|\frac{\partial T}{\partial x}\right|_{max}} , \tag{2.62}$$

where T_0 and T_{eq} are respectively the temperature in the fresh and in the burned gases. The diffusive thickness [33] provides an *a priori* estimation of the flame thickness that relies on the thermal diffusion of the fresh gases $\delta_L^d = D_{th}^0/S_L^0$. It is easy to compute although it usually underestimates the thickness value in comparison to δ_L^{th}. The blint thickness [34] is a corrected version of the diffusive thickness which relies on equilibrium thermochemistry $\delta_L^b = 2\delta_L^d(T_{eq}/T_0)^{0.7}$. It provides a much closer estimation of the thickness of the thermal layer. Finally the reaction zone thickness [35] is estimated from the region where the heat is released. It is usually one order of magnitude smaller than the thermal thickness. Along this thesis, only the thermal thickness will be employed using the relation 2.62.

2.3.2 Canonical problem: The diffusion flame

Diffusion flames are characterised by a separated injection of fuel and oxidiser. The flame develops inside of the diffusion layer and is stabilised exactly at the stoichiometric line. In opposition to the premixed flame, the diffusion one is **not associated to auto-propagative effects** and is **not characterised by any specific thickness** since it is largely piloted by the mixing of the reactants. The diffusion flame is illustrated on figure 2.4. The maximum temperature is located inside of the reaction zone and diffuses towards the fuel and the oxidiser streams. The structure inside of the diffusion flame is piloted by the external streams which influence the local stretch.

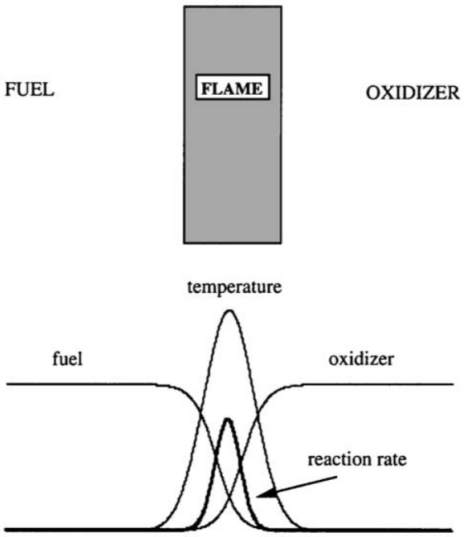

Figure 2.4: Structure of a laminar diffusion flame [32].

2.3.2.1 Passive mixture fraction

The mixing state is locally described using a mixture fraction Z. The use of the atomic conservation is one way to define Z as a passive scalar in a multi-species environment. Bilger [36] provides a description of the mixture fraction for hydrocarbon species of type C_mH_n:

$$Z = \frac{Z_C/(mW_C) + Z_H/(nW_H) + 2(Y_{O_2,2} - Z_O)/(\nu_O W_{O_2})}{Z_{C,0}/(mW_C) + Z_{H,0}/(nW_H) + 2Y_{O_2,2}/(\nu_O W_{O_2})} , \tag{2.63}$$

within which $Y_{O_2,2}$ represents the oxygen mixture fraction in the oxidiser inlet. Z_j corresponds to the mass fraction of the j^{th} atom and is computed for C, H and O atoms from relation:

$$Z_j = \sum_{k=1}^{N_{sp}} \frac{\alpha_{jk} W_j}{W_k} Y_k , \tag{2.64}$$

where α_{jk} is the number of j^{th} atom into species k, W_j is the molecular weight associated to the atom j and W_k represents the species k molecular weight.

2.3.2.2 Steady strained diffusion flame

One relevant canonical problem for the study of non-premixed combustion is the steady strained one dimensional diffusion flame. It is illustrated on figure 2.5. This approach is used frequently for the tabulated methodologies employed in non-premixed combustion.

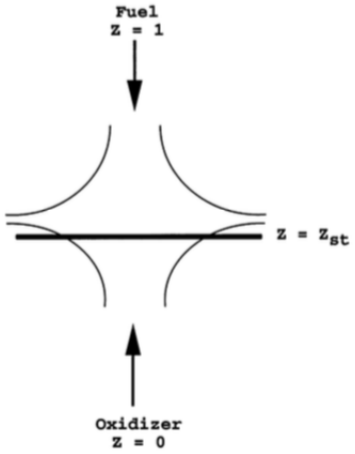

Figure 2.5: Counter-flowing diffusion flame [32]

2.3.3 Partially premixed combustion

2.3.3.1 Combustion regimes in real systems

Higher performances are reached for premixed combustion than for diffusion flames. However, in real systems for which efficient, easy and safe to operate strategies are necessary, the fuel and oxidiser cannot meet outside of the combustion chamber. For that reason, separated injections of the fuel and of the oxidiser are frequently retained and the actual design tendency is towards the development of technologies to enhance the mixing of the reactants before they enter the combustion zone. This may be done

by increasing turbulence (introducing a swirl) or by enhancing the interaction between the fuel and the oxidiser directly through the injection system. Nevertheless, a great majority of the industrial systems operate under conditions in which the reactants are not perfectly mixed together when they start burning or in conditions where local flame extinctions favour the mixing between the fuel and the oxidiser while they react in the flame zone. Accordingly, a point situated within the reactive layer faces a combustion regime that varies from perfectly premixed combustion to non-premixed combustion. In that case, the flame is said to operate in a partially premixed regime. This combustion mode has a drastic impact on the reaction rate. It moreover plays an important role in the stabilisation of a flame which is the result of an intense mixing between the fuel, the oxidiser and the burned gases that leads to the creation and propagation of partially premixed flamelets.

In order to locally identify the combustion regime, several indexes have been developed, from the Takeno index [37], based on fuel and oxidizer gradients, to the gradient free GFIR index [38, 39] based on mixture fraction and heat release rate. Eventually, a method based on convolutional neural networks [40] have also been proposed for a reliable combustion regime index based on thermochemical properties.

2.3.3.2 Stratified combustion

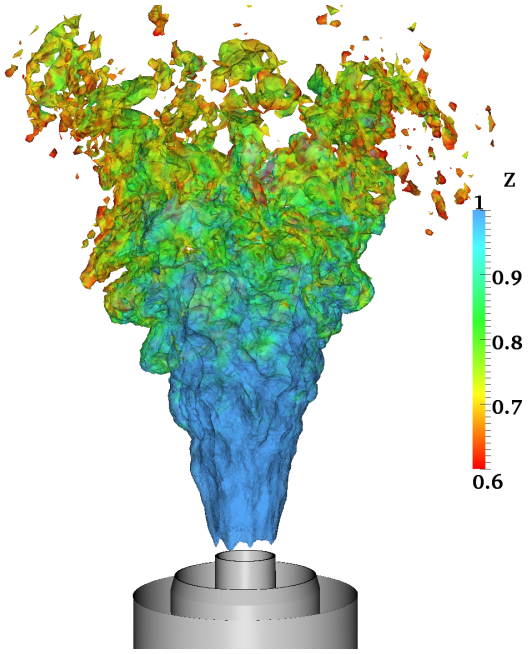

Figure 2.6: LES of a stratified turbulent flame colored by the filtered mixture fraction, by Mercier *et al.* [41].

A specific application of partially premixed flames is stratified combustion. It can be seen as a propagation of a flame within several layers of premixed fuel-air mixtures at different equivalence ratios. An example of stratified methane-air LES is presented Fig. 2.6. Stratified combustion is typically found in gas turbines, and internal combustion engines as well as in the majority of the industrial furnaces. This type of combustion mode is of interest thanks to its ability to provide high efficiencies while reducing the pollutants emissions. Typically CO and NO_x levels are minimised because of overall lean conditions and thanks to the lowering of the temperature. Stratification is also frequently encountered in premixed

combustion involving a dilution with cold air. The flamelet hypothesis, described in the next chapter, is usually employed to model stratified combustion.

2.4 Aerothermochemical equations in the LES formalism

2.4.1 Introduction to turbulence

In the flows characterised by low velocities, the small perturbations are instantly smoothed by the molecular viscosity which tends to maintain organisation. In that case, the flow is called laminar and is characterised by regular parallel trajectories. When the velocity increases, the viscosity is not strong enough to dissipate the perturbations which are furthermore amplified by several instabilities. The flow moves towards a turbulent state characterised by a disorganised appearance which is associated to a large range of macroscopic scales. The same set of equations is used to describe both states. The transition between the laminar and the turbulent state is explained by the non-linearity of these equations. Most of the flows encountered in industrial processes, in transportation or even in nature are non stationary and turbulent.

The turbulent nature of a flow may be quantified comparing the inertial forces that tend to disrupt the flow and create new turbulent scales to the viscous forces which have the tendency to dissipate the movement and restore a laminar regime. The Reynolds number is a non-dimensional number that provides such a comparison:

$$Re = \frac{uL}{\nu} \,. \tag{2.65}$$

It is expressed respectively from the velocity u and characteristic size L of the flow and from ν which represents the kinematic viscosity of the fluid. Small Reynolds numbers are representative of laminar flows while large Re correspond to turbulent conditions. The Kolmogorov theory [42] introduces the concept of turbulent energy cascade towards the small scales which is one way to describe the turbulent energy spectrum. It is illustrated within figure 2.7 by expressing the turbulent kinetic energy as a function of the wave number. Three different scales are used to describe this spectrum and then to calibrate the direct and large scales simulations.

- **Macroscopic scale:** The largest scales of the turbulence are geometry dependant. These are the most energetic turbulent structures. The turbulent kinetic energy is defined from the relation:

$$k_t = \sum_{i=1}^{3} \frac{1}{2} u_i^{'2} \,. \tag{2.66}$$

  Two scales may be employed to describe the macroscopic turbulent structures, namely the energetic length scale L_e and the integral length l_t. The energetic length L_e is expressed through the relation:

$$L_e = \frac{k_t^{3/2}}{\epsilon} \,, \tag{2.67}$$

  where ϵ corresponds to the turbulent dissipation. The integral length l_t is computed through:

$$l_t = \frac{u^{'3}}{\epsilon} \,. \tag{2.68}$$

  with $u^{'}$ defined under the hypothesis of local isotropy:

$$u^{'} = \sqrt{\frac{2}{3}k_t} \tag{2.69}$$

The turbulent Reynolds number Re_t is expressed from this integral scale using:

$$Re_t = \frac{u' l_t}{\nu} \, . \tag{2.70}$$

And the relation between the length scales L_e and l_t is simply:

$$\frac{l_t}{L_e} = \left(\frac{2}{3}\right)^{3/2} \, . \tag{2.71}$$

- **Intermediate scale:** The largest eddies become unstable and break to form smaller eddies. This transfer is done following the $k_t^{-5/3}$ law. The Taylor scale λ to which this is associated is the most dissipative scale.

- **Viscous dissipation scale:** This scale refers to the the smallest structure of the flows and is limited by the molecular agitation. It is referred as the Kolmogorov scale in which length and velocity are expressed from:

$$l_K = \left(\frac{\nu}{\epsilon}\right)^{1/4} \quad \text{and} \quad u_K = (\nu\epsilon)^{1/4} \, . \tag{2.72}$$

  ϵ refers to the dissipation rate through the formation of heat of the turbulent kinetic energy. A turbulent Reynolds number associated to the Kolmogorov length scale appears $Re_K = u_K^{'} l_K / \nu \approx 1$.

2.4.2 Strategies for the simulation of turbulent flows: RANS, LES, DNS

The Computational Fluid Dynamics (CFD) aims at simulating numerically the flows by solving for the discretised conservative equations. The large variety of scales observed while numerically solving for the flows depends on the viscosity of the simulated fluid. The turbulence modelling consists in the modification of the viscosity of the studied fluid to limit the scales to the ones that can be solved on the employed mesh.

Three different approaches are used to simulate turbulent flows, namely DNS, RANS and LES.

- The introduced set of conservative equations allows for solving directly the aerothermochemistry over all the space and time scales of the flow. This approach is called **DNS** for *Direct Numerical Simulation*. Such a method is expensive because it requires the use of a mesh capable of capturing the smallest scales of the flow through a resolution $\Delta = 2l_K$ (see [44]). This condition is expressed from the turbulent Reynolds number and the integral scale through the relation:

$$\Delta \approx \frac{l_t}{Re_t^{3/4}} \tag{2.73}$$

  Because of this elevated cost, DNS is today exclusively employed for the simulation of academic configurations limited to reasonably low Reynolds number.

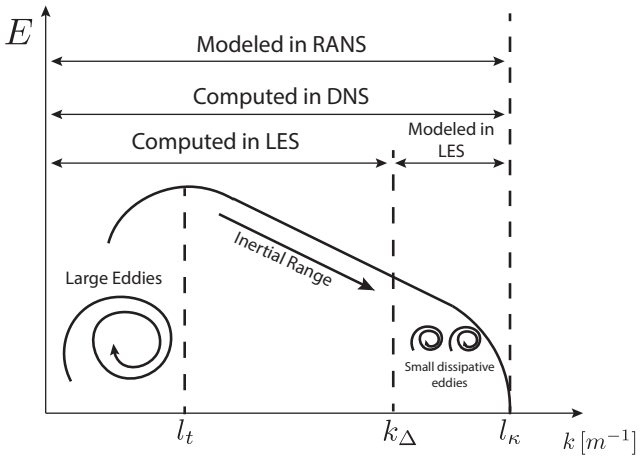

Figure 2.7: Illustration of the turbulent energetic spectrum along the energetic cascade. The solved and modelled scales are given for RANS, LES and DNS approaches. Image extracted from [43].

- To numerically solve for fluid dynamics at reasonable costs, time averaged equations have been derived. This approach is referred as **RANS** for *Reynolds Averaged Numerical Simulation*. The entire set of turbulence fluctuations are modelled and no scale from the turbulent energy spectrum is solved. Using this approach, the extracted informations concern only the mean behaviour of the flow. Since it allows for dealing with coarse meshes hence giving short runback times, the methodology has been largely studied in academia over the last decades and is still today a reference for most CFD based applications in industry.

- Finally, the **LES** for *Large-Eddy Simulation* consists in the solving of the non stationary large structures of the flow and on the modelling of the smallest scales. This approach still requires the introduction of specific models but these can be constructed from the information about the large scales of the flow which are numerically solved. The introduction of such models lies on the assumption that the cutting point between the solved and modelled informations is located within the inertial scale (as illustrated on figure 2.7). In practice, this cutting point is dependant on the used mesh. The added viscosity is of the order of the Reynolds number corresponding to the cutting length scale, hence of the order of the mesh size Δ.

2.4.3 Filtered equations for LES

The separation between the solved scales for LES and the scales that are modelled is given by a filtering operation of the equations that are solved for a DNS. For a scalar $\phi(\mathbf{x}, t)$, the filtering is performed through a spatial convolution that gives,

$$\overline{\phi}(\mathbf{x}, t) = \int_{\mathbb{R}^3} \phi(\mathbf{y}, t)\mathcal{G}_\Delta(\mathbf{y} - \mathbf{x})d\mathbf{y}\,, \tag{2.74}$$

where $\mathcal{G}_\Delta$ is the filter associated to the scale Δ that provides the filtered quantity $\overline{\phi}(\mathbf{x}, t)$. The filter must be normalised so that,

$$\int_{\mathbb{R}^3} \mathcal{G}_\Delta(\mathbf{x})d\mathbf{x} = 1\,, \tag{2.75}$$

and must verify the commutativity of both spatial and temporal derivation operators, so that:

$$\frac{\partial\overline{\phi}}{\partial t} = \overline{\frac{\partial\phi}{\partial t}} \quad \text{and} \quad \frac{\partial\overline{\phi}}{\partial x_i} = \overline{\frac{\partial\phi}{\partial x_i}} \,. \tag{2.76}$$

After the filtering separation, the ϕ variable may be seen in two parts: (1) a part $\overline{\phi}$ evolving above the scale Δ and (2) a fluctuating unresolved part ϕ' evolving at scales lower than Δ.

$$\phi(\mathbf{x},t) = \overline{\phi}(\mathbf{x},t) + \phi'(\mathbf{x},t) \,. \tag{2.77}$$

Because the density ρ of the flow varies from one point to another, the Favre filtered variable $\widetilde{\phi}$ is introduced. It corresponds to a filter weighted by density.

$$\widetilde{\phi} = \frac{\overline{\rho\phi}}{\overline{\rho}} \,. \tag{2.78}$$

The Favre convolution is applied to the system of conservative equations (2.19)-(2.20)-(2.22) and (2.28) leading to the following set of filtered relations:

- **Filtered mass conservation**

$$\frac{\partial\overline{\rho}}{\partial t} + \frac{\partial\overline{\rho}\widetilde{u}_i}{\partial x_i} = 0 \,. \tag{2.79}$$

- **Filtered momentum conservation**

$$\frac{\partial\overline{\rho}\widetilde{u}_j}{\partial t} + \frac{\partial\overline{\rho}\widetilde{u}_i\widetilde{u}_j}{\partial x_i} = -\frac{\partial}{\partial x_i}\underbrace{\left[\overline{\rho}(\widetilde{u_iu_j} - \widetilde{u}_i\widetilde{u}_j)\right]}_{(1)} - \frac{\partial\overline{P}}{\partial x_j} + \frac{\partial\overline{\tau}_{ij}}{\partial x_i} \,. \tag{2.80}$$

- **Filtered species conservation**

$$\frac{\partial\overline{\rho}\widetilde{Y_k}}{\partial t} + \frac{\partial\overline{\rho}\widetilde{u}_i\widetilde{Y_k}}{\partial x_i} = -\frac{\partial}{\partial x_i}\underbrace{\left[\overline{\rho}(\widetilde{u_iY_k} - \widetilde{u}_i\widetilde{Y_k})\right]}_{(2)} - \frac{\partial}{\partial x_i}\underbrace{\left(-\overline{\rho V_{k,i}Y_k}\right)}_{(3)} + \underbrace{\overline{\dot{\omega}}_k}_{(4)} \,. \tag{2.81}$$

- **Filtered energy conservation**

$$\frac{\partial\overline{\rho}\widetilde{h_s}}{\partial t} + \frac{\partial\overline{\rho}\widetilde{u}_i\widetilde{h_s}}{\partial x_i} = -\frac{\partial}{\partial x_i}\underbrace{\left[\overline{\rho}(\widetilde{u_ih_s} - \widetilde{u}_i\widetilde{h}_s)\right]}_{(5)} + \frac{D\overline{P}}{Dt} + \frac{\partial}{\partial x_i}\underbrace{\left(\overline{\lambda_{th}\frac{\partial T}{\partial x_i}}\right)}_{(6)} \tag{2.82}$$

$$-\frac{\partial}{\partial x_i}\underbrace{\left(\overline{\rho\sum_{k=1}^{N_{sp}} h_{s,k}Y_kV_{k,i}}\right)}_{(7)} + \underbrace{\overline{\dot{\omega}}_T}_{(8)} \,. \tag{2.83}$$

Unresolved terms (1)-(8) appear in the filtered conservative equations. Each of them is closed by introducing several models:

- **The sub grid Reynolds stress tensor (1)** $\tau'_{ij} = \overline{\rho}(\widetilde{u_iu_j} - \widetilde{u}_i\widetilde{u}_j)$ requires the introduction of a turbulence model for the transport of momentum by unresolved velocity fluctuations and account for the energy transfert between resolved and unresolved structures. The Boussinesq [45] approach

is employed in this thesis: turbulent fluxes are modelled using an expression similar to the laminar definition 2.21 and using a turbulent viscosity $\mu_t = \overline{\rho}\nu_t$ so that:

$$\tau_{ij}^{'} = \mu_t \left(\frac{\partial \widetilde{u_i}}{\partial x_j} + \frac{\partial \widetilde{u_j}}{\partial x_i} \right) - \frac{2}{3}\mu_t \frac{\partial \widetilde{u_k}}{\partial x_k}\delta_{ij} \, , \tag{2.84}$$

Several models may be introduced from this approach. The one employed in this thesis is discussed in the next section.

- **The sub grid species (2) and enthalpy fluxes (5)** respectively written:

$$\mathcal{F}_{k,i}^{'} = \overline{\rho}(\widetilde{u_i Y_k} - \widetilde{u_i}\widetilde{Y_k}) \tag{2.85}$$

$$\mathcal{Q}_{i}^{'} = \overline{\rho}(\widetilde{u_i h_s} - \widetilde{u_i}\widetilde{h_s}) \tag{2.86}$$

are modelled using a similar approach to the one for the sub grid Reynolds stress tensor. A turbulent Prandtl number Pr_t is introduced for the enthalpy fluxes:

$$\mathcal{Q}_{i}^{'} = -\frac{\mu_t}{Pr_t}\frac{\partial \widetilde{h_s}}{\partial x_i} \, . \tag{2.87}$$

and for the species fluxes, a turbulent Schmidt number is used Sc_t, so that:

$$\mathcal{F}_{k,i}^{'} = -\frac{\mu_t}{Sc_t}\frac{\partial \widetilde{Y_k}}{\partial x_i} \, . \tag{2.88}$$

These Prandtl and Schmidt may be constant over the entire domain or may vary in space and time depending on the formulation.

- **The filtered laminar diffusive fluxes of species (3) and enthalpy (6)-(7)** are usually expressed from their resolved part, neglecting their sub-grid scale contribution.

$$\overline{\lambda \frac{\partial T}{\partial x_i}} = \overline{\lambda}\frac{\partial \widetilde{T}}{\partial x_i} \, , \tag{2.89}$$

$$\overline{V_{k,i} Y_k} = -D_k \frac{W_k}{\overline{W}}\frac{\partial \widetilde{X}_k}{\partial x_i} \, , \tag{2.90}$$

$$\overline{\rho \sum_{k=1}^{N_{sp}} h_{s,k} Y_k V_{k,i}} = -\overline{\rho} \sum_{k=1}^{N_{sp}} D_k \frac{W_k}{\overline{W}}\frac{\partial \widetilde{X}_k}{\partial x_i}\widetilde{h}_{s,k} \, . \tag{2.91}$$

- **The filtered species chemical rate (4) enthalpy source term (8)** respectively $\overline{\dot{\omega}}_k$ and $\overline{\dot{\omega}}_T$ are critical points regarding the modelling of turbulent combustion. They will be discussed later in chapter 3.

2.4.4 Sub grid scale modelling for turbulence

Several approaches exist in the literature, however only the Boussinesq approximation is employed in this thesis. It relies on the assumption that the effect of the unresolved small structures are similar to an increase of the turbulent viscosity. The main difficulty lies in the calculation of this additional viscosity. It is at the origin of several modelling developments. Three of them are shortly described below.

- **The Smagorinsky model** relies on an equilibrium hypothesis between production and dissipation of kinetic energy at the scale of the filter. The turbulence is therefore only considered as a dissipative phenomena.

$$\nu_t = (C_S\Delta)^2 \left|\widetilde{\mathbf{S}}\right| = (C_S\Delta)^2 \sqrt{2\widetilde{S}^t_{ij}\widetilde{S}^t_{ij}}\,, \tag{2.92}$$

where C_S is the Smagorinsky constant (with a typical value $C_S = 0.17$ calculated from the Kolmogorov spectrum), Δ is the characteristic filter width and $\widetilde{\mathbf{S}}$ the filtered strain tensor that is expressed:

$$\widetilde{S}_{ij} = \frac{1}{2}\left(\frac{\partial\widetilde{u}_i}{\partial x_j} + \frac{\partial\widetilde{u}_j}{\partial x_i}\right)\,. \tag{2.93}$$

- **The dynamic Smagorinsky model** is derived by Germano [46] and Lilly [47]. This approach relies on a dynamic and local estimation of the C_S constant. The sub grid behaviour is estimated from the resolved small structures which require the filtering written $\widehat{(\cdot)}$ of the solved velocity field at a size Δ' that is larger than the size Δ. The sub grid tensor and the sub grid tensor based on the velocity field may be expressed from the Smagorinsky model through the following formulations:

$$\tau^{'}_{ij} = 2\overline{\rho}\,(C_S\Delta)^2\,|\widetilde{\mathbf{S}}|\widetilde{S_{ij}}\,, \tag{2.94}$$

$$\tau^{''}_{ij} = 2\widehat{\overline{\rho}}\left(C_S\Delta'\right)^2|\widehat{\widetilde{\mathbf{S}}}|\widehat{\widetilde{S_{ij}}}\,. \tag{2.95}$$

The Germano identity is used to link both tensors through a term that depend on the solved field and which may be explicitly computed:

$$L_{ij} = \tau^{'}_{ij} - \tau^{''}_{ij} = \rho\left(\widehat{\widetilde{u}_i}\widehat{\widetilde{u}}_j - \widehat{\widetilde{u_i}\widetilde{u}_j}\right)\,. \tag{2.96}$$

Combining the equations (2.94), (2.95) and (2.96) allows for computing the Smagorinsky constant from the filtered velocity field at two different scales. The dynamic Smagorinsky model applies to a large range of conditions, however it is more difficult and more expensive to use, since it requires an explicit filtering operator. This approach is the one retained for the LES simulations showed in chapter 4 and 6.

- **The WALE model** for *Wall-Adaptating Eddy-Viscosity* [48] aims at predicting the correct behaviour at walls and the transition to the turbulence. With this model the turbulent viscosity is computed from relation:

$$\nu_t = C_W^2\Delta^2\frac{(s^d_{ij}s^d_{ij})^{3/2}}{(\widetilde{S}_{ij}\widetilde{S}_{ij})^{5/2} + (s^d_{ij}s^d_{ij})^{5/4}}\,, \tag{2.97}$$

in which the C_W constant equals 0.5. The tensor s^d_{ij} reads,

$$s^d_{ij} = \frac{1}{2}\left(\widetilde{h}_{ij} + \widetilde{h}_{ji}\right) - \frac{1}{3}\widetilde{h}_{kk}\delta_{ij} \quad \text{with} \quad \widetilde{h}_{ij} = \widetilde{g}_{ik}\widetilde{g}_{kj} \quad \text{and} \quad \widetilde{g}_{ij} = \frac{\partial\widetilde{u}_i}{\partial x_j}\,. \tag{2.98}$$

2.5 Numerical description of the liquid phase

2.5.1 Two-phase flows modelling

A flow composed of particles rely on the presence of a carrying phase which may either be liquid or gas and on a dispersed phase composed of either liquid particles (such as kerosene droplets), solid particles

(such as coal) or bubbles into a gaseous phase. The interaction of the dispersed phase with the flow highly depends on the fraction of the volume occupied by the particles in the fluid domain. In the context of this thesis, only a diluted suspension phase is considered. It requires a two-way coupling [49] which means that the influence of the moving particles on the fluid also have to be accounted for in addition to the inclusion of the impact of the fluid on the dispersed phase.

Two different descriptions are found in the literature: (1) The Euler-Euler approach consists of considering the dispersed phase as a continuous environment similar to a fluid which is given the mean properties of the droplets mist. The characteristics of the dispersed phase are thus transported on a Eulerian mesh using a set of flow equations similar to the ones employed for the carrying phase. (2) The Lagrangian approach consists of following particles individually in the flow domain. The mass transfer, momentum and energy phenomena are solved in interaction with the carrying phase. Each droplet (particle) has its own properties (temperature, velocity and diameter). Efficient interpolation methods are required with this approach since the position of the particles does not coincide with the mesh nodes. The Lagrangian description is the methodology employed for the simulation presented in chapter 4.

2.5.2 Equations for the Lagrangian description

2.5.2.1 Kinematic of the droplets

Each particle is assumed to have a spherical form, the mass m_p of a particle thus reads:

$$m_\mathrm{p} = \rho_\mathrm{p} \frac{\pi}{6} d_\mathrm{p}^3 \,, \tag{2.99}$$

where d_p refers to the diameter of the particule and ρ_p to its density. The equations for the transport of the particles are as follows:

- **The particle kinematic formalism** expresses the evolution of the position x_i^p of the particle p moving with the velocity u_i^p from relation:

$$\frac{\mathrm{d}x_i^\mathrm{p}}{\mathrm{d}t} = u_i^\mathrm{p} \,. \tag{2.100}$$

- **The momentum conservation** is written as a function of F_i^p which represents the projection onto the i^{th} axis of the forces acting on the particle.

$$m_\mathrm{p} \frac{du_i^\mathrm{p}}{dt} = F_i^\mathrm{p} \quad \text{where} \quad F_i^\mathrm{p} = F_{i,G}^\mathrm{p} + F_{i,A}^\mathrm{p} + F_{i,I}^\mathrm{p} \,, \tag{2.101}$$

  F_i^p is associated to three contributions: $F_{i,G}^\mathrm{p}$ stands for the gravity and buoyancy forces, $F_{i,A}^\mathrm{p}$ for the aerodynamical and drag forces and $F_{i,I}^\mathrm{p}$ represents the interaction forces with the wall and the other Lagrangian particles.

  - **Gravity:** The gravitational and buoyancy forces acting on the particle may be written from the relation:

$$F_{i,G}^\mathrm{p} = (\rho_\mathrm{p} - \rho) \frac{\pi}{6} d_\mathrm{p}^3 g_i \tag{2.102}$$

    where ρ is the density of the carrier-phase and g_i is the acceleration due to gravity. In strongly turbulent flows, the gravity force is often neglected in comparison to the aerodynamical forces. Furthermore, $\rho_\mathrm{p} >> \rho$ for liquid droplets into a gaseous phase. The buoyancy forces will thus be neglected thereafter.

– **Aerodynamic:** The drag force induced by the gas on the particle reads:

$$F_{i,A}^{\mathrm{p}} = m_{\mathrm{p}} \frac{1}{\tau_{\mathrm{p}}} (u_i^{\mathrm{p}} - u_i) \,, \tag{2.103}$$

where τ_{p} is the time it takes to a particle to respond to the velocity fluctuations. This characteristic time is dependent on the flow regime that is defined by the particle Reynolds number Re_{p} expressed:

$$Re_{\mathrm{p}} = \frac{d_{\mathrm{p}} |u_i^{\mathrm{p}} - u_i|}{\nu} \,, \tag{2.104}$$

τ_{p} is described as a function of the drag coefficient C_D from the relation,

$$\tau_{\mathrm{p}} = \frac{4 \rho_{\mathrm{p}} d_{\mathrm{p}}^2}{3 C_D Re_{\mathrm{p}} \rho \nu} \,. \tag{2.105}$$

A large variety of correlations have been proposed for the drag coefficient C_D [50]. The correlation for numbers of the particle Reynolds Re_{p} lower than 1 is the Stokes law.

$$C_D = \frac{24}{Re_{\mathrm{p}}} \,. \tag{2.106}$$

For intermediate values, the correlation by Schiller and Naumann is employed [51],

$$C_D = \frac{24}{Re_{\mathrm{p}}} + \frac{3.6}{Re_{\mathrm{p}}^{0.313}} \,. \tag{2.107}$$

For values of the particle Reynolds number higher than 1000, the coefficient is considered to be constant and equal to 0.44.

2.5.2.2 Evaporation

Hypotheses of the evaporation model

The temperature and the composition of the droplet are estimated from the presented conservative equations. They are highly dependent on the ambient conditions. The composition at the surface of the droplet (particle) is defined by the subscript $_{\mathrm{p}}$ while the subscript notation $_{\infty}$ refers to the condition of the surrounding gas. This is illustrated on figure 2.8. Several hypotheses are here formulated in the context of a single-component droplet.

1. The droplet is considered to be perfectly spherical and isolated *i.e.* its interaction with the other droplets is not accounted for.

2. The temperature of the droplet is considered uniform, its thermal conductivity being infinite.

3. The surface of the droplet is assumed to be thermodynamically in equilibrium with the environment. The Clausius-Clapeyron law is therefore employed for the estimation of the saturation vapour pressure at the surface of the droplet.

4. Except for the evaporated portion, the properties of the surrounding gas are considered constant from the surface of the droplet up to infinity.

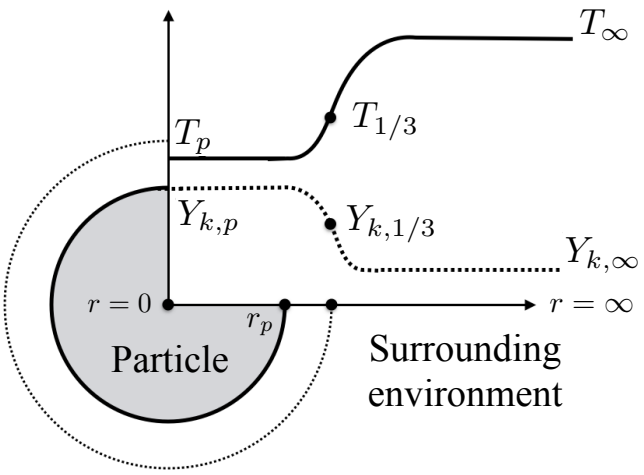

Figure 2.8: Illustration of a droplet p characterised by a temperature T_p and a composition $Y_{k,\mathrm{p}}$ evaporating into its surrounding gaseous environment at conditions T_∞ and $Y_{k,\infty}$ [52].

5. The formulation proposed by Hubbard *et al.* [53] also referred as the 2/3-1/3 law is retained to consider the properties of the gas in the small layer that forms around the droplet. The composition and temperature in this small region are computed from the surface conditions and from the infinite conditions considering different ponderations. The formulation is illustrated on figure 2.8.

$$T_{1/3} = \frac{2}{3}T_\mathrm{p} + \frac{1}{3}T_\infty \,, \tag{2.108}$$

$$Y_{k,1/3} = \frac{2}{3}Y_{k,\mathrm{p}} + \frac{1}{3}Y_{k,\infty} \,. \tag{2.109}$$

Mass evolution of the droplet

The mass evaporation rate of the droplet is computed from the integration of the conservation equations of the evaporated species from the droplet radius up to infinity. See the work by Kuo [54] and Sirignano [55] for more details.

$$\dot{m}_\mathrm{p} = -\pi d_\mathrm{p}(\rho D) Sh \log\left(1 + B_M\right) , \tag{2.110}$$

This formulation introduces several characteristic terms and numbers

1. The Spalding number expressed in terms of mass allows for describing the mass transfer effects as a function of the evaporated species mass fraction studied both at the droplet surface and in the surrounding gas. It is expressed from the relation:

$$B_M = \frac{Y_{k,\mathrm{p}} - Y_{k,\infty}}{1 - Y_{k,\mathrm{p}}} \tag{2.111}$$

The mass fraction $Y_{k,\infty}$ is expressed from an interpolation of the Eulerian mesh. The following expressions are employed for the estimation of the species mass fractions at the surface of the droplet:

$$Y_{k,\mathrm{p}} = \frac{X_{k,\mathrm{p}} W_k}{W_\mathrm{p}} \tag{2.112}$$

The species molar fraction $X_{k,\mathrm{p}}$ is computed from the Dalton's law:

$$X_{k,\mathrm{p}} = \frac{P_{k,\mathrm{p}}}{P} \,, \tag{2.113}$$

it is deduced from the Clausius-Clapeyron's law that gives the relation between the total pressure at saturation of a pure component as a function of its boiling temperature and of its latent heat of vaporisation. The estimation of the molecular weight at the surface of the droplet is deduced from the relation:

$$W_{\mathrm{p}} = X_{k,\mathrm{p}} W_k + (1 - X_{k,\mathrm{p}}) \overline{W}_{j \neq k,\mathrm{p}} \, . \tag{2.114}$$

The computation of the term $\overline{W}_{j \neq k,\mathrm{p}}$ is achieved from the relation:

$$\overline{W}_{j \neq k,\mathrm{p}} = \overline{W}_{j \neq k,\infty} = \frac{1 - Y_{k,\infty}}{1 - Y_{k,\infty} \frac{W_\infty}{W_k}} W_\infty \, , \tag{2.115}$$

which states, that the molecular weight of the gaseous phase except for the evaporated species is constant from the surface of the droplet up to the infinity.

2. The Sherwood number Sh gives the ratio between the convective mass flux and the diffusive mass flux. The correlation proposed by Ranz and Marshall [56] applies in the context of a forced convection around a sphere. It reads:

$$Sh = 2 + 0.55 Re_{\mathrm{p}}^{1/2} Sc^{1/3} \tag{2.116}$$

3. The diffusion term (ρD) in the equation 2.110 is usually simplified to the expression:

$$\rho D = \frac{\mu_{1/3}}{Sc} \tag{2.117}$$

Temperature evolution of the droplet

The temperature evolution of the droplet is computed from the integration of the energy conservative equation from the droplet surface up to infinity. Doing so, the following expression is obtained;

$$\frac{\mathrm{d}T_{\mathrm{p}}}{\mathrm{d}t} = -\frac{1}{\tau_h} \left(T_{\mathrm{p}} - \left(T_\infty - \frac{L_v B_T}{C_{p,1/3}} \right) \right) \, , \tag{2.118}$$

where τ_h is the characteristic time associated to the heating of the spherical droplet and defined from:

$$\tau_h = \frac{\rho_{\mathrm{p}} d_{\mathrm{p}}^2}{6} \frac{Sc}{\mu_{1/3} Sh} \frac{C_{p,k}}{C_{p,1/3}} \frac{B_T}{\log 1 + B_M} \, , \tag{2.119}$$

where $\mu_{1/3}$ and $C_{p,1/3}$ are respectively the dynamic viscosity coefficient and the specific heat capacity at constant pressure computed with the 2/3-1/3 law. An explanation on the derivation of relation 2.119 may be found in [55] or in Enjalbert's thesis [57]. The thermal Spalding number B_T is here expressed as a function of the mass Spalding number through the relation,

$$B_T = (1 + B_M)^{\frac{ShPr}{NuSc}} - 1 \tag{2.120}$$

The Nusselt number is used to describe the ratio between the convective and diffusive heat transfers. As for the Sherwood number it may be expressed from the relation by Ranz and Marshall for a spherical droplet:

$$Nu = 2 + 0.55 Re_{\mathrm{p}}^{1/2} Pr^{1/3} \, . \tag{2.121}$$

Boiling specific condition

The problem is simplified when the temperature of the carrying phase is higher than the boiling temperature T_{boil} associated to the droplet composition. In that case, the gaseous layer that forms around the droplet reaches saturation, hence $Y_{k,\text{p}}$ tends to unity and the Spalding number diverges towards infinity.

In that situation, the equation 2.118 is simplified to $\mathrm{d}T/\mathrm{d}t = 0$. The temperature of the droplet is assumed to be equal to T_{boil}, which gives,

$$B_T^{\text{sat}} = \frac{C_{p,\text{ref}}(T_\infty - T_{\text{boil}})}{L_v} \,. \tag{2.122}$$

The Spalding number at boiling conditions expressed in terms of mass is then extracted from 2.120:

$$B_M^{\text{sat}} = (1 + B_T^{\text{sat}})^{\frac{NuSc}{ShPr}} \,, \tag{2.123}$$

and the equation 2.110 is employed for the calculation of the mass variation of the droplet using the Spalding number at saturation B_M^{sat}.

Diameter evolution

The diameter of the droplet evolves according to the formulation for the mass evolution 2.110.

$$\mathrm{d}m_{\text{p}} = \left(\frac{\pi \rho_{\text{p}} d_{\text{p}}^2}{2}\right) \mathrm{d}d_{\text{p}} \tag{2.124}$$

The time evolution of the particle diameter is computed from the characteristic time τ_m and the initial diameter of the particle $d_{\text{p},0}$.

$$\frac{\mathrm{d}d_{\text{p}}^2}{\mathrm{d}t} = \frac{d_{\text{p},0}^2}{2 d_{\text{p}} \tau_m} \quad \text{with} \quad \tau_m = \frac{\rho d_{\text{p},0}^2 Sc}{4 Sh \mu_{1/3} \log(1 + B_M)} \tag{2.125}$$

2.5.3 Coupling with the gaseous phase

2.5.3.1 Interaction between the dispersed phase and the gas

Three source terms are introduced into 2.19, 2.20, 2.23 and 2.28 to account for the feedback information from the particle to the gaseous phase. Namely θ_M for the mass conservation, θ_D for the momentum conservation and θ_H for the enthalpy. They are computed locally where the particle is present. The expressions associated to these three terms are:

$$\theta_M(x_i, t) = \frac{1}{\Delta V} \sum_{\text{p}=1}^{N_{\text{p}}} -\dot{m}_{\text{p}} \delta(x_i - x_i^{\text{p}}(t)) \,, \tag{2.126}$$

$$\theta_D(x_i, t) = \frac{1}{\Delta V} \sum_{\text{p}=1}^{N_{\text{p}}} -\dot{F}_{\text{p}} \delta(x_i - x_i^{\text{p}}(t)) \,, \tag{2.127}$$

$$\theta_H(x_i, t) = \frac{1}{\Delta V} \sum_{\text{p}=1}^{N_{\text{p}}} \left(-\dot{m}_{\text{p}} C_{p,l} \frac{\mathrm{d}T_{\text{p}}}{\mathrm{d}t} + \dot{m}_{\text{p}} L_v\right) \delta(x_i - x_i^{\text{p}}(t)) \,, \tag{2.128}$$

where δ corresponds to the Dirac distribution and ΔV to the control volume which theoretically should be of the order of the particle size. In practice the volume control is defined from the size of the cell that contains the particle.

2.5.3.2 Formalism in LES

Influence of the sub-grid fluctuations on the particles.
The Lagrangian solver relies on the scalars that are solved on the Eulerian mesh. Using LES, the sub-grid scales are unresolved. Therefore, the dispersed phase only knows about the filtered information $\widetilde{\phi}$. A model should be introduced [58, 59] to account for the sub-grid information and rebuild ϕ from the filtered value $\widetilde{\phi}$. It is reported in the literature that the introduction of such a model is important for the drag term only when the unresolved velocity fluctuations are of the order of the particle velocity or higher to the particle velocity. For an evaporating spray this condition is encountered only at the end of the droplets life. The majority of the spray is therefore insensitive to the velocity fluctuations. Hence, in the present case the effect is neglected.

Influence of the particles on the sub-grid scale turbulence.
The presence of the dispersed phase may impact the sub-grid fluctuations in two different manners: (1) the particles may dissipate the scales with the same order of magnitude [60] hence modifying the form of the energy spectrum, (2) the two-way coupling effects may be incorrectly estimated because the segregation of the particles by the sub-grid fluctuations are not accounted for. Apart from a study by Yuu *et al.* [61], most of the recent applications neglect this influence [62, 63]. The same assumption is made in the present work.

2.6 Numerical solvers

The results presented in this thesis have been derived from computations performed with two different community developed softwares namely CANTERA and YALES2. The ORCh methodology, described in Chapter 4 and proposed for the reduction and the optimisation of combustion mechanisms employs the CANTERA package.

2.6.1 Chemistry 1D solver: CANTERA

CANTERA is an open source suite of object-oriented software tools employed for the computation of reacting flows involving detailed chemistry, thermodynamics and complex transport properties [64]. It is used for the computation of chemical equilibrium, and for the simulation of networks of stirred reactors. An adaptative mesh refinement algorithm is implemented in the code to optimise the mesh resolution in the regions of strong gradients. The C++ version of the code is employed in this thesis.

2.6.2 Large-Eddy Simulation 3D solver: YALES2

YALES2 is a parallel CFD code which solves the three-dimensional Navier-Stokes equations on reactive two-phase problems using DNS and LES approaches [65]. The code relies on the use of a finite volume method based on unstructured meshes composed of triangles, tetrahedrons, prisms and pyramides hence allowing for the simulation of complex geometries. YALES2 uses a low Mach number formulation which avoid to deal with the compressible tiny time scales. It relies on the *Courant Friedrichs Lewy* (CFL) criteria for the estimation of the time steps. The YALES2 solver is capable of dealing with complex chemistry [66] and is well adapted to the most advanced massively parallel supercomputers [67].

Chapter 3

Turbulent combustion models in LES formalism & The potential of neural networks

Contents

A major problem associated to turbulent combustion appears in the closure of the filtered source term $\overline{\dot{\omega}}_k$. This term which includes the interaction between the turbulence and the combustion is a key aspect in the computation of reactive LES. In this chapter, few models from the literature are briefly introduced, including the thickened flame model used for the LES results of this thesis, and a novel modelling framework using machine-learning is presented for the particular case of premixed flames with tabulated chemistry. A detailed description of the state of the art on the turbulent combustion models may be found in the work by Veynante and Vervisch [32] or Pitsch [68]. The approaches to model turbulent combustion may be organised into three groups:

- **The algebraic approach:** The reaction rate is controlled by the turbulent mixing described in terms of scalar dissipation rate [69]. The smallest structures of the dissipation rate regulate the

mixing between the reactants. This approach may be employed only when the characteristic time associated to the turbulence is large compared to the time scales of the combustion *i.e.* for very large Damköhler Da numbers.

- **The statistical approach:** The filtered scalars are evaluated from an *a priori* knowledge of the unresolved structures properties obtained from a PDF (*Probability Density Function*). This function provides a statistical distribution of the sub grid scales properties. The greatest difficulty rests in the solving of this PDF. This is addressed through several methodologies:
  - **PDF transport.** The first approach proposed in the literature consists in the transport of the PDF and on its solving. A transport equation is added to the original set of conservative equations for the estimation of the filtered PDF [70]. Pope [71] proposed the use of a Monte Carlo approach to solve for the PDF: a set of stochastic lagrangian particles carries thermochemical informations into the physical space. The joint PDF is then constructed from the particles informations. Although theoretically the approach may be used with large chemistries, in practice, the number of particles necessary to maintain precision increases with the dimension of the problem making the problem unfit.
  - **Presumed PDF.** This approach allows for lowering the cost related to the joint PDF methods. This methodology relies on a reduction of the number of scalars necessary for the description of the system and by presuming the shape of the PDF. For instance, this approach is commonly linked with the FPI in tabulated chemistry for which the problem is simplified to two dimensions: the progress variable c and the mixture fraction Z.
- **The geometric approach:** The flame front is considered to be a thin moving geometric surface. Several combustion models are derived from this approach. The majority of them is intended to model perfectly premixed flames since they rely on the hypothesis that there exists a clear interface between the fresh and the burned gases. First examples are the G-Equation and Levelset [72, 73] models which are defined from a level of potential. The species properties are reconstructed depending on their distance to the potential interface. Other well employed approaches are the flame surface density concept [74] and the thickened flame model. A few details on its derivation are given in the next sub section.

3.1 The thickened flame model: TFLES

3.1.1 Overall principal

The size of the cells necessary to properly solve for the variations in the thin layer that forms the flame is usually small in comparison to the size of the employed mesh. The concept of flame thickening was introduced in the seventies by Butler *et al.* [75] and O'Rourke *et al.* [76] to tackle this issue. It aims at increasing the number of points within the flame so as to capture its overall structure while conserving its key properties.

Williams [77] and Kuo [54] stated that the velocity S_L^0 and the laminar flame thickness δ_L^0 can be expressed from the reaction rate $\dot{\omega}$ and from the thermal diffusion coefficient D_{th}:

$$S_L^0 \propto \sqrt{D_{th}\dot{\omega}} \quad \text{and} \quad \delta_L \propto \frac{D_{th}}{S_L^0} \propto \sqrt{\frac{D_{th}}{\dot{\omega}}} \,. \tag{3.1}$$

Using this analysis Colin *et al.* [78] proposed to broaden the flame by a factor $\mathcal{F}$ from the relations,

$$D_{th}^{\mathcal{F}} = D_{th}\mathcal{F} \quad \text{and} \quad \dot{\omega}^{\mathcal{F}} = \frac{\dot{\omega}}{\mathcal{F}}\,, \tag{3.2}$$

hence thickening the flame while maintaining the proper laminar flame velocity since:

$$S_L^0 \propto \sqrt{D_{th}\dot{\omega}} \longrightarrow S_L^{\mathcal{F}} \propto \sqrt{D_{th}\dot{\omega}}\,, \tag{3.3}$$

$$\delta_L^0 \propto \sqrt{\frac{D_{th}}{\dot{\omega}}} \longrightarrow \delta_L^{\mathcal{F}} \propto \mathcal{F}\sqrt{\frac{D_{th}}{\dot{\omega}}}\,. \tag{3.4}$$

In the TFLES context, the transport of any reactive scalar ϕ follows the conservative equation,

$$\frac{\partial \overline{\rho}\widetilde{\phi}}{\partial t} + \nabla \cdot \overline{\rho}\widetilde{u}\widetilde{\phi} = \nabla \cdot (\overline{\rho}\mathcal{F}D\nabla\widetilde{\phi}) + \frac{\dot{\omega}_\phi}{\mathcal{F}}\,. \tag{3.5}$$

3.1.2 Conditions for the thickening $\mathcal{F}$

The objective of the TFLES approach is primarily to increase the number of points for the description of the species source terms. This is dependent on the local mesh size and flame thickness. For a chosen number n of points within the flame it appears that

$$n = \frac{\delta_L^0}{\Delta_{DNS}} = \frac{\mathcal{F}\delta_L^0}{\Delta_{LES}}\,, \tag{3.6}$$

where Δ_{DNS} corresponds to the size of the mesh necessary for a DNS on which the non-thickened profiles would be properly resolved and Δ_{LES} is the size of the LES mesh on which it is desirable to use the TFLES approach. The thickening factor $\mathcal{F}$ is then deduced:

$$\mathcal{F} = \frac{\Delta_{LES}}{\Delta_{DNS}} = \frac{n\Delta_{LES}}{\delta_L^0(\phi(x,t))}\,. \tag{3.7}$$

3.1.3 Interaction between the flame and the turbulence

Modifying the thickness of the reactive layer impacts the interaction between the turbulence and the flame. Poinsot *et al.* [79] and Meneveau *et al.* [80] demonstrated that the wrinkling of the flame under the influence of an eddy decreases with the increase of the flame thickness. The impact of the turbulence on the wrinkling of the flame was further studied by Angelberger *et al.* [81] and Colin *et al.* [78]. This is illustrated on figure 3.1 which compares a perfectly resolved flame structure to a thickened flame LES.

It is demonstrated that the non dimensional numbers describing the interaction between the flame and the turbulence are modified. For instance, the Dämkholer number Da which gives the ratio between the integral scale (mixing) and the chemical time scale reads:

$$Da = \frac{t_t}{t_c} = \frac{l_t}{u'}\frac{S_L^0}{\delta_L^0} \quad \text{hence leading to} \quad Da^{\mathcal{F}} = \frac{Da}{\mathcal{F}}\,, \tag{3.8}$$

where t_t is the turbulence characteristic time and t_c is the characteristic time associated to the chemistry. l_t is the integral scale and $u^{'}$ represents the sub grid fluctuations. This effect is accounted for through the introduction of an efficiency function $\mathcal{E}$ that increases the turbulent flame speed hence compensating for the diminution of the flame surface. This function corresponds to the sub grid thickening factor defined from [78, 82]:

$$\mathcal{E} = \frac{S_t^0}{S_L^0} = \frac{A_t}{A_l} \tag{3.9}$$

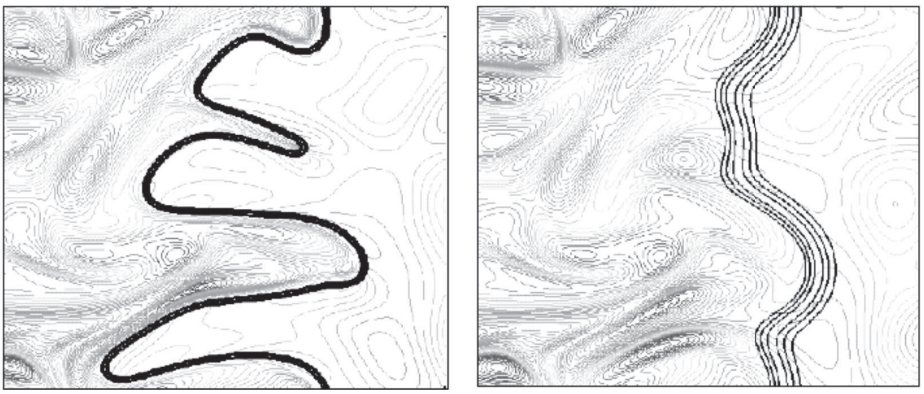

Figure 3.1: DNS of the interaction between the turbulence and the flame [33]. Left image: unthickened flame. Right image: Flame thickened by a factor $\mathcal{F} = 5$.

where S_t^0 is the turbulent flame speed, A_t is the turbulent flame surface and A_l is the laminar flame surface. Among the efficiency functions found in the literature, Colin *et al.* [78] introduced a function based on the ratio of the wrinkling factor of the initial flame with thickness δ_L^0 by the wrinkling factor of the thickened flame characterised by $\delta_{\mathcal{F}}^0$:

$$\mathcal{E} = \frac{\Xi(\delta_L^0)}{\Xi(\delta_{\mathcal{F}}^0)} = \frac{1 + \alpha\Gamma\left(\frac{\Delta}{\delta_L^0}\frac{u'}{S_L^0}\right)\frac{u'}{S_L^0}}{1 + \alpha\Gamma\left(\frac{\Delta}{\delta_{\mathcal{F}}^0}, \frac{u'}{S_L^0}\right)\frac{u'}{S_L^0}} , \tag{3.10}$$

where α and Γ are respectively a parameter and a function given by the model and where Δ stands for the filter size of the LES. This function may also be evaluated from a power law as introduced by Charlette [82] which writes the ratio between the surface of the resolved flame and the surface of the unresolved one from:

$$\mathcal{E} = \left(1 + \frac{\Delta}{\eta_c}\right)^{\beta} , \tag{3.11}$$

where η_c is the mean of the radius of curvature of the flame and β is a constant defined for the model. The LES results showed in the manuscript rely on the use of a corrected version of this model proposed by Wang *et al.* [83]:

$$\mathcal{E} = \left(1 + min\left[\frac{\Delta}{\delta_L^0} - 1, \Gamma\frac{u'}{S_L^0}\right]\right)^{\gamma} , \tag{3.12}$$

where γ is a constant of the model. The value $\gamma = 0.5$ is used thereafter. Introducing this efficiency factor into 3.5 gives:

$$\frac{\partial\overline{\rho}\widetilde{\phi}}{\partial t} + \nabla\cdot\overline{\rho}\widetilde{u}\widetilde{\phi} = \nabla\cdot(\overline{\rho}\mathcal{E}\mathcal{F}D\nabla\widetilde{\phi}) + \frac{\mathcal{E}\dot{\omega}_{\phi}}{\mathcal{F}} . \tag{3.13}$$

3.1.4 Dynamic TFLES

Unfortunately this formulation increases the overall diffusion of the domain. In the context of a perfectly premixed flame, the model may be employed using a constant value for the thickening factor $\mathcal{F}$. On the contrary in the case of other combustion regimes, increasing the diffusion over all the domain provokes modifications of the mixing. Légier *et al.* [84] introduced a dynamic formulation of the TFLES approach, relying on the flame sensor $\mathcal{S}$: a scalar which equals 1 in the reactive zones and 0 on the remaining zones

of the domain. The filtered conservative equation for the scalar ϕ is rewritten with the flame sensor to give:

$$\frac{\partial \overline{\rho}\widetilde{\phi}}{\partial t} + \nabla \cdot \overline{\rho}\widetilde{u}\widetilde{\phi} = \nabla \cdot (\overline{\rho}\mathcal{E}\mathcal{F}J_i^{lam} + (1-\mathcal{S})J_i^{sgs}) + \frac{\mathcal{E}\dot{\omega}_\phi}{\mathcal{F}} \,. \tag{3.14}$$

where J_i^{lam} is the laminar diffusive flux and J_i^{sgs} represents the sub grid diffusive flux. The coupling between the flame sensor $\mathcal{S}$ and both the thickening factor $\mathcal{F}$ and efficiency function $\mathcal{E}$ are:

$$\mathcal{F} = 1 + (\mathcal{F}_{max} - 1)\mathcal{S} \,, \tag{3.15}$$

$$\mathcal{E} = 1 + (\mathcal{E}_{max} - 1)\mathcal{S} \,. \tag{3.16}$$

where the maximum values $\mathcal{F}_{max}$ and $\mathcal{E}_{max}$ are respectively computed from relations 3.7 and 3.11. Several formulations have been proposed for the calculation of the flame sensor in the context of tabulated chemistry and of global chemistry (1 or 2 steps). Recently, Benard [85] proposed a methodology adapted from the one of Franzelli [86] for the implementation of a flame sensor that rely on the source terms of species CO, CO_2 and H_2O:

$$\begin{cases} \mathcal{S} = 1 & \text{if} \quad \dot{\omega} > \dot{\omega}_\mathcal{S} \\ \mathcal{S} = 0 & \text{if} \quad \dot{\omega} < \dot{\omega}_\mathcal{S} \end{cases} \quad \text{with} \quad \dot{\omega} = \dot{\omega}_{\mathrm{CO_2}} + \dot{\omega}_{\mathrm{CO}} + \dot{\omega}_{\mathrm{H_2O}} \,, \tag{3.17}$$

where $\dot{\omega}_\mathcal{S}$ is a threshold value. This threshold is frequently defined from a percentage of the maximum value of $\dot{\omega}$ within the flame. As illustrated on Figure 3.2, several steps are then employed to spread the zone where the sensor $\mathcal{S}$ equals unity over the adjacent nodes and to filter the solution; so as to finally get a smooth sensor that includes the entire flame zone. The threshold value $\dot{\omega}_\mathcal{S}$ is often set to 10% of

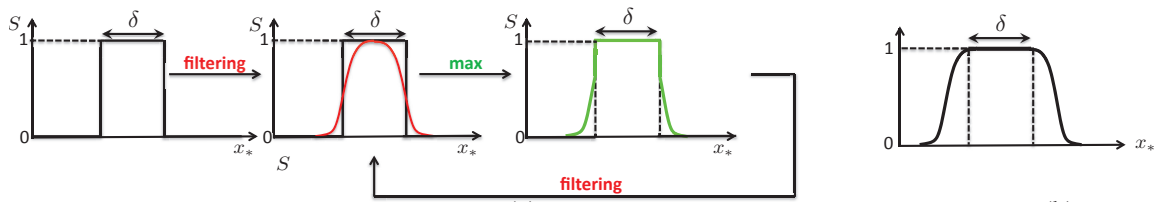

Figure 3.2: Procedure to spread the flame sensor and to filter it. Left illustrations: Initial profile and filtered profile. Right illustration: Final flame sensor. Image extracted from Benard [85].

the maximum source term computed with a 1D premixed laminar flame in similar operating conditions. Using this procedure, note that the threshold value $\dot{\omega}_\mathcal{S}$ must be compared with the unthickened value of the source term that is obtained from $\mathcal{F}\dot{\omega}$. Moreover, with a low Mach number formulation the time step is large in comparison to that for a compressible approach. The flame sensor may then vary significantly between two time steps which pauses some robustness issues. To address this limitation, the flame sensor is smoothed in time introducing a coefficient of relaxation α between the value $\mathcal{S}^n$ and the value at time $n-1$, so that:

$$\mathcal{S}^n = \alpha\mathcal{S}^n + (1-\alpha)\mathcal{S}^{n-1} \,. \tag{3.18}$$

In the present work, $\alpha = 0.7$ is used.

3.2 Machine learning for turbulent combustion modeling

3.2.1 Machine learning algorithms

The modelling of unresolved terms in the highly non-linear transport equations of turbulent and reacting flows being a challenging and daunting task, the ability to “learn" from the data directly, presents a promising alternative given the abundance of data available both from simulations and experiments. Direct Numerical Simulation (DNS) databases where all flow and time scales are resolved, are of the order of Petabytes [87] and machine-learning methods, especially neural networks, are a natural tool for extracting useful information from these databases and find patterns for modelling purposes.

The whole idea behind neural networks is to mimic biologic neurones, stylized in Fig. 3.3, using simplified mathematical models, represented on Fig. 3.4, of what limited knowledge we have on their inner workings: electric signals can be received from dendrites, and sent down the axon once enough signals were received. This outgoing signal can then be used as another input for other neurones, repeating the process. The human brain consists of 10^{10} neurones, and there is about 10^{15} connections (synapses) between. The neurone works with the frequency from 1 to 100 Hz. Consequently the approximated rate equals about 10^{18} operations per second and is many times greater than the one of nowadays computers.

As defined by K. Gurney [88], artificial neural network is an interconnected assembly of simple processing artificial neurones. The processing ability of the network is stored in the inter-unit connection strengths, or weights, obtained by a process of adaptation to, or learning from, a set of training patterns.

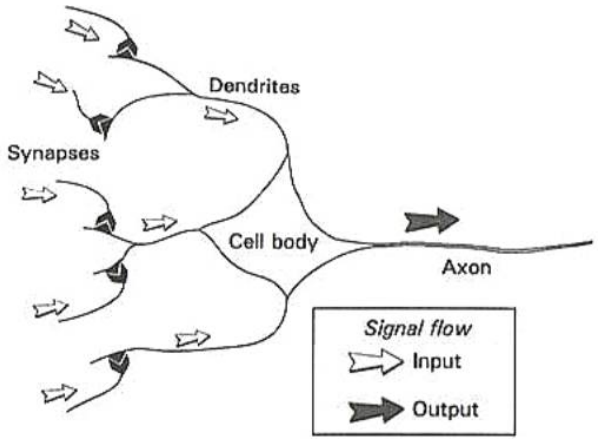

Figure 3.3: Main components of a biological neurone [88].

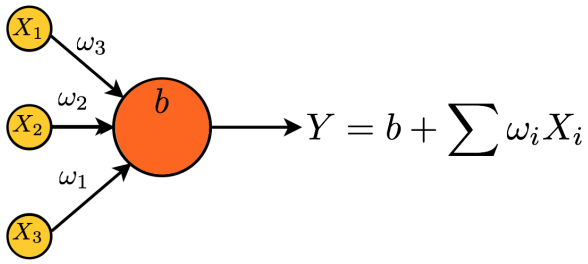

Figure 3.4: Simpliest neurone model (Perceptron), it takes X inputs, sums them up with inner weights ω, applies an activation function b and passes to the output layer Y.

Several architectures of neural network exist, see Fig. 3.5, depending on their use. In the context of

turbulent combustion modelling, Neural networks have been used mainly to deal with the introduction of complex chemistry in the simulations [89, 90, 91, 92, 93], or to manage complex multi-physics phenomena such as solid-fuel devolatilization [94]. Recently, Convolutional Neural Networks CNNs (or Deep Convolutional Networks DCN), originally developed for analysing visual representations [95, 96], have been introduced as a tool for the direct deconvolution of the filtered progress variable [97], which combined with explicit filtering allowed the modelling of the unresolved variance, a key parameter in flamelet modeling [98]. CNNs were also used for modelling the unresolved flame surface wrinkling in [99] surpassing state of the art explicit algebraic models. CNNs have also been used to extract the chemical rate constant from shock-tube measurements [100] and for predicting the combustion activation energy [101].

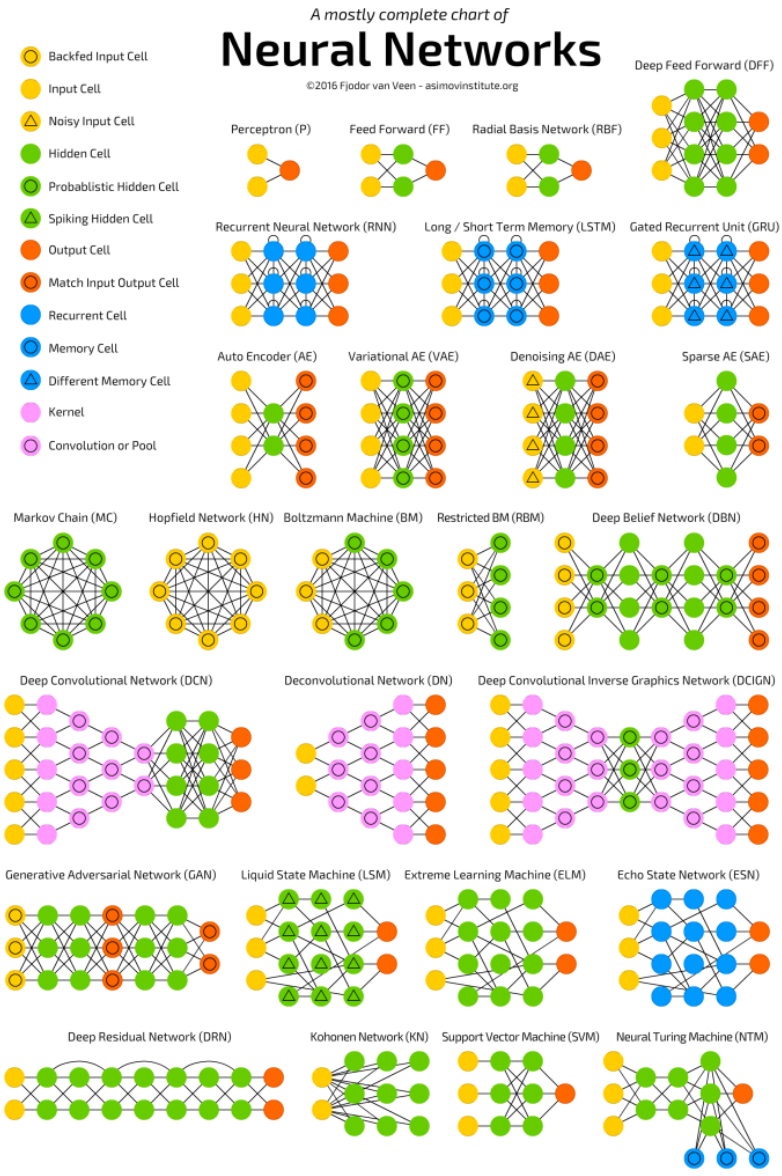

Figure 3.5: Mostly complete chart of neural network topologies, from the Asimov Institute [102].

The main idea behind CNNs is the image treatment before being proccessed by the neurones. As seen in Fig. 3.6, the image pixels (yellow) are treated with classically two operations (pink) : convolutional

layers that convolve the image with a set of N filters, giving N output features of the same size as the image. With this operation, we facilitate the neural network process to find the inner properties of the image. An example is given on Fig. 3.7 where an image A is being convolved by a filter K, randomly initialised. Considering the complete step, F_k is applied to all regions of image A to create the output B. The filtering overlaps the image size to get a feature of the same size (called padding)

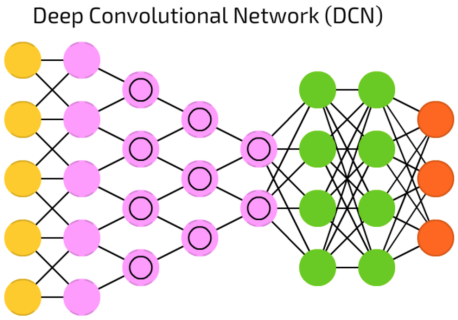

Figure 3.6: Deep convolutional neural network.

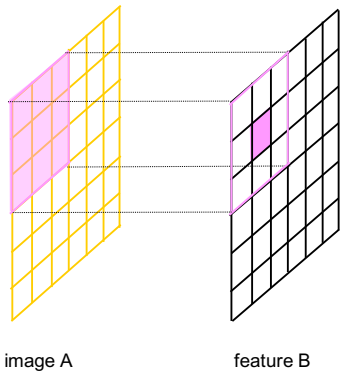

Figure 3.7: One convolution operation example between a convolution kernel F_k 3x3 and the image A 6x6.

Then, pooling layers are used to simplify and reduce unnecessary features. Several pool functions exist, the most common and used in this thesis being the "max pooling" function. For each input regions delimited by the filter size, the maximum value is extracted to form a smaller feature. For example, in Fig. 3.8, the feature B is reduced with a filter of size 3x3 and the output is a matrice of size 2x2.

At the end of the convolutional/pooling operations, the obtained features are then fed to a dense neural network, in which all the neurones are inter-connected to process the features.

3.2.2 Methodology

A turbulent premixed stoichiometric methane/air jet flame is considered in this study performing a priori evaluation of neural network based modeling from a fully resolved simulation following a strategy combining CNNs with the pioneering works of Bray and co-workers [98, 103]. According to their analysis, the departure between the non-linear chemical sources as computed from the node values resolved on a coarse mesh (*i.e.*, neglecting unresolved fluctuations) and their space-filtered (or averaged) counterparts (*i.e.*, accounting for unresolved fluctuations), evolves with the local three-dimensional flame topology,

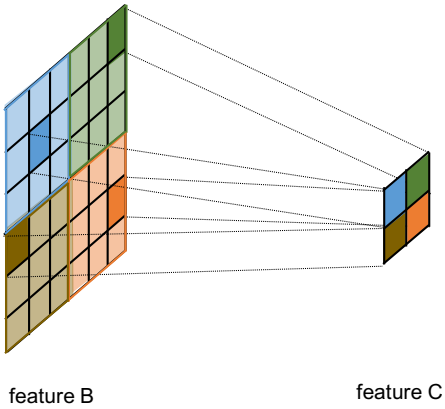

Figure 3.8: A max pooling operation example between a pool function of size 3x3 and the feature B of size 6x6. The result is a feature of size 2x2.

convoluted with the level of mesh resolution, which controls the amplitude of the unresolved fluctuations of temperature and species. Along these lines, we propose to explore the relationships between the three-dimensional distributions of chemical sources as computed from node values (thus a crude approximation of the filtered burning rates), and the filtered value of the non-linear source located at the center of this three-dimensional distribution, using a DNS database. The same procedure is adopted for the sum of the divergence of the unresolved part of the convective flux and of the molecular diffusive flux. The DNS database is then used to train convolutional networks in order to directly reconstruct the unresolved scalar sources and transport terms in the framework of tabulated detailed chemistry premixed flamelet LES. The major advantage of such a direct reconstruction of unresolved sources and fluxes from mesh-resolved quantities in the LES, is that by doing so there is no need for explicit filtering or solving additional transport equations, both of which save computational time and mitigate possible resolution issues [104].

In chemistry tabulation based on premixed flame generated manifolds, all thermochemical quantities ϕ are uniquely related to the progress variable c, so that knowledge of the progress variable distribution $c(\underline{x},t)$ is sufficient to characterise the reaction zones, *i.e.* $\phi(\underline{x},t) = \phi(c(\underline{x},t))$ [105, 106, 107, 108], including the burning rate

$$\dot{\omega}(\underline{x},t) = \dot{\omega}(c(\underline{x},t)) \,. \tag{3.19}$$

The progress variable may be defined from a set of species mass fractions, temperature, derived from optimisation [109, 110, 111] or following other strategies [112]. In any case, c should be a monotonic function through the laminar flamelet. In the context of LES, a transport equation for $\bar{\rho}\tilde{c}$ is solved,

$$\frac{\partial \overline{\rho}\tilde{c}}{\partial t} + \nabla \cdot (\overline{\rho}\tilde{\mathbf{u}}\tilde{c}) = \nabla \cdot (\overline{\rho} D_c(\tilde{c}) \nabla \tilde{c}) + \nabla \cdot \tau + \overline{\dot{\omega}} \,, \tag{3.20}$$

where ρ is the density, $\mathbf{u}$ is the velocity vector and $D_c(c)$ is the tabulated molecular diffusion coefficient of c, defined from the diffusion velocity of tabulated species (Eq. (15) in [113]). The notation $D_c(\tilde{c})$ means that the diffusion coefficient is here computed from the resolved filtered progress variable. $\overline{\dot{\omega}}(\underline{x},t)$ is the filtered burning rate of c. The sub-grid scale flux is

$$\tau = \tau_{D_c} - \tau_c \,, \tag{3.21}$$

where τ_{D_c} and τ_c are respectively the transport of c by unresolved fluctuations of molecular diffusive

flux and momentum,

$$\tau_D = \overline{\rho D_c(c)\nabla c} - \overline{\rho} D_c(\tilde{c})\nabla\tilde{c}\,, \tag{3.22}$$

$$\tau_c = \overline{\rho \mathbf{u} c} - \overline{\rho}\tilde{\mathbf{u}}\tilde{c}. \tag{3.23}$$

Numerous modeling strategies have been proposed in the literature for the unresolved terms of Eq. (3.20) in the context of tabulated chemistry, and a detailed review is given in [114]. Among those, many involve gradient transport models with an eddy viscosity hypothesis to close τ_c while τ_D is usually neglected.

Flamelet models for the burning rate $\overline{\dot{\omega}}$, are typically based on solving and additional balance equation for the variance of c, $c_v = \widetilde{c^2} - \tilde{c}\tilde{c}$. A function is then presumed for the progress variable probability density function (pdf), which is parameterised using the two moments of c namely $\tilde{c}(\underline{x}, t)$ and $c_v(\underline{x}, t)$ [115, 116, 117]. A chemical lookup table is constructed using results from 1D flame simulations, and variables of interest are obtained using these two parameters from the table. For example, the filtered burning rate in Eq. (3.20) is closed using

$$\overline{\dot{\omega}}(\underline{x}, t) = \int_0^1 \dot{\omega}(c^\star)\overline{P}(c^\star; \tilde{c}(\underline{x}, t), c_v(\underline{x}, t))dc^\star\,, \tag{3.24}$$

where $\overline{P}(c^*; \tilde{c}(\underline{x}, t), c_v(\underline{x}, t))$ is the presumed pdf. A characteristic length scale may also be added to the modeling framework, by combining the pdf with the Flame Surface Density (FSD) concept [118, 119]. In an attempt to account for the time history of micro-mixing, it has been proposed in [120] to include as a control parameter of the filtered thermo-chemistry lookup table, the age of fluid particles since their injection. Simulations coupling flame-generated manifolds with pdf transport using Eulerian stochastic fields have also been reported [121, 122]. The filtering of the tabulated one-dimensional flames is another option, providing closed expressions for τ_c and τ_D, in addition to $\overline{\dot{\omega}}$ [123, 113, 124]. More recently, deconvolution-based approaches have also been discussed and applied to the three terms $\overline{\dot{\omega}}$, τ_c and τ_D [125, 126, 127, 128, 129].

Overall, these modeling approaches directly or indirectly relate $\tilde{c}$ and $\nabla\tilde{c}$ to the unclosed terms. A slightly different approach is explored in this work. First, the statistical properties of $\overline{\dot{\omega}}$, τ_c and τ_D are examined using the results from the DNS database. Specific features are observed in the data connecting $\overline{\dot{\omega}}$ and $\nabla\cdot\tau = \nabla\cdot(\tau_D - \tau_c)$ to $\dot{\omega}(\tilde{c})$ and $\nabla\cdot(\overline{\rho}D_c(\tilde{c})\nabla\tilde{c})$ respectively, namely the burning rate and the divergence of the diffusive flux as computed from the resolved LES fields, i.e. the node values over the LES mesh. ($\nabla\cdot(\overline{\rho}D_c(\tilde{c})\nabla\tilde{c})$ is already calculated when solving for $\tilde{c}$ and is thus available without additional computational cost.) These features suggest that image-type deep learning can be readily applied to dynamically determine two mapping functions $\mathcal{G}$ and $\mathcal{F}$ from convolutional neural networks such that,

$$\overline{\dot{\omega}}(\underline{x}, t) = \mathcal{G}\left[\dot{\omega}(\tilde{c}(\underline{x}_1, t)), \cdots, \dot{\omega}(\tilde{c}(\underline{x}_N, t))\right]\,, \tag{3.25}$$

$$\nabla\cdot\tau(\underline{x}, t) = \mathcal{F}\left[\nabla\cdot(\overline{\rho}D_c(\tilde{c})\nabla\tilde{c})\,(\underline{x}_1, t), \cdots, \nabla\cdot(\overline{\rho}D_c(\tilde{c})\nabla\tilde{c})\,(\underline{x}_N, t)\right]\,, \tag{3.26}$$

where $\tilde{c}(\underline{x}_j, t)$ is known from the LES, with $\underline{x}_j$ the N points selected around $\underline{x}$ to build the input image of the networks. Note that the above relations are expressed in progress variable space *i.e.*, a single variable, $\tilde{c}$, is required in order to calculate the terms on the right-hand side of Eqs. (3.25) and (3.26) which constitute the inputs to the two networks $\mathcal{F}$ and $\mathcal{G}$. Provided $\mathcal{G}$ and $\mathcal{F}$ are known, Eq. (3.20) is fully closed without having to solve any additional transport equations. Also note that $\tilde{c}$ is a coordinate in which turbulent premixed flame properties are strongly depended on and feature a generic character

when studied in c-space [98]. As a result, the dependence of relations (3.25) and (3.26) to the flow regime are expected to be weak as long as the networks are trained for conditions in a Borghi regime-diagram [130] close to the ones of the flames subsequently addressed by LES. This is also more likely to be the case, when $\mathcal{G}$ and $\mathcal{F}$ are determined from a reference turbulent premixed flame featuring a large degree of flame wrinkling, as is the case for the turbulent premixed jet-flame DNS database used in this study [127].

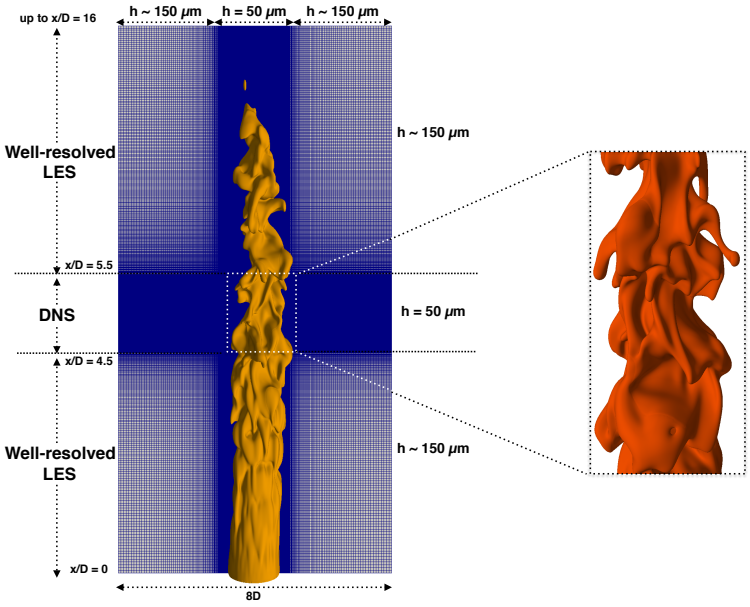

Figure 3.9: LES-DNS snapshot of the jet-flame simulation [127]. Mesh and iso-progress variable $c = 0.8$. h: resolution. Red iso-surface: zoom of iso-$c = 0.8$ in the DNS zone (different angle view).

3.2.3 Direct simulation database

A previously developed methane-air stoichiometric premixed jet-flame DNS database [127, 131, 132] is used for training the neural networks. The configuration is shown in Fig. 3.9. The DNS database is obtained downstream of a well-resolved LES of a piloted premixed stoichiometric fuel-air jet, which generates turbulent flame conditions for the DNS inlet plane located 4.5 diameters downstream of injection. The LES and the DNS are run simultaneously and this is achieved by embedding, inside the LES mesh, a zone where the resolution is sufficiently high so as to resolve the thin reaction zones and the Kolmogorov length scale. The configuration is inspired from the experiment by Chen *et al.* [133]. This turbulent Bunsen burner has a nozzle diameter of D = 12 mm, the jet Reynolds number is 24,000 (bulk nozzle velocity of 30 m·s^{-1} and turbulent kinetic energy of 3.82 m^2·s^{-2}). The pilot is set to fully burnt gases at T_b = 2200 K. The LES mesh consists of about 171 million nodes covering a domain 16D×8D×8D, with a resolution of the order of 150 μm (Fig. 3.9). The resolution in the DNS zone is fixed at 50 μm, which was calibrated to ensure a full resolution of the flow and flame scales for this jet flame having a Karlovitz number varying between 1 and 3 [127, 133]. Chemistry tabulation with a stoichiometric premixed flamelet with fresh gases at $T_o = 300$ K (GRI-3.0 mechanism [134] and progress variable defined from CO, CO_2, H_2O and NO_x as in [135]) is used for both LES and DNS, without any SGS modeling in the DNS part (SGS terms set to zero). The flame thermal thickness based on the progress variable field is of the order of $\delta_L \approx 400$ μm. The DNS zone consists of 28.58 million nodes

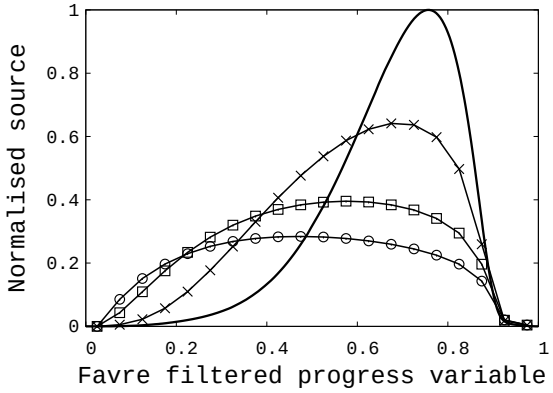

Figure 3.10: Thick-line: $\dot{\omega}^+(\tilde{c})$ vs $\tilde{c}$ as obtained from a 1D laminar flame (tabulated chemistry). $\left\langle \overline{\dot{\omega}^+} \mid \tilde{c} \right\rangle$ from DNS vs $\tilde{c}$ for filter sizes $\times$: 0.3 mm, $\square$: 0.6 mm, $\circ$: 0.9 mm ($\delta_L = 0.4$ mm).

(243×343×343), over a physical domain of 12 mm×18 mm×18mm. This DNS zone is located at $4.5D$ downstream of the nozzle, and at $5.5D$ the mesh is coarsened again to progressively resume the simulation using LES (Fig. 3.9). A progress variable presumed pdf approach is applied in the LES zones [115] and the SGS momentum fluxes are approximated with the Vreman model [136]. These simulations have been performed using the flow solver SiTCom [137], which solves the Navier-Stokes equations in their fully compressible form together with the balance equation for the filtered progress variable. The convective terms are discretised with a fourth-order centered skew-symmetric-like scheme [138] and the diffusive terms with a fourth-order centered scheme. Time is advanced explicitly with a third order Runge-Kutta method and NSCBC boundary conditions [139] are imposed at inlet and outlet, with the measured profiles with synthetic turbulence [140] prescribed at inlet. More details on the development and the use of this DNS database may be found in [127, 131, 132].

A Gaussian filtering operation, $G(\underline{x}) = (6/(\pi\Delta^2))^{3/2} \exp(-6\underline{x} \cdot \underline{x}/\Delta^2)$, with filter size $\Delta = 0.3$ mm $= 0.75\ \delta_L$, $\Delta = 0.6$ mm =1.50 δ_L and $\Delta = 0.9$ mm = 2.25 δ_L, is applied to the DNS variables in order to generate a priori LES filtered quantities, thus varying the resolution of the a priori fields from well-resolved to coarse LES (at least from the reaction zone point of view, $\Delta = 0.9$ mm is 18 times larger than the DNS grid resolution).

3.2.4 Statistical analysis of unresolved terms

3.2.4.1 Turbulent flame properties

Figure 3.10 shows $\left\langle \overline{\dot{\omega}^+} \mid \tilde{c} \right\rangle$, the statistical mean over the DNS domain of the normalised filtered progress variable source, conditioned on values of $\tilde{c}$. The subscript '$^+$' denotes source terms normalised by their maximum value in the tabulated freely-propagating laminar premixed flame. The result obtained using a 1D laminar flame, $\dot{\omega}^+(\tilde{c})$, is shown as a solid line. As expected, the maximum of $\left\langle \overline{\dot{\omega}^+} \mid \tilde{c} \right\rangle$ decreases with increasing filter size and thus with increasing unresolved fluctuations [98]. Following the thickening of the filtered flame front, the response of this conditional filtered source term also spreads in progress variable space for increasing filter sizes, up to Δ = 0.9 mm.

The statistical conditional means of $\langle \nabla \cdot \tau_c \mid \tilde{c} \rangle$ and of $\langle \nabla \cdot \tau_D \mid \tilde{c} \rangle$, the divergence of the convective

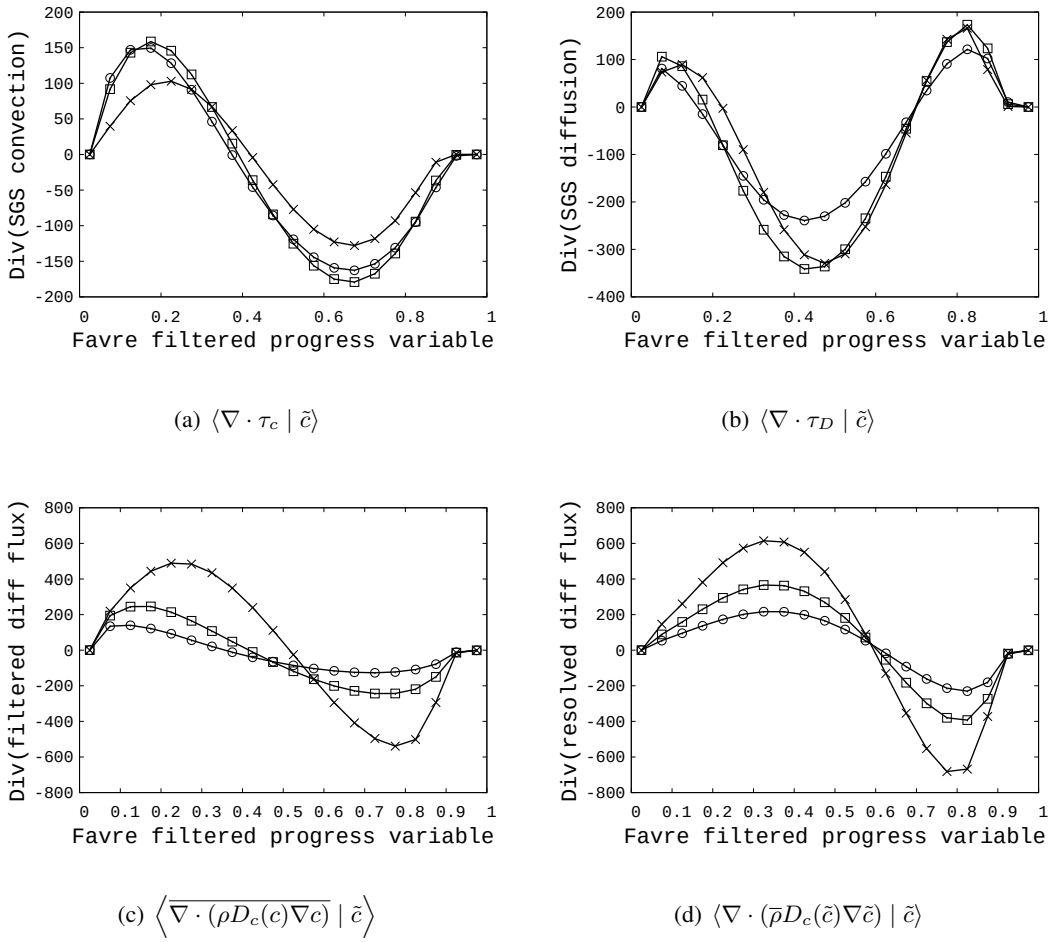

(a) $\langle \nabla \cdot \tau_c \mid \tilde{c} \rangle$

(b) $\langle \nabla \cdot \tau_D \mid \tilde{c} \rangle$

(c) $\left\langle \overline{\nabla \cdot (\rho D_c(c) \nabla c)} \mid \tilde{c} \right\rangle$

(d) $\langle \nabla \cdot (\overline{\rho} D_c(\tilde{c}) \nabla \tilde{c}) \mid \tilde{c} \rangle$

Figure 3.11: Conditional statistical means vs filtered progress variable. (a): Divergence of SGS convective scalar flux. (b): divergence of SGS diffusive flux. (c): filtered diffusive flux. (d): diffusive flux computed from the resolved quantities. Filter size $\times$: 0.3 mm, $\square$: 0.6 mm, $\circ$: 0.9 mm.

and diffusive fluxes (Eqs. (3.22) and (3.23)), are shown in Fig. 3.11. The maximum level of velocity fluctuations observed in the fresh gases in the experiment at the streamwise location of the jet where the DNS zone is located (Fig. 3.9), is of the order of $u' = 1.80$ m·s^{-1} [133]. Then, the ratio u'/S_L for this stoichiometric premixed methane-air flame is of the order of 5, with $S_L = 0.37$ m·s^{-1}.

The number $N_B = [(T_b - T_o)/T_o]S_L/(2\alpha u')$, as defined by Veynante *et al.* [141], which differentiates between gradient transport, $N_B < 1$, $-\tau_c \propto \nabla\tilde{c}$, and counter-gradient transport, $N_B > 1$, $-\tau_c \propto -\nabla\tilde{c}$, in a Reynolds Averaged Navier Stokes context (RANS), is above unity in the present case for an efficiency factor $\alpha \leq 0.6$. The factor α in N_B accounts for the variability in the capability of turbulent eddies to wrinkle the reaction zone [141].

Considering space-filtered (LES) quantities, for $1 \leq \Delta/\delta_L \leq 3$, counter-gradient SGS transport was recently reported from DNS analysis for the same level of u'/S_L [129]. Overall, counter-gradient transport is found when $\nabla \cdot \tau_c$ and $\nabla^2\tilde{c}$ are of same sign. This is also what is observed in Fig. 3.11(a), with $\langle \nabla \cdot \tau_c \mid \tilde{c} \rangle$ negative on the burnt gas side where $\nabla^2\tilde{c} < 0$ and $\langle \nabla \cdot \tau_c \mid \tilde{c} \rangle$ positive on the fresh side where $\nabla^2\tilde{c} > 0$. Almost zero fluxes on the burnt gas side appear before $\widetilde{c} = 1$, because of the

choice of the progress variable as in Godel et al. [135], which is designed as slowly varying approaching burnt gases to preserve a single-valued response of NOx versus progress variable. This behaviour is also observed in the scatter plot of the SGS convection divergence which is shown in Fig. 3.12, with the occurrence however of some negative values of $\nabla \cdot \tau_c$ around $\tilde{c} \to 0$, thus gradient transport in the preheat zone ensures the local flame propagation. On these scatter plots, the bounds of $\nabla \cdot \tau_c$ do not change much with the filter size Δ, but the spreading of the data for a given value of $\tilde{c}$ decreases with Δ.

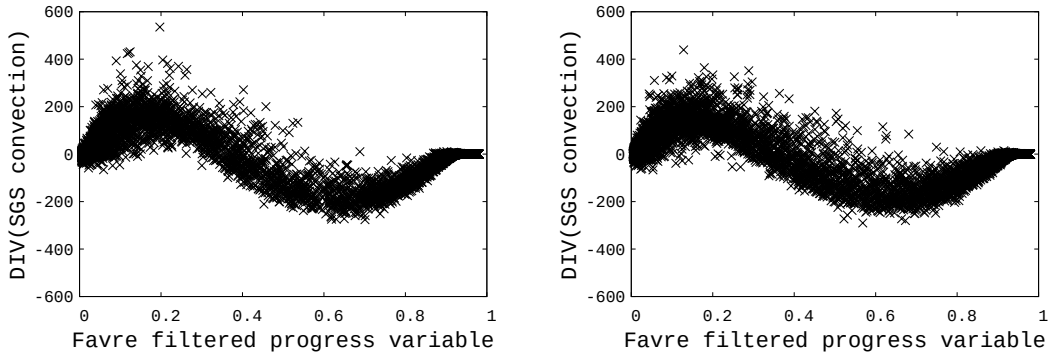

(a) $\Delta = 0.6$ mm (b) $\Delta = 0.9$ mm

Figure 3.12: Scatter plot of $\nabla \cdot \tau_c$ (1 every 100 DNS points shown).

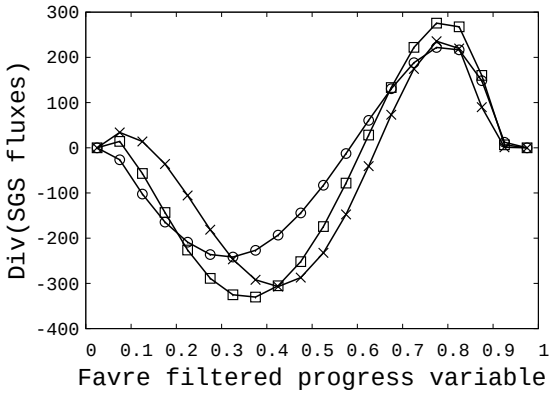

Figure 3.13: $\langle \nabla \cdot \tau \mid \tilde{c} \rangle = \langle \nabla \cdot (\tau_D - \tau_c) \mid \tilde{c} \rangle$ vs $\tilde{c}$. Filter size $\times$: 0.3 mm, $\square$: 0.6 mm, $\circ$: 0.9 mm.

The contribution of the SGS diffusive flux, $\nabla \cdot \tau_D$, in Fig. 3.11(b) cannot be neglected compared to the convective one, $\nabla \cdot \tau_c$, in Fig. 3.11(a). This would not be the case in the RANS context, where the SGS diffusive contribution would be inversely proportional to the turbulent Reynolds number of the flow, and thus could be neglected when compared to other transport terms [142]. The SGS diffusive fluxes in LES are actually inversely proportional to the turbulent Reynolds numbers of the LES mesh cells, based on the filter size and on the SGS velocity fluctuations. Therefore, the SGS turbulent Reynolds number appears too small for neglecting the divergence of τ_D. The response of the amplitude of $\langle \nabla \cdot \tau_D \mid \tilde{c} \rangle$ versus the filter size, is better understood by looking at the two terms $\left\langle \overline{\nabla \cdot (\rho D_c(c) \nabla c)} \mid \tilde{c} \right\rangle$

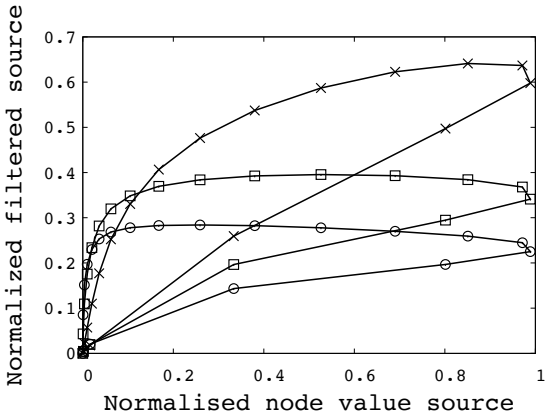

Figure 3.14: $\left\langle \overline{\dot{\omega}^+}(c) \mid \tilde{c} \right\rangle$ vs $\dot{\omega}^+(\tilde{c})$. Filter size $\times$: 0.3 mm, $\square$: 0.6 mm, $\circ$: 0.9 mm.

and $\langle \nabla \cdot (\overline{\rho} D_c(\tilde{c}) \nabla \tilde{c}) \mid \tilde{c} \rangle$ in Figs. 3.11(c) and 3.11(d). As expected, following the decay of the gradients with the increase of the filter size, these filtered transport terms decrease, leading to a decay of the amplitude of both the filtered and node-resolved diffusive budgets when Δ increases. In the case of $\langle \nabla \cdot (\overline{\rho} D_c(\tilde{c}) \nabla \tilde{c}) \mid \tilde{c} \rangle$ an almost self-similar behaviour is observed against Δ (Fig. 3.11(d)). This is not the case for $\left\langle \overline{\nabla \cdot (\rho D_c(c) \nabla c)} \mid \tilde{c} \right\rangle$, for which the response is also shifted against $\tilde{c}$ when Δ varies as one may observe from the results in Fig. 3.11(c). As a result, the difference between these two terms, $\nabla \cdot \tau_D$, is not monotonic against Δ (Fig. 3.11(b)). It is important also to note that the thickening of the flame front in physical space resulting from filtering, directly impacts these budgets here visualised in $\tilde{c}$-space. Finally, the sum of SGS fluxes $\langle \nabla \cdot \tau \mid \tilde{c} \rangle = \langle \nabla \cdot (\tau_D - \tau_c) \mid \tilde{c} \rangle$, which combines responses of both unresolved convection and molecular diffusion, is shown in Fig. 3.13.

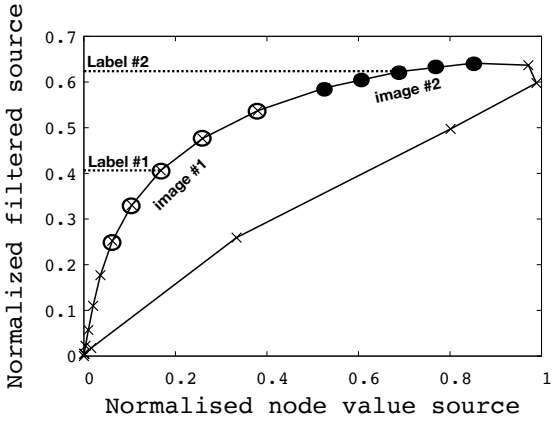

Figure 3.15: $\left\langle \overline{\dot{\omega}^+}(c) \mid \tilde{c} \right\rangle$ vs $\dot{\omega}^+(\tilde{c})$. Sketch of the construction of images and labels for training a CNN. Filter size: 0.3 mm.

3.2.4.2 Physical arguments for CNN training

As will be explained later in the text, two CNN will be used to approximate respectively the values of $\nabla \cdot \tau(\underline{x}, t)$ and $\overline{\dot{\omega}}(\underline{x}, t)$ from an input composed of a set of data (images). In practice, this is done by interpolating over a large number of relationships between 'images' and 'labels', which were the values of $\nabla \cdot \tau(\underline{x}, t)$ and $\overline{\dot{\omega}}(\underline{x}, t)$ "learned" during a training phase. Here the inputs (images) are composed of $\dot{\omega}(\tilde{c}(\underline{x}_j, t))$ and $\nabla \cdot (\overline{\rho} D_c(\tilde{c}) \nabla \tilde{c})\,(\underline{x}_j, t)$ for $j = 1, \cdots, N$, where N is the number of points surrounding a point $\underline{x}$, where the values of $\overline{\dot{\omega}}(\underline{x}, t)$ and $\nabla \cdot \tau(\underline{x}, t)$ are sought.

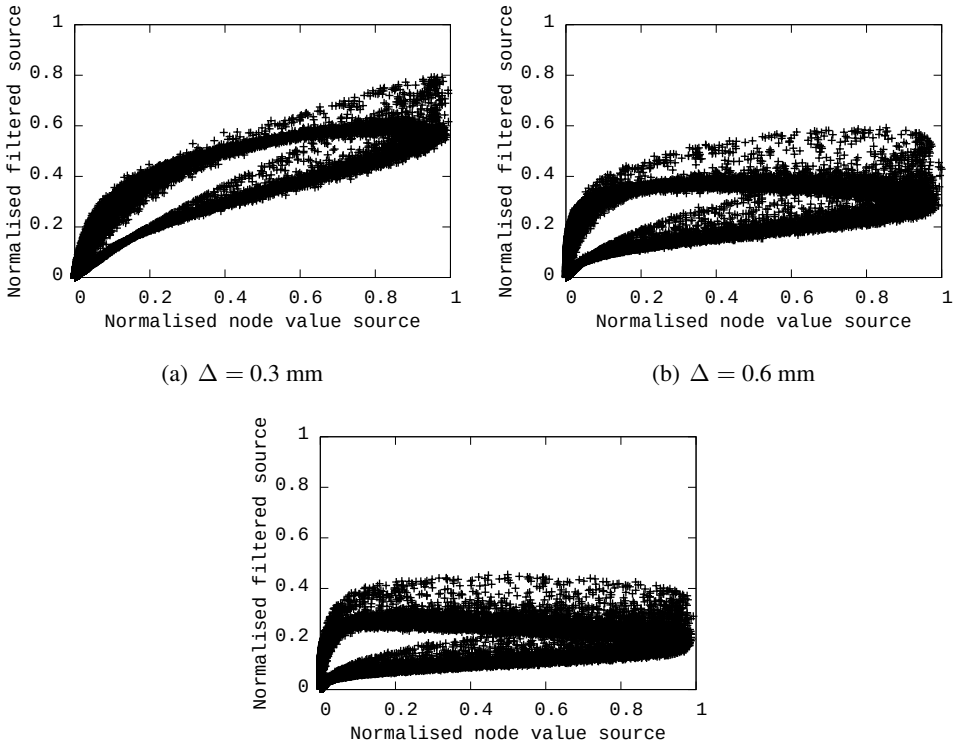

(a) $\Delta = 0.3$ mm

(b) $\Delta = 0.6$ mm

(c) $\Delta = 0.9$ mm

Figure 3.16: $\overline{\dot{\omega}^+}$ vs $\dot{\omega}^+(\tilde{c})$.

The input set of data should feature specific topological properties, which can be extracted by convoluting the data points with a series of filters and specific operations described in section 3.2.1. Figure 3.14 shows $\left\langle \overline{\dot{\omega}^+} \mid \tilde{c} \right\rangle$ versus $\dot{\omega}^+(\tilde{c})$ for different filter sizes and Fig. 3.15 illustrates the image-label relationship which could be implemented. Notice that the CNN will not operate on the statistical conditional means in the end, but directly on the raw data, however initiating the analysis at the statistical level helps to select the variables. As one may observe from Fig. 3.14, the filtered source term is not a single-valued function of the node resolved source, nevertheless accounting also for the local curvature of the data set as one of the features, should be sufficient to build a one-to-one response. Obviously, this constitutes only a very preliminary condition to secure the determination of the function $\mathcal{G}$ of Eq. (3.25) and more features will need to be extracted on the full set of turbulent data, as discussed thereafter. Because of non-deterministic local sub-grid scale wrinkling of the flame surface, the relation between $\dot{\omega}^+(\tilde{c})$ and $\overline{\dot{\omega}^+}$ is actually scattered as shown in Fig. 3.16, with some deviation from the response seen in Fig. 3.14, and this scattering should be reproduced by a reliable physical model. This is where numerical modelling

can take great benefit from deep learning, which automatically discovers the most relevant signal features through elementary operations, to then allow for interpolating over the very large dataset learned.

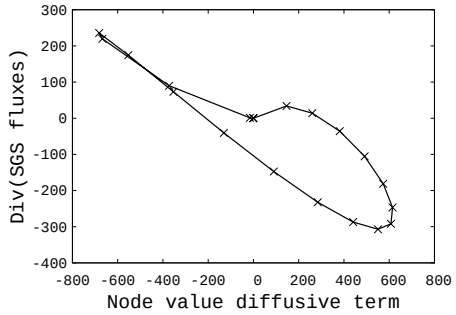

(a) $\Delta = 0.3$ mm

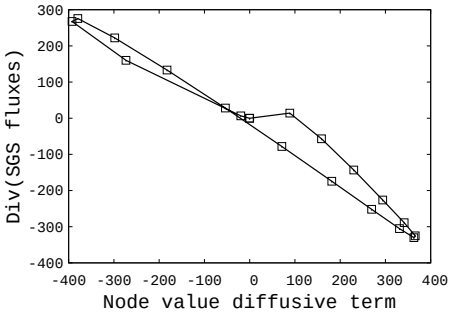

(b) $\Delta = 0.6$ mm

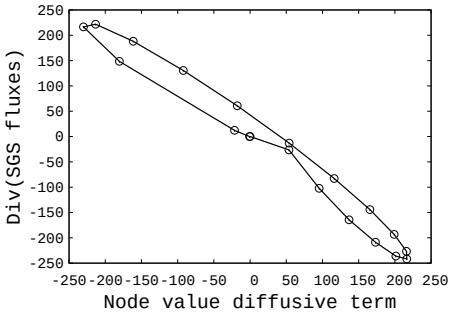

(c) $\Delta = 0.9$ mm

Figure 3.17: $\langle \nabla \cdot \tau \mid \tilde{c} \rangle$ vs $\langle \nabla \cdot (\overline{\rho} D_c(\tilde{c}) \nabla \tilde{c}) \mid \tilde{c} \rangle$.

Similarly, Fig. 3.17 shows $\langle \nabla \cdot \tau \mid \tilde{c} \rangle$ versus $\langle \nabla \cdot (\overline{\rho} D_c(\tilde{c}) \nabla \tilde{c}) \mid \tilde{c} \rangle$ and Fig. 3.18 the full set of data $\nabla \cdot \tau$ versus $\nabla \cdot (\overline{\rho} D_c(\tilde{c}) \nabla \tilde{c})$, revealing a dataset which can easily be analysed by CNNs for identifying the function $\mathcal{F}$ in Eq. (3.26). It will be seen thereafter that this is a valid option for the case considered. Because momentum also contributes to $\nabla \cdot \tau$, an alternative would consist of introducing information on velocity in the $\mathcal{F}$ neural network (Eq. (3.26)). An option that was not found necessary in the present study where both SGS convective and diffusive fluxes are combined to build a single CNN for the divergence of fluxes. For this set of data, various options in terms of neural network layers number and filtering kernels have been tried. Best results were obtained with two layers and the set of kernels and data organisation now reported.

3.2.5 CNN training process

The LES mesh size required to resolve with $n = 5$ points the filtered progress variable signal, may be estimated from $h = (\Delta/n)\sqrt{\pi/6 + \delta_L^2/\Delta^2}$ [128]. A three-dimensional test-box of size $(2h)^3$ is constructed around every of the M = 28.58 million DNS nodes. This test box is centered at $\underline{x}$ and contains $N = 27$ points which hold the three-dimensional distributions of $\dot{\omega}(\tilde{c}(\underline{x}_j, t))$ and $\nabla \cdot (\overline{\rho} D_c(\tilde{c}) \nabla \tilde{c})\ (\underline{x}_j, t)$, for $j = 1, \cdots, N$. These data are stored and constitute the 'images' that will be processed by the

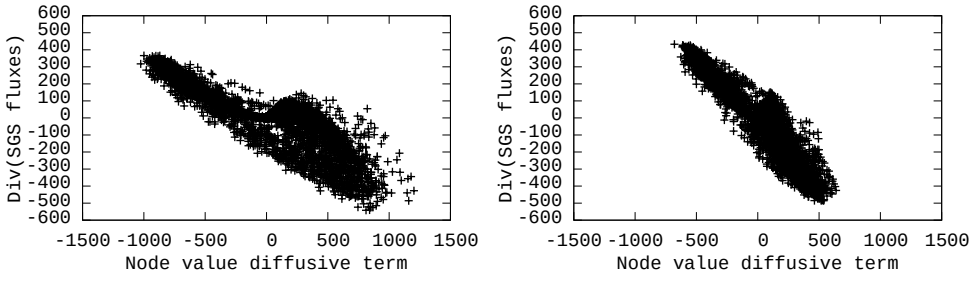

(a) $\Delta = 0.3$ mm

(b) $\Delta = 0.6$ mm

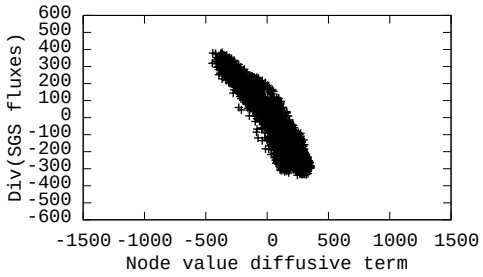

(c) $\Delta = 0.9$ mm

Figure 3.18: $\nabla \cdot \tau$ vs $\nabla \cdot (\overline{\rho} D_c(\tilde{c}) \nabla \tilde{c})$.

CNN as shown in Fig. 3.19. The 'labels' of each i-th image are $\overline{\dot{\omega}}[i] = \overline{\dot{\omega}}(\underline{x}, t)$ and $\nabla \cdot \tau[i] = \nabla \cdot (\tau_D(\underline{x}, t) - \tau_c(\underline{x}, t))$ for $i = 1, \cdots, N_L$. Two networks of similar structures (same number of layers, convolution kernels, etc.) are trained, one for the chemical source and one for the SGS fluxes.

To reduce the computational cost, only part of the database is used for training. For each value of Δ, the following procedure is applied:

- First, 1000 images with their associated i-th label are built. 20 values of $c^\star$ uniformly distributed between 0 and 1 ($\Delta c^\star = 0.05$) are defined. For each value of $c^\star$, 50 images are randomly selected so that $\tilde{c}(\underline{x}, t) \in [c^\star - \Delta c^\star/2; c^\star + \Delta c^\star/2]$ ($\underline{x}$ denotes the center of the test box, Fig. 3.19).

- Overfitting is avoided by adding uncorrelated random perturbations to the images, $\dot{\omega}(\tilde{c}(\underline{x}_j, t))$ and $\nabla \cdot (\overline{\rho} D_c(\tilde{c}) \nabla \tilde{c})\ (\underline{x}_j, t)$, as 10% of their maximum in the test box, to build a second image for each label. 2000 images are then available for 1000 labels.

Finally, the database used for training with two filter sizes contains 4000 images and $N_L = 2000$ labels. Hence, for every quantity studied, a set of 27×4000 =108000 data ($\dot{\omega}(\tilde{c}(\underline{x}_j, t))$ and $\nabla \cdot (\overline{\rho} D_c(\tilde{c}) \nabla \tilde{c})\ (\underline{x}_j, t)$) is involved, associated to the 2000 reference labels ($\overline{\dot{\omega}}[i]$ and $\nabla \cdot \tau[i]$ for $i = 1, \cdots, N_L$).

A series of convolution/sampling operations are done iteratively during the training phase, in which the neural weights are adjusted until a satisfying minimal error is obtained between the value of $\nabla \cdot \tau(\underline{x}, t)$ and $\overline{\dot{\omega}}(\underline{x}, t)$ used for training (labels) and the values returned by the neural networks prediction. Convolution/sampling operations are thus performed on the database to extract its features using a number of different kernels [96, 95]:

1. Each image is convoluted with 32 different convolution filter initialized with random values from a truncated normal distribution. Meaningful values of the obtained features are then extracted with a max pooling non-linear function to avoid excessive computational costs.

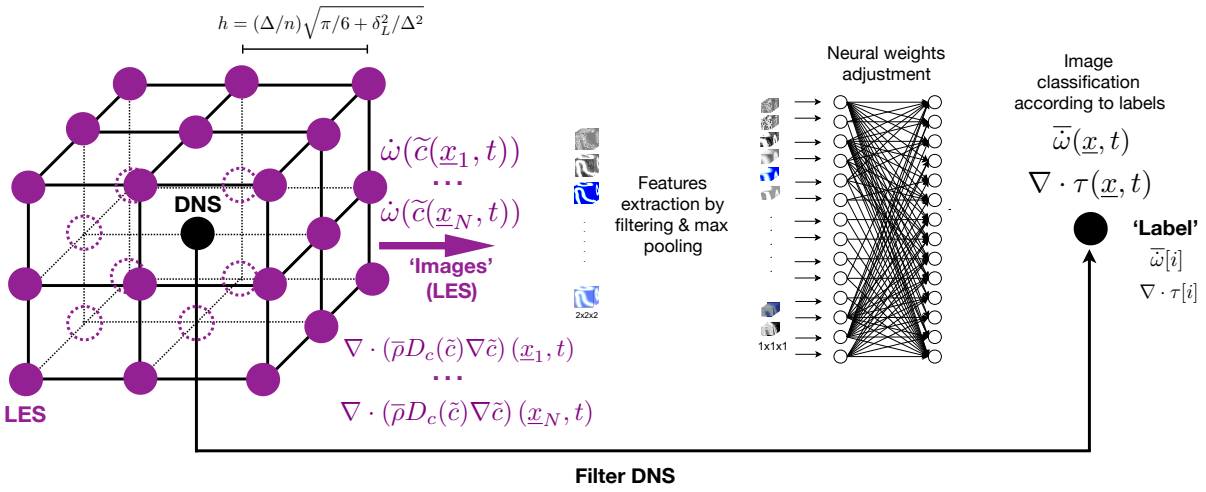

Figure 3.19: CNN training from DNS, sketch of the database construction.

2. The process is repeated with 64 filters, decomposing the image into several meaningful features, which is useful for seeking out the inner properties of the fluxes and sources.

3. Two fully connected layers are built to process the 64 obtained features, and to classify the image according to the learned labels. The probabilities linking this image to each of the learned labels are then known in the form of coefficients ranging between zero and unity.

The training of the network was conducted using the TensorFlow (www.tensorflow.org) library and breakdown of the network structure is given in Fig. 3.20. During this training phase, a 50% drop-out rate is applied, *i.e.*, 2000 images are randomly selected at every iteration and about 100 iterations (or 'epoch') are needed to reach convergence. The error function used for training is based on cross entropy [143], while the training is controlled by the Adam optimizer [144] for stochastic gradient descent, with a user-defined learning rate of 10^{-4}. Both normalised and non-normalised input ($\dot{\omega}(\tilde{c})$ and $\nabla \cdot (\overline{\rho} D_c(\tilde{c}) \nabla \tilde{c})$) and output values ($\overline{\dot{\omega}}$ and $\nabla \cdot \tau$) of networks have been used, without much difference, results are presented for the non-normalised training.

3.2.6 CNN mapping of fluxes and sources from LES resolved fields

In using the networks, the $N = 27$ values of the chemical sources and of the divergence of the fluxes computed from the resolved progress variable field in the test box surrounding the LES cell (Fig. 3.19), constitute the input. In this feasibility study, for each filter size, 1000 filtered DNS fields are used for a priori tests (the noised images introduced during the training phase do not enter these tests). The unknown terms are then approximated from interpolation over the $N_L = 2000$ labels values ($\overline{\dot{\omega}}[i]$ and $\nabla \cdot \tau[i]$) of the training phase,

$$\begin{aligned} \overline{\dot{\omega}}(\underline{x}, t) &= \mathcal{G}\left[\dot{\omega}(\tilde{c}(\underline{x}_1, t)), \cdots, \dot{\omega}(\tilde{c}(\underline{x}_N, t))\right] \\ &= \sum_{i=1}^{N_L} P_i(\underline{x}, t) \times \overline{\dot{\omega}}[i]\,, \end{aligned} \tag{3.27}$$

$$\begin{aligned} \nabla \cdot \tau(\underline{x}, t) &= \mathcal{F}\left[\nabla \cdot (\overline{\rho} D_c(\tilde{c}) \nabla \tilde{c}(\underline{x}_1, t))\,, \cdots, \nabla \cdot (\overline{\rho} D_c(\tilde{c}) \nabla \tilde{c}(\underline{x}_N, t))\right] \\ &= \sum_{i=1}^{N_L} T_i(\underline{x}, t) \times \nabla \cdot \tau[i]\,, \end{aligned} \tag{3.28}$$

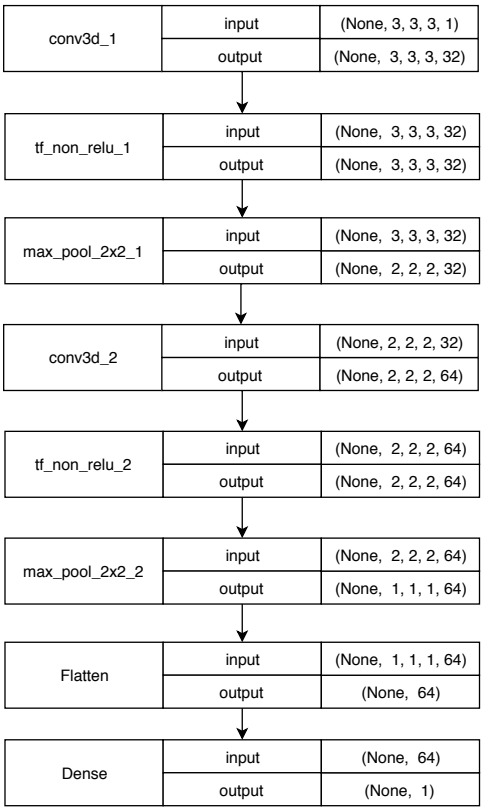

Figure 3.20: Structure of the convolutional neural network used (set of TensorFlow routines)

.

where $P_i(\underline{x}, t)$ and $T_i(\underline{x}, t)$, both $\in [0, 1]$, are the probability that the image belongs to the label 'i', as returned by the neural networks $\mathcal{G}$ and $\mathcal{F}$. In practice, the modelled filtered sources and divergence of SGS fluxes are thus non-linearly interpolated, according to the local LES resolved flame topology, over 2000 reference DNS values.

The training is performed for the smaller and largest filter sizes *i.e.*, Δ = 0.3 mm and Δ = 0.9 mm. Then, the prediction capabilities of the obtained CNN are tested a priori for these filter sizes and for intermediate values of $\Delta \in [0.3, 0.9]$, for which this network has not been trained (so-called 'untrained case'). Notice that the ratio of three between the filter sizes used for training can be considered large, as these filters vary between 0.75 δ_L and 2.25 δ_L. This ratio of more than one flame thickness is here intentional to test the method in the limit case where the neural networks are used for filter sizes far from those of their training.

Using GPU 'NVDIA Pascal', the training of the fluxes requires 4 hours. Compared to the fluxes, the filtered source terms have a larger range of variation between the two filter sizes used for training and they require 24 hours of training on the same GPU. Once trained, the network may be used directly in a flow-solver for a CPU cost of about the one required with a turbulent combustion closure based on chemistry tabulation and presumed probability density function [115].

The averages of the predicted divergence of the unresolved fluxes conditioned on the progress variable, $\langle \nabla \cdot \tau \mid \tilde{c} \rangle$, are first compared against the filtered DNS in Fig. 3.21. The CNN reproduces the expected behaviour and amplitude of $\nabla \cdot \tau$, the fluctuations are also well captured, as seen in Fig 3.22. (Note that because the binning intervals to compute conditional means are different than in Fig. 3.13, the

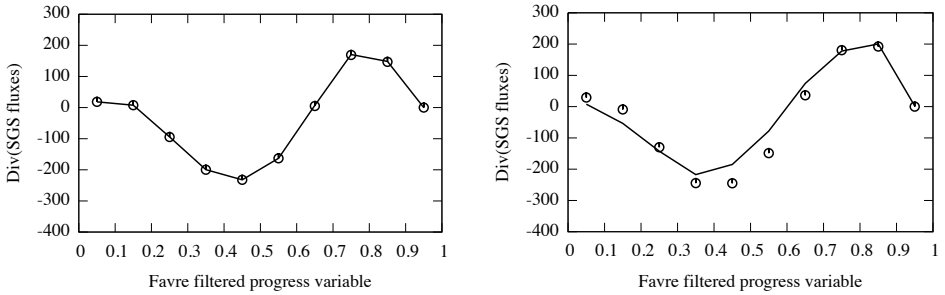

(a) $\Delta = 0.30$ mm (trained) (b) $\Delta = 0.45$ mm (untrained)

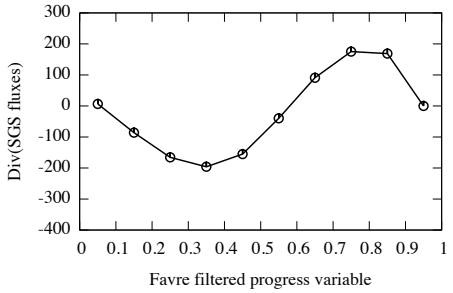

(c) $\Delta = 0.90$ mm (trained)

Figure 3.21: $\langle \nabla \cdot \tau \mid \tilde{c} \rangle$ vs $\tilde{c}$. Symbols: DNS reference. Line: CNN prediction.

extrema also differ.) The test for the untrained filter level is performed with a filter size $\Delta = 0.45\,\text{mm} = 1.125\delta_L$. This constitutes a stringent test case, because neural networks are known to be prone to rapid divergence when applied away from their training area. However, staying within the bounds of the training filter sizes, Fig. 3.21(b) shows that the response of the divergence of the unresolved fluxes is well captured. The plots showing conditional fluctuations in Fig. 3.22(b) confirm this moderate deviation from the reference filtered DNS. These results need to be put in perspective with predictions of unresolved fluxes using most advanced SGS models, where sometimes even the sign is not properly returned (see for instance Fig. 8 of [129] reporting strong departure from DNS in SGS transport modeling in turbulent premixed flames).

Similar results are obtained for the filtered source terms, which are shown in Figs. 3.23 and 3.24. For the trained filter sizes ($\Delta = 0.3$ and 0.9 mm), the filtered chemical source as predicted by the CNN matches the DNS reference, specifically for the largest filter, with a good reproduction of the parabolic shape. The conditional fluctuations of filtered burning rates are also well captured (Fig. 3.24). For the untrained case however, some departure from the DNS value is observed, but still reasonable, at least comparable to what could be expected using classic models to estimate the filtered source terms. This would particularly be the case against formulations where the Arrhenius form is kept at the resolved scales after simply applying a scaling factor, thus far from the parabolic shape developing with the increase in filter size. In a previous work [127], modeling of the filtered source based on 3D approximate deconvolution and 1D flame deconvolution was tested against the same DNS database. As shown in Fig.17(b) of [127], the error on the burning rate estimation conditioned on the progress variable could reached up to 25% for $\Delta = 3\delta_L$. In the present case with the neural network, the maximum error is of the order of 1% on the trained database and of 16% for the untrained ones, confirming the potential of

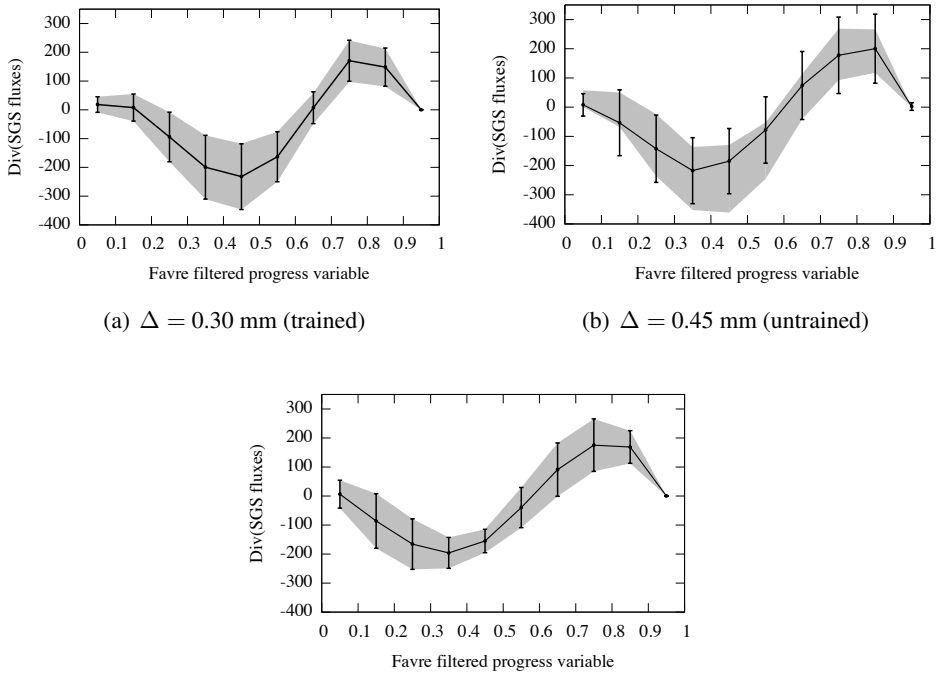

(a) $\Delta = 0.30$ mm (trained)

(b) $\Delta = 0.45$ mm (untrained)

(c) $\Delta = 0.90$ mm (trained)

Figure 3.22: Solid line: $\langle \nabla \cdot \tau \mid \tilde{c} \rangle$ vs $\tilde{c}$ from CNN. Gray: Range covered by the signal according to the RMS in DNS, vertical bar: CNN prediction.

the approach.

3.3 Conclusion

A novel modelling framework using machine-learning is proposed for providing closures for all unresolved terms in the filtered transport equation of the progress variable in large-eddy simulations of turbulent premixed flames in the context of flamelet tabulated chemistry. Convolutional neural networks are trained using data from a direct numerical simulation database, in order to predict the filtered progress-variable source term, and the unresolved fluxes in the filtered transport equation of the progress variable. The advantage of the approach proposed in this study, is that a single variable distribution which is readily available, the filtered progress variable, is sufficient. The convolutional neural networks are shown to provide quantitatively accurate predictions of both the source and flux terms, which are two substantially different terms and otherwise difficult to model in a single unified framework. The predictions capabilities of the networks are also demonstrated to be only weakly insensitive to variations in filter width, which is an important attribute for any sub-grid scale model. Because they are based on the progress variable, a generic parameter of premixed flames, the networks are expected to perform well for any turbulent premixed flame located in the Borghi regime-diagram close to the conditions used for training.

However, because the industrial LES combustors considered in this thesis are non-premixed, the use of the dynamic TFLES model presented section 3.1.4 will be selected thereafter to serve as a basis for soot modelling.

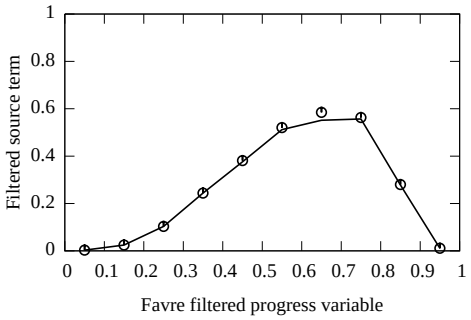

(a) Trained database. $\Delta = 0.30$ mm

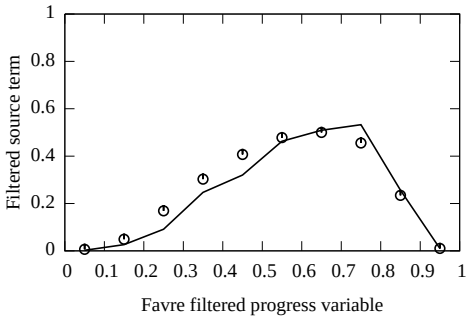

(b) Untrained database. $\Delta = 0.40$ mm

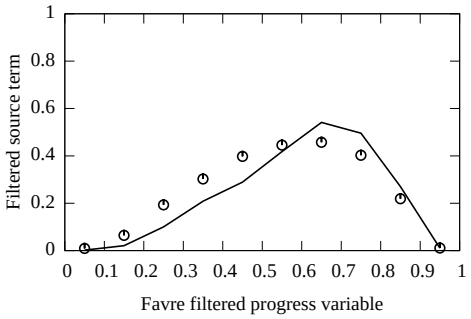

(c) Untrained database. $\Delta = 0.45$ mm

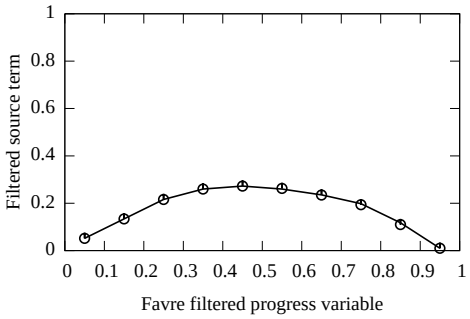

(d) Trained database. $\Delta = 0.90$ mm

Figure 3.23: $\left\langle \overline{\dot{\omega}^+} \mid \tilde{c} \right\rangle$ vs $\tilde{c}$. Symbols: DNS reference. Line: CNN prediction.

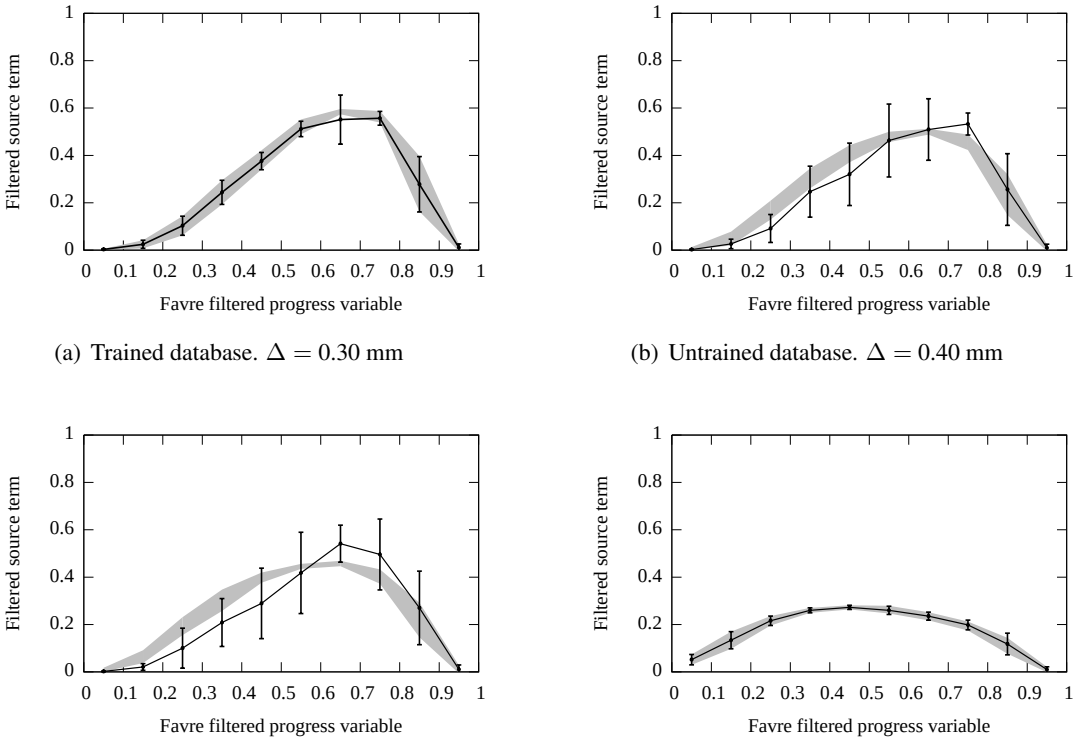

(a) Trained database. $\Delta = 0.30$ mm

(b) Untrained database. $\Delta = 0.40$ mm

(c) Untrained database. $\Delta = 0.45$ mm

(d) Trained database. $\Delta = 0.90$ mm

Figure 3.24: Solid line: $\left\langle \overline{\dot{\omega}^+} \mid \tilde{c} \right\rangle$ vs $\tilde{c}$ from CNN. Gray: Range covered by the signal according to the RMS in DNS, vertical bar: CNN prediction.

Chapter 4

Chemical schemes reduction for industrial applications

Contents

This chapter introduces ORCh [145, 146], a kinetic reduction methodology relevant for aeronautical combustion chamber, as detailed chemical mechanisms are too expensive in term of CPU cost for any industrial simulation. This methodology has been used and improved in this thesis for pollutant prediction, and tested in a Large Eddy Simulation (LES) of the industrial chamber Lemcotec, to capture the CO concentration while maintaining equilibrium temperature and flame velocity profiles at reasonable CPU cost.

4.1 Optimised and reduced chemistry

4.1.1 Context

ORCh [145, 146], for Optimised and reduced chemistry, is a fully automated method to reduce detailed chemical schemes at a given operating point. It has been developed by N. Jaouen [147] during his thesis, and improved in the present work. First, code restructuring and documentation with test cases were done in order to prepare the ORCh industrialization. Secondly, the update version of the flame

canonical generator CANTERA, coupled with ORCh, has allowed to gain CPU performances on flame generation. The modifications have prepared the future coupling with the soot model HYPE, presented in chapter 6, also running with this latest version of CANTERA. Finally, an Aj-optimisation strategy, detailed thereafter, has been implemented in ORCh to overpass the current reduction limits. In parallel, the Euclidian Minimum Spanning Tree mixing model has been implemented by Kaidi Wan to reduce chemistry with ORCh coupled with machine learning [148].

4.1.2 Reduction strategy

Any canonical problem may be used as reference for the ORCh procedure. The present thesis uses the ORCh canonical configuration [145], along with the flame canonical generator CANTERA. The reduction process is mainly composed of three steps:

- First, species and reactions that contribute poorly to the production of defined important (target) species are suppressed by directed relation graph methods introduced by Pepiot *et al.* [149].
- Next species respecting the quasi-steady state assumption can have their production analytically calculated with the transported species, and then be present into the CFD simulation without being transported.
- Eventually, the reduced chemical scheme obtained produces error on species predictions compared to the detailed one. This is due to the previous step with the species and reaction removal. This error is corrected with the last step, using genetic algorithm to optimise the Arrhenius constants until the species and temperature profiles match those of the detailed mechanism, following the procedure illustrated Fig. 4.1.

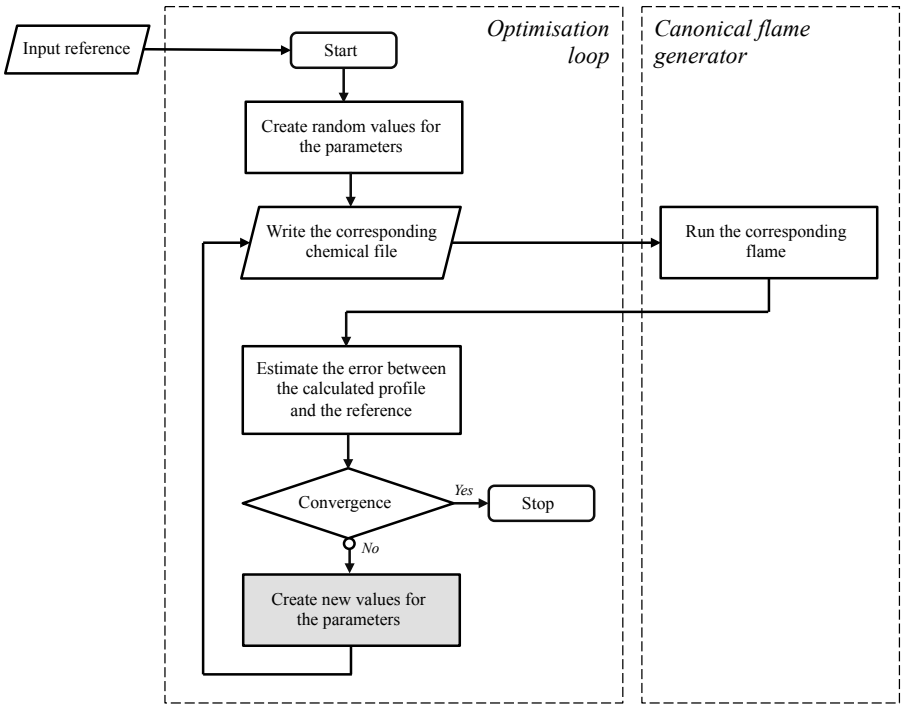

Figure 4.1: ORCh optimisation flowchart. Extracted from [147].

4.2 A more reduced kinetic mechanism using rates calibration versus equivalence ratio

4.2.1 Kerosene chemistry reduction including liquid fuel injection

It is under a Lemcotec operating point described in [147] that the ORCh [145, 146] strategy is applied in this chapter. To probe the chemical response in a CPU efficient manner and to allow for testing a large population of chemical parameters with a genetic algorithm, the ORCh stochastic turbulent micro-mixing canonical problem combined with kerosene droplets evaporation and chemical reactions is first used. The evolutions of the stochastic particles cover the full range of equivalence ratios, temperature and mixing with burnt gases, as encountered by fluid particles traveling in an aircraft engine. Moreover, to secure the response of the flame speed in the zones where the combustion would be stabilised by flame propagation, a freely propagating one-dimensional premixed flames canonical problem is also considered to test the chemical response.

In the ORCh stochastic approach, a set $\phi_k^p(t)$ of reference time evolutions of the thermochemical quantities, is obtained prior to any flow simulations after solving for the evolution of a number of N stochastic particles ($p = 1, \cdots, N$). These particles are distributed over a given number of inlets at initial time and are let to interact according to a stochastic turbulent micro-mixing model and to react following a chemical scheme.

In the present work, the elementary mass flow rate $\dot{q}_m = \dot{q}^p_{m_{\rm L}}(t) + \dot{q}^p_{m_{\rm G}}(t)$ carried by every p-th particle is decomposed into liquid ($\dot{q}^p_{m_{\rm L}}(t)$) and gas ($\dot{q}^p_{m_{\rm G}}(t)$) phases. The evolution of $\phi_k^p(t)$ reads

$$\frac{\partial \phi_k^p(t)}{\partial t} = \text{MIX}^p(\tau_{\rm T}) + \dot{\omega}^p_{\phi_k} + \dot{\omega}^p_{{\rm v}_{\phi_k}} \,, \tag{4.1}$$

where $\dot{\omega}^p_{\phi_k}$ is the gaseous phase chemical source and $\dot{\omega}^p_{{\rm v}_{\phi_k}}$ relates to the evaporation of the fuel (mass or heat), computed from the particle properties. $\text{MIX}^p(\tau_{\rm T})$ denotes the Curl [150] micro-mixing closure in which $\tau_{\rm T}$ is a characteristic mixing time.

To ease the graphic visualisation and limit the number of elements entering the fitness function controlling the genetic algorithm, the information contained in the $\phi_k^p(t)$ is compacted into a limited number of deterministic trajectories $\phi_k^{\rm D}(t)$ issued from the liquid fuel and air inlets. These deterministic trajectories are obtained by solving the usual LMSE (or IEM) [151, 152] PDEs, with the inlet composition serving as initial condition and the relaxation calculated toward the algebraic average of the stochastic particles, see [146]:

$$\frac{\partial \phi_k^{\rm D}(t)}{\partial t} = \frac{1}{\tau_{\rm T}} \left(\frac{1}{N} \frac{\sum_{p=1}^N \dot{q}^p_{m_G} \phi_k^p(t)}{\sum_{p=1}^N \dot{q}^p_{m_G}} - \phi_k^D(t) \right) + \dot{\omega}^D_{\phi_k} + \dot{\omega}^D_{{\rm v}_{\phi_k}} \,. \tag{4.2}$$

The number of stochastic particles taking the concentration of the j-th inlet,

$$N_{P_j} = N \times (\dot{Q}_{{\rm m}_j} / \sum_{\ell=1}^{n_I} \dot{Q}_{{\rm m}_\ell}), \tag{4.3}$$

is proportional to the fraction of this inlet total mass flow rate. The total number of particles is $N = 880$ and three inlets are here considered ($n_I = 3$).

- The first inlet composed of liquid kerosene at $T = 450$ K, represents 3% of the total mass flow rate $\dot{Q}_{\rm m}$

- Air is injected through the second inlet at $T = 703$ K, with a contribution of 52% to $\dot{Q}_{\mathrm{m}}$. Because in a typical aeronautical chamber part of this air actually reaches the reaction zone after the fuel started to burn, only 60% of the total mass of air is introduced at the initial time, the rest of air particles being released progressively over 1 ms.

- In the nominal operating condition, at initial time 45% of $\dot{Q}_{\mathrm{m}}$ is composed of burnt gases at chemical equilibrium for the equivalence ratio of the engine. These stochastic particles injected at $T = 1877$ K constitute the third inlet, which secures ignition of the fresh mixture and mimics the presence of recirculating burnt gases feeding the reaction zone downstream of the swirled injection. The amplitude ($0.45\dot{Q}_{\mathrm{m}}$) of this flux of burnt gases toward the reaction zone was also estimated from a preliminary large eddy simulation of a representative combustion chamber [147].

Figure 4.2 is a representative scatter plot of the temperature of the gas phase particles. Both fast chemistry close to equilibrium and finite rate chemistry effects are observed. It is also seen that large ranges of equivalence ratios and progress of reaction are present within the particles, a point that is of premier importance when reducing and optimising chemistry for non-premixed liquid fuel combustion.

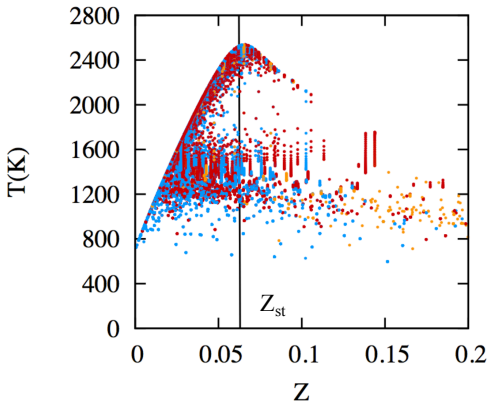

Figure 4.2: Scatter plot of stochastic particles temperature *vs* mixture fraction. Particles are coloured depending on their initial condition. Blue: air. Orange: kerosene. Red: burned gases. Z_{st} is the stoichiometric mixture fraction.

Several chemical mechanisms have been discussed for the combustion of jet fuels surrogates and n-decane [153, 154, 155, 156]. Among those is the detailed mechanism by Dagaut [157], which is composed of 225 chemical species and 3493 reactions. A simplified version of this mechanism was developed by Luche *et al.* [158], accounting for 91 species and 991 elementary reactions, with a surrogate fuel compostion described in table 4.1. This mechanism is employed as a starting point for both reduction and optimisation.

Name	**Formula**	**Mass fraction**	**Molar mass (g/mol)**
N-decane	$NC_{10}H_{22}$	0.767388	142.284
Propylbenzene	PHC_3H_7[1]	0.131402	120.194
Propylcyclohexane	CYC_9H_{18}	0.101210	126.241
Kero Luche	$C_{9.73957}H_{20.0542}$	1	137.195

Table 4.1: Liquid Kerosene composition as proposed by Luche [159].

In Jaouen thesis [147] the reduction capabilities of the ORCh strategy for the Lemcotec operating point have been tested up to a mechanism accounting only for the reproduction of the CO level. This obtained 'C' mechanism is composed of 222 elementary reactions, and 22 species, see table 4.2.

Transported species	**Analytically resolved species**
H_2, O_2, CO, CO_2, CH_4, C_2H_6, CH_2O, C_2H_2, C_2H_4, C_3H_6, C_4H_6, $NC_{10}H_{22}$, H, O, OH, HO_2, H_2O, CH_3, C_3H_3, AC_3H_5, BC_6H_{13}, N_2	HCO, CH_3OH, C_2H_5, CH_3O, CH_2OH, CH_2CO, C_2H_3, CH_2HCO, HCCO, NC_3H_7, PC_4H_9, AC_6H_{13}, AC_8H_{17}, $C_{10}H_{21}$(L)

Table 4.2: **Mechanism C.** Species of the reduced mechanism composed of 22 transported species associated to 14 QSS relations and 222 reactions [147].

This mechanism shows similar trajectories with the detailed mechanism for the stochastic reactor (Fig. 4.3) as for the premixed flame (Fig. 4.4).

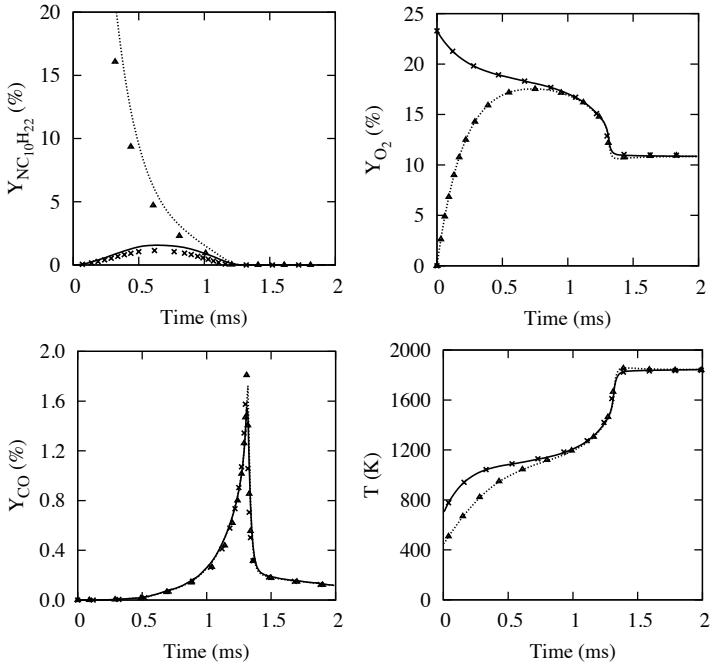

Figure 4.3: Representative species and temperature trajectories [147]. Symbols: Reference chemistry [158]. Cross: Air inlet. Triangle: Liquid fuel inlet. Black-line: Reduced mechanism C after optimisation (Genetic Algorithm). Solid-line: Air inlet trajectory. Dotted-Line: Liquid fuel inlet trajectory.

Now let's try to reduce even more this mechanism. By keeping only the 15 species found as the most influential ones, with 72 elementary reactions, we obtain the reduced mechanism presented table 4.3.

Transported species	**Analytically resolved species**
H_2, O_2, CO, CO_2, CH_2O, C_2H_4, C_3H_6, $NC_{10}H_{22}$, H, O, OH, HO_2, H_2O, CH_3, N_2	HCO, C_2H_5, CH_3O, C_2H_3, NC_3H_7, AC_6H_{13}, AC_8H_{17}, BC_6H_{13}

Table 4.3: **Mechanism D.** Species of the reduced mechanism composed of 15 transported species associated to 8 QSS relations and 72 reactions.

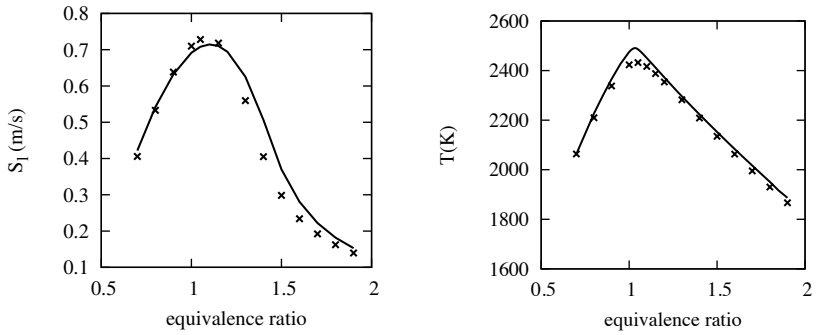

Figure 4.4: Freely propagating premixed flames [147]. Response versus equivalence ratio. Temperature taken in burnt gases. Symbols: Reference chemistry [158]. Black-line: Reduced mechanism C after optimisation (Genetic Algorithm).

Figure 4.5 shows the trajectories for representative species and temperature, after reduction and optimisation (black-line). The optimisation step allows for bringing the response back to the reference detailed mechanism along the trajectories for the target species, Fuel, CO, CO_2, O_2, H_2O and temperature. Moreover, for this reduced scheme, it was not found possible to converge toward a set of chemical rates able to reproduce the premixed flame speed responses for the full range of equivalence ratios (Fig. 4.6(a)) unlike the associated temperatures (Fig. 4.6(b)).

4.2.2 Pre-exponential constants tabulated reduced chemistry

Because it is not possible to cover with accuracy all equivalence ratios with a single mechanism containing 15 transported species, the optimisation is repeated with premixed flames, but considering independently every value of the equivalence ratio on the rich side ($\phi > 1.3$). The fitness function f of the optimisation process is based on the flame speed, the temperature, and the mass fractions of H_2O, CO, CO_2, O_2 and $NC_{10}H_{22}$, with f expressed as in [145]. Previous works have reported adjustments of chemical constants to equivalence ratio variations [160, 161, 162]. The optimisation is limited here to the pre-exponential constants, other parameters being kept fixed. Selecting a single equivalence ratio, the genetic algorithm indeed converges towards A_j pre-exponential constants, which allows for perfectly reproducing the major premixed laminar flame properties (Fig. 4.7).

Figure 4.8 shows the normalised variation, versus equivalence ratio, of the resulting pre-exponential constants for several representative elementary reactions. Aside from the reaction

$$C_2H_4 + OH \rightarrow H_2O + C_2H_3,$$

which features a linear growing behaviour of A_j versus ϕ, all other reactions require non-monotonic variations of A_j to capture the laminar flame properties with the 15 species reduced scheme. For instance, the A_j of the elementary reaction

$$H + C_2H_5 \rightarrow H_2 + C_2H_4$$

increases by more than 85% between $\phi = 1.5$ and $\phi = 1.6$, to then decrease again by 65% for $\phi = 1.7$ and $\phi = 1.8$. These strong variations are in fact inherent to the optimisation by genetic

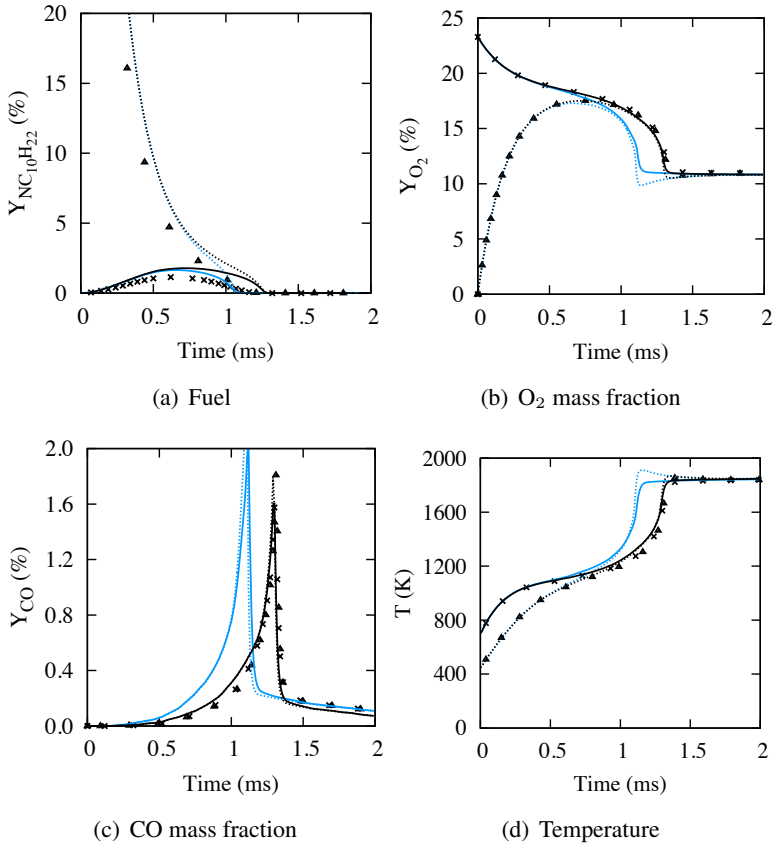

(a) Fuel (b) O_2 mass fraction

(c) CO mass fraction (d) Temperature

Figure 4.5: Representative species and temperature trajectories. Symbols: Reference chemistry [158]. Cross: Air inlet. Triangle: Liquid fuel inlet. Lines: Reduced mechanism D. Black-line: After optimisation (Genetic Algorithm). Solid-line: Air inlet trajectory. Dotted-Line: Liquid fuel inlet trajectory.

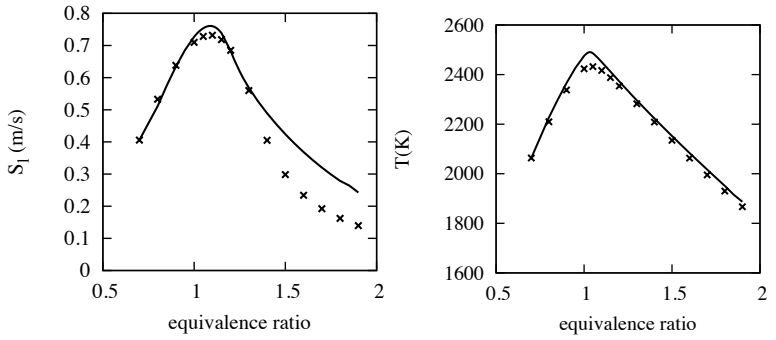

(a) Flame speed (b) Temperature

Figure 4.6: Freely propagating premixed flames. Response versus equivalence ratio. Temperature taken in burnt gases. Symbols: Reference chemistry [158]. Black-line: Reduced mechanism D after optimisation (Genetic Algorithm).

algorithm applied in a sequential manner to the various ϕ values, thus without ensuring continuities of the A_j versus ϕ.

The variations of the A_j may be compared when they are obtained by optimisation at a given equiv-

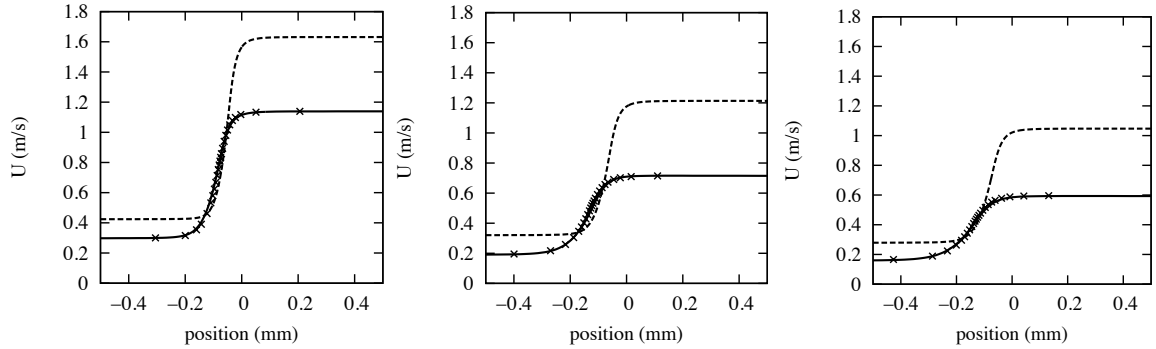

(a) $\phi = 1.5$ (b) $\phi = 1.7$ (c) $\phi = 1.8$

Figure 4.7: Velocity distribution across freely propagating premixed flames. Symbols: Reference chemistry [158]. Dotted-line: Reduced mechanism D. Black-line: D optimised for the given equivalence ratio.

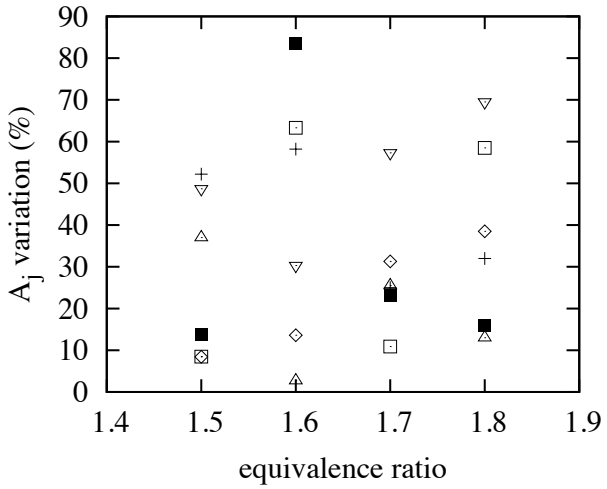

Figure 4.8: Variation with optimisation of the pre-exponential constant versus equivalence ratio. Black-square: H + C_2H_5 ⇋ H_2 + C_2H_4. Triangle-up: H_2O + C_2H_3 ⇋ C_2H_4 + OH. Triangle-down: H + C_2H_4 ⇋ H_2 + C_2H_3. Dotted-diamond: C_2H_4 + OH ⇋ H_2O + C_2H_3. Dotted-square: C_2H_4 + M ⇋ H + C_2H_3 + M. Cross: C_2H_5 + OH ⇋ CH_2O + H + CH_3.

alence ratio or by interpolation between two optimised sets of $A_j(\phi)$. Figure 4.9(a) shows for $\phi = 1.6$ the normalised deviation of the A_j to the reference scheme for all the reactions. In this graph, the length of the coloured line corresponds either to the optimised A_j (green) or to pre-exponential values linearly interpolated (red) between the optimised A_j terms at $\phi = 1.5$ and at $\phi = 1.7$. It is observed that for most of the reactions, the sign of the needed correction stays the same, except in the case of low variations from the reference scheme, as for example the elementary reactions :

#14: O_2 + OH → HO_2 + O,
#33: H + C_2H_5 → 2 CH_3 ,
#34: CH_3O + M → CH_2O + H + M,
#40: C_2H_5 + OH → CH_2O + H + CH_3 ,
#65: H + C_2H_4 (+ M) → C_2H_5 (+ M) and
#66: C_2H_5 + O_2 (+ M) → C_2H_4 + HO_2 (+ M).

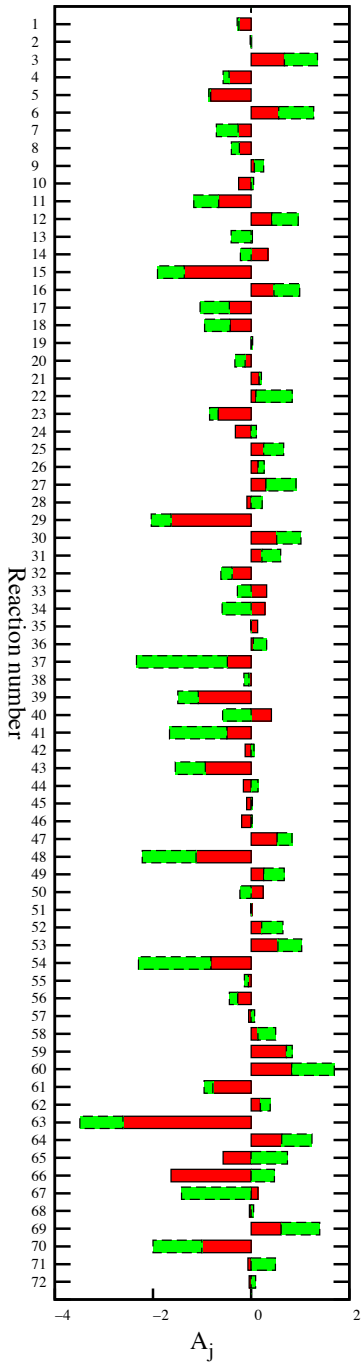

(a)

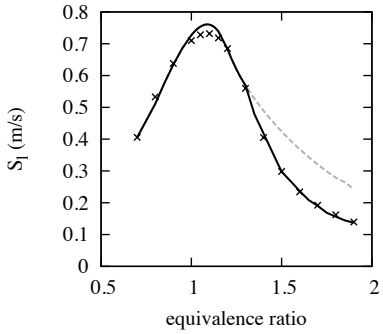

(b) Flame speed

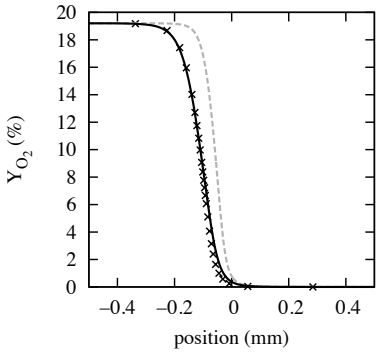

(c) O_2

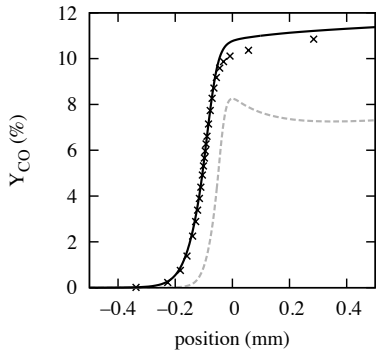

(d) CO

Figure 4.9: (a) Normalised variations of the 72 pre-exponential constants $(A_j - A_j^{\text{Ref}})/A_j^{\text{Ref}}$. Green: optimised. Red: interpolated. $\phi = 1.6$. (b): One-dimensional freely propagating premixed flame. Flame speed versus equivalence ratio. (c) O_2 mass fraction. (d): CO. $\phi = 1.55$. (b)-(c)-(d): Symbol: Reference chemistry [158]. Grey dotted-line: Reduced mechanism D. Black-line: Reduced mechanism D-A$_j$-Tabulated.

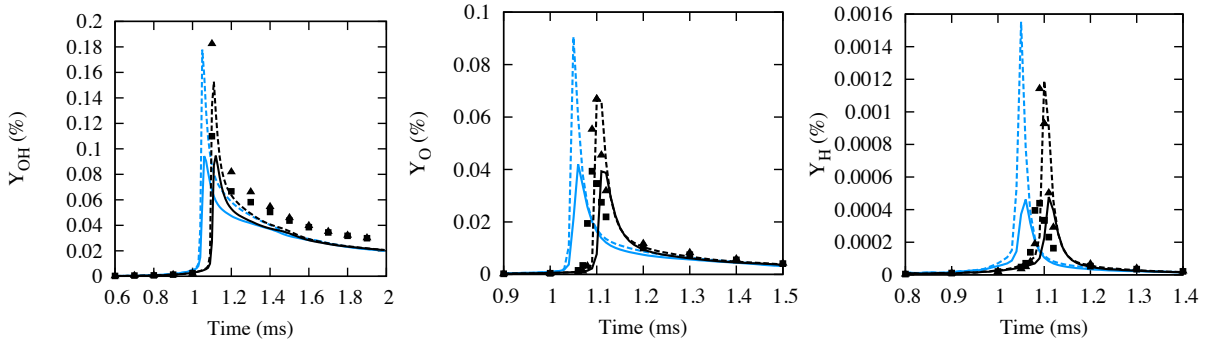

(a) OH (b) O (c) H

Figure 4.10: Representative intermediate species trajectories. Square: Air inlet. Triangle: Liquid fuel inlet. Symbols: Reference chemistry [158]. Black: Reduced mechanism D-A$_j$-Tabulated. Blue: Reduced mechanism D. Solid-line: Air inlet trajectory. Dotted-Line: Liquid fuel inlet trajectory.

The fact that the sign is mostly the same conforts the possibility of obtaining the whole range of A$_j$ from interpolation in a lookup table. Nevertheless, to avoid the large variations to spread over too many reactions, the discretisation in equivalence ratio should not be too coarse. In practice, $\Delta\phi = 0.2$ was found as a good compromise for the present chemistry.

The flame speed computed over the full range of equivalence ratios with this procedure is plotted in Fig. 4.9(b), confirming the possibility of reproducing the complex chemical decomposition of the heavy fuel on the rich side, with only 15 transported species combined with tabulated pre-exponential parameters for $\phi > 1.3$ and fixed below. The chemical structure of the flame from fresh to burnt gases is also captured, as seen in Figs. 4.9(c) and 4.9(d) for a premixed flame at $\phi = 1.55$, values for which the A_j have been interpolated. Applied back to the turbulent non-premixed micro-mixing problem with liquid fuel injection, thus covering at once the full range of equivalence ratios, the D mechanism with interpolated A_j on the rich side perfectly matches the response of the reference detailed mechanism (Fig. 4.10). This is observed for the target species, as it was already the case for a single set of A_j (Fig. 4.5), but also for intermediate species, which were not in the list of targets for optimisation and which were not captured previously for rich equivalence ratios. These species such as H, OH, and O are known to be essential for the prediction of the flame speed [163], it is therefore expected that they must indeed be captured with accuracy when both the non-premixed turbulent micro-mixing and the premixed laminar flame canonical problems are addressed.

4.3 Large Eddy Simulation of the LEMCOTEC combustor

4.3.1 Previous LES simulations

The Lemcotec operating point considered here was studied by T. Jaravel [43] using the LES code AVBP with a mechanism composed of 27 species and 452 chemical reactions, and N. Jaouen [147] with the LES code YALES2, using a reduced mechanism derived from Luche [159] with 26 species and 338 reactions. Both simulations were performed for Nox and CO predictions. In this section, the simulation from N. Jaouen was retrieved, with the same domain, represented Fig. 4.11, and with the numerical set up described in his thesis [147].

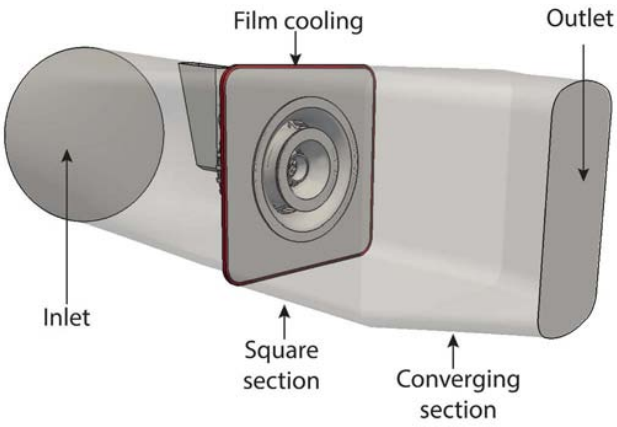

Figure 4.11: The Lemcotec computational domain, from Jaravel [43].

As we are interested here to validate the Aj-tabulated reduced mechanism 4.3 for CO predictions, we firstly changed the kinetic mechanism in the simulation. Secondly, we used the dynamic scheduler in YALES2, a useful algorithm for CPU reduction due to chemistry. It consists of sharing the chemical integration solving between all the available cores that will have the same amount of work. In a massively parallel code, it is ideal to have a better synchronisation between the cores and allows to gain a significant CPU time despite the increasing MPI connections. In this configuration, we gained a factor 2 on the CPU time.

4.3.2 Simulation results and experiment comparison

We are interested here in the CO level prediction. Figure 4.12 shows the CO source term evolution at different planes in the chamber. One can see the instantaneous CO level variation decreases drastically from plane Y1 located in the flame zone, to the exit plane Y6. However CO instantaneous variations on the exit plane Y6 are still present, and correlated with the temperature variation, see Fig. 4.13.

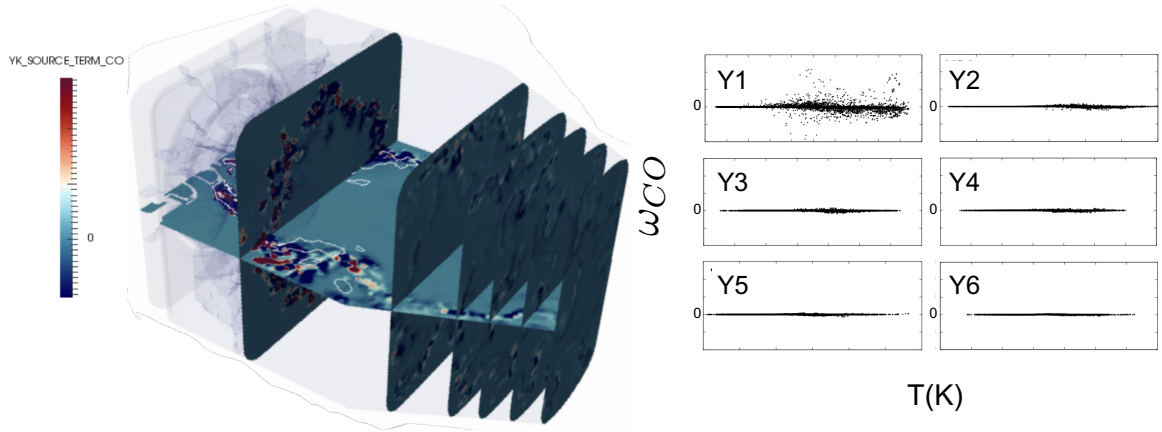

Figure 4.12: Instantaneous CO source term at 6 different planes, from plane Y1 to exit plane Y6.

In order to make comparison with the experimental CO levels, we are thus going to calculate the CO emission index, averaged over the 6 probes and over the 20 ms used for statistics, see Fig. 4.14 with the relation 4.4 :

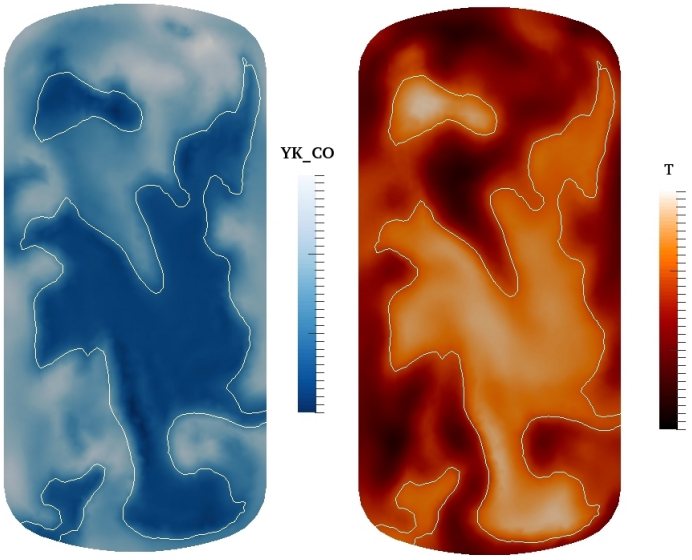

Figure 4.13: Instantaneous CO mass fraction and temperature in the exit plane. The isocontour represents the injected mixture fraction.

$$< \text{IECO} >^{\text{probes}} = \sum_{t} \frac{\sum_{i=1}^{6} Y_{\text{CO}_i}}{\sum_{i=1}^{6} Z_i} \tag{4.4}$$

The comparison between the experimental results and the averaged LES emissions (in g/kg of fuel) are given in table 4.4 for both the present simulation and the previous one presented N. Jaouen thesis. The CO emissions are predicted by both simulations, with a relative error of about 7%, and a CPU time reduced by a factor 4 with the present procedure compared as the previous one with the 26-species scheme.

	Experiment (g/kg of fuel)	**LES (g/kg of fuel)**	**Relative error (%)**
Jaouen 26sp scheme $< \textbf{EICO} >^{\textbf{probes}}$	51.47	55.30	7,4%
Aj-tab 15sp scheme $< \textbf{EICO} >^{\textbf{probes}}$	51.47	47.66	7,4%

Table 4.4: Experimental and simulated CO index comparison, mean over time and the 6 probes on the exit plane.

4.4 Conclusion

In this chapter, a strategy is discussed to enhance the reduction of a detailed kerosene chemical scheme. With the ORCh reduction procedure, schemes of decreasing complexity are generated from a reference detail mechanism, with the objective of finding the minimum level of complexity which allows for capturing fixed target properties. A stochastic micro-mixing problem including liquid fuel evaporation is built to probe the various chemical schemes generated and to perform the optimisation of the rates with a genetic algorithm. The inlet mass fluxes and residence time are those of the Lemcotec aeronautical

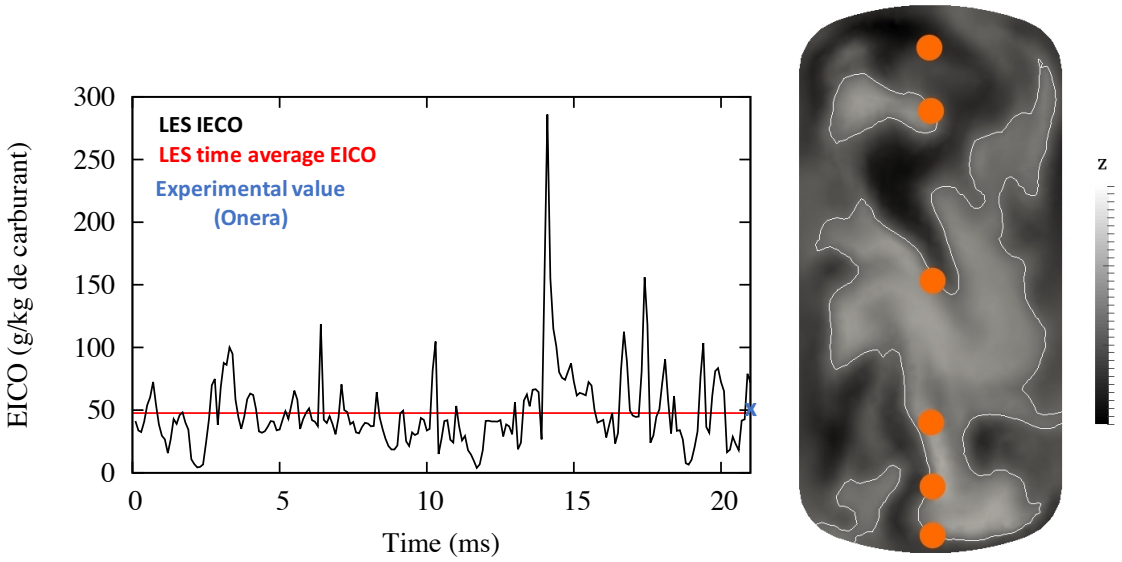

Figure 4.14: IECO averaged over the 6 probes (orange points represented in the exit plane of the combustion chamber) .

engine. It is shown that up to a given level of complexity, securing the accuracy in the reproduction of the micro-mixing problem also allows for computing premixed laminar flame properties. The number of species below which a single set of chemical parameters cannot secure accuracy over a large range of equivalence ratios, typically in the rich side region, is then determined. To further reduce the chemistry, still preserving the wanted flame properties, a different optimisation strategy in which the Arrhenius pre-exponential constants are allowed to evolve with the equivalence ratio is adopted. The obtained Aj-tabulated mechanism is applied back through cross validation between the micro-mixing problem and premixed laminar flame calculations. Finally, the Aj-tabulation is tested on the 3D LES Lemcotec chamber simulation, allowing to predict the CO level on the chamber exit with only 15 transported species, and 72 associated elementary reactions. Compared to the 26 transported species by N. Jaouen [147] the mechanism reduction resulted to a CPU reduction by a factor 2, leading with the dynamic scheduler, by a total CPU reduction by a factor 4 without degrading the CO level prediction and thus confirming the use of the strategy.

Chapter 5

Review on soot and fuel model issues

Contents

As the phenomena leading to the presence of soot in aircraft engines are deeply complex, the following chapter will try to bring some key elements in order to prepare the introduction of the methodology retained in Chapter 6 for soot prediction in a 3D LES simulation of a real aircraft engine. The first key aspect is the fuel model and the gaseous description, both critical for soot formation. Secondly, as the research on soot formation and evolution is still on-going, several hypothesis coexist along with a growing number of soot population solving methods. A selection will be presented hereinafter.

5.1 Jet fuel models

When it comes to real fuel simulation, several issues appear. This section lists the industrial issues and presents the methodology retained to model real fuel affordable for an industrial LES simulation including soot description.

5.1.1 Real jet fuels

Jet fuels for airlines companies vary depending on the country and services, see Table 5.1. Common standards have been establish after the World War II, and today the Jet A-1 is mostly used for the airlines companies and refining industries in Europe. All these fuels are liquid kerosene-based, meaning the carbon distribution varies from 8 to 16, and their complex mixture contains hundreds of hydrocarbons, classed in groups presented Fig. 5.1, with the paraffin, synonym of saturated alcane C_nH_{2n+2}, n $\in$ [8,19],

representing 77% of the fuel composition, and aromatic hydrocarbons (naphtalenes and alkylbenzenes) representing 20%.

Fuel name	Use
Jet A-1	Standard commercial jet fuel
Jet A	U.S. domestic jet fuel
JP-8	U.S. military jet fuel
JP-5	U.S. navy jet fuel
TS-1	Russian jet fuel

Table 5.1: Most common jet fuels around the world.

Large variations in these fuel compositions have been observed during an intensive measure campaign, the “world fuel sampling program" [164], and if it is reasonable to consider an average composition for model purposes, see 5.2, it does not imply the different fuels have a similar behaviour in different configurations. In typical gas turbine operating conditions, the fuel mixture does not impact the combustion, but with recent technologies operating close to stability limits, typically in lean partially premixed conditions, the sensitivity to the fuel composition may become of greater importance, especially concerning the auto ignition properties. Soot production is also strongly dependent on chemical properties according to Edwards *et al.* [165].

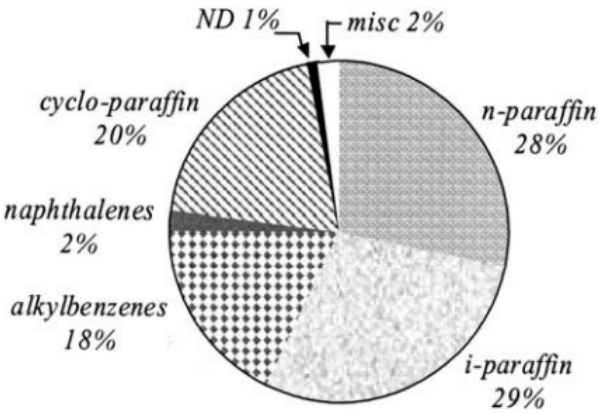

Figure 5.1: Hydrocarbon class distribution for Jet-A fuels [166].

5.1.2 Review of the detailed fuel models and associated issues

5.1.2.1 Surrogates

One of the main issues for the chemists, when it comes to model such complex fuels, is to determine which and how many components the surrogate will need to simulate the real fuel thermo-physical properties. Surrogates can be built through the following methodologies [168]: First, starting from a real fuel sample, a chemical analysis is performed in order to build a set of potential mixtures, mostly with components representative of a group of chemical species. Secondly, these potential surrogates are computed and the final one is chosen depending on his predictability on target properties. Early fuel models were built on a physical property of the fuel: the distillation curve, which characterises the volatility of the

Property	Avgas	JP-4	JP-5	JP-7	JP-8 (Jet A/A-1)	RP-1
Approximate formula[a]	C_7H_{15}	$C_{8.5}H_{17}$	$C_{12}H_{22}$	$C_{12}H_{25}$	$C_{11}H_{21}$	$C_{12}H_{23}$
H/C ratio	2.09	2.00	1.92	2.07	1.91	1.95
Boiling range, °F (°C)	115–295 (46–145)	140–460 (60–240)	360–495 (180–260)	370–480 (190–250)	330–510 (165–265)	350–525 (175–275)
Freeze point, °F (°C)[b]		−80 (−62)	−57 (−49)	−47 (−44)	JP-8/Jet A-1: −60 (−51); Jet A: −50 (−45)	−55 (−48)
Flash point, °F (°C)		−10 (−23)	147 (64)	140 (60)	127 (53)	134 (57)
Net heating value, Btu/lb (kJ/kg)		18,700 (43,490)	18,500 (43,025)	18,875 (43,895)	18,550 (43,140)	18,650 (43,370)
Specific gravity, 16°C (60°F)	0.72	0.76	0.81	0.79	0.81	0.81
Critical temperature, °F (°C)		620 (325)	750 (400)	750 (400)	770 (410)	770 (410)
Critical pressure, psia (atm)		450 (30.5)	290 (19.5)	305 (20.5)	340 (23)	315 (21.5)
Average composition						
Aromatics, vol%	25	10	19	3	18	3
Naphthenes		29	34	32	35	58
Paraffins		59	45	65	45	39
Olefins	10	2	2		2	
Sulfur, ppm		370	470	2	490	20

[a]For illustration of average carbon number, not designed to give accurate H/C ratios.
[b]Typical.

Figure 5.2: Average properties for different jet fuels, Edward *et al.*(2003) [167].

fuel along the entire boiling range, see Fig. 5.3. Wood *et al.*[169] were the first to attempt a surrogate model. They developed a 14-component fuel model, built to match the distillation curve of the JP-9 fuel.

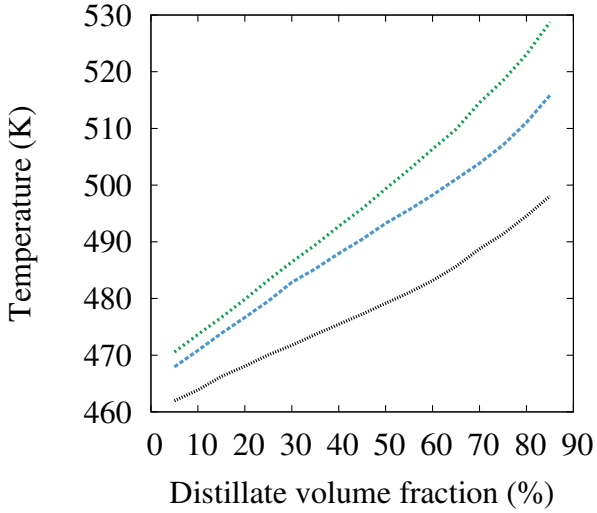

Figure 5.3: Representative distillation curves for three samples of Jet-A : Jet-A-3602 (blue) Jet-A-3638 (black) Jet-A-4658 (green). Presented in [170].

A non exhaustive list of the developed surrogates over the years are presented Tab. 5.2 .

In 1994, the kerosene combustion in low-temperature jet-stirred reactors, based on jet A-1, was constructed with a single component, N-decane, by Dagaut *et al.*[171]. The authors argued that the oxidation of the N-decane alone can predict the overall combustion behaviour of a kerosene fuel. Indeed, alkanes constitutes the major fraction. The 20% aromatics mass fraction is shown to have a negligible effect on the combustion chemistry. Good predictions of the major species were found with Dagaut's scheme, using jet-stirred reactors at elevated pressures.

Then, two other key phenomena, the real fuel distillation curve and the phase behaviour, have been targeted by several studies [176, 177] to recover the physical properties of the fuel combustion such

Authors	date	Fuel composition	Size	Validity
Dagaut *et al.*[171]	1994	100% n-decane	90 species, 573 reactions	JSR 10-40 bars 750-1150 K
Voisin [172]	1997	78% n-decane, 12.2% toluene 9.8% cyclohexane	225 species, 1800 reactions	JSR 10-40 bars
Cathonnet *et al.*[173]	1999	78% n-decane, 9.8% cyclohexane, 12.2% toluene	188 species, 1463 reactions	JSR 10-40 bars
Patterson *et al.*[174]	2001	89% n-decane, 11% toluene	84 species, 440 reactions	JSR 10-40 bars 1 bar Premixed flame
Luche [175]	2003		91 species, 991 reactions	JSR 10-40 bars

Table 5.2: Non exhaustive list of different kerosene surrogates

as mixing, vaporisation, evaporation. Indeed, according to Slavinskaya *et al.*[177], the capacity of the model to recover the phase-equilibrium properties is not sufficient and distillation curve must be taken into account before considering chemical kinetic and gas phase transport properties. They point out that the behaviour of the functional groups and their interactions that are key to chemical time scales result in different intermolecular forces and molecular weight, properties to which physical properties are most sensitive. In 2002, Violi *et al.*[166] produced a semi-detailed surrogate model for JP-8 and jet A fuels with 6 hydrocarbons. The scheme was able to recover physical properties like distillation curve, flash point, and chemical kinetics at atmospheric conditions.

In 2010, Bruno *et al.* [178, 179] presented a mixture evaluation tool to compare surrogates against real fuel properties. Results showed that surrogates with a small number of component have difficulties to reproduce the distillation curve and other thermo-physical properties. Generally a surrogate with only two or three components tends to behave like a single component fuel, meaning that the fuel mixture has to be composed by more than four components, which leads to significantly more complex kinetic mechanisms to recover properly both physical and chemical kinetics properties.

5.1.2.2 Hybrid chemistry

Another approach has been suggested in 2017 by Xu *et al.*[180]. With the study of heavy fuels thermal decomposition in lighter species when heated, they demonstrate that the thermal decomposition does not depend on the exact fuel mixture, the thermodynamic properties nor the oxidiser composition. Moreover, the fuel decomposes entirely into pyrolysis products before diffusing in the flame zone, giving the possibility to numerically separate the thermal decomposition and the oxidation. The timescale of the pyrolysis products being 10 times smaller than the oxidation reactions, the decoupling of the two phenomena can also be done in time. A simplified modelling of the high temperature oxidation of heavy fuels called HyChem, for Hybrid Chemistry, has then been presented, with on one hand the kinetics of the fuel thermal decomposition, and on the other hand a detailed reaction model for the oxidation of the decomposed species, a simple representation is shown Fig. 5.4. The advantage of the HyChem method is to propose a simplified fuel model with a single lumped component fuel.

Several applications have already been conducted [181], showing the potential of the HyChem method. Pyrolysis products are found to be between 6 and 10, with ethylene being the major intermediate for all conventional jet fuels.

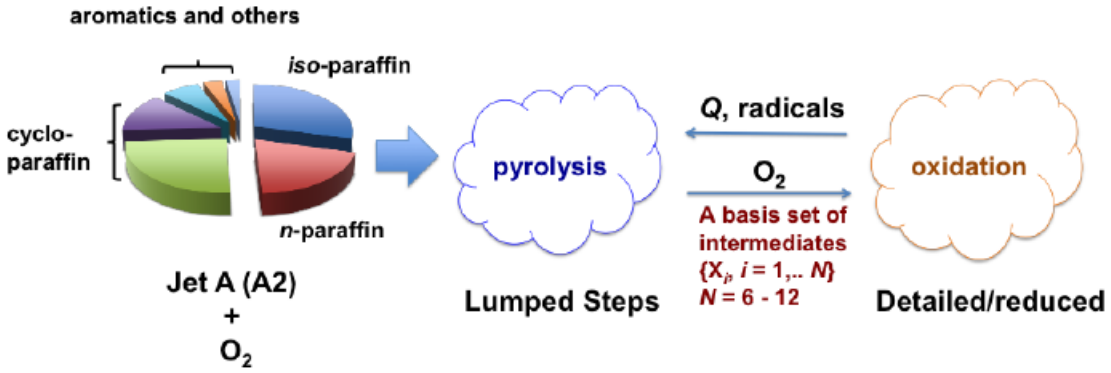

Figure 5.4: Schematic of the HyChem approach. Taken from [180].

The model for pyrolysis relies on global lumped reactions, described further, with empirical rates, determined against Standford's experimental data. Seven lumped reactions are needed to model a jet A fuel pyrolysis, with one C-C fission like reaction and 6 H-abstraction followed by fuel radical breakdown :

$$C_mH_n \rightarrow e_d(C_2H_4 + \lambda_3\ C_3H_6 + \lambda_{4i}\ \text{i-}C_4H_8 + \lambda_{4n}\ \text{1-}C_4H_8) + b_d(\chi C_6H_6 + (1\text{-}\chi)C_7H_8) + \alpha H + (2\text{-}\alpha)CH_3$$

$$C_mH_n + R \rightarrow RH + \gamma\ CH_4 + e_a(C_2H_4 + \lambda_3\ C_3H_6 + \lambda_{4i}\ \text{i-}C_4H_8 + \lambda_{4n}\ \text{1-}C_4H_8) + b_a(\chi C_6H_6 + (1\text{-}\chi)C_7H_8) + \beta H + (1\text{-}\beta)CH_3$$

with R = H, CH_3, O, OH, O_2, HO_2, and e_a, e_d, b_a, b_d, λ_3, λ_{4i}, λ_{4n}, χ, α, β, γ 11 stoichiometric parameters, found by experimental data.

Note that the coefficients e_a, e_d, b_a, b_d are linked because of elemental conservation.

5.2 Soot modeling

This section presents a description of soot stake, morphology, physical and chemical properties, and the main theories about their creation, evolution and destruction in the conditions of an aircraft combustion chamber. A brief review of soot models is shown, including the HYPE model [182] whose implementation in ORCh is presented in chapter 6.

5.2.1 Soot characterization

Because of their complex nature and their presence in such various and different fields, soot particles are very difficult to be properly defined. Their physicochemical properties change depending on combustion conditions, fuel or time residency in the atmosphere. A common definition can stand in that way: they are solid components, essentially composed of carbon with a small percentage of hydrogen, formed through an incomplete hydrocarbon combustion at elevated temperature. Soot particles are difficult to classify, because of their highly various size and structure, see for example Fig. 5.5.

Soot present different structures, shown Fig. 5.6, the most common in their natural state being:
- Amorphous carbons, with chaotic structures,
- Hydrocarbon chains, in the form of linear particles,

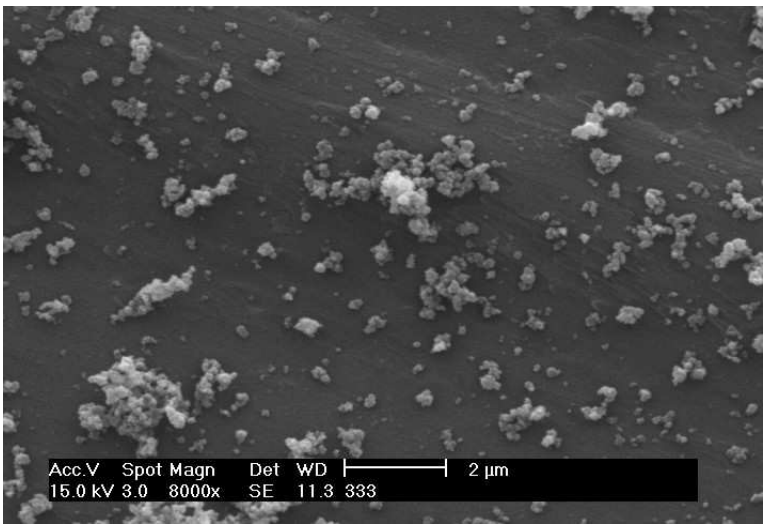

Figure 5.5: Soot formed by wood chip pyrolysis observed under a microscope [183].

- Polycyclic aromatic hydrocarbon PAH,
- Fullerene, with 3D spherical shape structures. The first, a C60, was discovered in laboratory in 1985 [184], and then in space in 2010 [185]. Fullerenes are found in very small quantities in soot from aircraft and car combustion.
- Diamond and graphite, solid carbon having the most ordered structure. They are found in negligible quantity in interstellar dust.

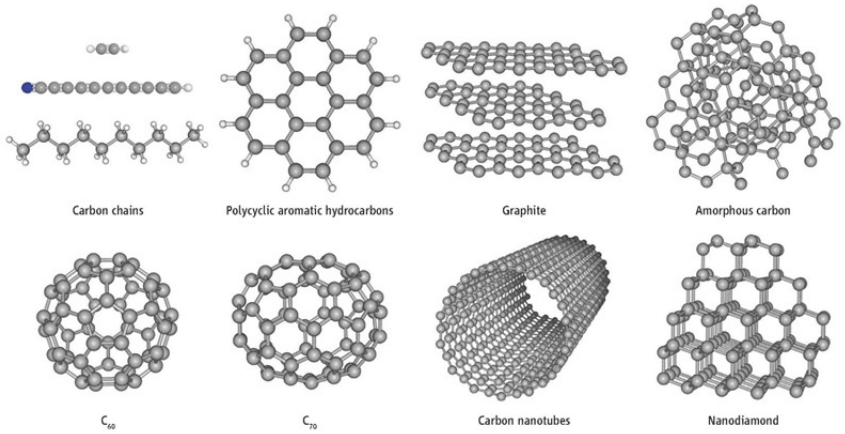

Figure 5.6: Main structures of carbon [186].

Along with their structure, the complexity of soot characterisation is also due to their morphology and texture. Soot morphology is defined through the fractal dimension that characterises how the soot fills the space. The fractal dimension is usually between 1 and 3, linked to the compactness of the soot as described Fig. 5.7.

Soot morphology also varies with the time residency, the “older" the soot is, the more its morphology is compact because of its interaction with other elements (HCl, H_3PO_4...) see Fig. 5.8. In the atmosphere, soot can act like a transport vector for those elements, and studies are still on-going to determine the

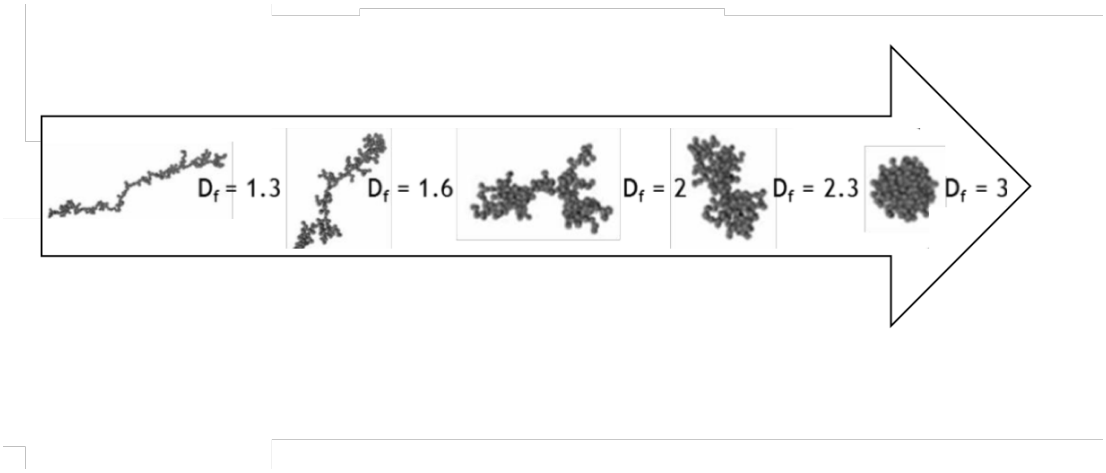

Figure 5.7: Different soot morphologies linked to their fractal dimension [187].

interaction effect on the soot absorption [188].

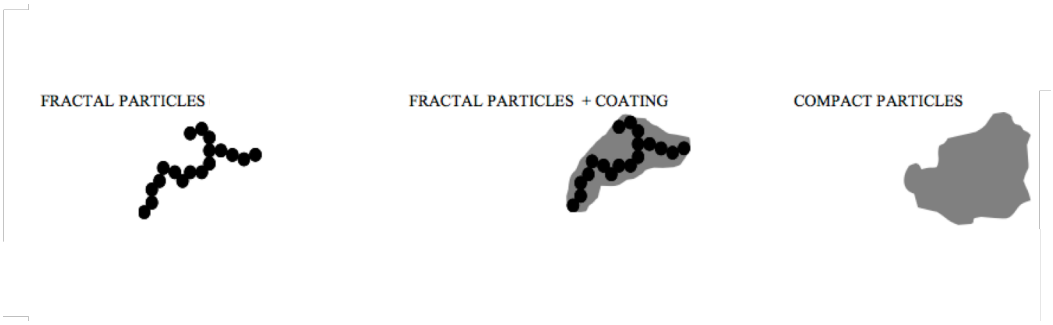

Figure 5.8: Atmospheric soot evolution: interaction with other elements.

An equally important soot property experimentalists are usually looking at to get to the radiative transfer is the optical index. It is a complex macroscopic value strongly dependant on the soot composition, the H/C ratio, the absorbing property and structure. All these properties are changing during the soot life.

At a nano-scale level, soot particles are also observed to be organised in PAH layers as shown Fig 5.9.

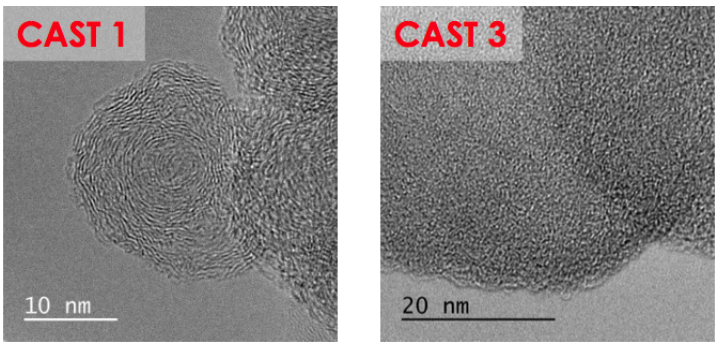

Figure 5.9: Soot nano-structures organised (left) and amorphous (right) for rich combustion conditions [187].

5.2.2 Soot evolution and formation

Soot formation steps can be relatively easily identified in laminar diffusion flames.
Fig 5.10 summarises the soot formation and size evolution steps that are described in this chapter:
- The **inception**, or the formation of the first soot precursors in the gaseous phase through the aromatics growth.
- The **nucleation**, a mechanism that transforms heavy gaseous molecules into the first solid soot particles.
- The soot **surface growth** by chemical reaction.
- The **coagulation**, a collision mechanism between soot particles, from the coalescence to agglomeration, leading to soot volume and surface increase.
- The soot **oxidation**, mainly through O_2 and HO, leading to soot mass decrease.
- The **fragmentation**, a soot particle break-up mechanism.

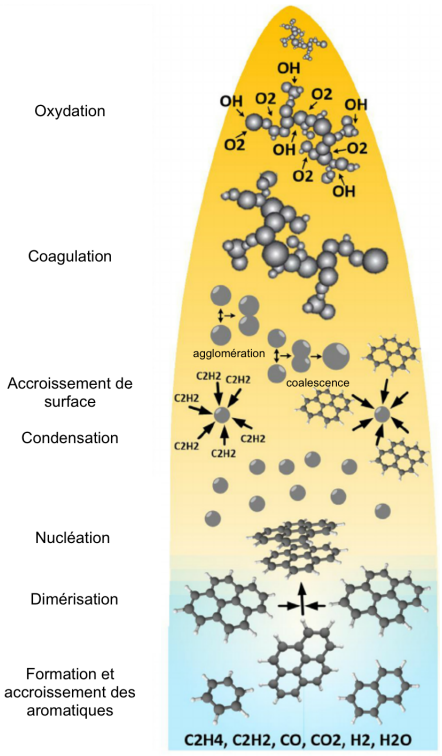

Figure 5.10: Main evolution mechanisms considered in soot models [189].

5.2.2.1 Soot particle formation

Inception

It is usually poor oxygen combustion conditions that boost hydrocarbon radicals recombination. These radicals are then evolving into bigger intermediate gaseous species that, by nucleation, will form the first soot particles.
In the community, PAH have been recognised to be these intermediate gaseous species. However, several studies are still ongoing concerning the importance of the first aromatic cycle formation, and on the exact involved species in the PAH formation [190].

The following section presents the main hypothesis of the PAH formation and growth.

Aromatics formation

For more than thirty years, the first aromatic species formation that leads to PAH has been and is still an ongoing question. Some studies suggest that the formation of multi-cycle is directly done through poly-acetylene condensation [191], other that it is done by C_4H_x recombination [192], but the majority of nowadays studies makes the hypothesis that PAH formation is directly controlled and limited by one-cycle aromatics formation, typically the benzene C_6H_6, widely investigated.
Experimental [193] and numerical studies [194] have shown the importance of propargyl C_3H_3 and radical C_3H_5 in benzene formation. Several chemical pathways have then been proposed [195], despite the difficulty given by the lack of experimental data. Among them, there is the reaction (5.1) involving radical n-C_4H_3 and (5.2) involving n-C_4H_5 [196, 197], but also (5.3) involving propargyl and acetylene [190].

$$\text{n-}C_4H_3 + C_2H_2 \rightarrow \text{phenyle} \tag{5.1}$$

$$\text{n-}C_4H_5 + C_2H_2 \rightarrow \text{benzene} + H \tag{5.2}$$

$$C_3H_3 + C_2H_2 \rightarrow \text{c-}C_5H_5 \tag{5.3}$$

Acetylene being abundant in soot formation zones, the chemical pathways involving acetylene was for a long time considered as the main benzene formation pathways. However, the reaction (5.4) has recently been demonstrated [198, 199, 194] to be of the first importance, involving two propargyls resonance-stabilized. Nevertheless, reactions (5.1), (5.2) and (5.3) are still being considered important to the benzene formation in a less extent.

$$C_3H_3 + C_3H_3 \rightarrow C_6H_6 \tag{5.4}$$

Once benzene formed, it is supposed to evolve to PAH species through the HACA mechanism, illustrated Fig. 5.11 and described in the next section.

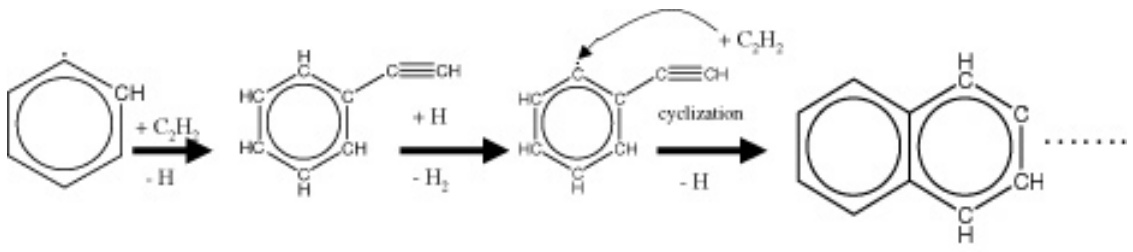

Figure 5.11: HACA mechanism scheme.

Aromatic growth

A general agreement has been reached on the PAH growth via the HACA model, an H-abstraction and C_2H_2 addition process, first introduced by Frenklach and Wang in 1991 [200]. A strong acetylene concentration is observed in soot formation zones, making it the main species taken into account in all aromatic growth models. The two-step HACA mechanism is also supported by several experimental studies in shock tubes [196, 201, 202], in which the H-abstraction has been observed as followed:

First, a hydrogen atom is ripped of the PAH molecule surface by a gaseous hydrogen atom:

$$A_i + H \leftrightarrow A_{i-} + H_2$$

with A_i a peri-condensed i-cycles aromatic, in which two cycles have exactly either zero or two common atoms, and A_{i-} the corresponding radical. Next, the second step concerns the acetylene addition with the present radical:

$$A_{i-} + C_2H_2 \leftrightarrow A_iC_2H_2.$$

When the pressure and the molecule size increase, a second reaction intervenes:

$$H + A_{i-} \rightarrow A_i$$

The acetylene addition is extremely reversible, and it is only with the formation of very stable aromatics, called stabilomers, that the reaction will become irreversible. The HACA mechanism is then based on a thermodynamic and kinetic pairing, the most likely pathway being the one with the weakest thermodynamic resistance. Finally, when the stabilomer, controlled by kinetic, is formed, the aromatic growths through the reaction:

$$A_iC_2H_2 + C_2H_2 \rightarrow A_{i+1} + H.$$

Surface migration

Theoretical chemical pathways have been highlighted in 1998 [203], that may double the PAH cycle rate, mostly at high temperature [190]. This is due to hydrogen migration on carbon structures, see Fig. 5.12. The 5-carbon cycle migration due to hydrogen atom travel, shown Fig 5.13, has important consequences on soot growth. Indeed, as soon as the 5-carbon cycle meets a 6-carbon cycle, it promotes the structure cyclisation.

Figure 5.12: Surface migration on a 5-carbon aromatic cycle.

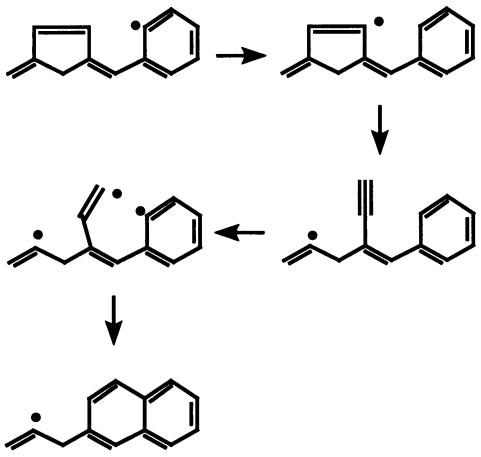

Figure 5.13: Reaction pathway of a 5-carbon cycle aromatic.

5.2.2.2 Nucleation

Nucleation is the transition phenomenon between the gaseous species and the solid soot, and one of the less understood soot evolution mechanism. Over the years, several models have tried to approach nucleation. The first kind considers the PAH growth until a given size for which the PAH shows condensed phase properties and is then considered as a soot [196]. This kind of model, only based on growth by chemical reaction, under predicts particle sizes.

A second type of nucleation model, first introduced by Frenklach *et al.*in 1994 [204], and mainly used today in soot modeling, is based on chemical reaction and molecular growth. In this scenario, PAH collide with other PAH when they grow up to a certain size. The impact of two PAH creates a dimer, and when those dimers collide between themselves, trimers are created and so on until PAH clusters are formed. In this model, the limit between gaseous species and soot is fixed at the PAH dimers, as shown Fig. 5.14. Chemical and molecular growth happen simultaneously, and this model also takes into account the condensation, i.e. the incrustation, of a dimer on a soot surface that then become more spherical.

The majority of nucleation models now uses the dimer description, either of a PAH set or the pyrene, an extremely stable species, from both thermodynamic and kinetic points of view. The validation of the dimer hypothesis can be found in several studies [205, 206].

5.2.2.3 Soot size growth

Soot particles are growing by collision with other particles and by mass adding through surface chemical reaction. It is a difficult task to propose a growth mechanism as the phenomena are complex and the species involved are plentiful. The main mechanisms found by experiment and modelled are described bellow.

Surface growth

After the primary soot particle formation comes the soot mass growth by surface carbon addition. This mechanism, first described with empirical approaches, has then been explained with the hypothesis of chemical similarity [200], in which the chemical reactions at the soot surface are similar to the ones one the gaseous PAH surface. Surface active sites are then associated to PAH ending C-H liaisons.

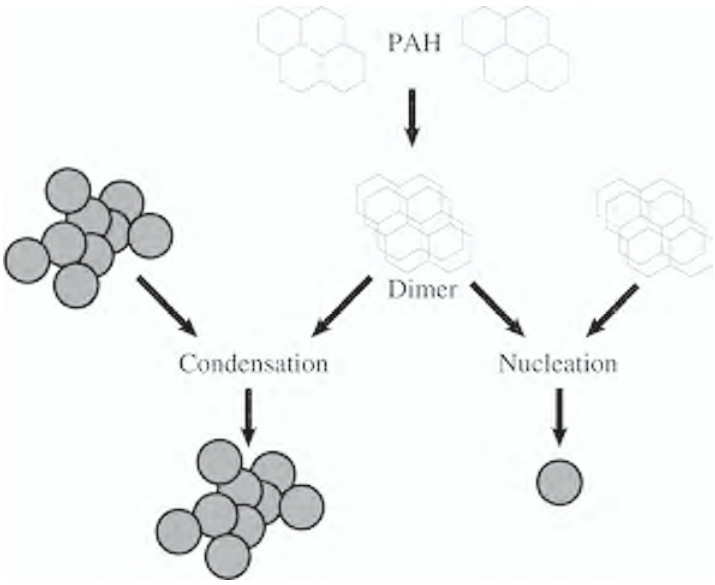

Figure 5.14: Dimer nucleation and condensation.

Those sites are then activated by the abstraction on a hydrogen atom. Experimental studies [207] demonstrated that the gaseous species mainly reacting with soot is acetylene, leading the community to consider the HACA model for surface growth, that has been validated for experimental premixed [208, 209, 210] and diffusive flames [211] and can be described as bellow:

$$\mathrm{C}_{soot}\text{ - H} + \mathrm{H} \leftrightarrow \mathrm{C}^{*}_{soot} + \mathrm{H}_2$$
$$\mathrm{C}^{*}_{soot} + \mathrm{H} \rightarrow \mathrm{C}_{soot}\text{ - H}$$
$$\mathrm{C}^{*}_{soot} + \mathrm{C}_2\mathrm{H}_2 \rightarrow \mathrm{C}_{soot}\text{ - H} + \mathrm{H}$$

with C_{soot} - H the localised surface active site and C^{*}_{soot} the corresponding radical.

One may note that in reality other gaseous species may participate to the surface growth.

In 2002, Frenklach [190] shows concerns about the hypothesis of chemical similarity that doesn't take into account the reactive sites influence in the surrounding area, changing the global kinetic of of the surface migration.

Site deactivation

Several studies [191, 207] have noted a decrease of soot surface growth rate during time. This phenomenon called "ageing surface" has several explanations supported by numerical studies of Frenklach *et al.*[200, 204]:

- A first hypothesis links ageing surface to hydrogen concentration fall, stopping the kinetic and reaching an equilibrium.
- The second one suggests a diminution of active sites, explained by surface migration. The 5-carbon cycle migration could left empty spot behind, therefore conducting to active sites deactivation .
- At last, the mass adding on the soot surface could also be responsible, but this phenomenon has not been modelled yet.

Coagulation

Coagulation is a mechanical phenomenon between soot particles, that must imperatively be modelled for accurate soot size prediction. Coagulation leads to soot size increase and soot number density decrease. Experiments by Haynes *et al.*[191] have shown that the newly formed soot particles by coagulation are first spherical and then evolve into aggregates. Two different mechanisms contribute to this evolution: The coalescence, describing two spherical particles merging into a bigger one, and the agglomeration, for bigger soot particles agglutinating and forming aggregates, represented Fig. 5.15.

The transition between these two mechanisms is not fully understood yet and several hypothesis have been made over the last decades: A first one suggests soot particles behave like liquid particles, the smaller ones merge and the bigger ones have insufficient merging rate, thus creating aggregates. Zhao *et al.*[212] have even showed experimentally that small soot particles act like liquid.

At last, Michel and Frenklach [213] proposed a second explanation. They saw through DNS studies that the spherical shape is caused by two factors: a fast surface increase and the size of colliding particles. If particles are too big, surface reactions are not fast enough for the particles to merge. The merging is then incomplete, causing aggregates. The spherical shape is then caused by a strong nucleation coupled with fast surface reaction. This study shows the critical importance of the simultaneity of all soot mechanisms: nucleation, surface reaction and agglomeration, that are usually separated in other soot formation scenarios. This simultaneity has then been confirmed by latest soot formation simulations [214] in agreement with the global evolution of experimental soot distribution. In terms of mathematical description, the Smoluchowski equations are used for coagulation, with a Knudsen dependant collision rate. Two opposite regimes can be distinguished, a first one called “free molecular", characterised by a Knudsen number Kn $>$ 1, corresponding to a pure coalescence regime, and a second one “continuous" with Kn $<<$ 1, corresponding to pure agglomeration. Models usually use only these two limit cases, whereas more complete descriptions like the one of Kazakov *et al.*[215] take into account the whole spectrum of Knudsen values with harmonic functions.

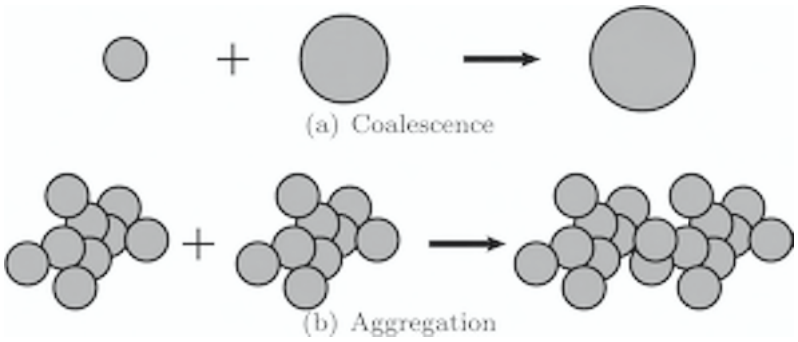

Figure 5.15: The two limit cases of coagulation.

The whole set of soot evolution mechanisms leads to a bimodal particle size distribution (PSD), observed in a vast majority of experiments, for example Zhao *et al.*[216] measured the PSD Fig. 5.16 at different burner distances. Several conclusions can be made: A first peak of small particles is observed whatever the position in the flame, and a second bigger size peak on the PSD is present in a higher position, this peak moves toward bigger sizes as the distance from the burner grows.

These two particle types differ not only with the size but also with the chemical and structural properties. The bimodal distribution aspect may be explained by the competition between nucleation and

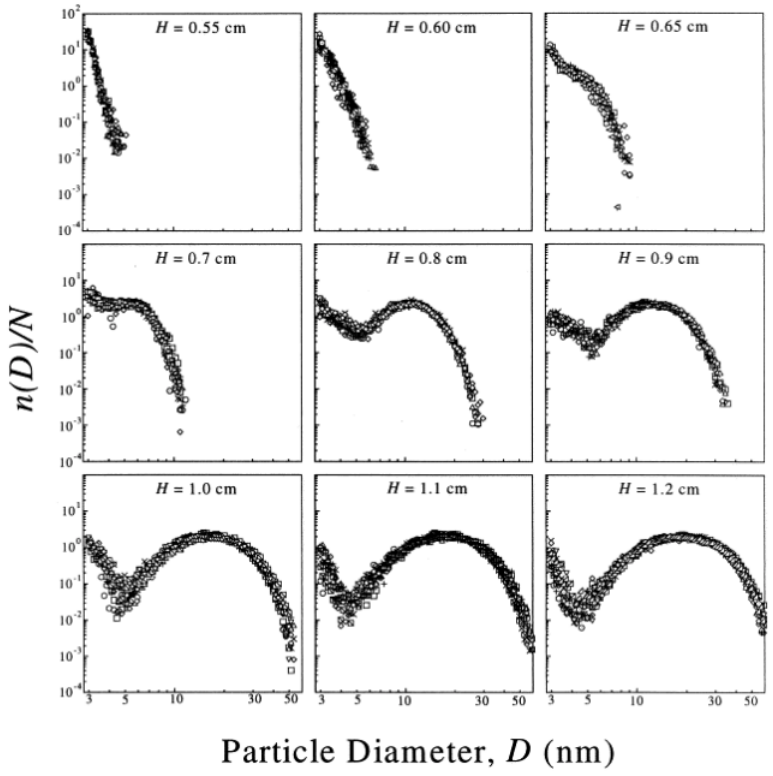

Figure 5.16: PSD variation at different distances H from the burner [216].

coagulation. Moreover, soot property studies like the one of Commodo *et al.*[217] show that the second peak appears not only by coagulation but also through surface reaction and condensation involving gaseous species.

In 2012, K. Zhou [218] proposed a qualitative explanation for the distribution bimodal property. At the flame base, only nucleation is involved, producing only one peak. Then, the particle number density decreases by condensation. Surface reactions increase the particle size moving the peak to larger sizes, where a concentration loss is observed. Meanwhile, nucleation still produces small particles so the first peak is still present, and as for the second peak, nucleation is largely balanced by coagulation between small and large particles.

5.2.2.4 Soot size reduction

Soot particles are also losing mass through two phenomena: Surface oxidation and large particle fragmentation into pieces.

Oxidation

Soot surfaces are mainly oxidised by hydroxy OH and oxygen O_2, following the reactions:

$$C^*_{soot} + O_2 \rightarrow \text{products}$$
$$C_{soot} - H + OH \rightarrow \text{products}$$

For hydroxy, the most common oxidation rate, from Neoh *et al.*[219], is based on a collision rate measured between OH and soot particles. As for oxygen, an oxidation model is proposed by Nagle et al [220], based on O_2 reaction with two types of active soot sites. A second one, the Kazakov model [221] sometimes preferred because of its simplicity, describes soot oxidation with O_2 and the radical C^*_{soot}.

Fragmentation

Soot fragmentation is more rare than oxidation. It has been observed for the first time in rich methane flame conditions by K. G. Neoh [222, 223], and in lean equivalent conditions by C.A. Echavarria [224] with a number density particle increasing observed. Neoh *et al.*[223] have then suggested fragmentation is caused by oxygen entering into the soot. The soot structure is first weakened by OH-oxidation and then cracked by oxygen entering which has a longer reaction time than hydroxy.

There are very few fragmentation models, one from Harris and Maricq [225], based on shearing and with good corresponding with experiment, another form Mueller *et al.* [226], based on oxygen entering the soot particle. This model follows a linear fragmentation rate with O_2 oxidation rate and it is matching with the flames studied by Neoh [222, 223].

Through several numerical studies, Mueller *et al.*[226] have made several conclusions: In lean premixed flames, a soot number density increase is observed due to fragmentation, whereas in rich flames, the soot number density remains constant because the lack of oxygen does not allow fragmentation. Moreover, in diffusion flames, fragmentation rate is two, even three times lower than in premixed flames. A possible explanation would be that in premixed flames soot coexists with oxygen while passing through hydroxy zones, whereas in diffusion flames, soot and oxygen are separated by a hydroxy zone, and once soot particles go through that zone being oxidized, there is no more aggregate to break in the oxygen zone.

5.2.3 Soot models

Soot model implementation must take into account couplings between soot formation and flow. Soot particles are transported and if there is turbulence, the impact won't be negligible. In 2007, Yoo *et al.*[227] have demonstrated with DNS simulations and a 2-equation soot model [228] that turbulence increases soot rate by increasing flame surface and diminishing soot growth because of the smaller soot time residency in hot zones where soot production is the most intense. Also, Olson *et al.*[229] made several correlations for the critical temperature for which the soot particles appear.

The first steps of soot formation necessitate a precise gaseous phase description of the involved species. The kinetic mechanism must be chosen carefully. Soot models to be designed for industrial aircraft chamber simulations must take into account the combustion regime influence, partially premixed and highly turbulent. Regarding those difficulties, the community have elaborated many strategies to implement soot in the CFD field.

Soot models have been classified in three categories by Kennedy (1997) [23]:

- Empirical models, based only on experimental data.
- Semi-empirical models, coupling mathematical description of soot with empirical parameters.
- Detailed models, seeking to solve the reaction equations leading to soot formation.

5.2.3.1 Empirical models

These models are the most simple and the less expensive to implement. They are widely used in aircraft and automobile industries. These models are based on experimental configurations and validated on configurations closed to the initial ones used for calibration. These models do not take into account the fundamental phenomena that govern soot formation and reduction, so they cannot be used on other configurations and are not predictive.

An example is the model of Khan *et al.*[230], widely represented in the literature, for diesel soot emission. The formation rate depends on the pressure P_u, the temperature T_u and the equivalent ratio χ of the studied case under the relation:

$$\frac{dC_s}{dt} = c\frac{V_u}{V_{NTP}} P_u \chi^n exp\Big(\frac{-E}{RT_u}\Big) \tag{5.5}$$

with C_s the motor load ($kg \cdot m^{-3}$), the other parameters being empirical values of the studied case.

In the aircraft field, we can find a more complete model, of Edelman and Harsha [231], which includes soot oxidation. This model has been used for chamber simulation [232] with a similar relation than the one of Khan, but with a second negative term for soot oxidation.

Empirical models are coupled with CFD through the temperature and the equivalence ratio without taking account the fluctuations, and give soot quantities with no information on the particle size distribution (PSD).

5.2.3.2 Semi-empirical models

Usually, semi-empirical models are composed of two transport equations coupled with empirical parameters. These models do not have information on PSD or collision. Similar to empirical models, they cannot be generalised for other fuels or other conditions.

Among them, the most complete model in term of formation mechanisms taken into account is the Leung model [228], also easy to implement. This model transports two variables: the particle number density and the soot mass fraction. The C_2H_2 species is used as a precursor, and the soot formation is described by inception through reaction (5.6) and surface growth by C_2H_2 condensation on the soot surface by the reaction (5.7).

$$C_2H_2 \rightarrow 2\ C(s) + H_2 \tag{5.6}$$

$$C_2H_2 + n\ C(s) \rightarrow (n+2)\ C(s) + H_2 \tag{5.7}$$

The reaction constants are empirical, and different hypothesis are made like the soot sphericity and the exclusion of surface ageing.

5.2.3.3 Detailed models

The complete description of PAH kinetic and soot growth is still mandatory for model generalisation. Detailed models have then been constructed to be applied in any configuration in which the main phenomena occurs: fuel pyrolysis, nucleation, surface growth, coagulation and oxidation. Statistical methods have a great success in the literature in the attempt of modelling soot formation and evolution. They are used to obtain the number density function (NDF), in order to get the soot volume fraction and agglomeration

properties. Two methods have been used to estimate the NDF: Monte Carlo models or discrete sections models that can give an approximate shape of the NDF, and moment method with mean quantities prediction.

Direct methods

Monte Carlo simulations are based on random stochastic particle evolution generations, allowing for a very precise prediction of the NDF. Unfortunately, the cost is high so it is impossible to apply those simulations to an industrial configuration. Usually, those simulations are used to validate other models.

The second main method is based on discrete sections: the group of soot particles is represented by an aerosol distribution divided into several finite elements. Each set of particles in each finite element of the discretised NDF is solved, so the NDF can be approximate with a good precision. However, these methods are still expensive and generally applied only to 1D cases.

Method of moments

In order to have a close prediction of the NDF, the method of moments has also been used. It was introduced by Hulbert and Katz [233] for soot formation. Here, the resolution of mean quantities allows a good coupling with CFD. Moreover this method uses less variables than direct methods, making it cheaper. In detail, we start from the population balance equation (PBE) [234] describing the evolution of a given soot particle set.

$$\frac{\partial \mathrm{M}_{x,y}}{\partial t} + \nabla \cdot (u\overrightarrow{\mathrm{M}_{x,y}}) = \dot{\mathrm{M}}_{x,y} \tag{5.8}$$

with $\mathrm{M}_{x,y}$ the soot bivariant moment (by unity of density) expressed as:

$$\mathrm{M}_{x,y} = \sum_j \mathrm{V}_j^x \mathrm{S}_j^y \mathrm{N}_j \tag{5.9}$$

V_j being the volume variable, S_j the surface variable and N_j the j class probability density (with j= 1 or 2 depending on the mode).

The drawback of this method is that the source terms need another moments to be closed. Several closure models were introduced, among which the Direct Quadrature Method of Moments (DQMOM) [235], which shows good estimations with a NDF approximated by a multidimensional Dirac sum, but causing numerical difficulties with the associated matrix inversion.

Another closing model, the Method of Moments with Interpolative Closure (MOMIC), uses a logarithmic polynomial interpolation for closure, it is simple to implement but does not retrieve the bimodality of the PSD.

One last example would be the hybrid method of moment (HMOM) [236] that combine the two closure methods above. Here the mean quantities are predicted as well as with DQMOM and the bimodality of the PSD is retrieved. Numerically, HMOM is more robust than DQMOM because even if the closure is made by a polynomial interpolation, a Dirac function is added in order to capture the first nucleation size.

$$\mathrm{M}_{x,y}^{\mathrm{HMOM}} = \mathrm{N}_o \mathrm{V}_o^x \mathrm{S}_o^y + \exp\Big(\sum_{r=0}^{R}\sum_{k=0}^{r} a_{r,k} x^k y^{r-k}\Big) \tag{5.10}$$

with N_o the Dirac function weight, V_o and S_o the fixed volumes and surfaces of the first nucleation size.

Mueller *et al.* [236] have validated this model on Monte Carlo simulations for premixed and diffusion flames. Moreover, the two expected particle sizes are predicted, see Fig. 5.17.

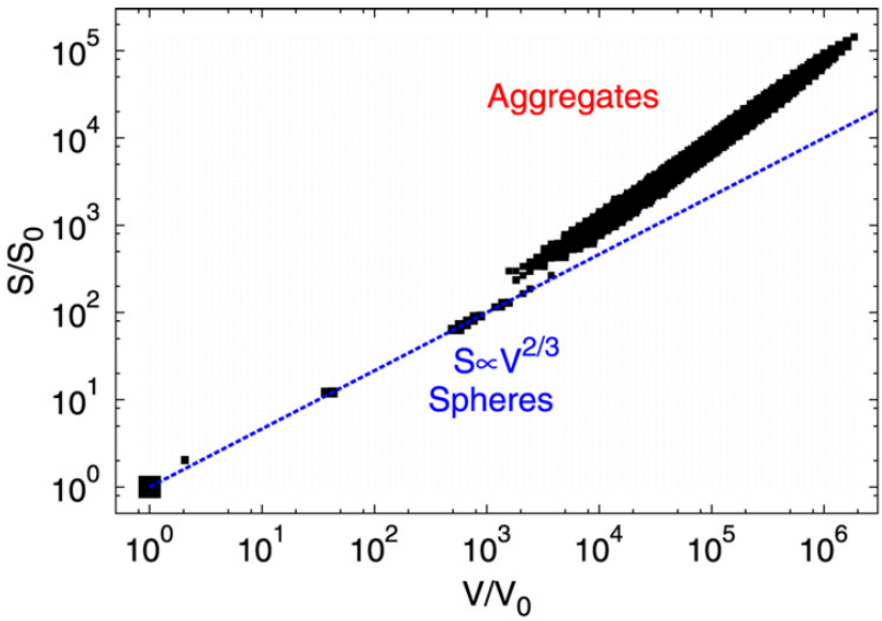

Figure 5.17: Bimodal particle size distribution retrieved by HMOM, with symbols size proportional to the number of particles with the same size [236].

5.2.4 The hybrid stochastic/ fixed sectional method (HYPE)

The HYPE method [182] is a new approach (2019) which combines a Monte Carlo description and fixed-sectional methods. The method is based on a fixed number of stochastic particles and sections, with a numerical algorithm organised to minimise discretisation errors even for a moderate number of stochastic particles and sections.

It relies on the resolution of the particle size distribution (PSD) $n(v;\underline{x},t)$, number of particles of characteristic size v (in terms of volume or mass, v is a continuous independent variable), per unit of flow volume and per unit of characteristic size of an aerosol submitted to simultaneous nucleation, surface variation and agglomeration. It is governed by a Population Balance Equation (PBE) [237]:

$$\frac{\partial n(v;\underline{x},t)}{\partial t} + \mathbf{u}\cdot\nabla n(v;\underline{x},t) + \frac{\partial}{\partial v}\left[G(v)n(v;\underline{x},t)\right] = \dot{h}(v_o;\underline{x},t) \tag{5.11}$$
$$+\frac{1}{2}\int_0^v \beta(v-\bar{v},\bar{v})n(v-\bar{v};\underline{x},t)n(\bar{v};\underline{x},t)d\bar{v} - n(v;\underline{x},t)\int_0^\infty \beta(v,\bar{v})n(\bar{v};\underline{x},t)d\bar{v}\,,$$

where usual notations are adopted. $G(v) > 0$ is the surface growth rate or $G(v) < 0$ the surface loss rate. $\dot{h}(v_o) > 0$ is the nucleation rate or $\dot{h}(v_o) < 0$ the disappearance rate, seen at size v_o. The integral source term on the RHS accounts for agglomeration following the continuous counterpart of Smoluchowski equation, with $\beta(v, \bar{v})$ the collision kernel for two particles of volume v and $\bar{v}$.

A summary of the method is presented on flowchart 5.18,

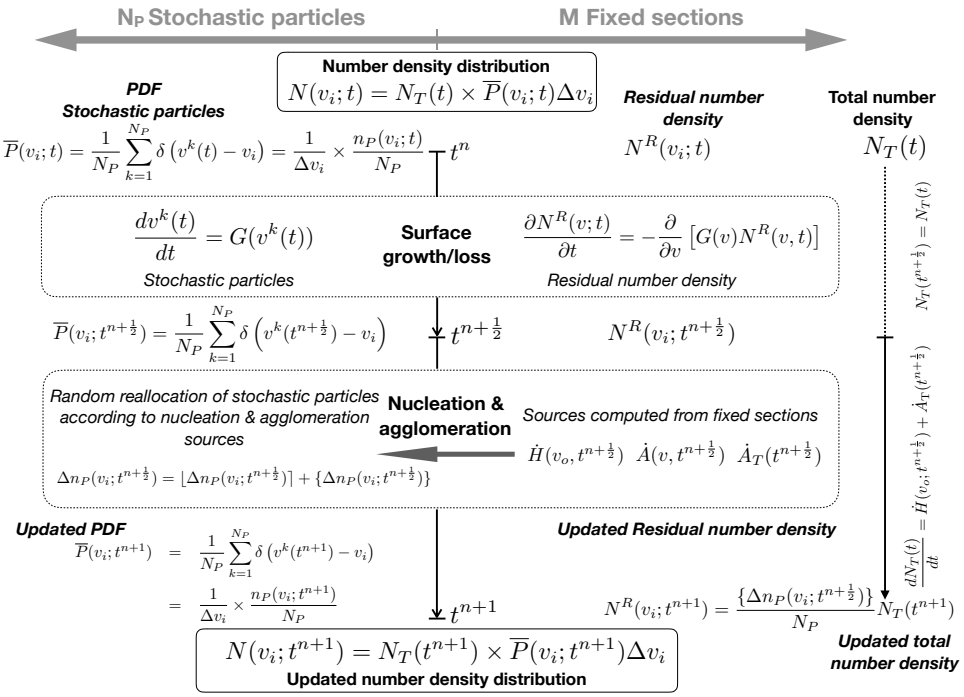

Figure 5.18: HYPE flowchart. [182].

In recent simulations of a one-dimensional laminar sooting flame [238], the hybrid stochastic/fixed-sectional method allowed for analysing the relation between the mobility diameter, measured in the experiments, and the equivalent sphere diameter, introduced in the modelling. The influence of the fractal particle shape on the simulated particle size distribution was also explored. This method offers interesting PSD predictions but unfortunately, the CPU time required jeopardises the application to three-dimensional unsteady simulations of real combustion chambers.

Chapter 6

Soot prediction in a real combustion chamber

Contents

In this final chapter, a strategy is proposed to predict a soot size distribution in the large eddy simulation of a turbulent flame. It relies on neural networks, applied to replace the HYPE complete soot solving. First, this strategy is successfully tested on a well known 1D premixed sooted flame. The CPU cost is discussed for further applications. The HYPE solving is next coupled with the ORCh 0D canonical problem for turbulent combustion. This coupling allows to obtain a dense database. A neural network is then trained with this database, network that will be used for the Mermose 3D LES. Eventually, the obtained soot description is discussed and compared to experiment.

6.1 Strategy for reduction model

The HYPE model has been found interesting for the prediction of particle size distributions [238]. Nevertheless, the complexity and the cost of this hybrid method make it unsuitable for complex applications. Consequently, we now present a model reduction strategy based on neural networks, with three goals:

- Keeping the same predictions level as the HYPE solving.
- Reducing the computational cost to make it suitable for 3D LES simulations.
- Lowering the implementation complexity by getting rid of stochastic particles and growth/loss soot phenomena modelling.

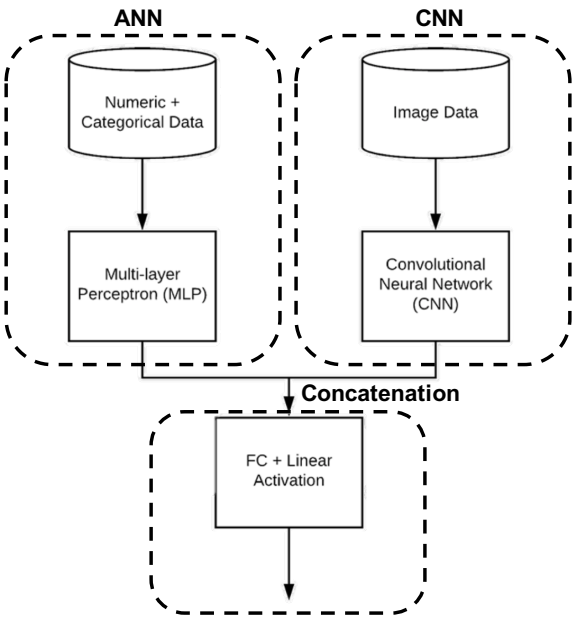

Figure 6.1: Example of a functional API used here with two sub-models.

In order to do so, the HYPE solving simulations are considered as training databases, and an adequate neural network architecture must be found to retrieve the whole complexity of soot formation.

For complex problems, sequential neural networks such as the ones presented in section 3.2.1 are mostly not sufficient. So this time, we use the open source neural network library Keras (https://keras.io/) based on Tensorflow, allowing to code complex neural networks in a very efficient way.

The architecture employed here is a functional API, see Fig. 6.1 , where each input series can be handled by a separate neural network and the output of each of these sub-models can be combined before a prediction is made for the output sequence. We can refer to this as a multi-headed NN model. It may offer more flexibility or better performance depending on the specifics of the problem that is being modelled. For example, it allows to configure each sub-model differently for each input series, such as the number of filter maps and the kernel size. The elaboration of this architecture has been done with the following 1D application.

6.2 1D application

6.2.1 Test case

In order to elaborate the neural network architecture, a first test case is considered. It is a one-dimensional fuel-rich (equivalence ratio $\phi = 2.07$) laminar premixed ethylene-argon-oxygen flame from the literature [216] at ambient pressure. The velocity, temperature and mole fractions in the fresh gases are 8.26 cm/s, 300 K, $X_{C_2H_4} = 0.133$, $X_{O_2} = 0.193$ and $X_{Ar} = 0.674$, respectively. Particles size distributions measurements were obtained with SMPS based measures along the flame central axis, see Fig. 6.2.

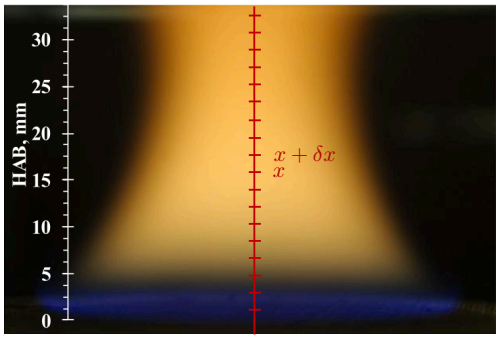

Figure 6.2: Flame from Zhao et al. [216]

This test case was investigated with the HYPE methodology, expanded in [238], in which the soot distribution was accurately reproduced. In order to do so, the one dimensional flame was solved with the 101-species kinetic scheme from Appel *et al.* [239] with the measured temperature profile imposed, using CANTERA. Figure 6.3 represents the main species mass fraction along with the PAH mass fraction. The soot phase is coupled with the gaseous phase through the pyrene species.

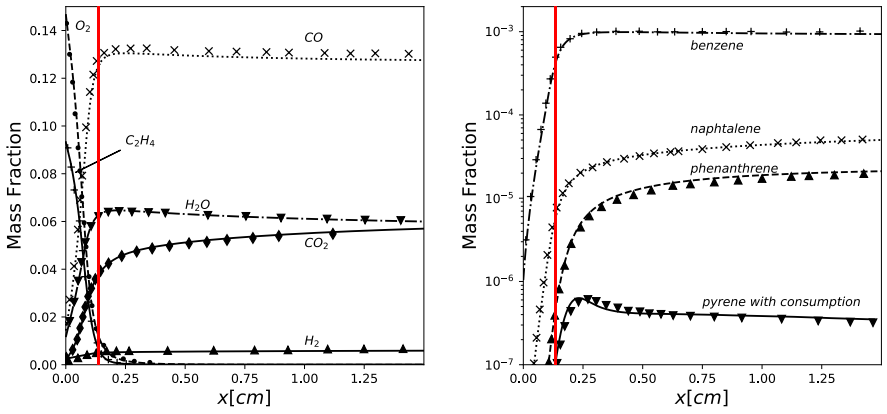

Figure 6.3: Main species and PAH species. Symbols: Reference from Zhao *et al.* [216], lines: CANTERA simulation from A. Bouaniche [238]. Vertical red line: Maximum heat release rate. In the next figures representing soot density, a shift by +0.25 cm of the computational distance above the burner is added, to account for the probe cooling effect.

The problem begin stationary, the flame space domain is changed into a residency time through:

$$\tau(x) = \int_0^x \frac{1}{u\left(x^+\right)} dx^+,$$

with u the velocity distribution.

In this chapter, we are working with the integral form of the equation 5.11, that reads:

$$u\frac{dN_i(x)}{dx} = \frac{dN_i(x(\tau))}{d\tau} = \int_{I_{v_i}} \left(-\frac{\partial}{\partial v^*} \left[G\left(v^*\right) n\left(v^*; x(\tau), \tau\right) \right] + \dot{A}\left(v^*; x(\tau)\right) \right) dv^* \tag{6.1}$$

with G the surface growth/loss rate, A the agglomeration source and where the particle size space is discretised in M sections of characteristic volume v_i, representative of the mass in the i-th section $I_{v_i} \equiv [v_i^{inf}, v_i^{sup}]$. The employed grid is geometric:

$$v_i^{inf} = v_o F_s^i,$$

with $F_s = 1.5$. The corresponding mean primary soot diameter in the first section is equal to d_0 = 0.87 nm.

The HYPE time step "δt_H" is determined to secure the stability of the method, the thermochemical properties are interpolated. The PSD initialisation in HYPE is done with a density of 1 [cm-3] for the first section in which all the stochastic particles are concentrated and 0 [cm-3] for the other sections.

Once the HYPE solving done, a large database becomes available, with a PSD $\underline{N}$ at every "x" location .This database can be used to train the neural network, so it can predict the PSD evolution at "$x+\delta x$" from the one at "x", coupled with the thermochemical parameters controlling the soot modeling at "x".

6.2.2 Neural network architecture

The neural network used for PSD prediction, represented by Fig. 6.4 is described as followed.

The neural network $\mathcal{F}$ is a combination of an artificial neural network (ANN), and a convolutional neural network (CNN), see Fig. 6.4.

- The ANN tracks the evolution of the thermochemical parameters $\underline{\phi}(\underline{x}, t)$ controlling the soot modelling, namely the temperature T(K), the C_2H_2, O_2, OH and pyrene $C_{16}H_{10}$ mass fraction. These quantities having very different scales, we chose to normalize them by their maximum value. Then, they enter a recurrent long short-term memory neural layer (LSTM) composed of 100 neurones, to which a 60-neurones layer is connected. This ANN features feedback connections, meaning it keeps track of time history of the thermochemical evolution.

- The CNN is trained from the time PSD shape. It offers the possibility of analyzing in a single inference the full PSD profile in size space. In this so-called "image segmentation" approach, the input line is seen as a whole while the output classifies each pixel, thus preserving the locality of the information. The CNN input is thus composed of the one-dimensional PSD profiles $\underline{N}(\underline{x}, t)$.

  Because of large scale differences of the PSD over the flame, the difficulty of the problem being modelled is significantly increased. An inputs standardisation solution is applied as followed:

  $$\underline{N}_{standardised}(x) = \frac{\underline{N}(x) - mean(N))}{std(N)}$$

  with "x" the flow position on the flame central axis and

  $$mean(N) = \frac{1}{M}\frac{1}{x_{tot}} \sum_{i=1}^{M} \sum_{x=x_{init}}^{x_{tot}} N_i(x),$$

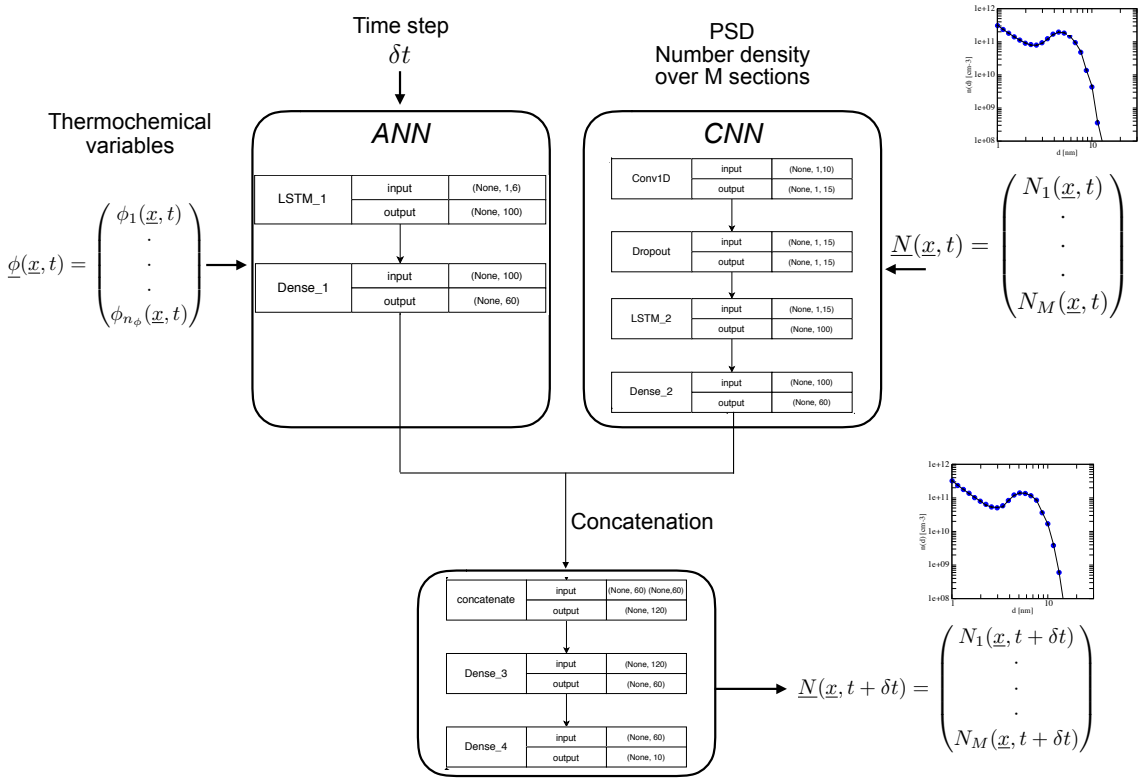

Figure 6.4: Architecture of the employed neural network. Example with a PSD of $M = 10$ sections.

$$std(N) = \frac{1}{M}\frac{1}{x_{tot}}\sum_{i=1}^{M}\sum_{x=x_{init}}^{x_{tot}}(N_i(x) - mean(N))^2$$

before being fed in the CNN. It allows to reduce the database range, for example from the database presented Fig. 6.5(a) to the standardised one presented Fig. 6.5(b).

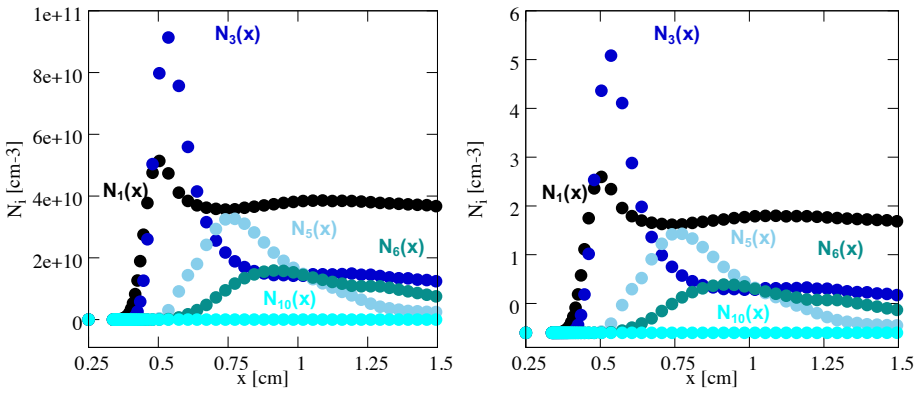

(a) Database (b) Standardised database

Figure 6.5: Standardisation of the database before entering the CNN. Example with a PSD discretised into $M = 10$ sections, among which 5 are presented. PSD mean diameters d_1 = 0.87 nm , d_3 = 2.02 nm , d_5 = 4.66 nm, d_6 = 7.08 nm , d_{10} = 37.63 nm.

Next the inputs go through 15 convolutional filters layers, a dropout of 10% is applied, and a 100-neurone LSTM layer is connected to a 60-neurone dense layer, also to keep track of the PSD time history.

- The 60 neurones of each branch are then concatenated, leading to a 120-neurone layer. Finally two dense connected layers make the final prediction of the M sections at the following time.

6.2.3 Neural network training

The architecture described in section 6.2.2 is next trained using randomly selected 80% of the x-series data, with an adam optimizer and a loss function based on mean absolute percentage error. The 20% remaining data are used for neural network testing. At each epoch, the loss function of the trained and the tested data is plotted, see for example the ones of the 30-section training Fig. 6.25(a), and the predicted values are directly plotted against target ones, see Fig. 6.6(b), 6.6(c). Figure 6.25(a) shows the error going down and stabilising for both train and test dataset up to less than 10% of mean error, after 1500 epochs. A total of 100 000 elements composes this database.

The time step variation of the training database is represented Fig. 6.7 with a mean of 1.03e-5 s and a variance of 1.66e-5 s.

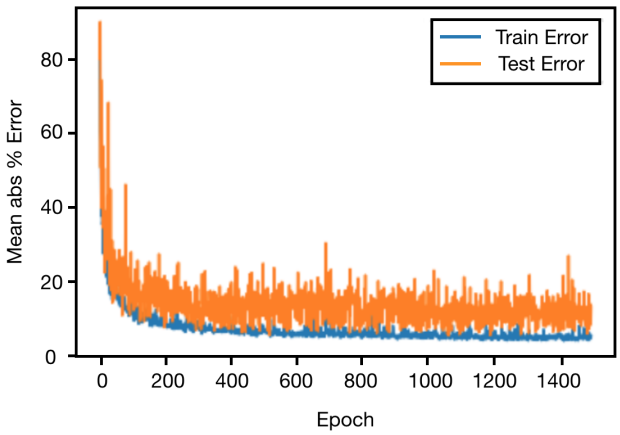

(a) Loss function evolution

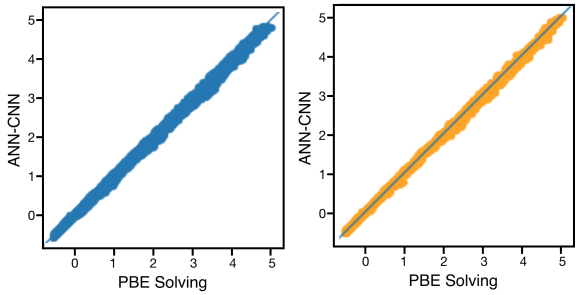

(b) Train prediction (c) Test prediction

Figure 6.6: Training neural network results with trained (orange) and tested (blue) predictions at each epoch.

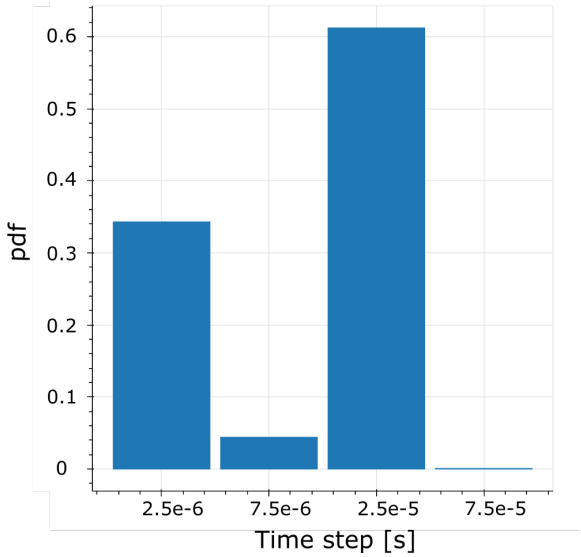

Figure 6.7: Database time step variation used for training, in second.

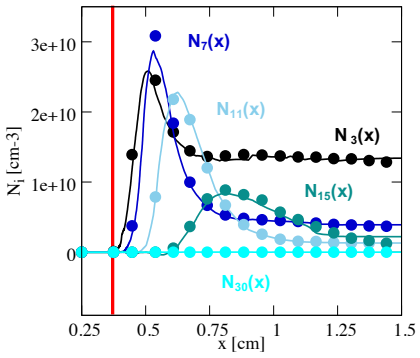

Figure 6.8: Particle Size Distribution evolution in the central flame axis for different i-th fixed-section of mean diameters d_3 = 1.15 nm , d_7 = 1.97 nm , d_{11} = 3.3 nm, d_{15} = 5.82 nm , d_{30} = 44.22 nm . Symbols: HYPE simulation with 1000 stochastic particles and 30 sections.Solid line: Neural network prediction. Vertical red bar: Maximum heat release rate.

6.2.4 Neural network validated with a 30 sections-discretised PSD

Once the neural network is fully trained, its prediction can replace the right side of the PBE 6.1 such as:

$$\frac{dN_i(x(\tau))}{d\tau} = \dot{\Omega}_i(x(\tau)) \tag{6.2}$$

with

$$\dot{\Omega}_i(x(\tau)) = \frac{(\mathcal{F}[\phi(\tau), \underline{N}(x(\tau)), \delta t_H] - N_i(x(\tau)))}{\delta t_H}$$

$\mathcal{F}$ being the neural network and $\phi(\tau) = [\delta t_H, Y_{C_{16}H_{10}}, Y_{C_2H_2}, Y_{O_2}, Y_{OH}, T]$ the ANN inputs. The temporal integration of the PBE 6.2.4 is then done with a third order Runge-Kutta method [240] through:

$$\begin{cases} N_i(x(\tau')) = N_i(x(\tau)) + \frac{8}{15} \cdot \delta\tau \cdot \dot{\Omega}_i(x(\tau)) \\ N_i(x(\tau'')) = N_i(x(\tau)) + 0.25 \cdot \delta\tau \cdot \dot{\Omega}_i(x(\tau)) \\ N_i(x(\tau''')) = N_i(x(\tau'')) + \frac{5}{12} \cdot \delta\tau \cdot \dot{\Omega}_i(x(\tau')) \\ N_i(x(\tau + \delta\tau)) = N_i(x(\tau'')) + 0.75 \cdot \delta\tau \cdot \dot{\Omega}_i(x(\tau''')) \end{cases}$$

As performed into the HYPE model, thermochemistry variables profiles are constant over time and the profile of the consumed pyrene from Fig. 6.3 is considered for neural network training and validation.

Figure 6.8 shows the results of the Runge-Kutta integration presented above, solved with the trained neural network over 30 sections. It represents the PSD integrals evolution on each size ranges along the x-abscissa, compared to the reference HYPE simulation with 30 sections. The evolution is well predicted for all ranges of size.

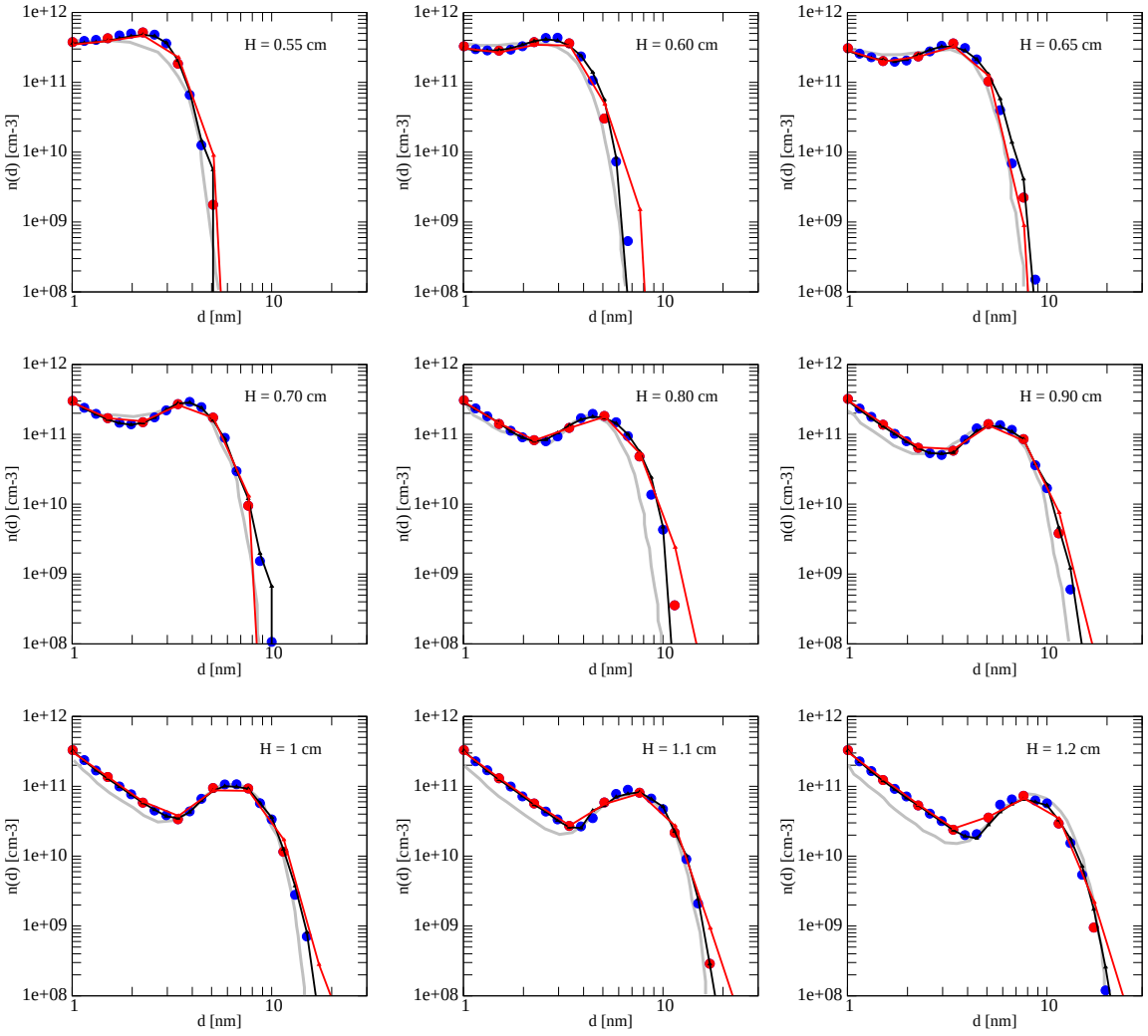

Figure 6.9: Particle Size Distribution for several heights above the burner. Symbols: HYPE simulation with 1000 stochastic particles and 30 sections. Black line: ANN-CNN prediction with 30 sections. Red line: ANN-CNN trained with 10 sections (red symbols). Grey line: Reference simulation from Zhao [216]

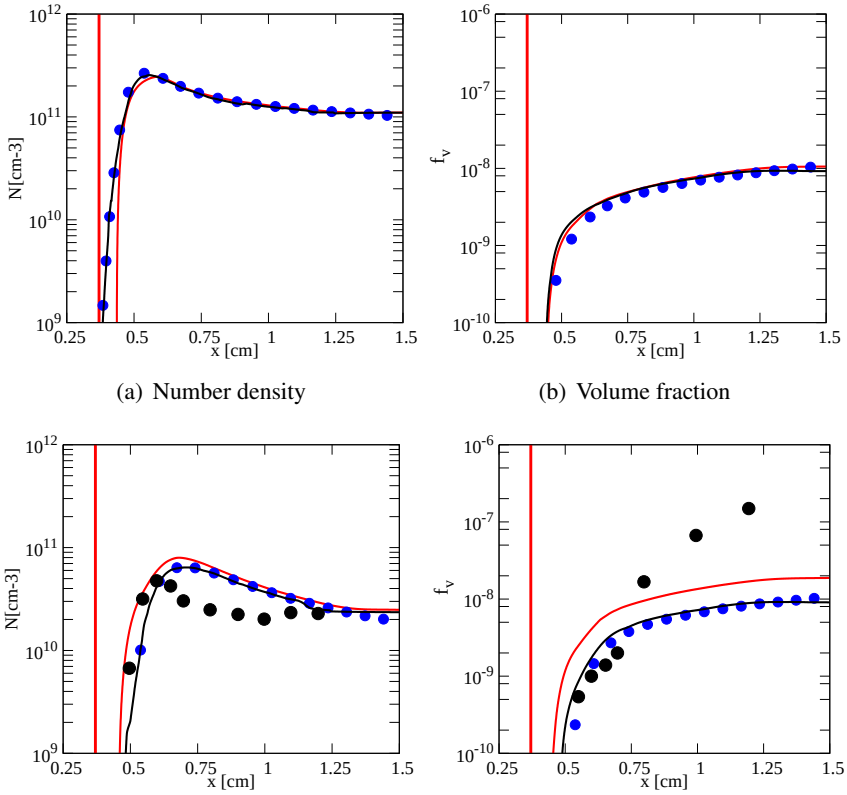

(a) Number density (b) Volume fraction

(c) Number density (diameter above 3nm) (d) Volume fraction (diameter above 3nm)

Figure 6.10: Soot number density and volume fraction vs height above burner. Blue-symbols: HYPE simulation with 1000 stochastic particles and 10 sections. Solid line: ANN-CNN prediction with (black) 30 sections and (red) 10 sections used for training. (c) and (d) Black-symbols: experiments . [216]. Vertical red bar: Maximum heat release rate.

Methods	**CPU cost [s]**
Sectional 30 sections	81.764
HYPE 30 sections	100.581
Neural network trained with 30 sections	18.014
Neural network trained with 10 sections	16.602

Table 6.1: Cost of the different soot methods to predict a 30-sectional PSD over the present 1D flame test case.

Figure 6.9 represents the PSD evolution n(d) = = $\frac{dN}{dlog(d)} = \frac{Nv}{(log(d_{Sup})-log(d_{Inf}))}$ against the soot diameter size for several heights above the burner, for which the neural prediction fits well the HYPE solving with 30 sections (black) with 5 % of mean error, and the reference stochastic simulation from Zhao [216] (grey). A second training and validation is also done with a coarse PSD discretisation of 10 sections (red) built from the reference HYPE solving. The neural network also shows predictions with a mean error of 64 % compared to the reference HYPE solving, allowing to describe this particle size distribution with only 10 integrals. This behaviour is also retrieved for the total soot number density 6.10(a) and soot volume fraction 6.10(b) plotted for all soot diameter.

Then, in order to directly compare with experimental datas, only soot sizes above 3 nm must be considered as it is the limit size detected in the experimental studies [216], like it was done in A. Bouaniche

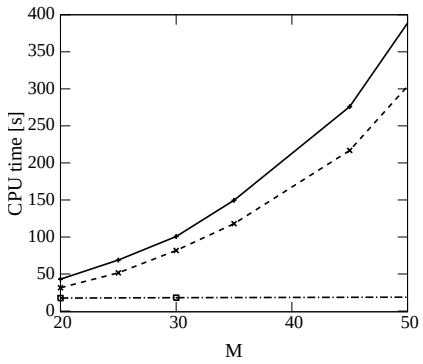

Figure 6.11: Normalised CPU cost as a function of the number of sections M. Dashed line: Sectional method. Solid line: Hybrid method. Dash dotted line: Neural network method.

analysis [238]. The comparison versus experiment is shown Fig. 6.10(d), 6.10(c) with an accurate prediction for the ANN-CNN trained with the reference HYPE database, showing a mean error of 20 % compared to the HYPE reference, and an over prediction (mean error of 86 % compared to the HYPE reference) observed for the ANN-CNN trained with the coarse 10 sections, that can be linked to the over-prediction of this coarse database on the bigger soot diameters on Fig. 6.9.

When comparing the cost of the neural network-PBE solving against the HYPE solving and an equivalent 2-point upwind sectional method, we can see from table 6.1 that not only the cost is is divided by a factor 10 with the neural network approach, but also that the neural network CPU solving poorly increases with the section number, presented Fig. 6.11.

6.3 Implementation of a soot model into a reduced kinetic mechanism

In this section, we describe the coupling between ORCh, allowing a significantly reduced finite rate chemistry description, and HYPE, providing detailed soot population evolution. The final objective is to create a precise and affordable kerosene-based kinetic mechanism with soot description.

6.3.1 Soot and gas phase coupling

The earlier mentioned ORCh stochastic configuration seems adequate to allow an implementation of HYPE, as both configurations use stochastic methods to model fluid and soots.

The link between the gas phase and soot production goes through the pyrene density, as the nucleation model chosen in HYPE is based on pyrene dimerisation. The pyrene species is consumed by HYPE simulation, giving birth to the first soot particles.

It is then critical to use a detailed enough kinetic mechanism, at least with a PAH formation mechanism that forms the pyrene species. A study from Doute *et al.* [241] compared kerosene flames to pure N-decane flames and showed how it is inevitable to take into account the fuel aromatic part for soot formation, as it leads to PAH creation.

That is why we chose the PAH growth mechanism of Wang [242], based on the same light species oxidation mechanism coupled to the pyrolysis part of HyChem [243]. In this mechanism, PAH species grow until coronene, see Fig 6.12.

Several reasons motivated our choice. First, as HyChem is mono-component fuel, it allows to go further in the ORCh reduction strategy. Indeed, a multi-component surrogate reduction imposes to keep

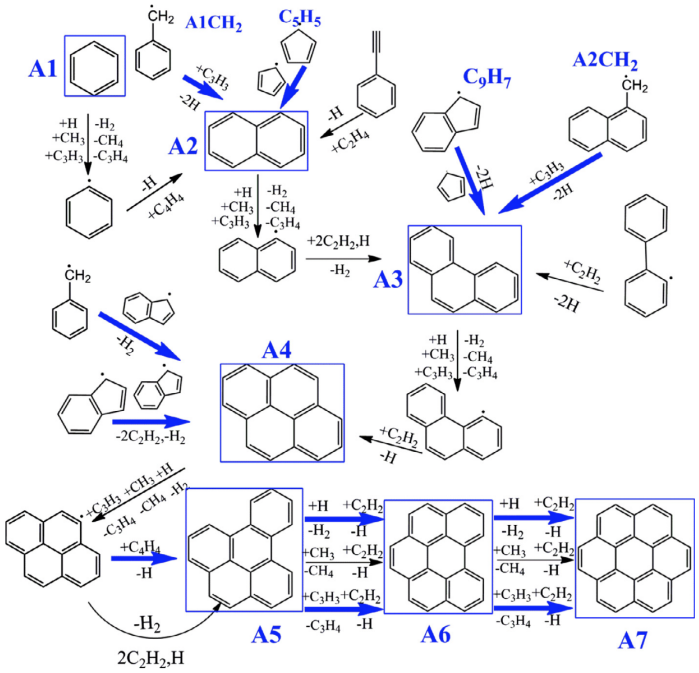

Figure 6.12: Kinetic pathways from benzene to coronene (A7) for fuel mixtures. A1: benzene, A2: naphthalene, A3: phenanthrene, A4: pyrene, A5: benzo[e]pyrene, A6: benzo[ghi]pyrene, A7: coronene. [242].

much more species for a sufficiently described oxidation. Moreover, a study from T. Zhang *et al.* [244] which compared HyChem with the 4-component fuel MURIA [245] for soot prediction, showed similar results, confirming the potential of HyChem. A second argument for the use of HyChem is the lack of validation studies on multi-component kerosene-based surrogates for soot production. Most of the PAH growth mechanism validations are made on ethylene and methane flames. In our case, the PAH formation is independent of the fuel, and has been well validated on ethylene premixed and counterflow diffusion flames, ethylene which is the major light species obtained by pyrolysis with HyChem description.

6.3.2 Interaction between HYPE and the ORCh canonical configuration for turbulent combustion

In this section, we describe the coupling between ORCh and HYPE. The HYPE method is based on the transport of stochastic particles representing a set of real soot particles at different sizes, and the the ORCh canonical configuration for turbulent combustion relies on stochastic particles (called fluid particles starting from now to avoid any confusion) that are mixed and react together.

Here we couple these two codes by calculating a soot population evolution for each ORCh fluid particle that contain a pyrene density higher to a limit value, defined to obtain a reasonable large database. Each fluid particle reacts during a time step defined in ORCh, and the associated soot particle population is calculated during the same time step. Note that once a soot population is created, it will continue to react in this fluid particle until the end of the simulation. The implementation strategy is resumed Fig 6.13.

Concerning the impact of turbulence on soot, several studies report different soot production be-

haviours in turbulent flames compared to laminar flames [246, 247], that can be explained by the PAH gaseous species sensitivity to turbulent flow [248]. Morevover, F. Sewerin and S. Rigopoulos [249] showed the weak impact of turbulence on soot formation compared to gaseous species micro-mixing, confirming our decision to let solid particles not directly influenced by turbulence, but indirectly through the PAH precursors response to turbulence.

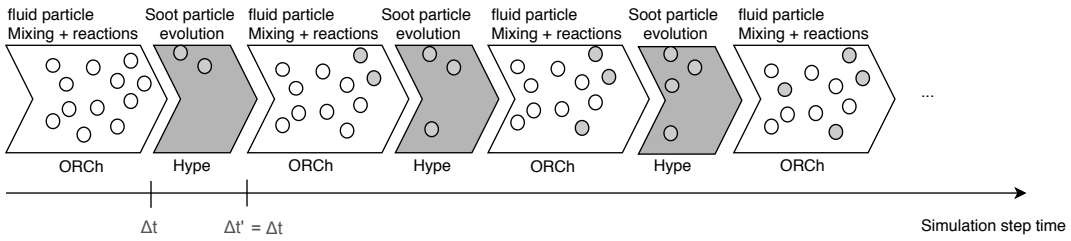

Figure 6.13: HYPE implementation strategy in ORCh. white circle : fluid particles, grey circle : fluid particle transporting a soot distribution. δt : ORCh time step, δt' : HYPE total time step we put equal to ORCh time step.

To conclude, the ORCh simulation allows the species density to evolve, including the pyrene species, which at each ORCh time step will be send to HYPE for soot population simulation calculation that will continue to evolve at the next ORCh time step. There is also a two-way coupling between gas and solid soots through the pyrene density. This strategy, named ORCHydS (for Optimised and Reduced Chemistry with HYbriD Soot description), will be applied for the soot prediction in the industrial Mermose configuration (see section 6.4.3).

6.4 Industrial application

6.4.1 The Mermose project

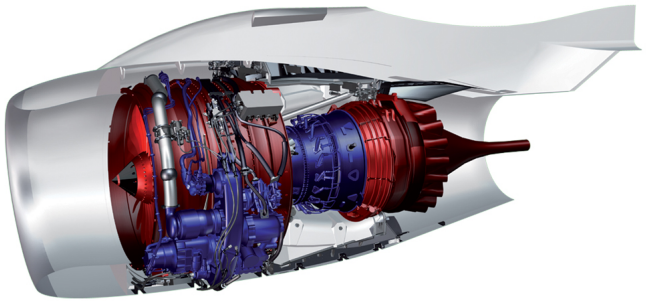

Figure 6.14: SaM146-1S17 turbofan, certified in 2010, based on RQL technology [250].

In the context of aircraft pollution reduction and soot prediction, the french DGAC founded several projects, among which MERMOSE, led by ONERA and Safran in 2013, aimed to provide a modern aircraft engine emission dataset. The goal was to completely characterise fine particles, first behind the SaM146 turbofan, see Fig. 6.14, from Safran Aircraft Engines, secondly in a representative tubular com-

bustor with the same injection system and the same air flow distribution. The combustor test estimated cruise emissions in real conditions, following a LTO cycle, see Fig. 6.15.

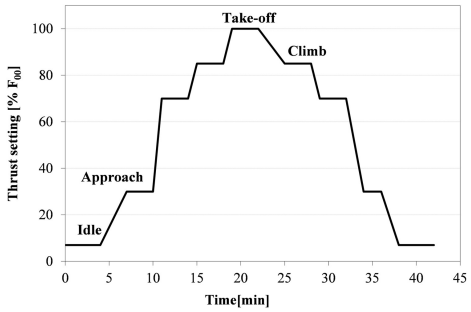

Figure 6.15: Typical engine cycle conducted during the first MERMOSE test campaign [250].

The probe used to collect soot in the tubular combustor campaign was made by Safran aircraft Engines, and is constituted of a tube of 6 mm inner diameter and several holes of 0.5 mm, cooled down by water. It is located right after the exit chamber. The particle size distribution, mass density and number density were measured at each operating point, respectively by intrusive SMPS and PPS methods. The CO_2 percentage of the gas was simultaneously quantified. We are here interested in one operating point, the climb of the LTO cycle, at 85 % thrust, at a pressure P = 18 bars, for which the mean primary particle diameter was found to be around 20 nm, see Fig. 6.16(a), and the mean particle diameter around 40 nm, with aggregates morphologies observed, see Fig. 6.16(b).

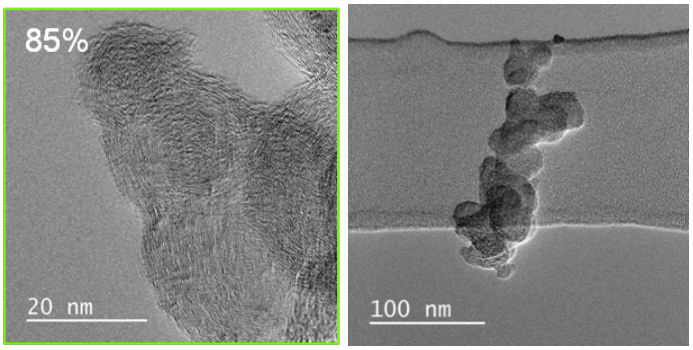

(a) Primary particle (b) Aggregate

Figure 6.16: Observation of soot particles at 85 % thrust of the tubular combustor campaign.

6.4.2 HyChem & PAH mechanism reduction

Choosing the PAH growth mechanism of Wang [242], coupled to the pyrolysis part of HyChem [243], conducts to a 203 species and 1358 mechanism, that must necessarily be reduced for the later 3D simulation of the Mermose combustor chamber.

The ORCh strategy described in Chapter 4 is once again applied in this section. This time the total number of stochastic particle is $N = 1414$ for the three inlets considered ($n_I = 3$). The first inlet is composed of the gaseous fuel at $T = 300$ K, representing 3% of the total mass flow rate. The second inlet, composed of air at $T = 734$ K, releases 80% of the air mass flow rate in the mixing, the rest being introduced progressively starting at 37% of the total time simulation as we are trying to be representative

of the air distribution in the chamber. The third inlet, injecting 40% of the mass flow rate, is composed of burnt gases at chemical equilibrium for the equivalence ratio of the engine, at $T = 1745$ K.

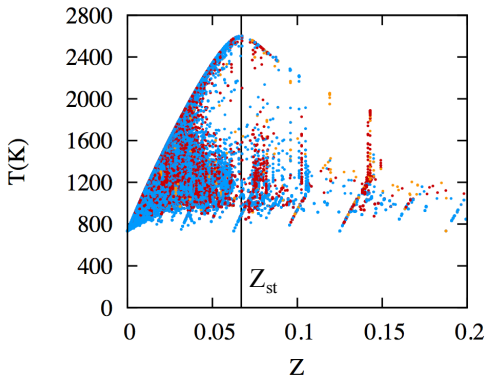

Figure 6.17: Scatter plot of stochastic particles temperature *vs* mixture fraction. Particles are coloured depending on their initial condition. Blue: air. Orange: kerosene. Red: burned gases. Z_{st} is the stoichiometric mixture fraction.

Figure 6.17 shows a representative scatter plot of the temperature of the gas phase particles, using the Curl model. A large range of equivalence ratios is observed, critical for the scheme reduction in this configuration.

For the reduction and optimisation steps, we chose to target the essential species involved in the HYPE soot production model, namely the pyrene $C_{16}H_{10}$ for nucleation, O_2 and OH for oxidation and C_2H_2 for soot mass adding, along with the main reactants, resumed in Table 6.2. By doing so, we obtain a “H" mechanism, composed of 32 transported species with 16 QSS species and 240 reactions, presented Table 6.3 . The still high number of transported species after reduction can be explained firstly because of the 8 additional pyrolyse species contained in the jet-A HyChem version, and secondly because of the pyrene. The kinetic pathways from Fig. 6.12 leading to pyrene shows numerous intermediate species, which must be conserved in order to obtain pyrene density, becoming the reduction limiting species in our case.

	$N_{species}$	$N_{reactions}$	N_{QSS}	**Targets**
Detailed HyChem with PAH	203	1358	–	fuel, T, O_2, OH
Reduced mechanism	32	240	16	C_2H_2, $C_{16}H_{10}$

Table 6.2: Reduction summary of the HyChem model coupled to Wang mechanism with PAH description.

Transported species	**Analytically resolved species**
N_2, H, O, OH, HO_2, H_2, H_2O, H_2O_2, O_2, CH_3, CH_4, CH_2O, CO, CO_2, C_2H_2, C_2H_4, C_2H_6, CH_2CO, C_3H_3, C_3H_6, i-C_4H_7, C_4H_8-1, i-C_4H_8, C_5H_4O, A1, $C_6H_5CH_3$, OC_6H_4O, A2R5, A3-4, A4, C_9H_7, POSF10325	A1CH_2O, CH_3O, HCO, C_2H_3, C_2H_5, A2R5-, A1-, CH_2CHO, CH_2, HCCO, C_6H_5O, C-C_5H_5, C_3H_5-A, C_9H_8, A1CHO, C_6H_4O

Table 6.3: **Mechanism H.** Species of the reduced mechanism composed of 32 transported species associated to 16 QSS relations and 240 reactions.

When tested back in the ORCh stochastic case after optimisation, the reduced H mechanism shows similar trajectories to the detailed HyChem mecanism, for the target species, see Fig. 6.18. It is noted

that the pyrene trajectory of the H mechanism Fig. 6.18(f), does not fit perfectly the HyChem trajectory, the observed error can be avoided by keeping 82 additional species in the reduced mechanism, which is not compatible with the following 3D LES solving. Moreover, the error observed on the pyrene density has been applied back in the trained neural network input of the 1D application of section 6.2, showing that a maximum error of 70 % and a mean error of 35 % on the pyrene involves a maximum error of 2 % on the total soot density prediction with a mean error of 0.13 %. The H mechanism is also able to predict the same flame speed and temperature of premixed flames at different ratio, see Fig. 6.19.

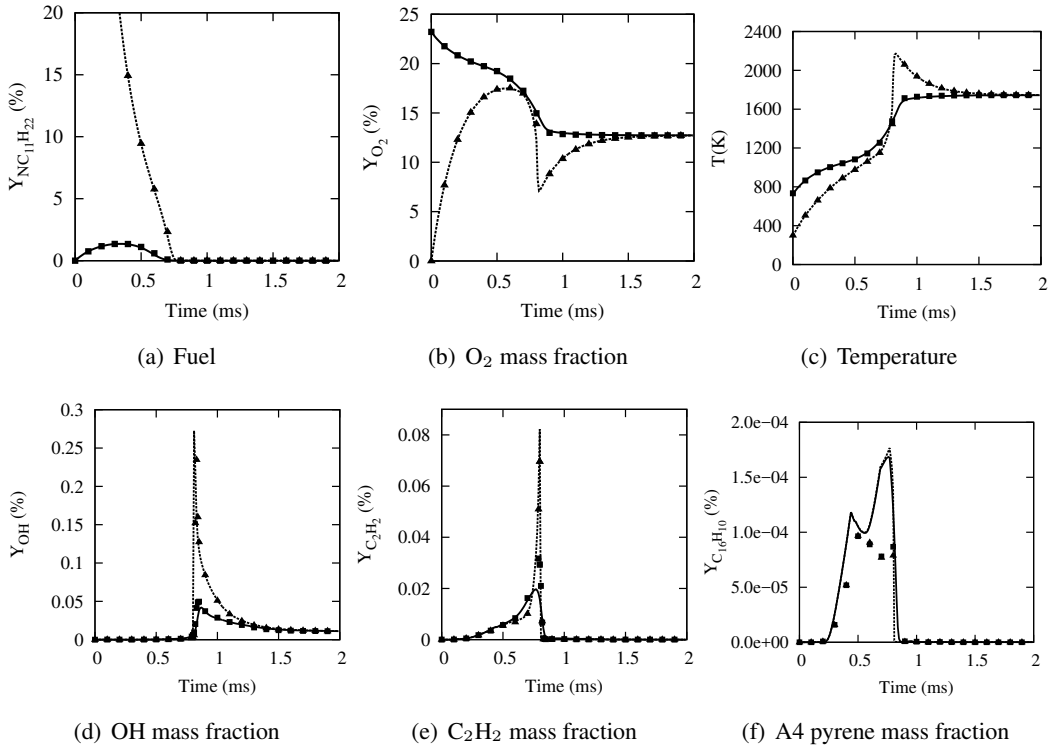

(a) Fuel (b) O_2 mass fraction (c) Temperature

(d) OH mass fraction (e) C_2H_2 mass fraction (f) A4 pyrene mass fraction

Figure 6.18: Representative species and temperature trajectories. Symbols: Reference HyChem mechanism. Cross: Air inlet. Triangle: Liquid fuel inlet. Lines: Reduced mechanism Solid-line: Air inlet trajectory. Dotted-Line: Liquid fuel inlet trajectory.

Figure 6.20(a) represents the temperature profile of a freely propagating 1D flame with the H mechanism on Yales2, in the physical space. As presented in chapter 5, the HyChem mechanism is fundamentally different than any surrogate mechanism. Indeed the fuel first decomposes into pyrolysis species, represented by the red zone in the figure where 99.9 % of the fuel disappears. The whole pyrolysis species are showed Figure 6.20(b) in the c-space with Yc = $\mid Y_{CO} \mid + \mid Y_{CO_2} \mid + \mid Y_{H_2O} \mid$. As the pyrolysis reactions are endothermic, they need a heat adding, typically the burned gases, to be activated. Those species are then oxidised in the flame zone, represented in blue in the figure 6.20(a) where the maximum of O, H and OH term source are observed.

6.4.3 0D stochastic database with ORCHydS

In this section, we are presenting the database obtained with the coupling introduced in section 6.3, in order to train the neural network architecture presented section 6.2.2.

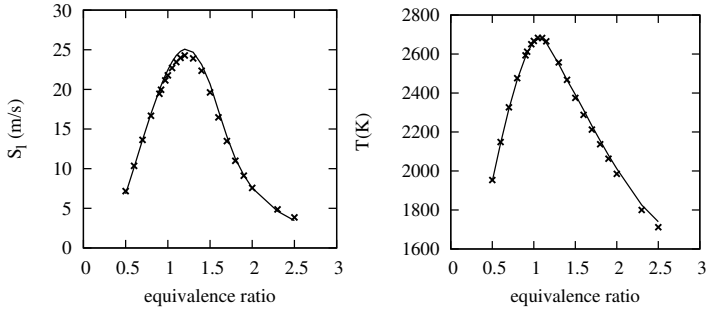

(a) Flame speed (b) Temperature

Figure 6.19: Freely propagating premixed flames. Response versus equivalence ratio. Temperature taken in burnt gases. Symbols: Reference HyChem mechanism. Line: Reduced mechanism before after optimisation (Genetic Algorithm).

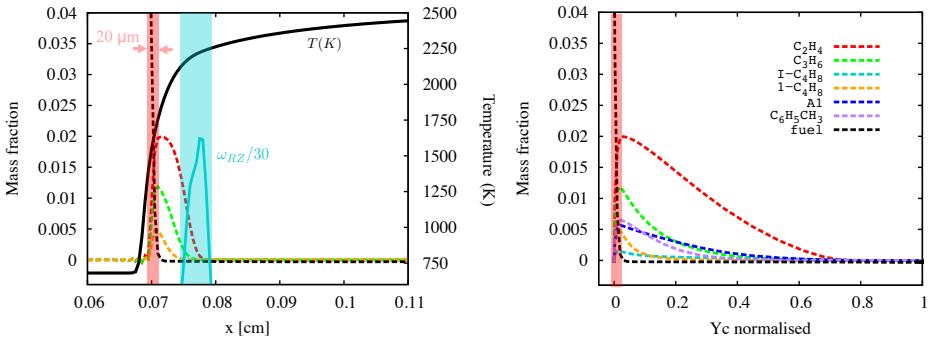

(a) Temperature profile (b) Pyrolyse species

Figure 6.20: Freely propagating premixed flames computed with the H mechanism. Dotted-coloured lines: Main pyrolysis species. Red zone: Pyrolyse zone where 99.9% od the fuel is consumed. Blue zone: reaction zone defined by the production of H, O and OH species. (a) Physical space. Black-line: Temperature. Turquoise line: Source term $\dot{\omega}_{RZ} =\mid \dot{\omega}_O \mid + \mid \dot{\omega}_{OH} \mid + \mid \dot{\omega}_H \mid$. (b) phase-space with Yc normalised = $\frac{Yc}{Yc,eq}$

The reduced “H" mechanism has been used in the ORCh stochastic configuration at the operating point presented above, during 200 iterations. The mixing EMST model (short for Euclidean minimum spanning tree) [251] implemented in ORCh by K. Wang is used for database build.

The ORCh time step is δ_t = 0.01 ms for a total time of 2 ms. The total HYPE time at each ORCh time step is equal to the ORCh time step, and the HYPE sub time steps are controlled by the agglomeration and growth/loss source term variations. Over $n_p = 10000$ HYPE stochastic particles are considered for accurate soot description, all placed in the first section for the PSD initialisation.

The soot primary particle is set to 21 nm, which is extracted from the experiment and consistent with the literature for heavy fuels [252]. A first geometric grid of M = 10 sections is considered, with a factor F_s = 1.8 over a soot diameter range from 21 to 140 nm.

Figure 6.21 represents the different soot density number created and transported by a total of 40 fluid particles in the ORCh solving, as long with the mean soot density. Figure 6.21 also shows the pyrene determinist trajectory for the same simulation without soot consumption. As the pyrene is consumed, the

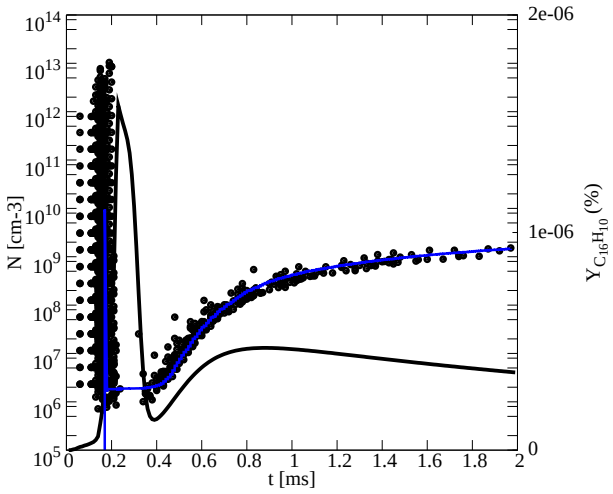

Figure 6.21: Black symbols: Soot density of 40 fluid particles in the ORCHydS simulation at different times during the ORCh simulation. Line: Pyrene determinist trajectory of the ORCh air inlet. Blue line: Mean soot density over the 40 fluid particles.

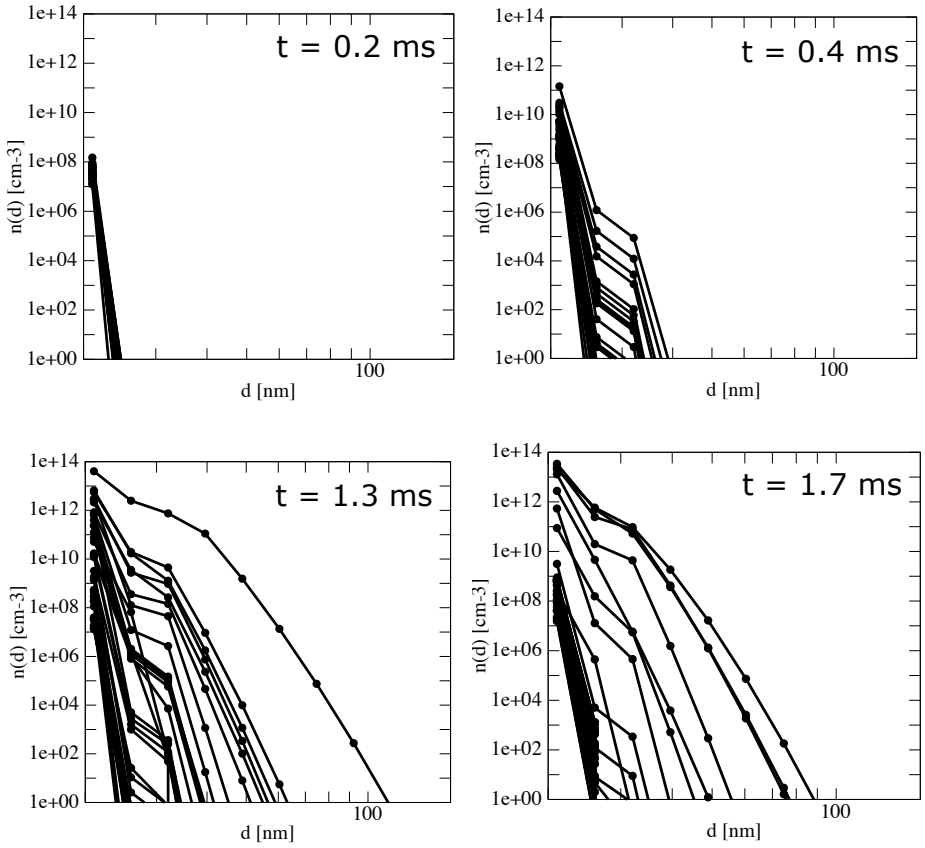

Figure 6.22: Particle size distributions of the 40 soot descriptions in the ORCHydS simulation at different times during the ORCh simulation.

soot density follows the pyrene pattern. Figure 6.22 shows the corresponding particle size distribution n(d) with different behaviours over the simulation time. At $t = 0.2\ ms$, the abrupt pyrene density growth

creates an important primary soot particle density (with a diameter $d = 21\ nm$). As the simulation goes forward, the particles size starts increasing, as seen at $t = 0.40\ ms$. The different PSD then continue to evolve, reaching a diameter of 140 nm at $t = 1.3\ ms$.

All these soot densities, along with the thermochemical parameters of the corresponding fluid particles constitute the database used for the neural network training hereafter.

6.4.4 Neural network training

The neural network architecture elaborated in section 6.2.2 is once again trained, this time with the newly database from ORCHydS, corresponding to the mermose operating point we are interested in. Unlike the 1D application section 6.2, the generated database is now 40 times more important, as 40 fluid particles in ORCh contain a soot distribution, for a total of 5 millions elements. The database time step variation $\Delta\delta t_{ORCHydS}$ controlled by the hybrid method ranges from 1.73e-17 ms to 0.02 ms, as shown Fig. 6.24, with a mean value of $\delta t_{ORCHydS,mean}$ = 5.8e-5 ms and a variance of 0.1 ms. In comparison the typical time step in the present YALES2 simulation stays constant at δt_{Y2} = 2e-7 ms.

Before entering in the CNN branch, each particle soot distribution N_i is rescaled by the minimum and maximum values of the i-th section , in a defined range through the relations :

$$N_{i,rescaled} = N_{i,std} \cdot (\mathrm{range}_{\max} - \mathrm{range}_{\min}) + \mathrm{range}_{\min}, \tag{6.3}$$

with

$$N_{i,std} = (N_i - N_{i,\min})/(N_{i,\max} - N_{i,\min})$$

$i \equiv [1:10]$, and range = [-50:50] . This rescale is essential to reduce the original range width of the inputs from [0:1e14] to [-50:50] and eventually facilitate the training of the neural network. It also changes the shape of the inputs, see Fig. 6.23. In further applications where the trained neural network is used, two vectors $\underline{N_{\min}}$ and $\underline{N_{\max}}$ of size 10 need to be kept in order to rescale the $\underline{N}$ input before entering the CNN.

The training is once again done on 80% of the data, and the remaining 20% are used for test. It took 100 epochs to obtain a 2 % of mean error on both trained and test datas. Then, once trained, the neural network is validated with the balance equation:

$$\frac{dN_i(t)}{dt} = \dot{\Omega}_i(t) \tag{6.4}$$

with $i \equiv [1:10]$. This equation is solved with a temporal third order Runge-Kutta method described in [240] with:

$$\dot{\Omega}_i(t) = \frac{\mathcal{F}[\phi(t),\underline{N}(t),\delta t_{ORCHydS}] - N_i(t))}{\delta t_{ORCHydS}}$$

This validation is presented on Fig. 6.26, in which the mean soot density and volume fraction predictions are compared to the mean soot density and volume fraction obtained over the HYPE database. It is observed that the soot density is well recovered, except between 0.2 and 0.6 ms where it is over-predicted. Looking at representative fluid particle distributions on Fig. 6.27 confirms over-predictions at t = 0.2 ms and t=0.4 ms, which is caused by the shape complexity of the soot density learned by the neural network, and especially the soot density peak observed at 0.17 ms. As the general soot behaviour

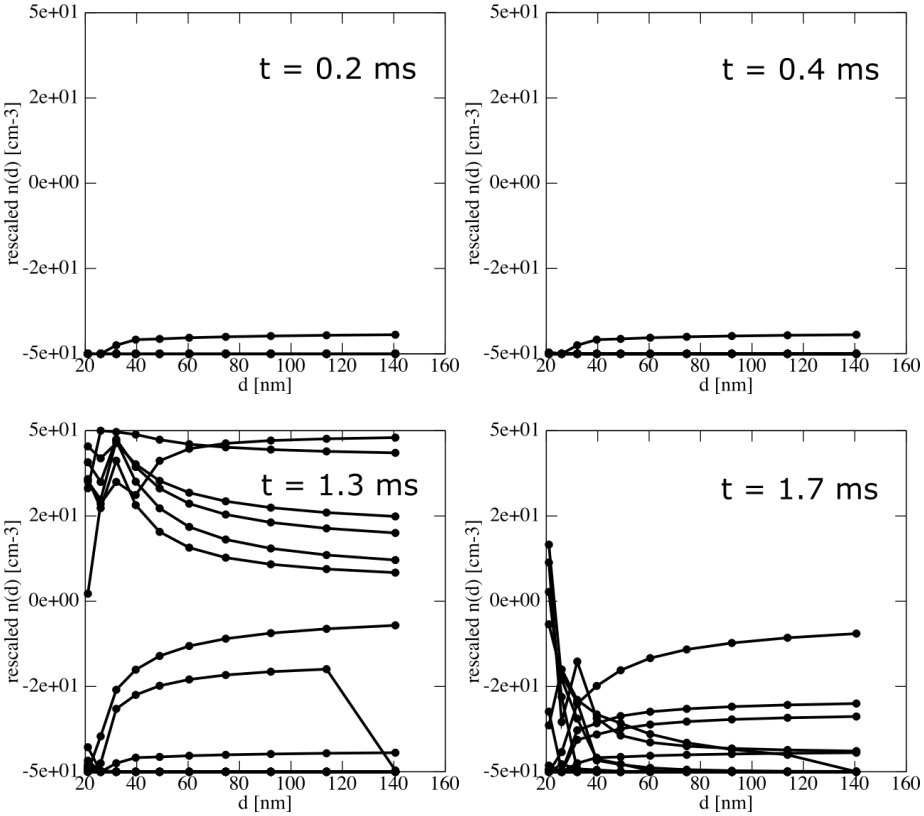

Figure 6.23: PSD database rescaled through equation 6.3 before entering the neural network, at different times.

is well recovered at the final time, this trained neural network will be used in the 3D LES, presented as a work in progress in the perspectives, see 6.4.5.5.

6.4.5 3D simulation

6.4.5.1 Numerical settings

The simulation concerns the computational domain presented Fig. 6.28. The injector system is the one from the SAM146 engine. The airflow in the combustor is splited into primary zone, dilution zone and wall cooling.

The mesh was provided by CERFACS and is composed of 18 million cells and 5 million nodes. the characteristic mesh size in the pilot injection system varies from 0.6 mm and 1.5 mm, as seen Fig. 6.29, and goes up to 3 mm in the rest of the pilot region, except at the intermediate and dilution holes where the characteristic size is about 1 mm. Near the exit, the cell size vary from 4 to 6 mm.

For this YALES2 simulation, the TFV4A time integration scheme is considered, developed by M. Kraushaar [253], with a fourth-order centred scheme for space integration. The turbulence model used here is the dynamic Smagorinsky presented section 2.4.4.

With the lack of experimental data on liquid fuel repartition for the injection system, it was chosen to simulate the chamber with a gaseous fuel injected trough the venturi walls, as shown Fig. 6.31, in order to respect the liquid film observed experimentally on these walls.

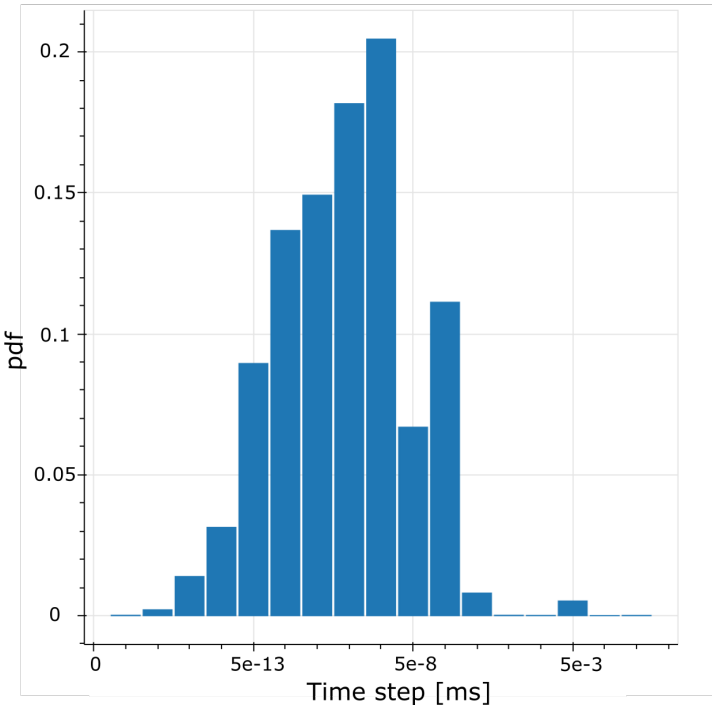

Figure 6.24: Database time step variation used for training, in milisecond.

6.4.5.2 TFLES settings

The dynamic TFLES model described in section 3.1.4 is employed in this simulation , and the efficiency function of Charlette *et al.* [82] is used with a filter size dependent of the mesh size with 5 points set in the flame layer.

Considering the mechanism thermal decomposition before oxidation, the flame sensor from P. Benard [85] appeared not well suited. Figure 6.30(a) represents the heat release rate and the corresponding flame sensor ω, which fails to encompass the pyrolysis zone. Consequently, the flame thickening is piloted by a newly defined flame sensor more adapted to the HyChem mechanism, based on:

$$\dot{\omega}_P = 0.1 \times (\dot{\omega}_{CO_2} + \dot{\omega}_{CO} + \dot{\omega}_{H_2O}) + 7.0 \times (\dot{\omega}_O + \dot{\omega}_H + \dot{\omega}_{OH}) + \dot{\omega}_{C_2H_4} \tag{6.5}$$

with

$$\begin{aligned} \mathcal{S} &= 1 \quad \text{if} \quad \dot{\omega}_P > \dot{\omega}_{\mathcal{S}} \\ \mathcal{S} &= 0 \quad \text{if} \quad \dot{\omega}_P < \dot{\omega}_{\mathcal{S}} \end{aligned} \tag{6.6}$$

and with a threshold set at 10% of the maximum laminar flame $\dot{\omega}_P$. By taking into account the source term of the main pyrolysis species C_2H_4, as well as the intermediate species O, H and OH, we are certain to encompass the whole flame region, as shown Fig. 6.30(b).

6.4.5.3 Fuel decomposition and oxidation

Figure 6.31 represents the fuel mass fraction in an instantaneous middle plan, with two isocontours: The first one in red is the zone where the source term of the main pyrolysis species, C_2H_4, is higher. 99% of the C_2H_4 is produced in these zones. The second isocontour in black is the zone where 99% of the C_2H_4

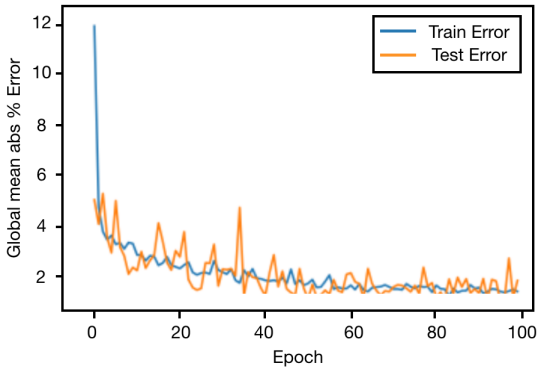

(a) Loss function evolution

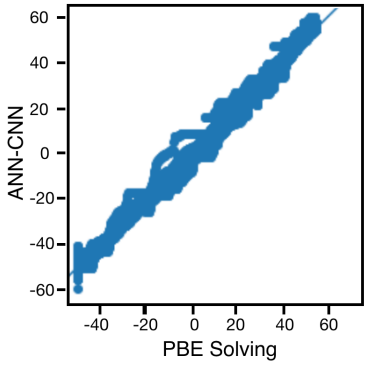

(b) Train prediction

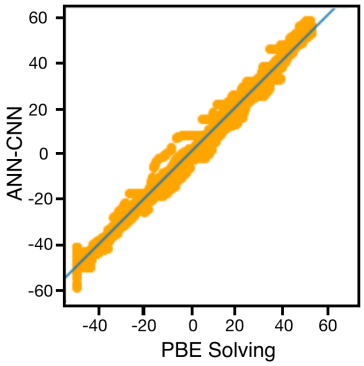

(c) Test prediction

Figure 6.25: Training neural network results with trained (orange) and tested (blue) predictions at each epoch.

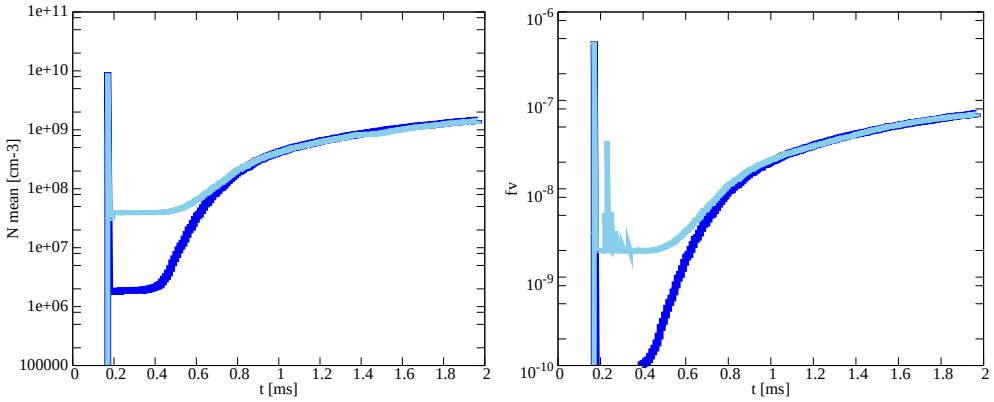

(a) Soot density N

(b) Volume fraction fv

Figure 6.26: Mean soot density and volume fraction over the 40 ORCh fluids particles. Blue: HYPE simulation with 10000 stochastic particles and 10 sections. Clear blue: Neural network prediction.

species disappears. As the rest of the pyrolyse species source terms follow the same pattern, the red zone is representative on where the pyrolyse is located, and the black zone where the oxidation begins.

Figure 6.32 represents temperature profile, with a V shape flame, and in blue the pyrene mass fraction

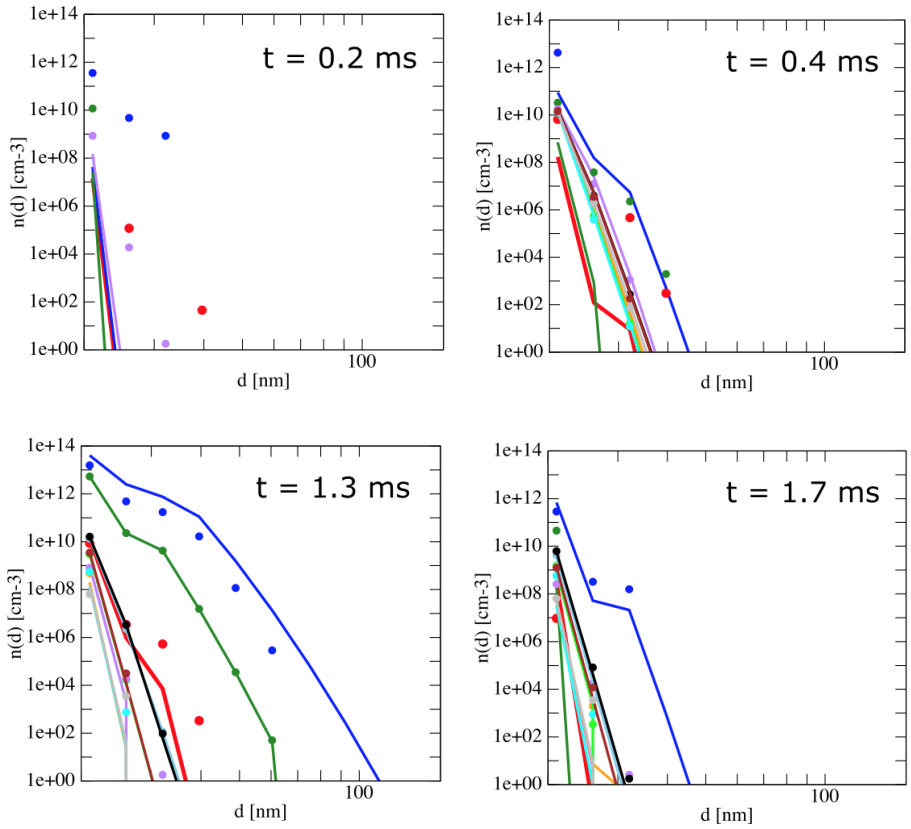

Figure 6.27: Soot prediction on representative fluid particle distributions. Line: reference. Symbols : prediction with PBE 6.4.

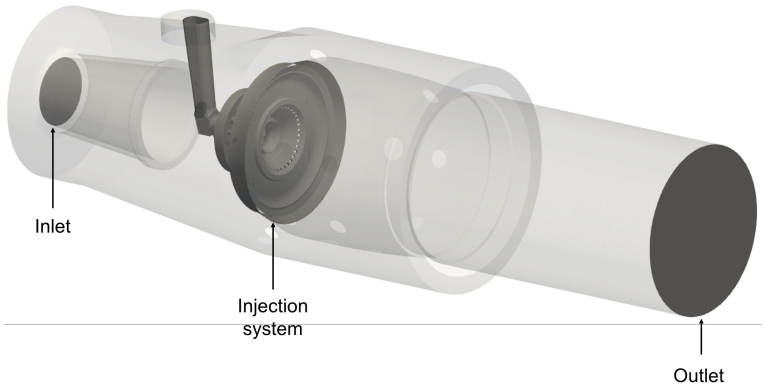

Figure 6.28: Combustor computational domain.

field. The primary soot are expected to be created in the blue zone.

6.4.5.4 First validation: CO_2 measures

Table 6.4 presents the comparison between the experimental CO_2 percentage and the averaged LES CO_2 percentage over the probe holes of the present simulation, presented Fig 6.33. The CO_2 emissions are predicted with a relative error of about 21.3%.

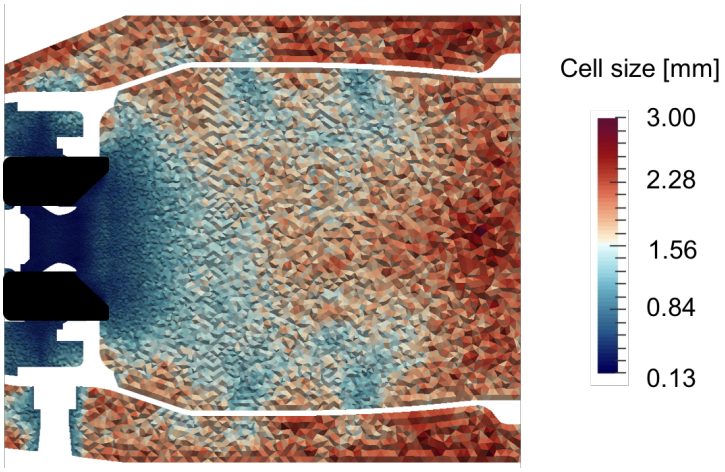

Figure 6.29: Resolution of the mesh with 18 million cells.

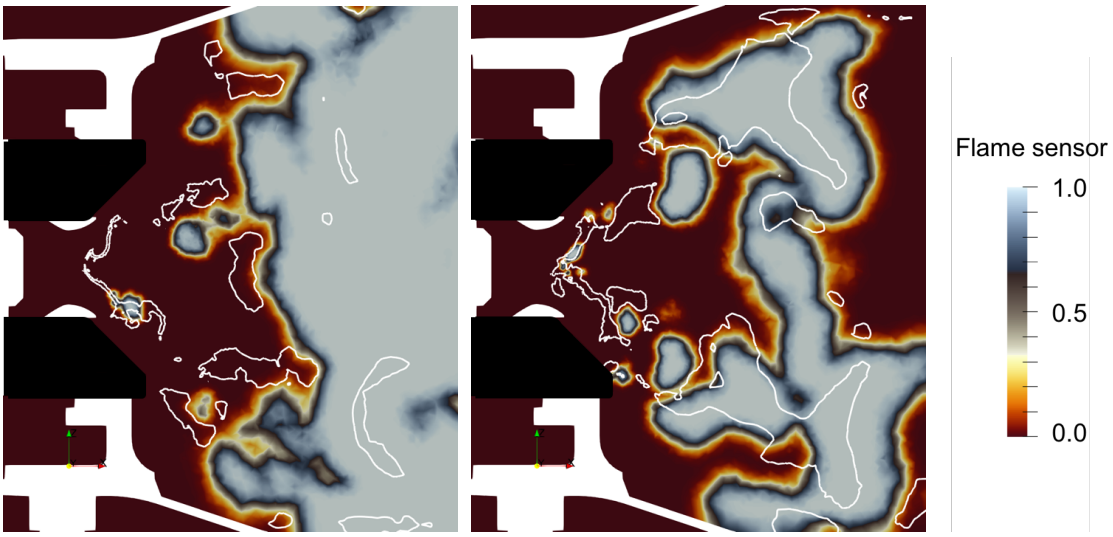

(a) case with $\dot{\omega}$ (b) case with $\dot{\omega}_P$

Figure 6.30: Instantaneous flame sensor field in the middle plan based on (a) $\dot{\omega}$ from P. Benard [85], (b) $\dot{\omega}_P$ proposed here 6.5. The isocontour represents the heat release rate.

	Experiment (Percentage in gas)	LES (Percentage in gas)	Relative error (%)
$< \mathbf{CO_2}\ \mathbf{\%} >^{\mathbf{probes}}$	5.25	6.37	21.3%

Table 6.4: Experimental and simulated CO_2 percentage comparison, mean over time and probes on both sides of the central axis, on the exit plane.

6.4.5.5 Mermose soot prediction

Ten additional transport equations are added into the YALES2 solving for the particle size distribution prediction:

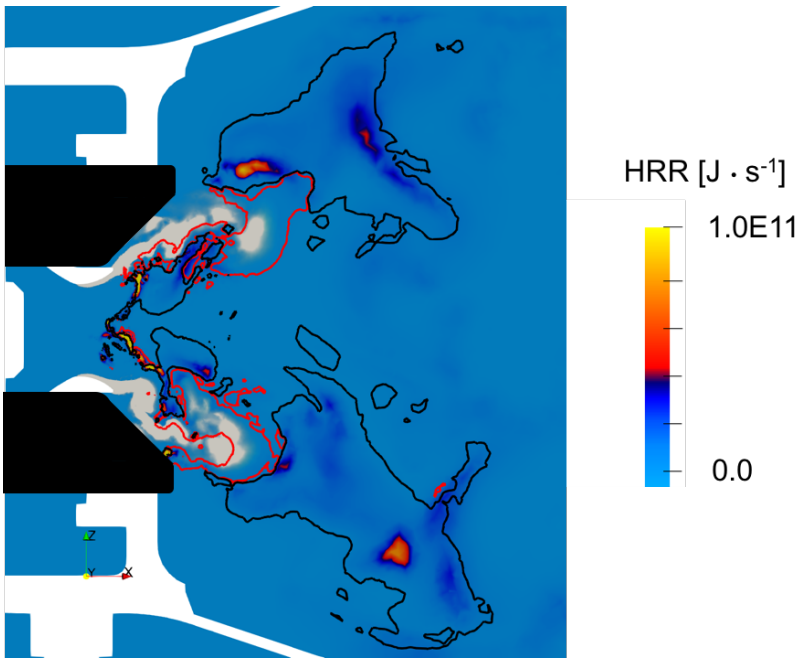

Figure 6.31: Instantaneous Heat Release Rate field in the middle plane. Fuel mass fraction in grey. Isocontours: C_2H_4 term source, positive (red) and negative (black).

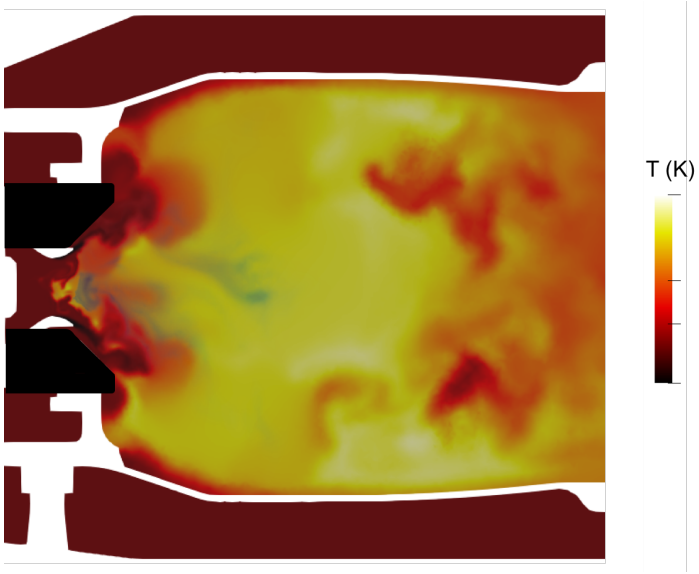

Figure 6.32: Instantaneous temperature field in the middle plane. Blue: Pyrene mass fraction field.

$$\frac{\partial \overline{\rho}\widetilde{N_i}}{\partial t} + \nabla \cdot \overline{\rho}\widetilde{u}\widetilde{N_i} = -\nabla \underbrace{\left[\overline{\rho}(\widetilde{uN_i} - \widetilde{u}\widetilde{N_i})\right]}_{(1)} - \nabla \underbrace{\left(-\overline{\rho V_{k,i} N_i}\right)}_{(2)}. \tag{6.7}$$

with $i \in [1:10]$ the size sections number. 2 unresolved terms appear in the filtered soot equations:

- **The sub grid soot density (1)** is modelled just like the sub grid species, see Chapter 2, same for the species fluxes with a constant turbulent Schmidt number over the entire domain.

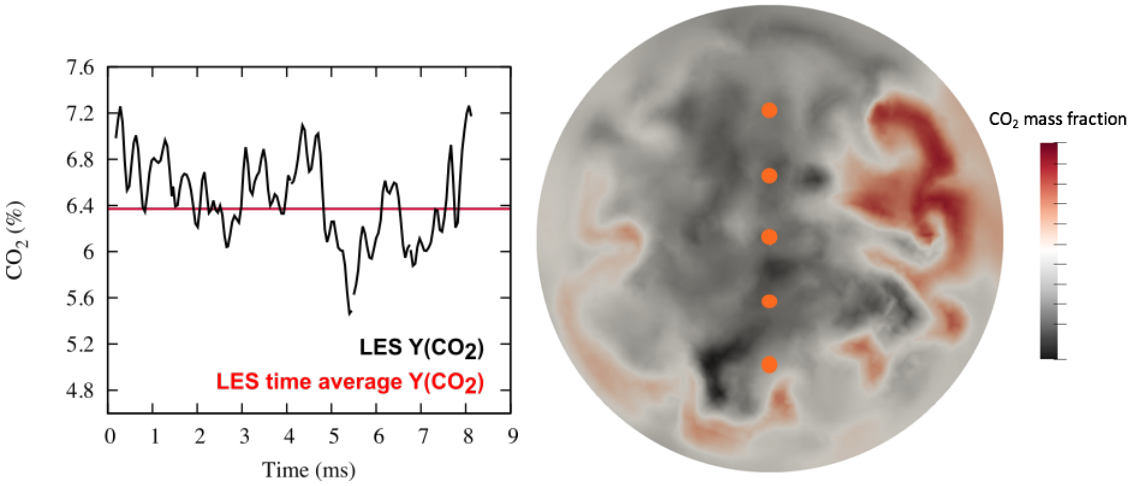

Figure 6.33: CO_2 mass fraction on the probe plane near the combustion chamber exit. The orange points represent the 5 probe holes.

- **The filtered laminar diffusive fluxes of soot density (2)** is neglected because of the absence of molecular particle diffusion, see [249].

After the transport solving, the obtained $\widetilde{N_i}^*$ is taken as input for the neural network, along with the corresponding thermochemical variables, to obtain the prediction of $\widetilde{N_i}(t+\delta t)$ for the next iteration.

For CPU purpose, the trained neural network is loaded for every group element in YALES2, allowing a cost multiplied only by 1.4, due to the 10 added balance equations and the neural network call.

Figure 6.34 represents the obtained instantaneous soot density field at the 10 characteristic sizes in the combustion chamber middle plane, as long with the corresponding total density and soot mass fraction Fig. 6.35. The final comparison with experimental soot density and mass is done in the exit probe plane, on table 6.5. A large over-prediction is observed, that must be investigated in regard of the several hypothesis made on the kinetic mechanism and the soot transport model. However, LES soot density and volume fraction are expected to be greater than measurements, as not all particles entering the probe will actually be carried to the detector by the flow. Indeed even if the isokinetic hypothesis is validated at the entrance of the probe, soot deposit occur in bends that separate particles from the flow, also by thermophoresis due to the temperature gradient between the sampling tube and the flow [254].

	Experiment	**LES**	**Relative error**
$<$ **fv** $>^{\text{probes}}$ **[mg/cm-3]**	1.15e-6	1.57e-6	0.36
$<$ **N(d**$_{mean}$**)** $>^{\text{probes}}$ **[cm-3]**	1.28e7	2.43e7	0.92
$<$ **N** $>^{\text{probes}}$ **[cm-3]**	1.28e7	3.24e8	24

Table 6.5: Total mean soot density, mean soot density of the mean diameter and soot volume fraction over the 5 probes on the exit probe plane. Comparison with experiment.

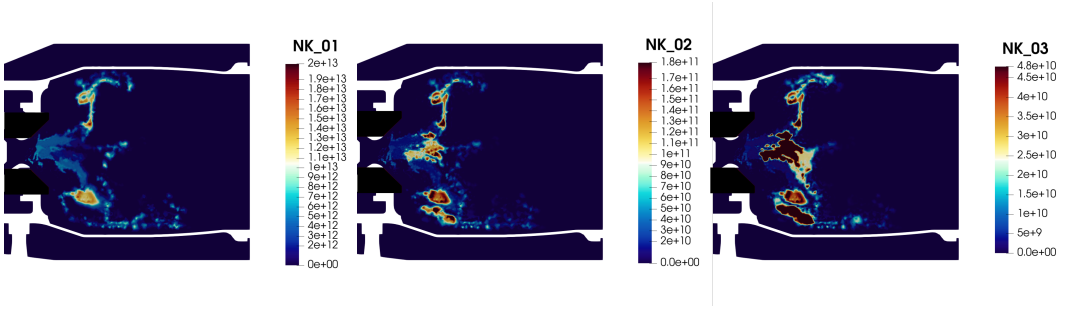

(a) $N_{k=1}$, $d_{average} = 21$ nm (b) $N_{k=3}$, $d_{average} = 25$ nm (c) $N_{k=3}$, $d_{average} = 32$ nm

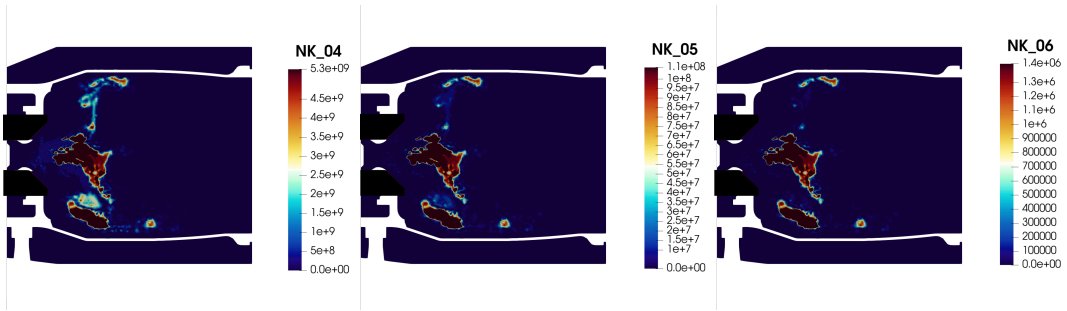

(d) $N_{k=4}$, $d_{average} = 39$ nm (e) $N_{k=5}$, $d_{average} = 48$ nm (f) $N_{k=6}$, $d_{average} = 60$ nm

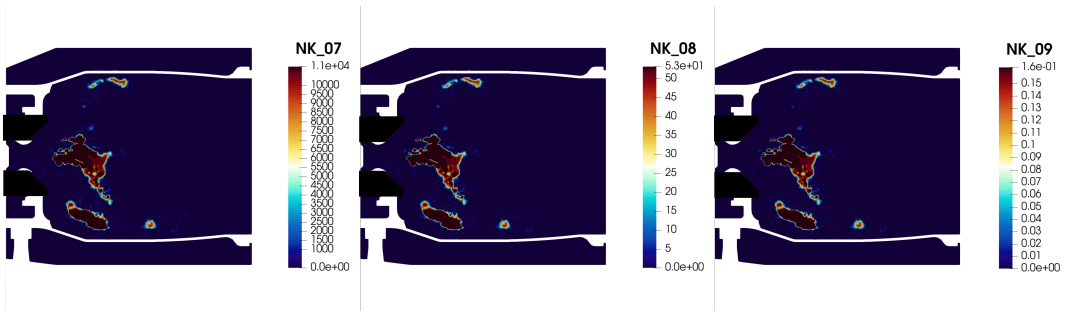

(g) $N_{k=7}$, $d_{average} = 74$ nm (h) $N_{k=8}$, $d_{average} = 92$ nm (i) $N_{k=9}$, $d_{average} = 113$ nm

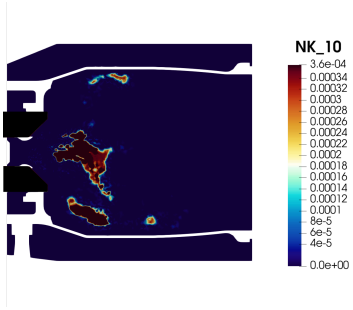

(j) $N_{k=10}$, $d_{average} = 140$ nm

Figure 6.34: Density particles number of 10 characteristic diameter d, in cm-3. Instantaneous fields in the middle plane.

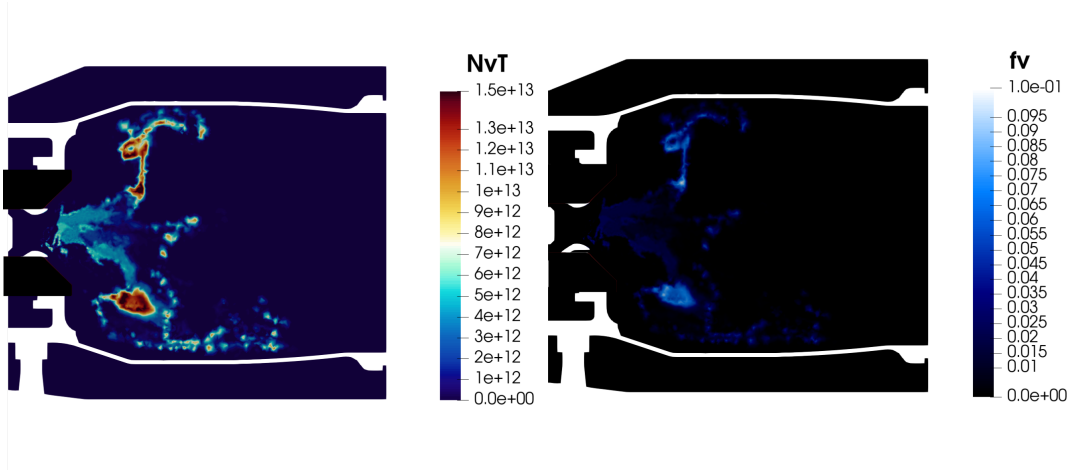

(a) Total soot density in cm-3 (b) Soot volume fraction in mg/cm-3

Figure 6.35: Instantaneous soot (a) density and (b) volume fraction field in the middle plane.

6.5 Conclusion

With the future norms on soot production applied to aircraft engines, it is primordial to develop new models, able to predict soot formation at low cost and compatible with industrial time scales. The already available models in the literature are still struggling to merge prediction quality with low cost, especially for the particle size distribution.

In this chapter, we propose to test an alternative solution, based on neural networks, allowing to reduce an highly predictive soot model. This strategy is first employed to retrieve a particle size distribution of a premixed 1D sooted flame, and shows correct predictions when compared to the HYPE model. This first test also allowed us to estimate the adding cost to employ this strategy further.

Next, we continued to develop this strategy for a 3D LES combustion chamber simulation with complex chemistry. In order to train the neural network, we created a soot database, based on HYPE coupled with the ORCh stochastic configuration.

The final goal here is to simulate a combustor representative of the turbofan SAM146, at one operating point. It is done with the HyChem complex chemistry model and the use of the neural network, previously trained with the corresponding soot database. Eventually are able to predict the particle size distribution along with the total soot mass in the chamber, for an extra cost only 1.4 times higher.

Chapter 7

Conclusions and perspectives

7.1 Conclusions

This thesis can be detached into three different works, all distincts yet complementary. The main motive in those works was to propose models and tools for LES of aircraft engines with real fuels, in order to accurately predict and control greenhouse gas and particulates emissions, under affordable CPU cost.

7.1.1 Improvement on the kinetic reduction code ORCh

A major part of the thesis was dedicated to improve the ORCh code, to obtain highly reduced kerosene kinetic mechanisms with the same predictability as detailed ones. In order to do so, the ORCh reduction methodology is enhanced with pre-exponential coefficient ratio-tabulated. When the kinetic mechanism is drastically reduced, it allows to secure the flame speed prediction, even in the rich zones.

Application: The CO prediction on the LEMCOTEC industrial chamber

This strategy was first applied to the air/kerosene Luche mechanism [175], in an industrial operating point of the LEMCOTEC chamber. The pre-exponential tabulation allowed to derive a 15-species and 72-reactions mechanism from an already reduced mechanism of 22 species and 222 reactions. A final 3D LES simulation of the chamber demonstrated a fair CO prediction with the 15-species mechanism, with the same percentage of error as a previous simulation with a less reduced mechanism [147], and for a lower CPU cost.

7.1.2 Toward the modelling of unresolved non-linear terms

The second part of this work aimed at proposing a novel framework, allowing to bypass closure models for unresolved terms in the LES filtered transport equations with a neural network. The idea was to use the already available physical information in a DNS flame for training the neural network, to propose a closure directly based on data analysis.

Application: The 3D tabulated turbulent flame

The DNS database used for the neural network training is a methane-air stoichiometric premixed jet-flame [127, 131, 132], computed with the compressible flow solver SiTCom [137]. The GRI-3.0

mechanism used for chemistry is tabulated with a progress variable defined from CO, CO2, H2O and NOx as in [135]. The DNS zone consists of 28.58 million nodes with a resolution fixed at 50 μm.

The convolutional neural networks were shown to provide quantitatively accurate predictions of both the source and flux terms, which are two substantially different terms and otherwise difficult to model in a single unified framework. The predictions capabilities of the networks are also demonstrated to be only weakly sensitive to variations in filter width, which is an important attribute for any sub-grid scale model.

7.1.3 Reduction method for soot prediction

We once again use neural networks, this time for model reduction in the case of soot modelling, to propose a reduction strategy able to cast a precise soot model into a more affordable one with the same level of prediction accuracy. This strategy decomposed in two parts, first the building of a large enough database, then the training of a functional API neural network architecture with this database. The network output is the soot distribution prediction at one (time or space) step, and the inputs are the soot distribution of the precedent step, processed with CNN layers, and meaningful species mass fractions and the temperature, processed with ANN layers.

In order to build the database for one of the two applications below, the ORCh multi-inlet configuration was merged with the hybrid soot modeling from A. Bouaniche [182], to obtain a large database of fluid particules, mixing and reacting together, and transporting soot description (namely the ORCHydS merging).

Applications

- **1D premixed flame**: This strategy is first employed to retrieve the particle size distribution of a 1D laminar premixed ethylene-argon-oxygen sooted flame. The neural network architecture is calibrated during this first application. The neural network is first trained with the solution from HYPE [238] and shows correct predictions when used back in a digital-twin PBE of the soot PSD. This first test also allowed us to estimate the adding CPU cost of this strategy.

- **3D Mermose configuration**: The final goal here is to predict soot production of a combustor representative of the turbofan SAM146, at one operating point. The used reduced kinetic mechanism was extracted from the HyChem complex chemistry model. Because of its differences with classic surrogates mechanisms, this new chemistry model requires a modified flame sensor for the TFLES model based on species covering both fuel pyrolysis and oxidation. The soot prediction was done with a the neural network, previously trained with the corresponding soot database generated with ORCHydS. This neural network was implemented in the YALES2 3D LES solver. Eventually we expect to predict the particle size distribution along with the total soot mass in the chamber, for an extra cost only 1.4 times higher than the computation without soot modelling. This still on-going work is presented in the perspectives.

7.2 Perspectives

7.2.1 Perspectives to conclude the CNN application

The trained networks being based on the progress variable, a generic parameter of premixed flames, we hypotheses that they will perform well for any turbulent premixed flame located in the Borghi regime-diagram close to the conditions used for training. Nevertheless, it is an application that must be done in order to validate the generalisation of those networks.

7.2.2 Toward a less expensive pollutant prediction

The next step would be to gain CPU performances on the LES solving presented in this thesis, especially with soot solving that necessitates relatively large kinetic mechanisms, and to prepare the future studies with bio-fuels mechanisms. One solution is to use neural networks to directly predict species source terms, as it was done in the work of Wan *et al.* [148], in which a major CPU reduction cost was obtained by avoiding Arrhenius rates calculation and the direct integration of the stiff chemical system.

7.2.2.1 Soot modelling

The presented soot model strategy in this thesis has been deployed with several hypothesis that are worth to be analysed in a future work.

Firstly, the soot radiation was not taken into account in this work. It would be wise to add a radiation model to soot description in YALES2, in order to quantify its effect. Also there was only one-way coupling with the temperature and the pyrene fraction in the 3D simulation. A future work would be to code a two-way coupling. The soot transport model may at the same time be improved for the Mermose case, for example by defining different Schmidt numbers per soot size section. Eventually, the impact of gaseous modelling compared to liquid fuel on soot production should be quantified.

The 3D solving with the neural network should be directly compared, with a similar solving with the Leung model, in term of soot density prediction and CPU cost. Also, the influence of the soot discretisation grid should be more carefully analysed, as it conditioned greatly the PSD in this thesis. Concerning the whole strategy validation, an ultimate application will be done, the Soprano burner.

7.2.3 A second application : The Soprano burner

The ORCHydS strategy will be applied for a different configuration, namely the SOPRANO (EC project) burner of CORIA. It would allow to rely on less models and hypothesis, with a simpler kinetic mechanism based on acetylene, a gaseous experiment and experimental soot distributions measured at different operating points. As soot measurements were done with non intrusive methods, see the work by M. Bouvier *et al.* [255], the soot distribution of the 3D LES solved with the ORCHydS strategy could be directly compared to the experimental soot distributions in the reactive zone.

Bibliography

[1] G. Aad, T. Abajyan, B. Abbott, J. Abdallah, S. A. Khalek, A. A. Abdelalim, O. Abdinov, R. Aben, B. Abi, M. Abolins, *et al.*, "Observation of a new particle in the search for the standard model higgs boson with the atlas detector at the lhc," *Physics Letters B*, vol. 716, no. 1, pp. 1–29, 2012.

[2] B. P. Abbott, R. Abbott, T. Abbott, M. Abernathy, F. Acernese, K. Ackley, C. Adams, T. Adams, P. Addesso, R. Adhikari, *et al.*, "Observation of gravitational waves from a binary black hole merger," *Physical review letters*, vol. 116, no. 6, p. 061102, 2016.

[3] 'Can automatic calculating machines be said to think?' n.d. TS of a broadcast discussion transmitted on BBC Third Programme, 14 and 23 Jan. 1952, http://www.turingarchive.org/browse.php/B/6.

[4] D. Silver, T. Hubert, J. Schrittwieser, I. Antonoglou, M. Lai, A. Guez, M. Lanctot, L. Sifre, D. Kumaran, T. Graepel, *et al.*, "Mastering chess and shogi by self-play with a general reinforcement learning algorithm," *arXiv preprint arXiv:1712.01815*, 2017.

[5] A. Denlèle, "L'ère des robots astronomes," *Ciel & espace*, vol. 561, pp. 38–43, 2018.

[6] Anonymous, "The world most valuable resource is no longer oil, but data," *The Economist*, 2017.

[7] 2018 Financial Facebook report, https://investor.fb.com/financials/default.aspx.

[8] 2018 Financial Google report, https://abc.xyz/.

[9] B. Arcas, M. Mitchell, and A. Todorov, "Physiognomy's new clothes," *Medium*, 6 mai 2017.

[10] S. Levin, "Lgbt groups denounce "dangerous" AI that uses your face to guess sexuality," *The Guardian*, 9 septembre 2017.

[11] F. Hölker, C. Wolter, E. K. Perkin, K. Tockner, *et al.*, "Light pollution as a biodiversity threat.," *Trends in ecology & evolution*, vol. 25, no. 12, pp. 681–682, 2010.

[12] R. Chepesiuk, "Missing the dark: health effects of light pollution," 2009.

[13] R. Pachauri and L. Meyer, *Changements climatiques 2014: Rapport de synthèse. Contribution des Groupes de travail I, II et III au cinquième Rapport d'évaluation du Groupe d'experts intergouvernemental sur l'évolution du climat*. GIEC, 2014.

[14] F. Wania and D. MacKay, "Peer reviewed: Tracking the distribution of persistent organic pollutants," *Environmental Science & Technology*, vol. 30, pp. 390A–396A, 08 1996.

[15] E. Grun, *Interplanetary Dust*. Springer Berlin Heidelberg, 2001.

[16] H. Reeves, *L'origine de l'univers*, vol. 2. Horizons philosophiques, 1992.

[17] T. C. Bond and al., "Bounding the role of black carbon in the climate change system: A scientific assessment," *J. Geophys. Res. Atmos.*, vol. 118, pp. 5380–5552, 2013.

[18] M. Schulz and al., "Radiative forcing by aerosols as derived from the aerocom present-day and pre-industrial simulations," *Atmos. Chem. Phys.*, vol. 6, pp. 5225–5246, 2006.

[19] World Health Organisation, http://www.euro.who.int/en/health-topics/environment-and-health/air-quality/data-and-statistics.

[20] C. Opio, P. Gerber, A. Mottet, A. Falcucci, G. Tempio, M. MacLeod, T. Vellinga, B. Henderson, and H. Steinfeld, *Greenhouse gas emissions from ruminant supply chains–A global life cycle assessment*. Food and agriculture organization of the United Nations, 2013.

[21] S. Airbus, "Global market forecast 2019–2038," *Future Journeys, Blagnac, France*, 2019.

[22] D. Rutherford, M. Zeinali, *et al.*, "Efficiency trends for new commercial jet aircraft 1960-2008," 2009.

[23] I. M. Kennedy, "Models of soot formation and oxidation," *Prog. Energ. Combust. Sci.*, vol. 23, pp. 95–132, 1997.

[24] J. O. Hirschfelder, C. F. Curtiss, R. B. Bird, and M. G. Mayer, *Molecular theory of gases and liquids*, vol. 165. Wiley New York, 1964.

[25] V. Giovangigli, "Multicomponent flow modeling," *Science China Mathematics*, vol. 55, no. 2, pp. 285–308, 2012.

[26] C. F. Curtiss and J. O. Hirschfelder, "Transport properties of multicomponent gas mixtures," *The Journal of Chemical Physics*, vol. 17, no. 6, pp. 550–555, 1949.

[27] R. J. Kee, F. M. Rupley, E. Meeks, and J. A. Miller, *CHEMKIN-III: A FORTRAN chemical kinetics package for the analysis of gas-phase chemical and plasma kinetics*. 1996.

[28] F. A. Lindemann, S. Arrhenius, I. Langmuir, N. Dhar, J. Perrin, and W. M. Lewis, "Discussion on "the radiation theory of chemical action"," *Transactions of the Faraday Society*, vol. 17, pp. 598–606, 1922.

[29] U. Maas and S. B. Pope, "Simplifying chemical kinetics: intrinsic low-dimensional manifolds in composition space," *Combustion and Flame*, vol. 88, no. 3, pp. 239–264, 1992.

[30] O. Gicquel, N. Darabiha, and D. Thévenin, "Laminar premixed hydrogen/air counterflow flame simulations using flame prolongation of ildm with differential diffusion," *Proceedings of the Combustion Institute*, vol. 28, no. 2, pp. 1901–1908, 2000.

[31] J. A. V. Oijen and L. P. H. de Goey, "Modelling of premixed laminar flames using flamelet-generated manifolds," *Combustion Science and Technology*, vol. 161, no. 1, pp. 113–137, 2000.

[32] D. Veynante and L. Vervisch, "Turbulent combustion modeling," *Progress in Energy and Combustion Science*, vol. 28, no. 3, pp. 193 – 266, 2002.

[33] T. Poinsot and D. Veynante, *Theoretical and Numerical Combustion*. R. T. Edwards Incorporated, 2005.

[34] R. J. Blint, "The relationship of the laminar flame width to flame speed," *Combustion Science and Technology*, vol. 49, no. 1-2, pp. 79–92, 1986.

[35] C. K. Law, *Combustion Physics*. Cambridge: Cambridge University Press, 009 2006.

[36] R. Bilger, "The structure of turbulent nonpremixed flames," *Symposium (International) on Combustion*, vol. 22, no. 1, pp. 475 – 488, 1989.

[37] H. Yamashita, M. Shimada, and T. Takeno, "A numerical study on flame stability at the transition point of jet diffusion flames," in *Symposium (International) on Combustion*, vol. 26, pp. 27–34, Elsevier, 1996.

[38] S. Hartl, D. Geyer, A. Dreizler, G. Magnotti, R. S. Barlow, and C. Hasse, "Regime identification from raman/rayleigh line measurements in partially premixed flames," *Combustion and Flame*, vol. 189, pp. 126–141, 2018.

[39] D. Butz, S. Hartl, S. Popp, S. Walther, R. S. Barlow, C. Hasse, A. Dreizler, and D. Geyer, "Local flame structure analysis in turbulent ch4/air flames with multi-regime characteristics," *Combustion and Flame*, vol. 210, pp. 426–438, 2019.

[40] K. Wan, S. Hartl, L. Vervisch, P. Domingo, R. S. Barlow, and C. Hasse, "Combustion regime identification from machine learning trained by raman/rayleigh line measurements," *Combustion and Flame*, vol. 219, pp. 268–274, 2020.

[41] R. Mercier, P. Auzillon, N. Darabiha, O. Gicquel, D. Veynante, B. FIORINA, and V. Moureau, "Modeling flame stabilization by heat losses using filtered tabulated chemistry for les," 01 2013.

[42] A. N. Kolmogorov, "The local structure of turbulence in incompressible viscous fluid for very large reynolds numbers," in *Dokl. Akad. Nauk SSSR*, vol. 30, pp. 299–303, 1941.

[43] T. Jaravel, *Prediction of pollutants in gas turbines using large eddy simulation*. Phd thesis, INP Toulouse, 2016.

[44] P. Moin and K. Mahesh, "Direct numerical simulation: a tool in turbulence research," *Annual review of fluid mechanics*, vol. 30, no. 1, pp. 539–578, 1998.

[45] J. Boussinesq, *Théorie de l´écoulement troubillonant*, pp. 23–46. Mem. Pres. Acad. Sci., 1877.

[46] M. Germano, U. Piomelli, P. Moin, and W. H. Cabot, "A dynamic subgrid-scale eddy viscosity model," *Physics of Fluids A: Fluid Dynamics (1989-1993)*, vol. 3, no. 7, pp. 1760–1765, 1991.

[47] D. K. Lilly, "A proposed modification of the germano subgrid-scale closure method," *Physics of Fluids A: Fluid Dynamics (1989-1993)*, vol. 4, no. 3, pp. 633–635, 1992.

[48] F. Nicoud and F. Ducros, "Subgrid-scale stress modelling based on the square of the velocity gradient tensor," *Flow, turbulence and Combustion*, vol. 62, no. 3, pp. 183–200, 1999.

[49] S. Elgobashi, "An updated classification map of particle-laden turbulent flows," in *IUTAM Symposium on Computational Approaches to Multiphase Flow*, pp. 3–10, Springer, 2006.

[50] R. L. C. Flemmer and C. L. Banks, "On the drag coefficient of a sphere," *Powder Technology*, vol. 48, no. 3, pp. 217 – 221, 1986.

[51] L. Schiller and Z. Naumann, "A drag coefficient correlation," *Vdi Zeitung*, vol. 77, no. 318, p. 51, 1935.

[52] B. Farcy, *Analyse des mécanismes de destruction non-catalytique des Oxydes d´Azote (DeNOx) et application à la simulation aux grandes échelles (LES) d´un incinérateur*. Phd thesis, Rouen, INSA, 2015.

[53] G. L. Hubbard, V. E. Denny, and A. F. Mills, "Droplet evaporation: effects of transients and variable properties," *International Journal of Heat and Mass Transfer*, vol. 18, no. 9, pp. 1003–1008, 1975.

[54] K. K. Kuo, "Principles of combustion," 1986.

[55] W. A. Sirignano, *Fluid dynamics and transport of droplets and sprays*. Cambridge University Press, 2010.

[56] W. E. Ranz and W. R. Marshall, "Evaporation from drops," *Chemical Engineering Progress*, vol. 48, no. 3, p. 141446, 1952.

[57] N. Enjalbert, *Modélisation avancée de la combustion turbulente diphasique en régime de forte dilution par les gaz brûlées*. Phd thesis, INSA of Rouen, 2015.

[58] N. A. Okong´o and J. Bellan, "Consistent large-eddy simulation of a temporal mixing layer laden with evaporating drops. part 1. direct numerical simulation, formulation and a priori analysis," *Journal of Fluid Mechanics*, vol. 499, pp. 1–47, 2004.

[59] M. Bini and W. P. Jones, "Particle acceleration in turbulent flows: A class of nonlinear stochastic models for intermittency," *Physics of Fluids*, vol. 19, no. 3, p. 035104, 2007.

[60] M. Boivin, O. Simonin, and K. D. Squires, "Direct numerical simulation of turbulence modulation by particles in isotropic turbulence," *Journal of Fluid Mechanics*, vol. 375, pp. 235–263, 1998.

[61] S. Yuu, T. Ueno, and T. Umekage, "Numerical simulation of the high reynolds number slit nozzle gas–particle jet using subgrid-scale coupling large eddy simulation," *Chemical Engineering Science*, vol. 56, no. 14, pp. 4293–4307, 2001.

[62] W. Jones, S. Lyra, and S. Navarro-Martinez, "Large eddy simulation of a swirl stabilized spray flame," *Proceedings of the Combustion Institute*, vol. 33, no. 2, pp. 2153–2160, 2011.

[63] M. Sanjosé, J. M. Senoner, F. Jaegle, B. Cuenot, S. Moreau, and T. Poinsot, "Fuel injection model for euler–euler and euler–lagrange large-eddy simulations of an evaporating spray inside an aeronautical combustor," *International Journal of Multiphase Flow*, vol. 37, no. 5, pp. 514–529, 2011.

[64] D. Goodwin, N. Malaya, H. Moffat, and R. Speth, "Cantera: An object oriented software toolkit for chemical kinetics, thermodynamics, and transport processes,," 2012.

[65] V. Moureau, P. Domingo, and L. Vervisch, "From large-eddy simulation to direct numerical simulation of a lean premixed swirl flame: Filtered laminar flame-pdf modeling," *Combustion and Flame*, vol. 158, no. 7, pp. 1340–1357, 2011.

[66] P. Benard, G. Lartigue, V. Moureau, and R. Mercier, "Large-Eddy Simulation of the lean-premixed PRECCINSTA burner with wall heat loss," *Proceedings of the Combustion Institute*, vol. 37, pp. 5233–5243, Jan. 2019.

[67] V. Moureau, P. Domingo, and L. Vervisch, "Design of a massively parallel cfd code for complex geometries," *Comptes Rendus Mécanique*, vol. 339, no. 2, pp. 141–148, 2011.

[68] H. Pitsch, "Large-eddy simulation of turbulent combustion," *Annu. Rev. Fluid Mech.*, vol. 38, pp. 453–482, 2006.

[69] K. Bray, "The challenge of turbulent combustion," *Symposium (International) on Combustion*, vol. 26, no. 1, pp. 1 – 26, 1996.

[70] E. E. O´Brien, "The probability density function (pdf) approach to reacting turbulent flows," in *Turbulent reacting flows*, pp. 185–218, Springer, 1980.

[71] S. B. Pope, "Pdf methods for turbulent reactive flows," *Progress in Energy and Combustion Science*, vol. 11, no. 2, pp. 119–192, 1985.

[72] F. Williams, "Turbulent combustion," *The mathematics of combustion*, vol. 2, pp. 267–294, 1985.

[73] H. Pitsch, "A consistent level set formulation for large-eddy simulation of premixed turbulent combustion," *Combustion and Flame*, vol. 143, no. 4, pp. 587–598, 2005.

[74] M. Boger, D. Veynante, H. Boughanem, and A. Trouvé, "Direct numerical simulation analysis of flame surface density concept for large eddy simulation of turbulent premixed combustion," in *Symposium (International) on Combustion*, vol. 27, pp. 917–925, Elsevier, 1998.

[75] T. D. Butler and P. J. O´Rourke, "A numerical method for two dimensional unsteady reacting flows," in *Symposium (International) on Combustion*, vol. 16, pp. 1503–1515, Elsevier, 1977.

[76] P. J. O´Rourke and F. V. Bracco, "Two scaling transformations for the numerical computation of multidimensional unsteady laminar flames," *Journal of Computational Physics*, vol. 33, no. 2, pp. 185–203, 1979.

[77] F. Williams, *Combustion Theory: The Fundamental Theory of Chemically Reacting Flow Systems*. Combustion science and engineering series, Perseus Books Group, 1985.

[78] O. Colin, F. Ducros, D. Veynante, and T. Poinsot, "A thickened flame model for large eddy simulations of turbulent premixed combustion," *Physics of Fluids (1994-present)*, vol. 12, no. 7, pp. 1843–1863, 2000.

[79] T. Poinsot, D. Veynante, A. Trouvé, and G. Ruetsch, "Turbulent flame propagation in partially premixed flames," pp. 111–136, Center for turbulent reasearch, NASA Ames/Stanford University, USA, 1996.

[80] C. Meneveau and T. Poinsot, "Stretching and quenching of flamelets in premixed turbulent combustion," *Combustion and Flame*, vol. 86, no. 4, pp. 311–332, 1991.

[81] C. Angelberger, D. Veynante, F. Egolfopoulos, and T. Poinsot, "Large eddy simulations of combustion instabilities in premixed flames," in *Proc. of the summer program*, pp. 61–82, 1998.

[82] F. Charlette, C. Meneveau, and D. Veynante, "A power-law flame wrinkling model for les of premixed turbulent combustion part II: dynamic formulation," *Combustion and Flame*, vol. 131, no. 1–2, pp. 181 – 197, 2002.

[83] G. Wang, M. Boileau, and D. Veynante, "Implementation of a dynamic thickened flame model for large eddy simulations of turbulent premixed combustion," *Combustion and Flame*, vol. 158, no. 11, pp. 2199–2213, 2011.

[84] J. P. Legier, T. Poinsot, and D. Veynante, "Dynamically thickened flame les model for premixed and non-premixed turbulent combustion," in *Proc. of the summer program*, pp. 157–168, Citeseer, 2000.

[85] P. Benard, *Analyse et amélioration d´une chambre de combustion centimétrique par simulation aux grandes échelles*. Phd thesis, Rouen, INSA, 2015.

[86] B. G. Franzelli, *Impact of the chemical description on direct numerical simulations and large eddy simulations of turbulent combustion in industrial aero-engines*. PhD thesis, INPT, 2011.

[87] K. Kanov, R. Burns, C. Lalescu, and G. Eyink, "The johns hopkins turbulence databases: an open simulation laboratory for turbulence research," *Comput. Sci. Eng.*, vol. 17, pp. 10–17, 2015.

[88] K. Gurney, *An introduction to neural networks*. CRC press, 2014.

[89] J. A. Blasco, N. Fueyo, C. Dopazo, and J. Ballester, "Modelling the temporal evolution of a reduced combustion chemical system with artificial neural network," *Combust. Flame*, vol. 113, no. 1-2, pp. 38–52, 1998.

[90] F. C. Christo, A. R. Masri, and E. M. Nebot, "Artificial neural network implementation of chemistry with pdf simulation of H2/CO2 flames," *Combust. Flame*, vol. 106, pp. 406–427, 1996.

[91] B. A. Sen, E. R. Hawkes, and S. Menon, "Large eddy simulation of extinction and reignition with artificial neural networks based chemical kinetics," *Combust. Flame*, vol. 157, no. 3, pp. 566–578, 2010.

[92] B. A. Sen and S. Menon, "Large eddy mixing based tabulation and artificial neural networks for large eddy simulations of turbulent flames," *Combust. Flame*, vol. 157, no. 1, pp. 62–74, 2010.

[93] L. L. Franke, A. K. Chatzopoulos, and S. Rigopoulos, "Tabulation of combustion chemistry via Artificial Neural Networks (ANNs): Methodology and application to LES-PDF simulation of Sydney flame L," *Combust. Flame*, vol. 185, pp. 245–260, 2017.

[94] T. Abbas, M. M. Awai, and F. C. Lockwood, "An artificial intelligence treatment of devolatilization for pulverized coal and biomass in co-fired flames," *Combust. Flame*, vol. 132, no. 3, pp. 305–318, 2003.

[95] Y. Lecun, Y. Bengio, and G. Hinton, "Deep learning," *Nature*, vol. 521, pp. 436–444, 2015.

[96] J. Schmidhuber, "Deep learning in neural networks: An overview," *Neural Networks*, vol. 61, pp. 85–117, 2015.

[97] Z. M. Nikolaou, C. Chrysostomou, L. Vervisch, and S. Cant, "Modelling turbulent premixed flames using convolutional neural networks: application to sub-grid scale variance and filtered reaction rate," *arXiv preprint arXiv:1810.07944*, 2018.

[98] K. N. C. Bray, "The challenge of turbulent combustion," *Symp. (Int.) on Combust.*, vol. 26, pp. 1–26, 1996.

[99] C. J. Lapeyre, A. Misdariis, N. Cazards, D. Veynante, and T. Poinsot, "Training convolutional neural networks to estimate turbulent sub-grid scale reaction rates," *Combust. Flame*, vol. 203, pp. 255–264, 2019.

[100] R. Ranade, S. Alqahtani, A. Farooq, and T. Echekki, "An ANN based hybrid chemistry framework for complex fuels," *Fuel*, vol. 241, pp. 625–636, 2019.

[101] W. Jiang, X. Xing, X. Zhang, and M. Mi, "Prediction of combustion activation energy of naoh/koh catalyzed straw pyrolytic carbon based on machine learning," *Renewable energy*, vol. 130, pp. 1216–1225, 2019.

[102] AI Research Institute Asimov, https://www.asimovinstitute.org/.

[103] J.-B. Moss and K. Bray, "A unified statistical model of the premixed turbulent flame," *Acta Astronautica*, vol. 4, pp. 291–319, 1977.

[104] C. Mehl, J. Idier, and B. Fiorina, "Evaluation of deconvolution modelling applied to numerical combustion," *Combust. Theory Modelling*, vol. 22, no. 1, pp. 38–70, 2018.

[105] O. Gicquel, N. Darabiha, and D. Thevenin, "Laminar premixed hydrogen / air counterflow flame simulations using flame prolongation of ILDM with differential diffusion," *Proc. Comb. Inst.*, vol. 28, pp. 1901–1908, 2000.

[106] J. A. van Oijen, F. A. Lammers, and L. P. H. de Goey, "Modeling of complex premixed burner systems by using flamelet-generated manifolds," *Combust. Flame*, vol. 127, no. 3, pp. 2124–2134, 2001.

[107] P.-D. Nguyen, L. Vervisch, V. Subramanian, and P. Domingo, "Multidimensional flamelet-generated manifolds for partially premixed combustion," *Combust. Flame*, vol. 157, no. 1, pp. 43–61, 2010.

[108] A. Scholtissek, P. Domingo, L. Vervisch, and C. Hasse, "A self-contained progress variable space solution method for thermochemical variables and flame speed in freely-propagating premixed flamelets," *Proc. Combust. Inst.*, vol. 27, no. 2, pp. 1529–1536, 2019.

[109] Y.-S. Niu, L. Vervisch, and P. D. Tao, "An optimization-based approach to detailed chemistry tabulation: Automated progress variables definition," *Combust. Flame*, vol. 160, no. 4, pp. 776–785, 2013.

[110] U. Prufert, S. Hartl, F. Hunger, D. Messig, M. Eiermann, and C. Hasse, "A constrained control approach for the automated choice of an optimal progress variable for chemistry tabulation," *Flow Turbulence Combust.*, vol. 94, no. 3, pp. 593–617, 2015.

[111] M. Ihme, L. Shunn, and J. Zhang, "Regularization of reaction progress variable for application to flamelet-based combustion models," *J. Comput. Phys.*, vol. 231, pp. 7715–7721, 2012.

[112] M.-S. Benzinger, R. Schiessl, and U. Maas, "A versatile coupled progress variable / REDIM model for auto-ignition and combustion," *Proc. Combust. Inst.*, vol. 36, no. 3, pp. 3613–3621, 2017.

[113] S. Nambully, P. Domingo, V. Moureau, and L. Vervisch, "A Filtered-Laminar-Flame PDF subgrid scale closure for LES of premixed turbulent flames. Part I: Formalism and application to a bluff-body burner with differential diffusion," *Combust. Flame*, vol. 161, no. 7, pp. 1756–1774, 2014.

[114] J. A. van Oijen, A. Donini, R. J. M. Bastiaans, J. H. M. tenThije Boonkkamp, and L. P. H. de Goey, "State-of-the-art in premixed combustion modeling using flamelet generated manifolds," *Progress Energy Combust. Sci.*, vol. 57, pp. 30 – 74, 2016.

[115] P. Domingo, L. Vervisch, and D. Veynante, "Large-Eddy Simulation of a lifted methane-air jet flame in a vitiated coflow," *Combust. Flame*, vol. 152, no. 3, pp. 415–432, 2008.

[116] V. Subramanian, P. Domingo, and L. Vervisch, "Large-eddy simulation of forced ignition of an annular bluff-body burner," *Combust. Flame*, vol. 157, no. 3, pp. 579–601, 2010.

[117] J. Lai and N. Chakraborty, "Modeling of progress variable variance transport in head-on quenching of turbulent premixed flames: A direct numerical simulation analysis," *Combust. Sci. Tech.*, vol. 188, no. 11-12, pp. 1925–1950, 2016.

[118] G. Lecocq, S. Richard, O. Colin, and L. Vervisch, "Hybrid presumed pdf and flame surface density approach for large-eddy simulation of premixed turbulent combustion, part 1: Formalism and simulations of a quasi-steady burner," *Combust. Flame*, vol. 158, no. 6, pp. 1201–1214, 2011.

[119] G. Lecocq, S. Richard, O. Colin, and L. Vervisch, "Hybrid presumed pdf and flame surface density approach for large-eddy simulation of premixed turbulent combustion, part 2: Early flame development after sparking," *Combust. Flame*, vol. 158, no. 6, pp. 1215–1226, 2011.

[120] N. Enjalbert, P. Domingo, and L. Vervisch, "Mixing time-history effects in large eddy simulation of non-premixed turbulent flames: Flow-controlled chemistry tabulation," *Combust. Flame*, vol. 159, no. 1, pp. 336–352, 2012.

[121] L. Valino, "A field monte carlo formulation for calculating the probability density function of a single scalar in turbulent flow," *Flow Turbulence Combust.*, vol. 60, no. 2, pp. 157–172, 1998.

[122] A. Avdić, G. Kuenne, and J. Janicka, "Flow physics of a bluff-body swirl stabilized flame and their prediction by means of a joint eulerian stochastic field and tabulated chemistry approach," *Flow Turbulence Combust.*, vol. 97, no. 4, pp. 1185–1210, 2016.

[123] B. Fiorina, R. Vicquelin, P. Auzillon, N. Darabiha, O. Gicquel, and D. Veynante, "A filtered tabulated chemistry model for LES of premixed combustion," *Combust. Flame*, vol. 157, pp. 465–475, 2010.

[124] R. Mercier, T. Schmitt, D. Veynante, and B. Fiorina, "The influence of combustion sgs submodels on the resolved flame propagation. application to the les of the cambridge stratified flames," *Proc. Combust. Inst.*, vol. 35, no. 2, pp. 1259–1267, 2015.

[125] P. Domingo and L. Vervisch, "Large Eddy Simulation of premixed turbulent combustion using approximate deconvolution and explicit flame filtering," *Proc. Combust. Inst.*, vol. 35, no. 2, pp. 1349–1357, 2015.

[126] Q. Wang and M. Ihme, "Regularized deconvolution method for turbulent combustion modeling," *Combust. Flame*, vol. 176, pp. 125–142, 2017.

[127] P. Domingo and L. Vervisch, "DNS and approximate deconvolution as a tool to analyse one-dimensional filtered flame sub-grid scale modeling," *Combust. Flame*, vol. 177, pp. 109–122, 2017.

[128] Z. Nikolaou and L. Vervisch, "A priori assessment of an iterative deconvolution method for les sub-grid scale variance modelling," *Flow Turbulence Combust.*, vol. 101, no. 1, pp. 33–53, 2018.

[129] Z. Nikolaou, R. S. Cant, and L. Vervisch, "Scalar flux modelling in turbulent flames using iterative deconvolution," *Phys. Rev. Fluids.*, vol. 3, no. 4, p. 043201, 2018.

[130] R. Borghi, "Mise au point sur la structure des flammes turbulentes," *J. Chimie Physique*, vol. 81, no. 6, pp. 361–370, 1984.

[131] L. Cifuentes, C. Dopazo, J. Martin, P. Domingo, and L. Vervisch, "Local volumetric dilatation rate and scalar geometries in a premixed methane-air turbulent jet flame," *Proc. Combust. Inst.*, vol. 35, no. 2, pp. 1295–1303, 2015.

[132] L. Cifuentes, C. Dopazo, J. Martin, P. Domingo, and L. Vervisch, "Effects of the local flow topologies upon the structure of a premixed methane-air turbulent jet flame," *Flow Turbulence Combust.*, vol. 96, no. 2, pp. 535–546, 2016.

[133] Y.-C. Chen, N. Peters, G. A. Schneemann, N. Wruck, U. Renz, and M. S. Mansour, "The detailed flame structure of highly stretched turbulent premixed methane-air flames," *Combust. Flame*, vol. 107, no. 3, pp. 223–244, 1996.

[134] G. P. Smith, D. M. Golden, M. Frenklach, N. W. Moriarty, B. Eiteneer, M. Goldenberg, C. T. Bowman, R. K. Hanson, S. Song, W. C. Gardiner, V. V. Lissianski, and Z. Qin tech. rep., 1999. http://www.me.berkeley.edu/gri-mech/.

[135] G. Godel, P. Domingo, and L. Vervisch, "Tabulation of nox chemistry for large-eddy simulation of non-premixed turbulent flames," *Proc. Combust. Inst.*, vol. 32, pp. 1555–1561, 2009.

[136] A. W. Vreman, "An eddy-viscosity subgrid-scale model for turbulent shear flow: Algebraic theory and applications," *Phys. Fluids.*, vol. 16, no. 10, pp. 3670–3681, 2004.

[137] L. Bouheraoua, P. Domingo, and G. Ribert, "Large-eddy simulation of a supersonic lifted jet flame: Analysis of the turbulent flame base," *Combust. Flame*, vol. 179, pp. 199–218, 2017.

[138] F. Ducros, F. Laporte, T. Soulères, V. Guinot, P. Moinat, and B. Caruelle, "High-order fluxes for conservative skew-symmetric-like schemes in structured meshes: application to compressible flows," *J. Comput. Phys.*, vol. 161, pp. 114–139, 2000.

[139] G. Lodato, P. Domingo, and L. Vervisch, "Three-dimensional boundary conditions for direct and large-eddy simulation of compressible viscous flows," *J. Comput. Phys*, vol. 227, no. 10, pp. 5105–5143, 2008.

[140] M. Klein, A. Sadiki, and J. Janicka, "A digital filter based generation of inflow data for spatially developing direct numerical or large eddy simulations," *J. Comp. Physics*, vol. 186, no. 2, pp. 652–665, 2002.

[141] D. Veynante, A. Trouvé, K. Bray, and T. Mantel, "Gradient and counter-gradient scalar transport in turbulent premixed flames," *J. Fluid Mech.*, vol. 332, pp. 263–293, 1997.

[142] D. Veynante and L. Vervisch, "Turbulent combustion modeling," *Prog Energy Combust Sci*, vol. 28, pp. 193–266, 2002.

[143] P.-T. de Boer, D. P. Kroese, S. S. Mannor, and R. Y. Rubinstein, "A tutorial on the cross-entropy method," *Annals Operations Research*, vol. 134, no. 1, pp. 19–67, 2005.

[144] D. P. Kingma and J. L. Ba, "ADAM: A method for stochastic optimization." https://arxiv.org/pdf/1412.6980, 2017.

[145] N. Jaouen, L. Vervisch, P. Domingo, and G. Ribert, "Automatic reduction and optimisation of chemistry for turbulent combustion modeling: Impact of the canonical problem," *Combust. Flame*, vol. 175, pp. 60–79, 2017.

[146] N. Jaouen, L. Vervisch, and P. Domingo, "Auto-thermal reforming (ATR) of natural gas: An automated derivation of optimised reduced chemical schemes," *Proc. Combust. Inst.*, vol. 36, no. 3, pp. 3321–3330, 2017.

[147] N. Jaouen, *An automated approach to derive and optimise reduced chemical mechanisms for turbulent combustion*. Phd thesis, INSA Rouen, 2017.

[148] K. Wan, C. Barnaud, L. Vervisch, and P. Domingo, "Chemistry reduction using machine learning trained from non-premixed micro-mixing modeling: Application to dns of a syngas turbulent oxy-flame with side-wall effects," *Combustion and Flame*, vol. 220, pp. 119–129, 2020.

[149] P. Pepiot and H. Pitsch, "Systematic reduction of large chemical mechanisms," in *4th joint meeting of the US Sections of the Combustion Institute, Philadelphia, PA*, 2005.

[150] R. I. Curl, "Dispersed phase mixing. Theory and effects in simple reactors," *AIChE*, vol. 9, no. 2, pp. 175–181, 1963.

[151] C. Dopazo and E. O'Brien, "Functional formulation of nonisothermal turbulent reactive flows," *Phys. Fluids*, vol. 17, pp. 1968–1975, 1974.

[152] R. Borghi, "Turbulent combustion modelling," *Prog. Energy Combust. Sci.*, vol. 14, pp. 245–292, 1988.

[153] K. Narayanaswamy, H. Pitsch, and P. Pepiot, "A component library framework for deriving kinetic mechanisms for multi-component fuel surrogates: Application for jet fuel surrogates," *Combust. Flame*, vol. 165, pp. 288–309, 2016.

[154] C. Montgomery, S. Cannon, M. Mawid, and B. Sekar, "Reduced chemical kinetic mechanisms for JP-8 combustion," in *40th AIAA Aerospace Sciences Meeting*, 2002.

[155] Z. Zhao, J. Li, A. Kazakov, F. L. Dryer, and S. P. Zeppieri, "Burning velocities and a high-temperature skeletal kinetic model for n-decane," *Combust. Sci. Tech.*, vol. 177, no. 1, 2004.

[156] S. Vasu, D. Davidson, and R. Hanson, "Jet fuel ignition delay times: Shock tube experiments over wide conditions and surrogate model predictions," *Combust. Flame*, vol. 152, no. 12, pp. 125–143, 2008.

[157] P. Dagaut, "On the kinetics of hydrocarbons oxidation from natural gas to kerosene and diesel fuel," *Physical Chemistry Chemical Physics*, vol. 4, no. 11, pp. 2079–2094, 2002.

[158] J. Luche, M. Reuillon, J.-C. Boettner, and M. Cathonnet, "Reduction of large detailed kinetic mechanisms: application to kerosene/air combustion," *Combust. Sci. and Tech.*, vol. 176, no. 11, pp. 1935–1963, 2004.

[159] J. Luche, *Elaboration of reduced kinetic models of combustion. Application to a kerosene mechanism*. PhD thesis, LCSR Orleans, 2003.

[160] L. Vervisch, B. Labegorre, and J. Réveillon, "Hydrogen-sulphur oxy-flame analysis and single-step flame tabulated chemistry," *Fuel*, vol. 83, no. 4-5, pp. 605–614, 2004.

[161] E. Fernández-Tarrazo, A. L. Sánchez, A. Liñán, and F. A. Williams, "A simple one-step chemistry model for partially premixed hydrocarbon combustion," *Combust. Flame*, vol. 147, no. 1-2, pp. 32–38, 2006.

[162] B. Franzelli, E. Riber, M. Sanjosé, and T. Poinsot, "A two-step chemical scheme for kerosene-air premixed flames," *Combust. Flame*, vol. 157, no. 7, pp. 1364–1373, 2010.

[163] G. Tsatsaronis, "Prediction of propagating laminar flames in methane, oxygen, nitrogen mixtures," *Combust. Flame*, vol. 33, pp. 217–239, 1978.

[164] O. Hadaller and J. Johnson, "World fuel sampling program," *Coordinating Research Council, Inc., CRC Report*, no. 647, 2006.

[165] T. Edwards, M. Colket, N. Cernansky, F. Dryer, F. Egolfopoulos, D. Friend, E. Law, D. Lenhert, P. Lindstedt, H. Pitsch, *et al.*, "Development of an experimental database and kinetic models for surrogate jet fuels," in *45th AIAA Aerospace Sciences Meeting and Exhibit*, p. 770, 2007.

[166] A. Violi, S. Yan, E. Eddings, A. Sarofim, S. Granata, T. Faravelli, and E. Ranzi, "Experimental formulation and kinetic model for jp-8 surrogate mixtures," *Combustion Science and Technology*, vol. 174, no. 11-12, pp. 399–417, 2002.

[167] T. Edwards, "Liquid fuels and propellants for aerospace propulsion: 1903-2003," *Journal of propulsion and power*, vol. 19, no. 6, pp. 1089–1107, 2003.

[168] M. L. Huber, E. W. Lemmon, and T. J. Bruno, "Surrogate mixture models for the thermophysical properties of aviation fuel jet-a," *Energy & Fuels*, vol. 24, no. 6, pp. 3565–3571, 2010.

[169] C. Wood, V. McDonell, R. Smith, and G. Samuelsen, "Development and application of a surrogate distillate fuel," *Journal of propulsion and Power*, vol. 5, no. 4, pp. 399–405, 1989.

[170] B. L. Smith and T. J. Bruno, "Improvements in the measurement of distillation curves. 4. application to the aviation turbine fuel jet-a," *Industrial & engineering chemistry research*, vol. 46, no. 1, pp. 310–320, 2007.

[171] P. Dagaut, M. Reuillon, J.-C. Boettner, and M. Cathonnet, "Kerosene combustion at pressures up to 40 atm: Experimental study and detailed chemical kinetic modeling," in *Symposium (International) on Combustion*, vol. 25, pp. 919–926, Elsevier, 1994.

[172] D. Voisin, *Cinétique chimique d'oxydation d'hydrocarbures et obtention d'un modèle pour la combustion du kérosène*. PhD thesis, Université d'Orléans, 1997.

[173] M. Cathonnet, D. Voisin, A. Etsouli, C. Sferdean, M. Reuillon, J. Boettner, and P. Dagaut, "Kerosene combustion modelling using detailed and reduced chemical kinetic mechanisms," in *RTO Meeting proceedings*, 1999.

[174] P. Patterson, A. Kyne, M. Pourkashanian, A. Williams, and C. Wilson, "Combustion of kerosene in counterflow diffusion flames," *Journal of Propulsion and Power*, vol. 17, no. 2, pp. 453–460, 2001.

[175] J. Luche, *Obtention de modèles cinétiques réduits de combustion-Application à un mécanisme du kérosène*. PhD thesis, Université d'Orléans, 2003.

[176] T. Edwards and L. Q. Maurice, "Surrogate mixtures to represent complex aviation and rocket fuels," *Journal of Propulsion and Power*, vol. 17, no. 2, pp. 461–466, 2001.

[177] N. A. Slavinskaya, A. Zizin, and M. Aigner, "On model design of a surrogate fuel formulation," *Journal of Engineering for Gas Turbines and Power*, vol. 132, no. 11, p. 111501, 2010.

[178] T. J. Bruno and B. L. Smith, "Evaluation of the physicochemical authenticity of aviation kerosene surrogate mixtures. part 1: Analysis of volatility with the advanced distillation curve," *Energy & Fuels*, vol. 24, no. 8, pp. 4266–4276, 2010.

[179] T. J. Bruno and M. L. Huber, "Evaluation of the physicochemical authenticity of aviation kerosene surrogate mixtures. part 2: Analysis and prediction of thermophysical properties," *Energy & Fuels*, vol. 24, no. 8, pp. 4277–4284, 2010.

[180] R. Xu, H. Wang, R. Hanson, D. Davidson, C. Bowman, and F. Egolfopoulos, "Evidence supporting a simplified approach to modeling high-temperature combustion chemistry," in *10th US National Meeting on Combustion, College Park, MD*, 2017.

[181] R. Xu, D. Chen, K. Wang, Y. Tao, J. Shao, T. Parise, Y. Zhu, S. Wang, R. Zhao, D. Lee, *et al.*, "Hychem model: application to petroleum-derived jet fuels," in *10th US National Meeting on Combustion, College Park, MD*, vol. 69, pp. 70–77, 2017.

[182] A. Bouaniche, L. Vervisch, and P. Domingo, "A hybrid stochastic/fixed-sectional method for solving the population balance equation," *Chemical Engineering Science*, vol. 209, p. 115198, 2019.

[183] J. McKinnon and J. Howard, "The roles of pah and acetylene in soot nucleation and growth," *in Twenty-Fourth Symposium (International) on Combustion. The Combustion Institute*, pp. 965–971, 1992.

[184] H. W. Kroto, J. R. Heath, S. C. O'Brien, R. F. Curl, and R. E. Smalley, "C60: Buckminsterfullerene," *nature*, vol. 318, no. 6042, pp. 162–163, 1985.

[185] J. Cami, J. Bernard-Salas, E. Peeters, and S. E. Malek, "Detection of c60 and c70 in a young planetary nebula," *Science*, vol. 329, no. 5996, pp. 1180–1182, 2010.

[186] P. Ehrenfreund and B. H. Foing, "Fullerenes and cosmic carbon," *Science*, vol. 329, no. 5996, pp. 1159–1160, 2010.

[187] J. Nyons, "Advanced diagnostics and experimentally derived optical properties," in *GDR Suie*, 2017.

[188] D. Liu and al., "Black-carbon absorption enhancement in the atmosphere determined by particle mixing state," *Nature Geoscience*, vol. 10, pp. 184–188, 2017.

[189] M. R. Kholghy, A. Veshkini, and M. J. Thomson, "The core-shell internal nanostructure of soot - a criterion to model soot maturity," *Carbon*, vol. 100, pp. 508–536, 2016.

[190] M. Frenklach, "Reaction mechanism of soot formation in flames," *Phys. Chem. Phys. Chem.*, vol. 4, pp. 2028–2037, 2002.

[191] B. S. Haynes and H. G. Wagner, "Soot formation," *Prog. Energy Combust. Sci.*, vol. 7, pp. 229–273, 1981.

[192] H. Bockhorn, F. Fetting, and H. W. Wenz, "Investigation of the formation of high molecular hydrocarbons and soot in premixed hydrocarbon-oxygen flames," *Phys. Chem.*, vol. 87, pp. 1067–1073, 1983.

[193] C. S. McEnally and L. D. Pfefferle, "Improved sooting tendency measurements for aromatic hydrocarbons and their implications for naphthalene formation pathways," *Comb. Flame*, vol. 148, pp. 210–222, 2007.

[194] J. A. Miller and S. J. Klippenstein, "The recombination of propargyl radicals and other reactions on a c6h6 potential," *The Journal of Physical Chemistry A*, vol. 107, pp. 7783–7799, 2003.

[195] P. Westmoreland, *The prehistory of soot: small rings from small molecules in: Combustion Generated Fine Carbonaceous Particles*. KIT Scientific Publishing, Chap. 3, 2009.

[196] M. Frenklach and D. W. Clary, "Detailed kinetic modeling of soot formation in shock-tube pyrolysis of acetylene," *Symposium (International) on Combustion*, vol. 20, pp. 887–901, 1985.

[197] J. D. Bittner and J. B. Howard, "Composition profiles and reaction mechanisms in a near-sooting premixed benzene/oxygen/argon flame," *Symposium (International) on Combustion*, vol. 18, pp. 1105–1116, 1981.

[198] J. A. Miller and C. F. Melius, "Kinetic and thermodynamic issues in the formation of aromatic compounds in flames of aliphatic fuels," *Comb. Flame*, vol. 91, pp. 21–39, 1992.

[199] U. Alkemade and K. H. Homann, "Formation of c6h6 isomers by recombination of propynyl in the system sodium vapour/propynylhalide," *Z. Phys. Chem. N. F.*, vol. 161, pp. 19–34, 1989.

[200] M. Frenklach and H. Wang, "Detailed modeling of soot particle nucleation and growth," *Symposium (International) on Combustion*, vol. 23, pp. 1559–1566, 1991.

[201] H. Wang and M. Frenklach, "A detailed kinetic modeling study of aromatics formation in laminar premixed acetylene and ethylene flames," *Comb. Flame*, vol. 110, pp. 173–221, 1997.

[202] M. Frenklach and J. Warnatz, "Detailed modeling of pah profiles in a sooting low-pressure acetylene flame," *Combust. Sci. Technol.*, vol. 51, pp. 265–283, 1987.

[203] M. Frenklach, N. W. Moriarty, and N. J. Brown, "Hydrogen migration in polyaromatic growth," *Symposium (International) on Combustion*, vol. 27, pp. 1655–1661, 1998.

[204] M. Frenklach and H. Wang, *Soot Formation in Combustion: Mechanisms and Models*. Springer Science, pp. 165, 1994.

[205] C. A. Schuetz and M. Frenklach, "Nucleation of soot: Molecular dynamics simulations of pyrene dimerization," *Proc. Comb. Inst.*, vol. 29, pp. 2307–2314, 2002.

[206] D. Wong, R. Whitesides, C. A. Schuetz, and M. Frenklach, *Combustion Generated Fine Carbonaceous Particles*. Karlsruhe University Press, pp. 247-258, 2009.

[207] S. J. Harris and A. M. Weimer, "Chemical kinetics of soot particle growth," *Annu. Rev. Phys. Chem.*, vol. 36, pp. 31–52, 1985.

[208] F. Xu, P. B. Sunderland, and G. M. Faeth, "Soot formation in laminar premixed ethylene/air flames at atmospheric pressure," *Comb. Flame*, vol. 108, pp. 471–493, 1997.

[209] F. Xu, K.-C. Lin, and G. M. Faeth, "Soot formation in laminar premixed methane/oxygen flames at atmospheric pressure," *Comb. Flame*, vol. 115, pp. 195–209, 1998.

[210] F. Xu and G. M. Faeth, "Structure of the soot growth region of laminar premixed methane/oxygen flames," *Comb. Flame*, vol. 121, pp. 640–650, 2000.

[211] F. Xu and G. M. Faeth, "Soot formation in laminar acetylene/air diffusion flames at atmospheric pressure," *Comb. Flame*, vol. 125, pp. 804–819, 2001.

[212] B. Zhao, K. Uchikawa, and H. Wang, "A comparative study of nanoparticles in premixed flames by scanning mobility particle sizer, small angle neutron scattering, and transmission electron microscopy," *Proc. Comb. Inst.*, vol. 31, pp. 851–860, 2007.

[213] P. Mitchell and M. Frenklach, "Monte carlo simulation of soot aggregation with simultaneous surface growth-why primary particles appear spherical," *Symposium (International) on Combustion*, vol. 27, pp. 1507–1514, 1998.

[214] N. Morgan, M. Kraft, M. Balthasar, D. Wong, M. Frenklach, and P. Mitchell, "Numerical simulations of soot aggregation in premixed laminar flames," *Proc. Comb. Inst.*, vol. 31, pp. 693–700, 2007.

[215] A. Kazakov and M. Frenklach, "Dynamic modeling of soot particle coagulation and aggregation: Implementation with the method of moments and application to high-pressure laminar premixed flames," *Comb. Flame*, vol. 114, pp. 484–501, 1998.

[216] B. Zhao, Z. Yang, M. Johnston, H. Wang, A. Wexler, and M. Balthasar, "Measurement and numerical simulation of soot particle size distribution functions in a laminar premixed ethylene-oxygen-argon flame," *Comb. Flame*, vol. 133, pp. 173–188, 2003.

[217] M. Commodo, A. D'Anna, G. D. Falco, R. Larciprete, and P. Minutolo, "Illuminating the earliest stages of the soot formation by photoemission and raman spectroscopy," *Comb. Flame*, vol. 181, pp. 188–197, 2017.

[218] K. Zhou, "Monte carlo simulation for soot dynamics," *Thermal Science*, vol. 16, no. 5, pp. 1391–1394, 2012.

[219] K. G. Neoh, J. B. Howard, and A. F. Sarofim, *Particulate Carbon Formation during Combustion*. Plenum Press, pp. 261-277, 1981.

[220] J. Nagle and R. F. Strickland-Constable, *Proceedings of the fifth Carbon Conf.*, vol. 1. Pergamon Press, pp. 154-164, 1962.

[221] A. Kazakov, H. Wang, and M. Frenklach, "Detailed modeling of soot formation in laminar premixed ethylene flames at a pressure of 10 bar," *Comb. Flame*, pp. 111–120, 1995.

[222] K. Neoh, *Soot Burnout in Flames*. PhD thesis, Massachusetts Institute of Technology, 1981.

[223] K. Neoh, J. Howard, and A. Sarofim, "Effect of oxidation on the physical structure of soot," *Symposium (International) on Combustion*, vol. 20, pp. 951–957, 1985.

[224] C. Echavarria, I. Jaramillo, A. Sarofim, and J. Lighty, *Studies of soot oxidation on a two-stage burner under fuel-lean conditions*. Western States Section/Combustion Institute, pp. 357-367, 2009.

[225] S. J. Harris and M. M. Maricq, "The role of fragmentation in defining the signature size distribution of diesel soot," *J. Aerosol Sci.*, vol. 33, pp. 935–942, 2002.

[226] M. E. Mueller, G. Blanquart, and H. Pitsch, "Modeling the oxidation-induced fragmentation of soot aggregates in laminar flames," *Proc. Comb. Inst.*, vol. 33, pp. 667–674, 2011.

[227] C. S. Yoo and H. G. Im, "Transient soot dynamics in turbulent nonpremixed ethylene–air counterflow flames," *Proc. Comb. Inst.*, vol. 31, pp. 701–708, 2007.

[228] K. M. Leung and R. P. Lindstedt, "A simplified reaction mechanism for soot formation in nonpremixed flames," *Comb. Flame*, vol. 87, pp. 289–305, 1991.

[229] D. Olson, J.C.Pickens, and R.J.Gill, "The effects of molecular structure on soot formation II. diffusion flames," *Comb. Flame*, vol. 62, pp. 43–60, 1985.

[230] I. M. Khan, G. Greeves, and D. M. Probert, "Air pollution control in transport engines," *The institution of Mechanical Engineers*, vol. C142/71, pp. 205–217, 1971.

[231] R. B. Edelman and P. T. Harsha, "Laminar and turbulent gas dynamics in combustors – current status," *Prog. Energ. Combust. Sci.*, vol. 4, pp. 1–62, 1978.

[232] N. K. Rizk and H. C. Mongia, "Three-dimensional analysis of gas turbine combustors," *J. Propuls.*, vol. 7, pp. 445–451, 1991.

[233] H. M. Hulburt and S. Katz, "Some problems in particle technology - a statistical mechanical formulation," *Chem. Eng. Sci.*, vol. 19, pp. 555–574, 1964.

[234] A. Randolph and M. Larson, "Theory of particulate processes," *Academic Press*, 1971.

[235] D. L. Marchisio and R. O. Fox, "Solution of population balance equations using the direct quadrature method of moments," *Aero. Sci.*, vol. 36, pp. 43–73, 2005.

[236] M. E. Mueller, G. Blanquart, and H. Pitsch, "Hybrid method of moments for modeling soot formation and growth," *Comb. Flame*, vol. 156, pp. 1143–1155, 2009.

[237] D. Ramkrishna, "Theory and applications to particulate systems in engineering," *Population Balances. Academic Press, San Diego*, 2000.

[238] A. Bouaniche, J. Yon, P. Domingo, and L. Vervisch, "Analysis of the soot particle size distribution in a laminar premixed flame: A hybrid stochastic/fixed-sectional approach," *Flow, Turbulence and Combustion*, vol. 104, pp. 753–775, 2020.

[239] J. Appel, H. Bockhorn, and M. Frenklach, "Kinetic modeling of soot formation with detailed chemistry and physics: laminar premixed flames of c2 hydrocarbons," *Combustion and flame*, vol. 121, no. 1-2, pp. 122–136, 2000.

[240] A. A. Wray, "Minimal storage time advancement schemes for spectral methods," *NASA Ames Research Center, California, Report No. MS*, vol. 202, 1990.

[241] C. Doute, J.-L. Delfau, R. Akrich, and C. Vovelle, "Chemical structure of atmospheric pressure premixed n-decane and kerosene flames," *Combustion Science and Technology*, vol. 106, no. 4-6, pp. 327–344, 1995.

[242] Y. Wang, A. Raj, and S. H. Chung, "A PAH growth mechanism and synergistic effect on PAH formation in counterflow diffusion flames," *Combustion and flame*, vol. 160, no. 9, pp. 1667–1676, 2013.

[243] R. Xu, K. Wang, S. Banerjee, J. Shao, T. Parise, Y. Zhu, S. Wang, A. Movaghar, D. J. Lee, R. Zhao, *et al.*, "A physics-based approach to modeling real-fuel combustion chemistry–II. reaction kinetic models of jet and rocket fuels," *Combustion and Flame*, vol. 193, pp. 520–537, 2018.

[244] T. Zhang, L. Zhao, M. R. Kholghy, S. Thion, and M. J. Thomson, "Detailed investigation of soot formation from jet fuel in a diffusion flame with comprehensive and hybrid chemical mechanisms," *Proceedings of the Combustion Institute*, vol. 37, no. 2, pp. 2037–2045, 2019.

[245] S. Dooley, S. H. Won, J. Heyne, T. I. Farouk, Y. Ju, F. L. Dryer, K. Kumar, X. Hui, C.-J. Sung, H. Wang, *et al.*, "The experimental evaluation of a methodology for surrogate fuel formulation to emulate gas phase combustion kinetic phenomena," *Combustion and Flame*, vol. 159, no. 4, pp. 1444–1466, 2012.

[246] I. M. Kennedy, "The suppression of soot particle formation in laminar and turbulent diffusion flames," *Combustion science and technology*, vol. 59, no. 1-3, pp. 107–121, 1988.

[247] M. Lucchesi, A. Abdelgadir, A. Attili, and F. Bisetti, "Simulation and analysis of the soot particle size distribution in a turbulent nonpremixed flame," *Combustion and Flame*, vol. 178, pp. 35–45, 2017.

[248] F. Bisetti, G. Blanquart, M. E. Mueller, and H. Pitsch, "On the formation and early evolution of soot in turbulent nonpremixed flames," *Combustion and Flame*, vol. 159, no. 1, pp. 317–335, 2012.

[249] F. Sewerin and S. Rigopoulos, "An les-pbe-pdf approach for predicting the soot particle size distribution in turbulent flames," *Combustion and Flame*, vol. 189, pp. 62–76, 2018.

[250] D. Delhaye, F.-X. Ouf, D. Ferry, I. K. Ortega, O. Penanhoat, S. Peillon, F. Salm, X. Vancassel, C. Focsa, C. Irimiea, *et al.*, "The mermose project: Characterization of particulate matter emissions of a commercial aircraft engine," *Journal of Aerosol Science*, vol. 105, pp. 48–63, 2017.

[251] S. Subramaniam and S. Pope, "A mixing model for turbulent reactive flows based on euclidean minimum spanning trees," *Combustion and Flame*, vol. 115, no. 4, pp. 487–514, 1998.

[252] F. Douce, N. Djebaïli-Chaumeix, C.-E. Paillard, C. Clinard, and J.-N. Rouzaud, "Soot formation from heavy hydrocarbons behind reflected shock waves," *Proceedings of the Combustion Institute*, vol. 28, no. 2, pp. 2523–2529, 2000.

[253] M. Kraushaar, *Application of the compressible and low-mach number approaches to large-eddy simulation of turbulent flows in aero-engines*. PhD thesis, INPT, 2011.

[254] C. Pio, "General sampling techniques," in *Handbook of Air Pollution Analysis*, pp. 1–93, Springer, 1986.

[255] M. Bouvier, J. Yon, G. Lefevre, and F. Grisch, "A novel approach for in-situ soot size distribution measurement based on spectrally resolved light scattering," *Journal of Quantitative Spectroscopy and Radiative Transfer*, vol. 225, pp. 58–68, 2019.

French summary

Face à l'urgence climatique, la réduction des polluants et de la consommation de carburant sont devenues une priorité pour l'industrie aéronautique. Les motoristes doivent maintenant développer des outils numériques précis pour quantifier les émissions de suie et de GES en sortie moteur, dans lesquels la modélisation de la chimie joue un rôle critique. Cette thèse propose une amélioration des outils numériques de réduction de la chimie, pour sa prise en compte dans des simulations haute fidélité. Ces outils sont validés avec la prédiction du CO dans un calcul LES. Les réseaux de neurone ont ensuite été proposés pour la fermeture des termes LES non résolus. Puis, une stratégie de réduction de modèle, basée sur un réseau de neurone, est présentée afin d'inclure une description détaillée de suies dans des simulations haute fidélité. Cette stratégie est testée sur une flamme prémélangée 1D, puis dans une simulation de chambre industrielle, et comparée à des mesures expérimentales.

Résumé du chapitre 3

Un nouveau cadre de modélisation utilisant l'apprentissage automatique est proposé pour fournir une fermeture pour tous les termes non résolus dans l'équation de transport de la variable de progrès filtrée dans les simulations grandes échelles de flammes turbulentes prémélangées, avec chimie tabulée. Les réseaux de neurones convolutifs sont entraînés à l'aide de données provenant d'une base de données de simulation numérique directe, afin de prédire le terme source filtré de la variable de progrès et les flux non résolus dans l'équation de transport filtrée de la variable de progrès. L'avantage de l'approche proposée dans cette étude est qu'une seule distribution de variable, facilement disponible, la variable de progrès filtrée, suffit. Les réseaux de neurones convolutifs ont montré qu'ils pouvaient fournir des prédictions quantitativement précises à la fois des termes source et des flux de transport de sous-maille, qui sont deux termes sensiblement différents et classiquement difficiles à modéliser dans un seul cadre. Il a également été démontré que les capacités de prédiction des réseaux n'étaient que faiblement insensibles aux variations de largeur de filtre, ce qui est un attribut important pour tout modèle de sous-maille. Parce qu'ils sont basés sur la variable de progrès, un paramètre générique des flammes prémélangées, les réseaux de neurone devraient bien être tout aussi prédictifs pour toute flamme prémélangée turbulente située dans le diagramme de régime de Borghi, proche des conditions utilisées pour l'entraînement.

Cependant, comme les chambres de combustion industrielles LES considérées dans cette thèse ne sont pas prémélangées, l'utilisation du modèle TFLES dynamique a été par la suite retenue.

Résumé du chapitre 4

Dans ce chapitre, une stratégie est discutée pour améliorer la réduction d'un schéma chimique détaillé du kérosène. Avec la procédure de réduction ORCh, des schémas de complexité décroissante sont générés à

partir d'un mécanisme détaillé de référence, dans le but de trouver le niveau minimum de complexité qui permet de capturer des propriétés des espèces cibles. Un problème de micro-mélange stochastique incluant l'évaporation du carburant liquide est construit pour sonder les différents schémas chimiques générés et pour effectuer l'optimisation des constantes d'Arrhénius avec un algorithme génétique. Les flux massiques d'entrée et le temps de séjour sont ceux du moteur aéronautique Lemcotec. On montre que jusqu'à un niveau de complexité donné, la sécurisation de la précision dans la reproduction du problème de micro-mélange permet également de calculer les propriétés de flamme laminaire prémélangée. Le nombre d'espèces en dessous duquel un seul ensemble de paramètres chimiques ne peut garantir l'exactitude sur une large gamme de rapports d'équivalence, typiquement dans la région riche, est ensuite déterminé. Pour réduire davantage le schéma cinétique, tout en préservant les propriétés de flamme voulues, une stratégie d'optimisation différente dans laquelle les constantes pré-exponentielles d'Arrhenius peuvent évoluer avec la richesse du mélange est adoptée. Le mécanisme Aj-tabulé obtenu est appliqué en retour par validation croisée entre le problème de micro-mélange et les calculs de flamme laminaire prémélangée. Enfin, l'Aj-tabulation est testée sur la simulation de chambre 3D LES Lemcotec, permettant de prédire le niveau de CO en sortie de chambre avec seulement 15 espèces transportées, et 72 réactions élémentaires associées. Par rapport aux 26 espèces transportées par N. Jaouen [147], la réduction du mécanisme s'est traduite par une réduction du CPU d'un facteur 2, entraînant avec l'ordonnanceur dynamique de YALES2, par une réduction totale du CPU d'un facteur 4 sans dégrader la prédiction du niveau de CO et ainsi confirmer l'utilisation de la stratégie.

Résumé du chapitre 6

Avec les futures normes de réduction de suie appliquées aux moteurs d'avion, il est primordial de développer de nouveaux modèles, capables de prédire la formation de suie à faible coût et compatibles avec les délais industriels. Les modèles déjà disponibles dans la littérature peinent encore à combiner la qualité de la prédiction avec un faible coût CPU, en particulier pour la distribution de taille de particules de suie.

Dans ce chapitre, nous proposons de tester une solution alternative, basée sur des réseaux de neurones, permettant de réduire un modèle de suie hautement prédictif HYPE. Cette stratégie est d'abord employée pour récupérer une distribution de taille de particules de suie d'une flamme de suie 1D prémélangée, et montre des prédictions correctes par rapport au modèle HYPE. Ce premier test a également permis d'estimer le surcoût pour poursuivre l'utilisation de cette stratégie dans une configuration industrielle.

Ensuite, le développement de cette stratégie a continué pour une simulation de chambre de combustion LES 3D avec chimie complexe. Afin d'entraîner le réseau de neurones, une base de données de suie a été créé, basée sur le modèle HYPE couplé à la configuration stochastique ORCh.

Le but final ici a été de simuler une chambre de combustion représentative du turboréacteur SAM146, à un point de fonctionnement. Cela s'est fait avec le modèle de chimie complexe HyChem et l'utilisation du réseau de neurone, préalablement entraîné avec la base de données de suie correspondante. Finalement, une prédiction la distribution de taille de particules de suie ainsi que la masse totale de suie dans la chambre a été possible, pour un coût supplémentaire seulement de 40%. La fraction volumique de suie est relativement correcte comparée aux essaies ainsi que la density de suie au diamètre moyen mesuré.

Résumé des perspectives

Perspectives de l'application CNN

Les réseaux entraînés étant basés sur la variable de progrès, paramètre générique des flammes prémélangées, nous émettons l'hypothèse qu'ils fonctionneront bien pour toute flamme prémélangée turbulente située dans le diagramme-régime de Borghi proche des conditions utilisées pour l'entraînement. Néanmoins, c'est une application qu'il faut faire pour valider la généralisation de ces réseaux.

Vers une prévision des polluants moins coûteuse

La prochaine étape serait de gagner des performances CPU sur la résolution LES présentée dans cette thèse, en particulier avec la résolution de suie qui nécessite des mécanismes cinétiques relativement importants, et de préparer les études futures avec les mécanismes des biocarburants. Une solution consiste à utiliser des réseaux de neurones pour prédire directement les termes sources des espèces, comme cela a été fait dans les travaux de Wan *et al.* [148], dans lesquels un coût de réduction du processeur majeur a été obtenu en évitant le calcul des taux d'Arrhenius et l'intégration directe du système chimique rigide.

Modélisation des suies

La stratégie du modèle de suie présentée dans cette thèse a été déployée avec plusieurs hypothèses qui méritent d'Ítre analysées dans un futur travail.

Premièrement, le rayonnement des suies n'a pas été pris en compte dans ces travaux. Il serait judicieux d'ajouter un modèle de rayonnement à la description des suies dans YALES2, afin de quantifier son effet. De plus, il n'y avait qu'un couplage unidirectionnel avec la température et la fraction pyrène dans la simulation 3D. Un travail futur serait de coder un couplage bidirectionnel. Le modèle de transport de suie peut en mÍme temps Ítre amélioré pour le cas Mermose, par exemple en définissant différents nombres de Schmidt par section de taille de suie. à terme, l'impact de la modélisation gazeuse par rapport au carburant liquide sur la production de suie devrait Ítre quantifié.

La résolution 3D avec le réseau neuronal doit Ítre directement comparée, avec une résolution similaire avec le modèle de Leung, en termes de prédiction de densité de suie et de coût CPU. Aussi, l'influence de la grille de discrétisation des suies doit Ítre analysée plus attentivement, car elle conditionne grandement la PSD dans cette thèse. Concernant l'ensemble de la validation de la stratégie, une ultime application sera faite, le graveur Soprano.

Une deuxième application : Le brûleur Soprano

La stratégie ORCHydS sera appliquée pour une configuration différente, à savoir le brûleur SOPRANO (projet EC) de CORIA. Cela permettrait de s'appuyer sur moins de modèles et d'hypothèses, avec un mécanisme cinétique plus simple basé sur l'acétylène, une expérience gazeuse et des distributions de suie expérimentales mesurées à différents points de fonctionnement. Comme les mesures de suie ont été effectuées avec des méthodes non intrusives, voir les travaux de M. Bouvier emph et al. [255], la distribution de suie du LES 3D résolu avec la stratégie ORCHydS pourrait Ítre directement comparée à la suie expérimentale distributions dans la zone réactive.